High Pressure – High Temperature Synthesis and Studies of Nitride Materials

A thesis presented to the University of London in partial fulfilment of the requirements for the degree of Doctor of Philosophy

Emmanuel Soignard

University College London

October 2003

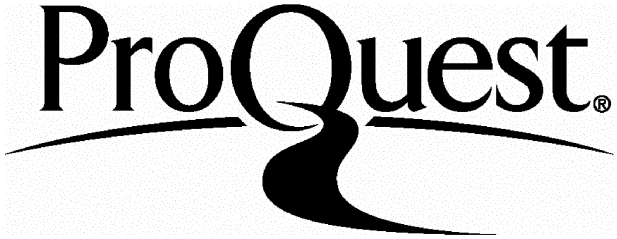

Abstract

This thesis develops the topics of synthesis and study of nitride materials under extreme conditions of high pressure and high temperature. The thesis presents two main research projects.

The investigations were only possible after developing and building the Raman spectroscopy and laser heating system presented in details in the second chapter of this thesis. We designed and built this equipment specifically for diamond anvil cell research and micro-Raman spectroscopy studies on very weakly scattering samples.

The first investigations develop the study of group IV nitrides, silicon and germanium nitrides. The experiments determined the compressibility of the high pressure phase γ-Si_3N_4 and the synthesis of the first ternary phases in the spinel system Si_3N_4 – Ge_3N_4. In particular, the phase $GeSi_2N_4$ was found to be a normal spinel with silicon atoms in octahedral sites and germanium atoms in octahedral sites. The Raman spectroscopy study of the spinel nitride phases following laser heating at high pressure indicated that they commonly possess N vacancies. Experiments were performed on the low pressure phases α- and β- germanium nitride at low temperature. Upon metastable compression, β-Ge_3N_4 transformed, into a new δ-Ge_3N_4 phase at 22 GPa, followed by amorphisation above 35 GPa.

The second set of investigations presents a study of transition metal nitrides at high pressure. Here we show the results of the first bulk modulus measurements for two phases of molybdenum nitride, TiN_x, Cr_2N and TaN. These materials are highly incompressible with bulk modulus values exceeding 300 GPa. We also performed for the first time a Raman spectroscopy study, including measurements at high pressure for selected transition metal nitrides. We observed that δ-MoN and ε-TaN, which are both hexagonal, have very similar Raman spectra, although the structures are different. Finally, we measured the Raman spectrum of B1-structured nitrides, TiN_x, VN_x and γ-Mo_2N and observed their phonon density of states. No phase transition was observed upon room pressure compression for any of the transition metal nitrides studied.

Table of Contents

Table of Figures

Table of Tables

Table of abbreviations

AD	Angular dispersive
ANL	Argonne National Laboratory
APS	Advanced photon source
ASU	Arizona State University
a. u.	Arbitrary units
bcc	Body centred cubic
BM-D	Bending magnet beamline station D
CCD	Charge coupled device
ccp	Cubic closed packed
CVD	Chemical vapour deposition
DAC	Diamond anvil cell
E	Energy
ED	Energy dispersive
EDXRD	Energy dispersive X-ray diffraction
eV	Electron volts
fcc	Face centred cubic
F-IR	Far-infra-red
FL	Flawless at a 10 x magnification
GPa	Giga-Pascal
GSECARS-CAT	GeoSoilEnviro Consortium for Advanced Radiation Sources Collaborative Access Team
GDFT	Generalised density functional theory
hcp	Hexagonal compact packing
IF	Internally flawless
K_0	Room pressure bulk modulus
K_0'	Room pressure bulk modulus pressure derivative
λ	Wavelength
LDA	Local density approximation
Nd:YAG	Neodymium doted yttrium aluminium garnet
Nd:YLF	Neodymium doped yttrium lithium fluoride
N-IR	Near infra-red

NSLS	National synchrotron light source
P	Pressure
SEM	Scanning electron microscopy
SRS	Synchrotron radiation source
T	Temperature
T_c	Superconducting transition temperature
TEM	Transvers electromagnetic mode
UCL	University College London
UV	Ultraviolet
VS	Very slightly included
VVS	Very very slightly included
XRD	X-ray diffraction

Acknowledgements

I first would like to thank Professor Paul F. McMillan, for his supervision, guidance and motivation throughout the course of this research. I am also extremely appreciative of the EPSRC, who funded this research.

In addition, I am very grateful to numerous people for their help and advices concerning many aspects of the work. Dr Guoyin Shen (APS) gave me access to state of the art facilities and taught me much about laser heating and X-ray diffraction. Dr Maddury Somayazulu (APS) was the first to show me how to build a CO_2 laser heating system and allowed me to build an energy dispersive X-ray diffraction beamline sector 9 of the APS. Dr Ho-Kwang (Dave) Mao and Dr Daniel Hausermann (APS) allowed me to work at the APS as part of his group during the first six months of my PhD. Dr Kurt Leinenweber (ASU) taught me multi anvil techniques and was always very supportive while I was in Arizona. Prof. Richard Nelmes, Dr Malcolm McMahon and Dr Clivia Hejny who allowed me to perform the X-ray diffraction experiment at the SRS using their equipment. Mr Roy Northeast and the UCL chemistry workshop built two of the diamond anvil cells used in most of the experiments as well as many little pieces required during the course of the research. All the people at the UCL chemistry technical support provided a tremendous help with the many problems encountered during the building of the UCL laboratory. Mr Daniel Rosen (4C's London), always sold us the excellent Raman diamonds used in the research. He always provided the best and fastest service possible and made this research possible.

In a more general way I say thank you to the members of Professor McMillan's research group at UCL - RI and in particular Dr Craig Bull, Dr Tracey Chaplin and Mr Dominik Daisenberger for their help and friendship. I also thank the people in sector 13 and 16 at the APS for their help during my stay at the APS and all the people from the office 301 who have now become very good friends.

Finally, gratitude is due to my parents and Tyson Winarski esq. who have continued to offer much encouragement and support.

Chapter 1.

Introduction to the Chemistry and Structure of Early Transition Metal and Group IV Nitrides.

1.1. Introduction

Nitrogen bonds to most of the elements of the periodic table to form binary nitrides. Often more than one nitride stoichiometry exists for a given element (see below). The solid state chemistry of nitride compounds has received increasing attention over the past two decades [1-6]. Binary and ternary compounds are nominally based on the N^{3-} ion and have structures analogous to the oxides. There is also a wide range of highly covalent nitrides like AlN and GaN. There are also numerous examples of complex nitrides and nitride imide (-N(NH)) structures that have no counterpart among the oxides [1-10]. To date, there are very few reports on the structural chemistry of nitrides under high pressure conditions [11]. This is the topic of the present thesis.

The first part of this thesis focuses on the high pressure chemistry of group IV nitrides, based on Si_3N_4 and Ge_3N_4. The group IV, or group 14, elements are C, Si, Ge, Sn and Pb. There are several reports on the synthesis and structure of silicon and germanium nitrides, as early as 1940 [12]. Both have the stoichiometry A_3N_4 with A = Si or Ge and have a structure related to that of the mineral phenacite. In 1932, Schwarz and Jeanmaire [13, 14] attempted the synthesis of Sn_3N_4. Unfortunately, their only synthesis products were tin imides and nitro-imides [13, 14]. Only in 1999 appeared the first report of a tin nitride phase [15]. The synthesis of lead nitride has not yet been reported in the literature.

The second part of the thesis concerns high pressure structure and properties of transition metal nitrides. Binary transition metal nitrides have relatively simple structures based on a simple packing of the metal atoms with nitrogen atoms in interstitial sites. There are two main groups of binary transition metal nitrides, depending upon the transition metal. The late transition metal nitrides never develop their highest oxidation states, they generally form compounds with low nitrogen contents (e.g., Cu_3N, Fe_2N) [3, 7, 9]. The early transition metal nitrides (group 4 to

group 7) can be non-stoichiometric (e.g., TiN_x) but they can form highly nitrided compounds close to the maximum oxidation state (e.g., Ta_3N_5). The early transition metal nitrides and transition metal carbides have very similar structures and physical properties. Here we have concentrated our study on early transition metal nitrides.

Nitrides possess properties that make them highly desirable for many different technological industrial applications [5, 6, 16, 17]. First, both group 14 nitrides and transition metal nitrides tend to form refractory ceramics with very high hardness (table 1-1). Current thrusts in nitride research include developing new materials and composites for abrasives and structural ceramics applications, as well as transition metal nitride thin films for ultra-hard coatings [3, 7, 18]. More recently, part of the scientific community showed a great interest in research on nanocomposites of materials such as $TiN\text{-}Si_3N_4$ which have hardness values and abrasive resistance that are superior to diamond [19, 20]. However, there is no report indicating that the measurement of the hardness in such nanocomposites using indentation methods is be higher than that of diamond.

	Vickers Microhardness ($kg\ mm^{-2}$)	Melting point (K)
TiN	2100	3220
VN	1500	2619
Cr_2N		2013
Mo_2N	1700	2223
TaN	1000	3366
HfN	1600	3660
$\beta\text{-}Si_3N_4$	1700	2173
WC	2400	3049
TaC	2500	4256
Al_2O_3	2080	2323
C (diamond)	7600	

Table 1-1 Table summarising some of the melting points and Vicker microhardness data available for selected nitrides, carbides, alumina and diamond [3, 7]. The values reported for the transition metal nitrides in particular TiN and VN were measured on samples with compositions close to the stoichiometric compound.

Covalent nitrides such as AlN have high thermal conductivity and they find applications as semiconductor substrates. The group 13 nitrides, GaN, InN and AlN form wide direct bandgap semiconducting materials, with tuneable direct band gaps in the ultraviolet to the green-blue visible range. These are finding applications in new families of optoelectronic devices, as light-emitting diodes and solid state lasers [21, 22]. Superconducting nitrides such as NbN and MoN are also of interest as they possess a high T_c [23] (e.g. T_c up to 17 K for NbN).

Despite the wide current interest in nitrides and their applications, there are large gaps in our knowledge about their solid state chemistry and mechanical properties. Our depth of knowledge for nitrides is not nearly as extensive as it is for the oxides.

1.2. Introduction to nitride chemistry

1.2.1. Introduction

Nitrogen is well known as a gas phase molecule that possesses a very strong triple bond (energy necessary to break the bond 945 kJ mol^{-1} [24]) between the two nitrogen atoms. In comparison, the double bond of diatomic oxygen requires an energy of 498 kJ mol^{-1} to be broken [24]. Furthermore, the ionization potential of N into N^{3-} ion is very large (47.44 eV [24]) in comparison with the ionization potential of O into O^{2-} ion (35.11 eV [24]).

$N_2 \rightarrow 2\,N$ $\quad E_{atomisation}(N_2) = 945\ kJ.mol^{-1}$

$O_2 \rightarrow 2\,O$ $\quad E_{atomisation}(O_2) = 498\ kJ.mol^{-1}$

Consequently, the free energy of formation of a nitride is less negative than that of the analogous oxides. For example (values from ref. [24]): $\Delta G_f(\alpha\text{-}Si_3N_4)$ = -153.6 $kcal.mol^{-1}$ = -643.1 $kJ.mol^{-1}$ and $\Delta G_f(\alpha\text{-}SiO_2)$ = -204.7 $kcal.mol^{-1}$ = -857.0 $kJ.mol^{-1}$. Furthermore, the M-N bond tends to have a more covalent nature than the M-O bond. The increase in covalency results in a decrease in the bandgap e.g. the system GaN – InN has band gaps in the UV, whereas the corresponding oxides have bandgaps in the hard UV. Also, metal nitrides, and carbides, tend to be "interstitial" and they do not develop the highest oxidation states (e.g. MoN and WC *vs* MoO_3 and WO_3). Furthermore, some of the nitrides are not easily synthesised, for example, SnO_2 is naturally occurring and Sn_3N_4 is difficult to synthesise; in the same way PbO_2 exists (in competition with PbO), but Pb_3N_4 does not.

1.2.2. Overview

Nitrides display a wide variety of structures and compositions that are reviewed in several articles and books [1, 3-10]. We can divide in two groups the nitrides discussed in this thesis. The group IV nitrides compose the first one. They have a stoichiometry M_3N_4 where M is silicon, germanium or tin. The early transition metal nitrides compose the second one. They have a stoichiometry MN_x with $0 < x < 1$ (M = Ti, Zr, Hf, V, Nb, Ta, Cr, Mo, W,). They have interstitial structures based on cubic or hexagonal packed metal sublattices. Their structures are similar to that of the related metal carbides. The most common structures for these materials are similar to that of rock salt (NaCl) or are related to that of tungsten carbide [6, 23, 25, 26].

1.3. Group IV nitrides and the first spinel nitrides

1.3.1. Group IV nitrides

Si_3N_4, Ge_3N_4 and Sn_3N_4 represent the group IV nitrides. Silicon and germanium nitrides are very similar in properties and structures. For years, industry has used silicon nitride (Si_3N_4) in its α and β polymorphic forms, which have very similar materials properties, as high performance engineering ceramics. Silicon nitride is hard and it is resistant to corrosion and oxidation. It also withstands high temperature processes up to about 1500 °C and possesses a low density (d = 3.19 $g.cm^{-3}$). Hot-pressed, reaction-bonded, and sintered materials are examples of silicon nitride based ceramics. In summary, silicon nitride is an excellent ceramic material and for example finds applications in gas turbines and heat exchanger systems [27-29].

Both silicon nitride and germanium nitride display two polymorphs at ambient conditions; the α-phase and the β-phase. The β-phase has a structure related to that of the mineral phenacite (Be_2SiO_4), structure shown in figure 1-1.

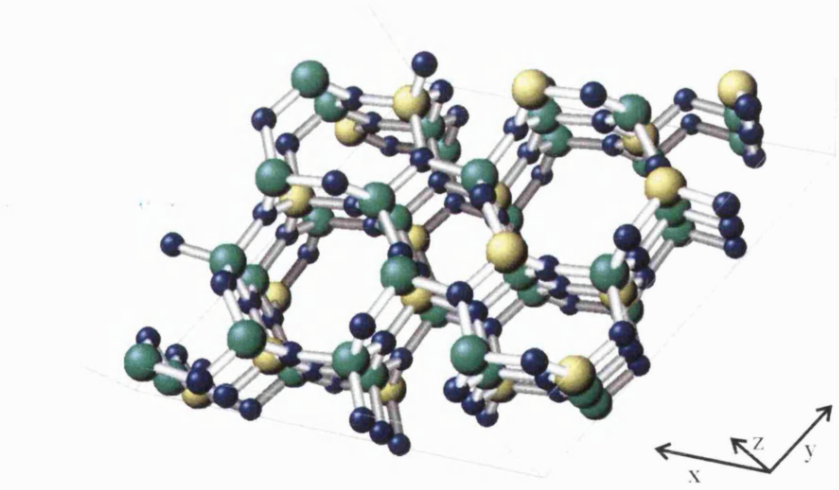

Figure 1-1 Structural representation of the phenacite structure. The small blue balls represent the oxygen atoms, the large yellow balls represent the Si atoms and the large green balls represent the Be atoms.

Wild et al. in 1972 originally thought that the α-Si_3N_4 phase was a oxynitride [30]. In 1974 and 1975, Blegen [31] and other groups [32, 33] disproved the previous observation. As a result, it is common to consider α-Si_3N_4 as the metastable phase of silicon nitride with respect to β-Si_3N_4. The structure of α-Si_3N_4 (figure 1-2) is doubled along the c axis and described as two β- unit cells (figure 1-3) with a 180 ° rotation of the top one with respect to the c- axis. The α- phase does not present the hexagonal and square channels of the β- structure due to the 180° rotation of one of the two superposed units.

In both phases, the Si and Ge cations are tetrahedrally coordinated to nitrogen. In the β-phase, the nitrogen atoms are within the plane formed by the three nearest cation atoms forming a triangle. This plane has an orientation perpendicular to the hexagonal basal plane of the structure. In the α- phase, the N atoms are slightly displaced from the triangular planes.

Atom	Position	α-Si_3N_4			α-Ge_3N_4		
		X	Y	Z	X	Y	Z
N	2a	0.0	0.0	0.384	0.0	0.0	0.349
N	2b	2/3	1/3	0.615	2/3	1/3	0.546
N	6c	0.3103	0.3210	0.6701	0.3288	0.3128	0.7032
N	6c	0.5936	0.6331	0.4001	0.5966	0.6426	0.3812
Si	6c	0.1673	0.2554	0.4509	0.1690	0.2558	0.4458
Si	6c	0.5013	0.0724	0.6462	0.5079	0.0801	0.6429

Table 1-2 Atomic positions for α-Si_3N_4 and α-Ge_3N_4 as described by Wild et al. [30]

α-Si_3N_4 is hexagonal and has the symmetry of the space group $P3_1c$ (No. 159). The atomic positions vary only slightly between different studies. Table 1-2 presents the atomic positions described by Wild *et al.* [30, 34, 35]. The lattice parameters determined by Wild *et al.* are: a = 7.753 Å, b = 7.753 Å, c = 5.617 Å, $\alpha = 90°$, $\beta = 90°$, $\gamma = 120°$.

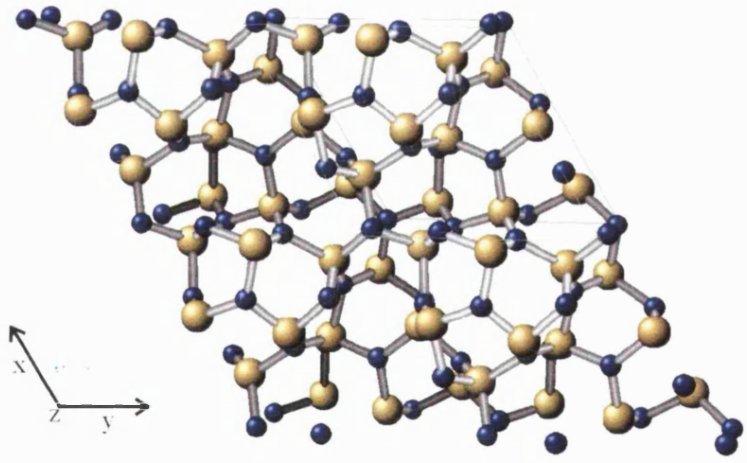

Figure 1-2 A ball-stick model of the α- structure of Si_3N_4 and Ge_3N_4. The small blue balls represent the N atoms and the large yellow balls represent the Si or Ge atoms.

The volume of α-Si_3N_4 is approximately 292.5 $Å^3$ with a density around 3.18 g cm^{-3}. The bulk modulus of α-Si_3N_4 is K_o = 228.5 (± 4) GPa assuming a pressure derivative $K_0' = 4$ [36].

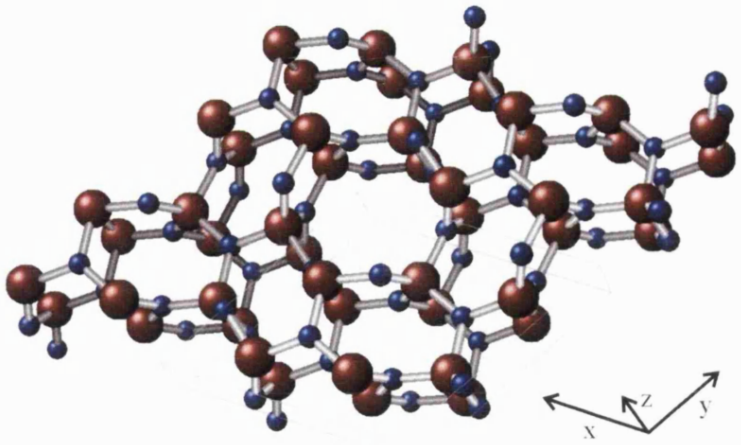

Figure 1-3 ball-stick model of the β- form of Si_3N_4 and Ge_3N_4. The small blue balls represent the N atoms and the large red balls represent the Si or Ge atoms.

Numerous authors have reported the existence of β-Si_3N_4. However, the structure is not consistent for all of the reports. The symmetry is reported as hexagonal and the space group as either being $P6_3$ (No. 173) [37] or $P6_3/m$ (No. 176) [30]. The more recent report of Goodman and O'Keeffe [38] determined that the space group is $P6_3/m$ using electron diffraction techniques on a single crystal. We chose to use the latest space group representation as it is most generally accepted in the literature. In fact, the atomic positions are the same in both space groups and reported in table 1-2. The lattice parameters reported by Wild *et al.* are a = 7.608 Å, b = 7.608 Å, c = 2.911 Å, α = 90°, β = 90°, γ = 120°. The volume is approximately 145 $Å^3$ and the density is approximately 3.19 $g.cm^{-3}$. The bulk modulus of β-Si_3N_4 is K_o = 270 (± 5) GPa and the pressure derivative is K_0' = 4 (± 1.8) [39].

		β-Si_3N_4			β-Ge_3N_4		
Atom	Position	X	Y	Z	X	Y	Z
N	6h	0.0314	0.3323	¼	0.0295	0.3335	¼
N	2c	2/3	1/3	¼	2/3	1/3	¼
Si	6h	-0.2306	0.1733	¼	-0.2342	0.1712	¼

Table 1-3 Atomic positions for β-Si_3N_4 and β-Ge_3N_4 as described by Wild et al. [30].

Ge_3N_4 is very similar to Si_3N_4 and possesses the same two low pressure structures α and β [30, 34]. The alpha phase has a symmetry $P3_1c$ and the lattice parameters are: a = 8.196 Å, b = 8.196 Å, c = 5.930 Å, α = 90°, β = 90°, γ = 120° [30]. The beta phase has a symmetry $P6_3/m$ and the lattice parameters are : a = 8.028 Å, b = 8.028 Å, c = 3.077 Å, α = 90°, β = 90°, γ = 120° [30]. The atomic positions are very similar to the ones determined for the Si_3N_4 phases as shown in table 1-2 and table 1-3. There was no report of the bulk modulus for the α- and β- germanium nitride phase and we determined those values as part of this study (see chapter 4).

1.3.2. Spinel nitrides

There are many examples of spinels in main group and transition metal oxides, sulphides, selenides and halides. However, there was no knowledge of any nitrides occurring with the spinel structure until 1999. In that year, simultaneous high pressure experiments carried out independently on group IV nitrides led to the synthesis of the first two spinel nitrides: γ-Si_3N_4 and γ-Ge_3N_4 [39-52]. Remarkably, in the same year, Sn_3N_4 was also synthesised for the first time, using a reaction involving chemical precursors at room pressure. The structure characterisation showed that it also had the spinel structure. Thus, within a few months of each other, independent groups reported the synthesis of the first three members of the nitride spinel series.

1.3.2.1. Spinel structure

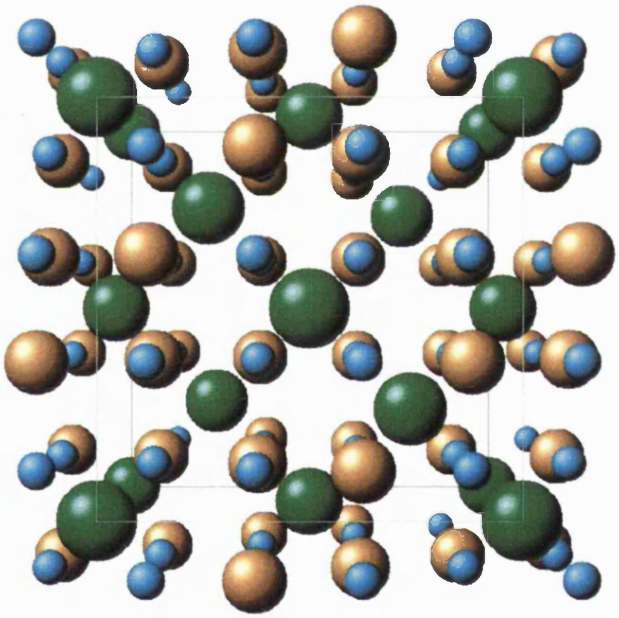

Figure 1-4 Representation of the spinel ($MgAl_2O_4$) structure with in blue the nitrogen atoms, in yellow the octahedrally coordinated aluminium atoms and in green the tetrahedrally coordinated magnesium atoms.

Bragg [53] and Nishikawa [54] first determined the structure "spinel" in 1915 from the type mineral spinel, $MgAl_2O_4$. The spinel structure is a common structure among oxides with a stoichiometry AB_2O_4. In a more general way, spinels have a composition AB_2X_4 where A and B are the cations and X the anions. The spinel structure is a face centred cubic structure with the space group $Fd\bar{3}m$ (No. 227). The primitive cell is rhombohedral and consists of two AB_2X_4 units. Thus there are Z = 8 formula units in the cubic structure (56 atoms). There are 32 X atoms in the structure (32 *e* site). The X atoms are in a pseudo cubic compact packing. There are 96

interstices (64 tetrahedral and 32 octahedral) between the X atoms. Only 8 (8 *a* site) tetrahedral and 16 (16 *c* site) octahedral sites are filled in the structure. The cations possess a MgB_2 structure sublattice [55]. The space group 227 has two possible origins. Thus, there are two possible sets of atomic positions depending upon the origin.

There are in fact two extreme types of spinel structure. In a "normal" spinel (for example, $Mg^{IV}Al_2{}^{VI}O_4$ mineral spinel had Mg in octahedral sites (VI) and Al in tetrahedral sites (IV)) the **A** atoms are located in tetrahedral sites and the **B** atoms have an octahedral coordination. In some cases, however, $\mathbf{A}^{2+}$ and some $\mathbf{B}^{3+}$ are distributed over octahedral sites and the remainder of the $\mathbf{B}^{3+}$ ions occupy the tetrahedral sites, thereby giving rise to the "inverse" spinels (e.g., $CoFe_2O_4$: $Fe^{3+}(Co^{2+}Fe^{3+})O_4$). The most common naturally-occurring spinel is magnetite, which is the oxide spinel Fe_3O_4. This contains Fe^{2+} in one-half of the **B** sites, and Fe^{3+} in the **A** and half of the **B** sites. This is an important material used in magnetic recording applications. In some cases, the composition can be $ABCO_4$ where **A**, **B** and **C** are three different atoms as in $MgAlFeO_4$. In this case, there is a partial solid solution between $MgAl_2O_4$ (normal spinel) and $MgFe_2O_4$ (inverse spinel). The solid solution is incomplete due to the site ordering in the structure. The spinel structure can in fact present a variety of compositions. Furthermore, there are some examples of partly occupied spinels like $Li_xMn_yO_4$ which is used as cathode for rechargeable lithium battery applications. In this case, one can vary the composition of the spinel by increasing the number of vacancies in both the Li and the Mn sites. Furthermore, the manganese displays an increase in its oxidation state with increase of the oxygen content [56, 57].

Spinel can also contain other anions instead of oxygen such as sulphur (i.e., $ZnAl_2S$ normal spinel [58]), selenium (i.e., $HgCr_2Se_4$ normal spinel [59]) and tellurium (i.e., $AgCr_2Te_4$ normal spinel [60]). Recent studies on spinel chalcogenides have shown the existence of colossal magnetoresistance [61, 62]. There are also some examples of spinel halides (e.g. Li_2ZnCl_4 [63, 64]) and chalcogenide halides [65].

1.3.2.2. γ-Si_3N_4

Zerr *et al.* first reported the synthesis of γ-Si_3N_4. They heated a sample of elemental silicon at high pressure within a nitrogen medium in a diamond anvil cell using a high-power near-IR laser [41]. The sample was then probed using Raman spectroscopy, and by transmission electron microscopy after recovery to ambient conditions in order to establish the cubic spinel crystal structure. They also used the electron micro-probe to determine the chemical composition. The results showed a spinel structure with a Si_3N_4 composition. The following report from Soignard *et al.* [46] described the first synthesis of γ-Si_3N_4 from the β-Si_3N_4 phase in the diamond anvil cell. Jiang *et al.* and Schwartz *et al.* later independently reported the bulk

synthesis of this material at high pressure and high temperature using a multi anvil press [44, 45]. Simultaneously, Sekine *et al.* reported the synthesis of the cubic silicon nitride using shock-induced transformation of β-Si_3N_4 [42].

Various studies have reported lattice parameter values for γ-Si_3N_4, varying between 7.7381 and 7.76 Å [41-45]. Part of this variation presumably results from differences in the data quality and details of the refinement among different laboratories, but some variation in the lattice parameter also related to oxygen contamination of the sample. This must be investigated in future studies. No single crystals of γ-Si_3N_4 have been prepared to date. Table 1-2 presents the atomic positions determined from Rietveld analysis of the data by Schwarz *et al.*

Atom	Position	X	Y	Z
Si	8b	0.125	0.125	0.125
Si	16d	0.5	0.5	0.5
N	32e	0.2597	0.2597	0.2597

Table 1-4 Atomic positions for γ-Si_3N_4 determined by Schwarz et al.[44].

We first established the equation of state for γ-Si_3N_4 using energy dispersive X-ray diffraction techniques and found a bulk modulus K_o = 308(5) GPa and a pressure derivative K_0' = 4.0(2) [46] (see chapter 3). A later measurement by Zerr *et al.* reports a bulk modulus K_0 = 302(6) GPa assuming K_0' set at 4; and K_0 = 290(5) GPa for K_0' = 4.9(6) [66].

Results of *ab initio* calculations within the local density approximation (LDA) indicate that the spinel phase of silicon nitride should have a direct band gap [40]. The gap is predicted to be 3.45 eV [40]. However, LDA calculations tend to underestimate the band gap by 50 to 100 % [51]. This estimated band gap is smaller than that predicted for β-Si_3N_4 > 4.2 eV [67], which has measured values between 4.6 and 5.3 eV [68-71].

Hardness measurements performed on γ-Si_3N_4 show that the high pressure phase of silicon nitride is an extremely hard material. The measurements give a hardness value of 37(8) GPa which is slightly greater than that of Al_2O_3 (corundum) (H = 32 GPa) [66].

1.3.2.3. γ-Ge_3N_4

Several groups have now reported the synthesis of γ-Ge_3N_4 [47-49]. Leinenweber *et al.* [49] first reported the synthesis of γ-Ge_3N_4 following observation of a metastable phase transition occurring during cold compression of β-Ge_3N_4 (see chapter 4). The synthesis of γ-Ge_3N_4 occurred during subsequent heating of the sample in the diamond anvil cell, followed by synchrotron X-ray diffraction [48, 49]. Leinenweber *et al.* also prepared well-crystallised samples of γ-Ge_3N_4 in a multi-anvil high pressure synthesis device, and determined the structure

by Rietveld methods [49]. In an independent study, γ-Ge_3N_4 was synthesised from Ge + N_2 in a laser-heated diamond cell, above 14 GPa and 2000 K [47]. Following these early syntheses, He *et al.* synthesised γ-Ge_3N_4 by shock wave compression methods [72].

The γ-Ge_3N_4 phase presents a spinel structure with a cubic symmetry $Fd\bar{3}m$ and the lattice parameter is 8.2125 Å. As observed in the spinel phase of silicon nitride, the germanium atoms occupy the tetrahedral and octahedral sites. Table 1-5 presents the atomic positions in γ-Ge_3N_4.

Atom	Position	X	Y	Z
Ge	8b	0.125	0.125	0.125
Ge	16d	0.5	0.5	0.5
N	32e	0.2577	0.2577	0.2577

Table 1-5 Atomic positions for γ-Ge_3N_4 Leinenweber et al. [49].

Somayazulu et al. established the equation of state for γ-Ge_3N_4 using energy dispersive X-ray diffraction and found a bulk modulus K_o = 295(5) GPa and a pressure derivative K_0' = 3.8(2.0) [48]. The bulk modulus found for the spinel phase of germanium nitride is a relatively high value.

The band gap calculated using the LDA for the spinel phase of germanium nitride is around 2.17 eV [51]. However, using a generalised density functional theory (GDFT), Dong *et al.* estimated a band gap of 4.0 eV [51]. There is an increase in the value of the band gap given by the LDA and the value calculated by the GDFT. However, the LDA notoriously underestimates the band gaps. Remediakis and co-workers tested the GDFT for a variety of semiconductors including AlN and GaN, and report typical errors of 10-20 % [73]. Therefore, the calculated band gap of 4.0 eV could be reasonable.

1.3.2.4. Sn_3N_4

Scotti *et al.* [15] first reported the synthesis of a tin nitride with the composition Sn_3N_4 in 1999. The synthesised tin nitride had the spinel structure. They performed the synthesis using SnI_4 and KNH_2 at room pressure and probed the newly synthesised nitride using X-ray diffraction. The refinement concluded that the material has a spinel structure similar to Ge_3N_4 and Si_3N_4 in the space group $Fd\bar{3}m$. The lattice parameter is 9.037(3) Å. Table 1-6 reports the atomic positions of Sn and N. Ching *et al.* have calculated a band gap of 1.29 eV for tin nitride using the LDA [74]. Again, a similar over-estimation of the band gap is expected.

Atom	Position	X	Y	Z
Sn	8b	0.125	0.125	0.125
Sn	16d	0.5	0.5	0.5
N	32e	0.25950	0.25950	0.25950

Table 1-6 Atomic positions for Sn_3N_4 from Scotti et al.[15].

1.3.2.5. Summary

The nitrides presented above are the first spinel nitrides ever reported. Moreover, the spinel phase of tin nitride is the first reported phase of this material. In the spinel structure silicon, germanium, and tin atoms occupy both tetrahedral and octahedral coordination sites. As expected, the lattice parameter of the spinel phase becomes larger from silicon nitride to tin nitride as the cations become larger.

The spinel structure is associated with a very high bulk modulus already measured for germanium and silicon nitride, and calculated for tin nitride [46, 48, 74]. The hypothetical cubic phase of C_3N_4 with a calculated bulk modulus around 377.6 GPa is expected to be "harder than diamond" [40].

1.4. Binary transition metal nitrides

1.4.1. General information

There are only a few examples of binary transition metal nitrides reported in mineralogy, i.e. TiN (Osbornite), CrN (Carlsburgite) [75]. In fact, those minerals are only reported in meteorites. Nevertheless, transition metal nitrides are a major component of hard ceramics and widely utilized in industry as coating materials for tools and metals[3, 7]. There is a wide range of composition and properties known for the transition metal nitrides. Titanium nitride and zirconium nitride exist in compositions ranging from the pure metal up to the 1:1 metal to nitrogen ratio (figure 1-5). Niobium nitride had the highest superconducting transition temperature (T_c ~17 K) among the simple binary compounds until the discovery of the superconductivity of magnesium diboride (MgB_2 T_c = 39 K) [76]. Those properties are interesting from the physicists' point of view in order to gain a better understanding of the superconductivity.

In over a century of transition metal nitride research, various scientists have used varying nomenclatures to describe the different structures and compositions formed. For clarity, we chose to use the same nomenclature as that used by Toth [7]. The phases have different names

depending upon their composition and also their structure. The α- phase usually corresponds to the pure metal with the Greek letter increasing with increasing nitrogen content. For example, figure 1-5 presents the phase diagrams of the Ti-N and Zr-N systems. Figure 1-6 shows the phase diagram of the Mo-N and Nb-N systems. Those diagrams display the complexity of the nitride systems, and also demonstrate the considerable range of uncertainty still existing within the metal nitride phase diagrams.

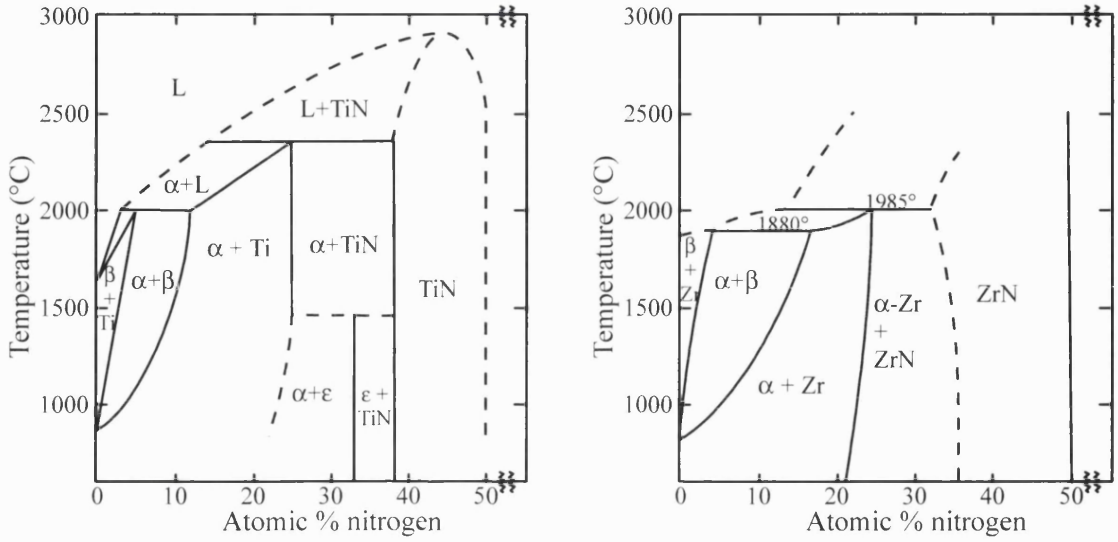

Figure 1-5 Room pressure phase diagram of the Ti-N and Zr-N systems [7].

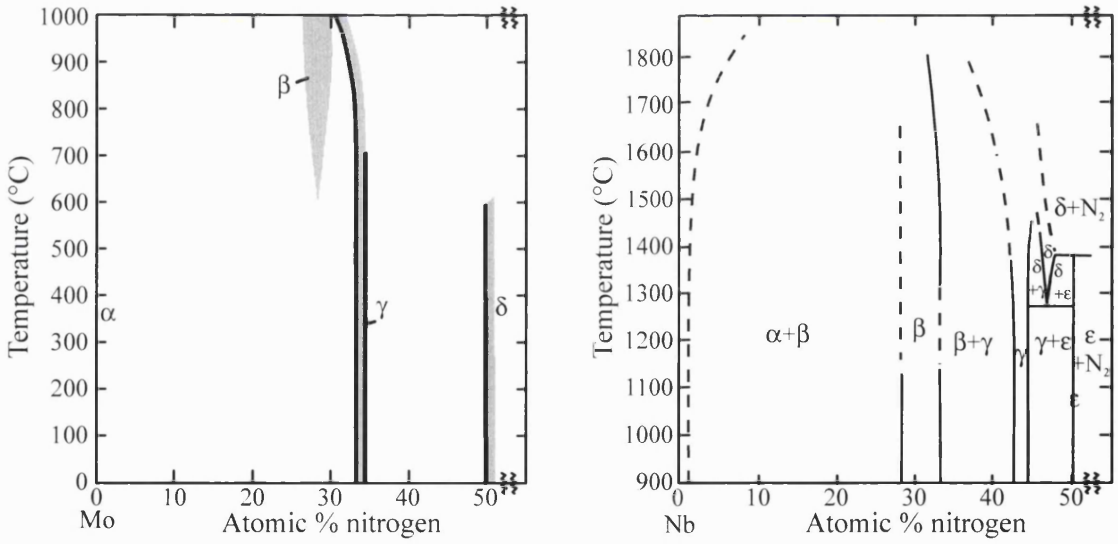

Figure 1-6 Room pressure phase diagram of the Mo-N and Nb-N systems [7].

It is common to describe transition metal nitrides as an interstitial structure based on a metal atom framework with interstitial nitrogen. However, the framework described by the metal atoms is not that of the elemental metal. In fact, the transition metals Cr, Mo, Ta, W have a body centred cubic (*bcc*) (space group $Im\bar{3}m$) structure at ambient conditions. As this structure is relatively open-packed, they are expected to transform to denser packing such as hexagonal

close packed (*hcp*) (space group $P6_3/mmc$) or cubic close packed (*ccp*) (identical with face centred cubic (*fcc*)) (space group $F\bar{4}3m$). Although this sequence is expected in some cases, the alkaline-earth metals Ca and Sr display a *hcp* to *bcc* transition. In fact, there is no report of a phase transition occurring for Cr, Mo, Ta or W upon pressurisation. Nevertheless, Cr for example has not been studied above 10 GPa. Therefore, the possibility of phase transitions is not excluded. However, Mo for example was studied up to 100 GPa at room temperature and showed no phase transition[77]. Ti, Zr and Hf are *hcp* at room pressure and temperature. Upon pressurisation, those three metals transform into a hexagonal (β-Po structure) ω-phase. However, at high temperature, above 900 °C, they become *bcc*. Therefore, the metals presented above would all be *bcc* in the nitride synthesis conditions.

It is worth emphasising a few points on transition metal nitrides before proceeding to a more developed study. First of all, the syntheses of transition metal nitrides performed at ambient pressure principally gives rise to materials with structures based on either the sodium chloride B1 structure (space group $Fm\bar{3}m$ (No. 225)), or structures related to that of tungsten carbide (space group $P\bar{6}m2$ (No. 187)), with hexagonal stacking of the metal atoms. Secondly, the composition of binary transition metal nitrides often covers a wide range. It is therefore common to refer to transition metal nitrides as non-stoichiometric materials. The compositions are typically MN_x with $0 < x < 1$ ($x = 0$ is the pure metal). Nevertheless, at low nitrogen either the nitride exists and has the structure of the pure metal (e.g. Ti-N and Zr-N systems presented in figure 1-5) or does not exist (e.g. Mo-N and Nb-N systems presented in figure 1-6). However, in most cases the composition limit of the binary transition metal nitrides is MN (M is the metal) [9, 26], even if there are some exceptions like Ta_3N_4 [78-80], Th_3N_4 [81] and Zr_3N_4 [82]. More recently, Zerr *et al.* have also reported the existence of high pressure cubic phases, Zr_3N_4 and Hf_3N_4 [83].

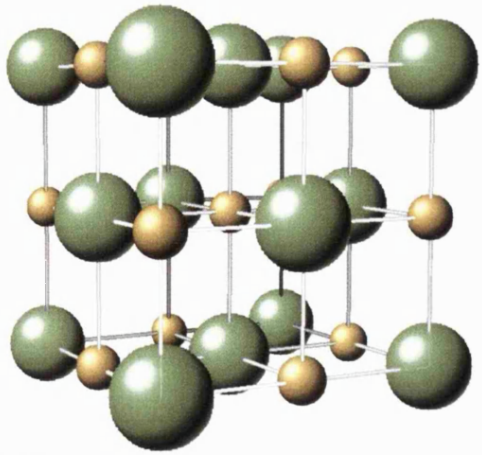

Figure 1-7 NaCl B1 Structure.

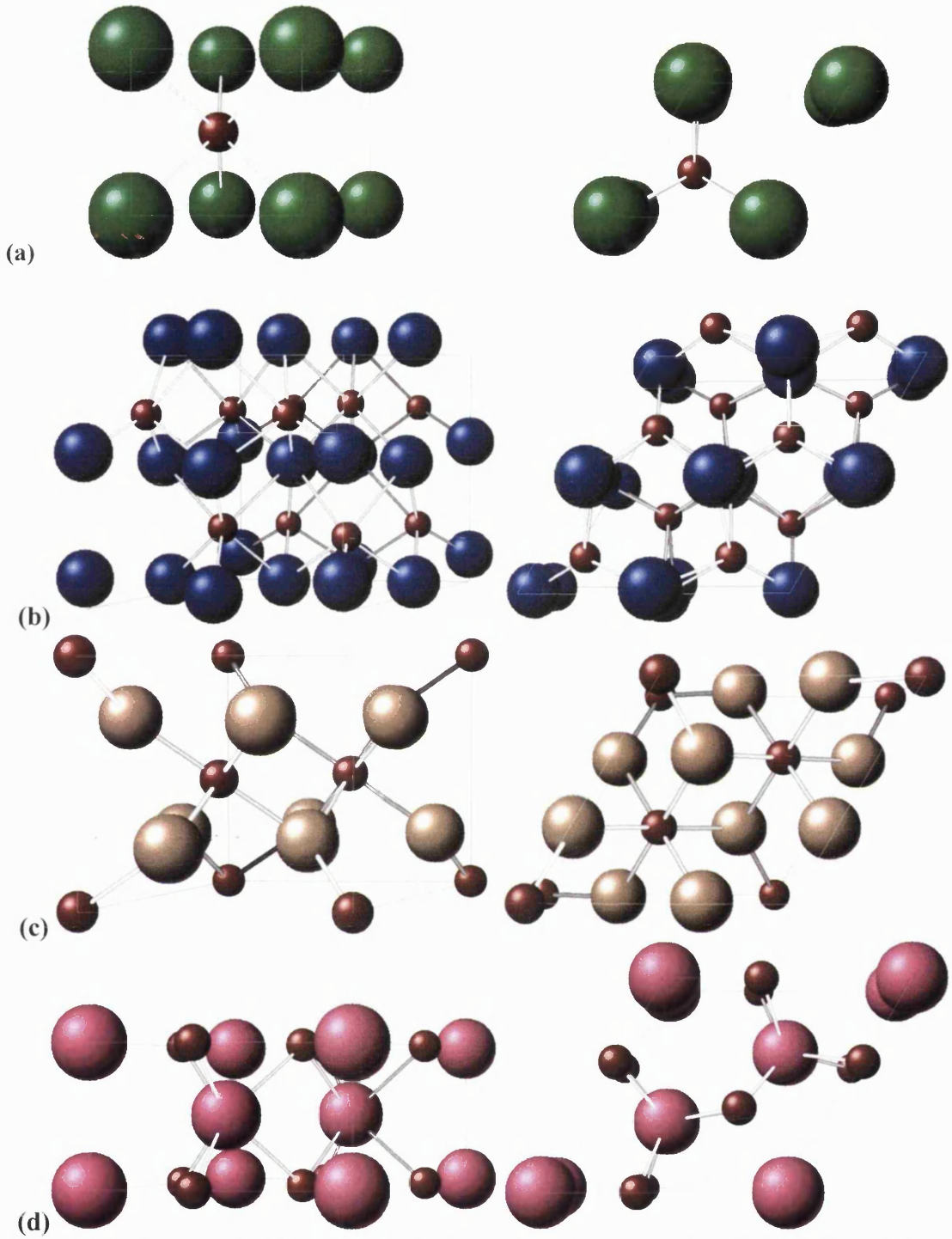

Figure 1-8 Tungsten carbide related structures of transition metal nitrides (a) WC structure, (b) δ-MoN structure, (c) Cr_2N, (d)ε-TaN. In each case, the small red balls represent the N atoms and the large balls represent the metal atoms.

As noted in the introduction, the cubic transition metal nitrides are: TiN, ZrN, HfN, VN, and δ-NbN. Figure 1-5 presents the phase diagram of the Ti-N, Zr-N and Nb-N systems. The nomenclature of the phases of transition metal nitride is as a function of composition and not structure.

	Lattice parameter Calculated (Å)	Lattice parameter Measured (Å)	Density ($g.cm^{-3}$)	Lattice parameter Metal (*bcc*) (Å)	Density ($g.cm^{-3}$)
TiN	4.26	4.24	5.39	--*hcp*--	4.50
ZrN	4.60	4.57	7.32	--*hcp*--	6.51
HfN	4.54	4.51	13.94	--*hcp*--	13.28
VN	4.12	4.13	6.12	3.026	6.11
δ-NbN	4.40	4.39	8.39	3.307	8.53
δ-TaN	4.38	4.36	15.62	3.297	16.77
CrN	4.14	4.14	6.18	2.884	7.20
γ-MoN	4.22	------	9.72	3.147	10.22
WN	4.20	------	17.74	3.165	19.26

Table 1-7 Lattice parameter and density of some B1 structured transition metal nitrides [84] along with the lattice parameter and density of bcc metals.

Although table 1-7 presents data on B1 TaN, CrN, TaN, MoN and WN, those compounds also possess a hexagonal structure related to tungsten carbide. Hexagonal ε-TaN has the Ta atoms in the position of the W and C atoms of the tungsten carbide structure with N atoms in interstitial positions leading to a doubling of the cell along the a axes. The Cr_2N structure is rather different as the N atoms are in octahedral sites. It is possible to describe the structure as a monoclinic distortion of the WC structure along the c axis with a displacement of the N atoms within the hexagonal plane as shown in figure 1-8. We present the δ-MoN structure below.

1.4.2. Molybdenum nitride "high pressure" synthesis

Molybdenum nitride is largely comparable with niobium nitride in particular for its superconducting properties (table 1-8). However, its phase diagram is much simpler (figure 1-6). Hägg first determined the Mo-N phase diagram in 1930. The phase diagram presents three phases. The δ- phase (hexagonal structure) has a composition restricted to MoN with very little variation allowed. The γ- phase (B1 like structure) possesses a composition very close to Mo_2N. The β- phase is a high temperature phase (above 700 °C) resulting from a tetrahedral distortion of the γ- phase. Its composition is more nitrogen deficient than γ-Mo_2N.

		T_c (K)			T_c (K)
δ-MoN	*Hex.*	12.0 [85]	MoC	*Hex.*	9.26 [86]
γ-Mo_2N	*B1*	5.0 [86]	α-Mo_2C	*Hex.*	2.78 [86]
NbN	*B1*	17.3 [7]	NbC	*B1*	10.3 [86]
TiN	*B1*	4.86 [86]	W_2C	*Hex.*	2.74 [86]
ZrN	*B1*	9.05 [86]			
VN	*B1*	7.5 [86]			

Table 1-8 Example of some superconducting transition temperatures for selected nitrides and carbides with hexagonal (hex.) or B1 structure.

Very few experiments on high pressure synthesis of transition metal nitrides are reported in the literature. Moreover, the synthesis pressures are often very low, only a few GPa [87, 88]. For example, the synthesis of MoN was performed at only 2 GPa [87]. However, the MoN phase synthesised at high pressure is hexagonal and not the cubic phase as originally expected (high T_c superconductor [89]). Hart *et al.* demonstrated that the B1 structured stoichiometric MoN is elastically unstable, thus demonstrating that a successful synthesis is unlikely [90]. However, Furio *et al.* recently calculated that small distortions of the structure leading to a doubling or tripling of the unit cell would stabilise the structure. In that case, a B1-like MoN phase should be accessible.

The synthesis of MoN_{1-x} ($x \sim 0.5$) at low temperature gives rise to a poorly crystalline cubic phase with the NaCl B1 structure space group $Fm\bar{3}m$ (No. 225). The molybdenum atoms are on the 4a sites and nitrogen atoms are on the 4b sites. You-xiang et al. calculated the lattice parameter a = 4.22 Å for pure γ-MoN [84]. Marchand et al. [91] have discussed the changes in X-ray diffraction peaks intensity as a function of nitrogen content. There are large changes. As a result, it is possible to estimate the composition of γ-MoN_{1-x} using X-ray diffraction (see chapter 5).

Zhao and Range have reported the synthesis of this hexagonal phase at "high" pressure and temperature [90]. They synthesised the hexagonal phase using molybdenum dioxide and ammonium chloride in a 2:1 ratio. The mixture was then pressurised at 20 kbar (2.0 GPa) and heated to 1500°C. The structure refinement performed on the X-ray diffraction patterns did not allow the differentiation between the $P\bar{3}m1$ (No. 164) and $P6_3/mmc$ (No. 194) space groups. The lattice parameters determined by Zhao et al. are a = 5.72(9) Å and c = 5.60(4) Å. In the $P6_3/mmc$ (194) space group, the molybdenum atoms are in the positions 2b (0,0,1/4) and 6h (x,2x,1/4) x = 0.48(9), the nitrogen atoms are in the positions 2a (0,0,0) and 6g(0.5,0,0). In fact, this structure is not correct for several reasons. Chapter 5 discusses the validity of the structure refinement performed by Zhao.

1.5. Summary and aims

The aim of this project is in the first part to explore and determine the properties and the possible compositions in the group IV spinel nitride field, in particular within the Si_3N_4 – Ge_3N_4 spinel system. In the second part of the thesis, we study the compressional behaviour and vibrational properties of early transition metal nitrides.

During these studies, we synthesised new materials using diamond anvil cell and laser heating techniques and multi anvil press techniques (see chapter 2). The materials are then characterised

using X-ray diffraction, Raman and infrared spectroscopy and electron microprobe. The completion of those experiments involved the design and building of a laser heating and micro-Raman spectroscopy system and access to synchrotron X-ray diffraction facilities.

Chapter 2.

High Pressure - High Temperature Research

Experimental Techniques

2.1. Introduction

The development of diamond anvil cells has led to the studies of condensed matter under static high pressure conditions. Today, the pressure is extending into the multi-megabar range, under simultaneously very high or ultra low-temperature conditions. The applications of these techniques are ranging from Earth and planetary science, to solid state physics and chemistry, and materials science [92-97]. Multi anvil press techniques also allow reaching high pressure and high temperature in a more modest regime. The pressure range encountered during the experiments presented in the thesis is from room pressure up to about 80.10^9 Pa or 80 GPa. The temperature ranges from room temperature up to about 4000 K. These experimental apparatuses are ideal for exploring synthesis of new materials under high pressure and high temperature [96, 97].

Chapter 2 introduces the major high pressure and high temperature synthesis apparatus and analytical techniques used to carry out our studies. The high pressure synthesis tools are diamond anvil cells, laser heating systems and multi-anvil presses. We used X-ray diffraction, primarily synchrotron X-radiation, and Raman spectroscopy in order to investigate the properties of the materials presented in the thesis. We are placing a particular emphasis on the Raman and laser heating system we designed and built in the laboratory during the past three years.

The last part of this chapter presents a brief overview of the thermodynamic principles and tools utilised during the design of the experiments and the data analysis.

2.2. Analytical techniques

2.2.1. X-ray diffraction

2.2.1.1. Introduction

Today, X-ray diffraction is a standard technique employed in the determination of the structure of single crystals and to a lesser extent powders. Research uses laboratory X-ray sources extensively. However, this type of X-ray source only provides a low intensity X-ray beam. Consequently, one requires large sample volumes (several mg) in order to obtain a good powder diffraction spectrum. A diamond anvil cell experiment involves only a small amount of sample ($< 10^{-4}$ mm^3), thus the use of a laboratory X-ray source would require us to collect for at least 24 to 48 hours in order to obtain an acceptable powder diffraction pattern. However, the use of very sensitive detectors can improve those collections times to some extend. Thus, diamond anvil cell research requires a much brighter X-ray source. Synchrotron sources and especially third generation synchrotrons sources have a considerably higher flux of X-rays (figure 2-4). Synchrotrons allow the collection of X-ray diffraction patterns from a sample in a diamond anvil cell in just a few seconds (or minutes). A further advantage of synchrotron X-rays is the possibility of tuning the energy of the monochromatic beam to the optimum wavelength. For example, the most common laboratory X-ray sources are from copper, molybdenum and silver. The copper radiation (CuKα: λ = 1.5406 Å; E = 8.06 keV) is not suitable for a diamond cell experiment as diamond strongly absorbs the radiations in that region of the electromagnetic spectrum (figure 2-8). A more standard choice of radiation for laboratory based diamond anvil cell experiments is MoKα which has a higher energy (λ = 0.7093 Å, E = 17.5 keV). At that energy, 4 mm of diamond, typical thickness for a diamond anvil cell experiment, only absorbs 50 % of the radiation.

2.2.1.2. How does X-ray diffraction work?

The X-rays range from soft X-ray: (0.1 keV – 1 keV) to hard X-rays (10 keV and over). X-ray diffraction experiments at high pressure require energies between 15 and 50 keV (~ 0.25 - 0.8 Å). The wavelength is in the order of the atomic size and interacts with the electrons of the atoms. Thus, rows of atoms acts as a dispersion grating and disperse the light. The same way a specific grating at a set angle would send a monochromatic light beam in a specific direction, the rows of atoms with a set interatomic distance are sending a monochromatic X-ray beam in a specific direction. The crystal is an array of atomic planes. Therefore, constructive and destructive interactions of the X-rays occur in the crystal. X-ray diffraction allows the determination of the crystal symmetry and the interatomic distances. Using Bragg's equation

(1) and Planck's equation (2) (for energy dispersive X-ray diffraction), one can translate the X-ray diffraction patterns into inter-planar distances.

$$n\lambda = 2d\sin\theta \tag{1}$$

where λ is the wavelength of the incident beam, d the inter-planar distance and θ the angle between the incident beam and the atomic planes. Figure 2-1 explains relation (1) geometrically. BG and BH are perpendicular to AB and BC respectively so AB = DG and BC = HF. In order to ensure that the waves are in phase GE + EH must be equal to $n\lambda$. Using trigonometry we see that GE = d sin θ and EH = d sin θ. Thus GE + EH = 2 d sin $\theta = n\lambda$.

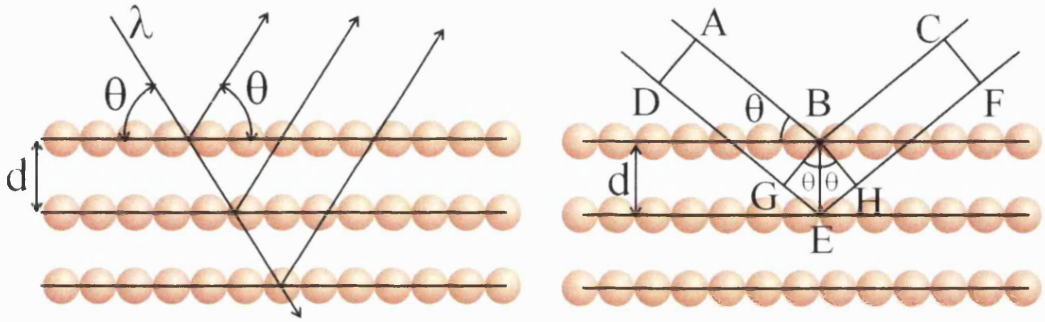

Figure 2-1 Geometry of X-ray diffraction. If there are other atoms present between the layers, the intensity of the diffraction spot will decrease.

$$E = \frac{hc}{\lambda} \tag{2}$$

where E is the energy, c the speed of light, λ is the wavelength and h is the proportionality constant known as Planck's constant ($h = 6.63\times10^{-34}\,J\cdot s$). One can also write this equation as equation (3) when E is in eV and λ in nm.

$$E = \frac{1241}{\lambda} \tag{3}$$

In the thesis, we present data from X-ray diffraction experiments performed only on powdered sample. In that case, the diffraction pattern results from a multitude of randomly oriented crystallites. Therefore, instead of obtaining one diffraction spot for each d-spacing, a full diffraction ring is generated (Figure 2-2).

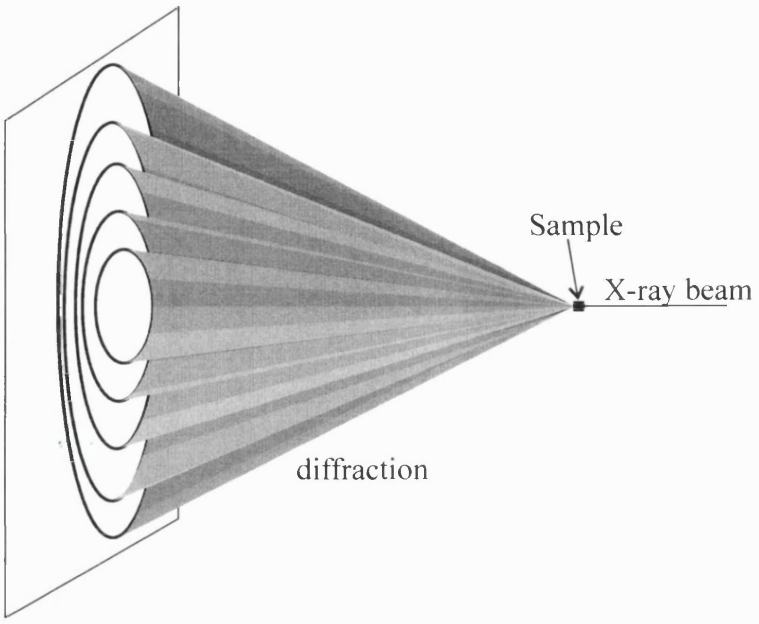

Figure 2-2 Illustration of an angular dispersive powder diffraction experiment.

In angular dispersive X-ray diffraction, a monochromatic X-ray beam passes through the sample. Thus, the diffraction from the sample collected on the detector corresponds to the intersection between the diffraction cones and the detector. The X-ray pattern (Figure 2-10) is the result of the integration around the rings (intersection between a cone and the orthogonal detector plane) (figure 2-2). Consequently, in angular dispersive diffraction, the variable in Bragg's equation is the angle θ. So the d spacing can be calculated as $d = f(\theta)$.

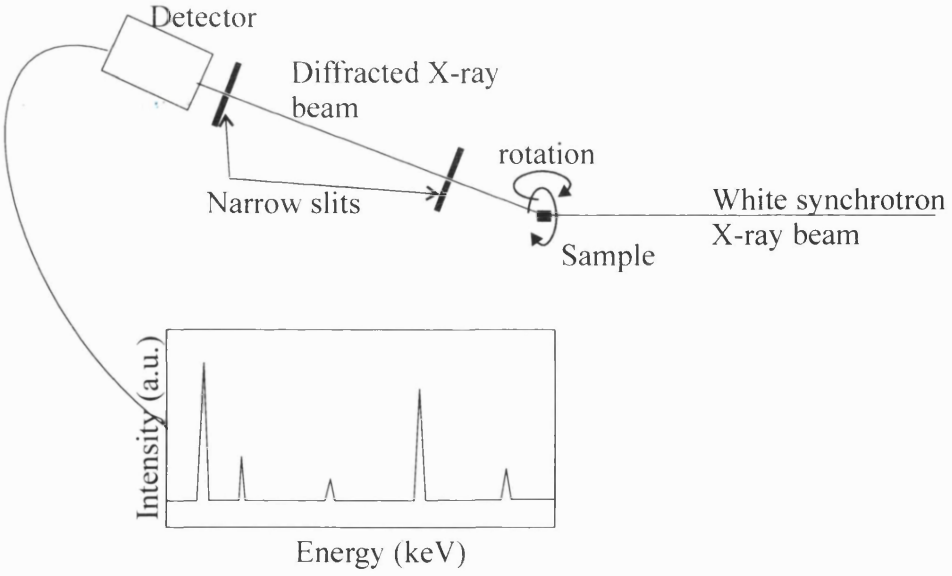

Figure 2-3 Diagram showing an example of energy dispersive diffraction experiment. Arrows indicate the rotations of the diamond anvil cell in order to reduce the texturing problems.

In energy dispersive X-ray diffraction experiments, a white beam passes through the sample (Figure 2-3). The detector is either a single one-dimension or a small number of one-dimension detectors aligned along a circle. Each detector reads the number of photons as a function of

energy. Thus, the d spacing is a function of the energy for a given angle: $d = f(E)$. Using equation 1 and 2 one can easily deduce the equation 4.

$$d = \frac{hc}{2E\sin\theta} \tag{4}$$

2.2.1.3. What is a synchrotron?

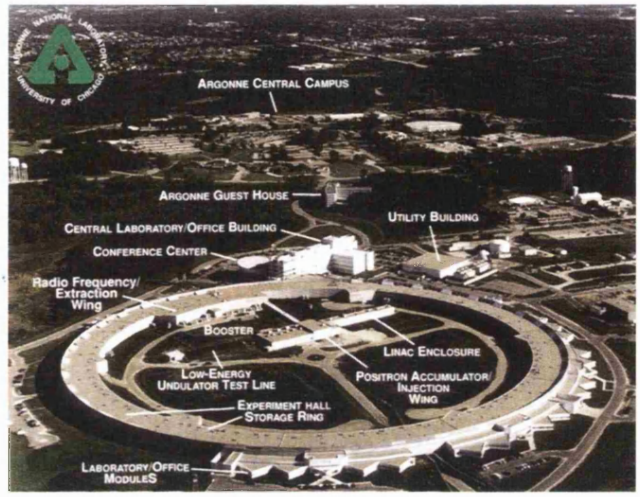

Figure 2-4 Picture of the Advanced Photon Source (APS), a third generation synchrotron located at the Argonne National Laboratory (ANL) south of Chicago (Illinois, USA).

Synchrotron radiation arises from the acceleration of a charged particle (positron or electron) circulating at a velocity close to the speed of light [98, 99]. The simplest way to create X radiation is to use a "bending magnet" (figure 2-5). The bending magnet gives the shape of the storage ring. However, progress in synchrotron radiation techniques gave rise to insertion devices (figure 2-5). The insertion devices generate a much higher flux of X-rays.

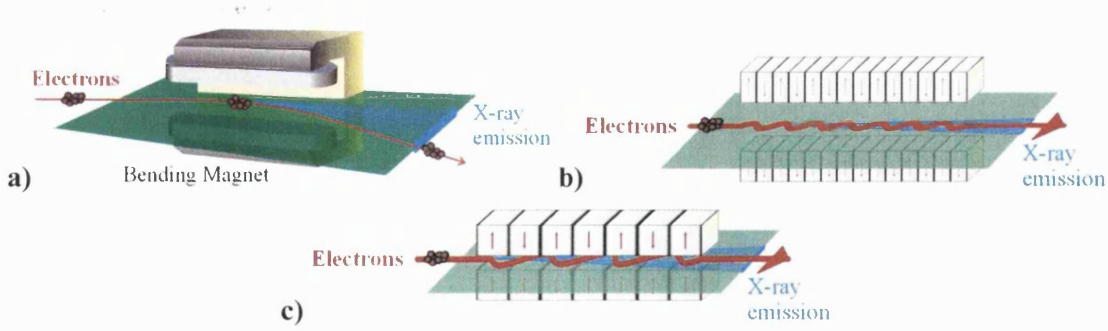

Figure 2-5 Schematic representation of a) bending magnet, b) undulator and c) wiggler.

To reach such a high speed the particles must accelerate. The first part of the acceleration process takes place in the electron gun where a cathode-ray emits electrons. A first magnetic field accelerates the particles up to 100 keV*. The linear accelerator (Linac) then pulses the electron and increases the energy up to 450 keV. In the following step, an injection process sends the particles into the booster synchrotron. The booster synchrotron then accelerates the particles up to 7 GeV using electromagnets. In the final step, an injection procedure sends the particles into the storage ring. Although the particles should only travel in a straight line, bending magnets curve their trajectory (figure 2-4). Each time a magnet bends the beam of particles the particle produces energy in the form of photons along the incoming direction of the particles. Thus, the photons are propagating in a tangent to the storage ring. The photons have energies ranging from the far-infrared (F-IR) to the X-ray regime (figure 2-6).

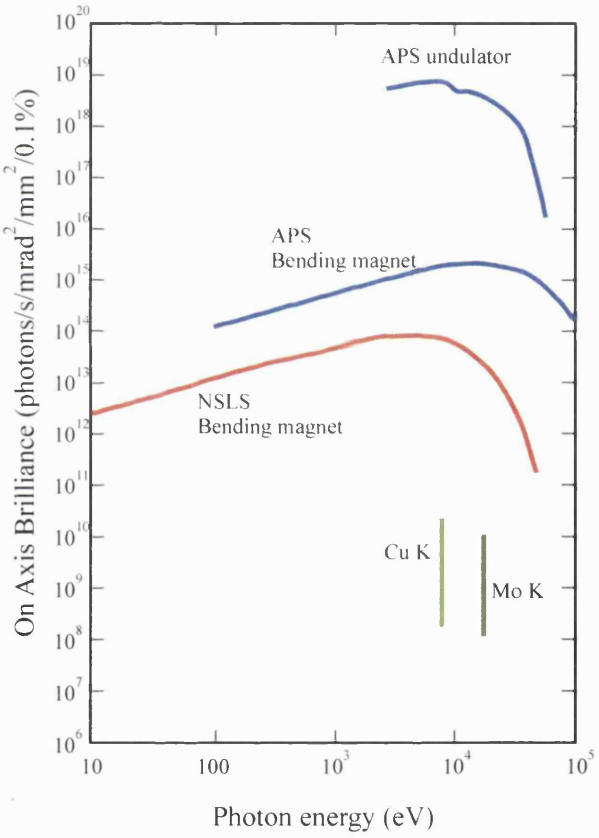

Figure 2-6 Examples of brilliance curves for synchrotron radiation. The vertical lines displaying the brilliance of Cu K and Mo K radiations show the range of brilliance available from various X-ray tube sources. Diagram adapted from that presented on the APS website.

---

* The values of energies given in this paragraph correspond to the Advanced Photon Source (APS) at Argonne national laboratory (USA).

In third generation synchrotrons, and to some extent first and second generation synchrotrons, the particles (positrons or electrons) also create X-rays by passing through insertion devices (wiggler or undulator). The wiggler/undulator is an array of positive and negative permanent magnets. The particles undulate while travelling through the device. At each deflection, the particle emits synchrotron radiation (X-rays form part of the emitted synchrotron radiation). The X-ray brilliance is increased by several orders of magnitude from a bending magnet beamline to an insertion device beamline. The increase in the brilliance is due to the much smaller angular dispersion of the radiation and the increased number of dipoles. A further advantage of wigglers in low energy synchrotrons is their capability of shifting the X-ray energy range to higher energies (undulators do not allow a shift in wavelength). This is particularly valuable for diamond anvil cell experiments as diamond strongly absorbs low energy X-rays (figure 2-8).

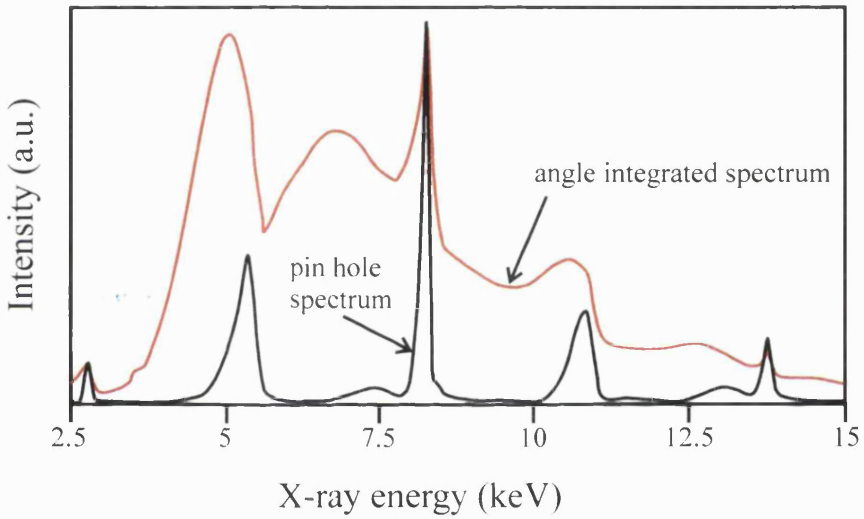

Figure 2-7 Radiation spectra from an undulator with a field of 0.2 T and a beam energy of 7.1 GeV through a pin hole and angle-integrated after removal of the pinhole after reference [98].

Wigglers are formed by a succession of superconducting magnets generating very high magnetic fields of several Tesla. The energy distribution resulting from a wiggler has a continuous spectrum. Typically, there is a much larger number of poles in an undulator. The magnetic field of an undulator is also weaker, usually less than 1 Tesla. Consequently, the deflection of the particles is much less. As a result, the wavelength of the X-ray should be monochromatic with some harmonics. The energy distribution of an undulator is a line spectrum (figure 2-7). The divergence of the beam coming out of an undulator is also smaller than that at the output of a wiggler. Changing the distance between the opposed magnets (gap) modifies the energy of the lines.

2.2.1.4. Energy dispersive X-ray diffraction

To perform an energy dispersive experiment we require a source capable of providing X-rays in an energy range between 10 and 55 keV. Diamond absorbs strongly between 5 eV (ultraviolet) and 10 keV (figure 2-8) and the sensitivity of the germanium detector, used for the experiment, decreases dramatically above 55 keV. The choice of the 2θ angle set for the experiment depends upon the size of the lattice. A smaller angle (8-10°) is better to measure large d spacing. We performed all of our experiments at 2θ angles ranging from 8° to 15°.

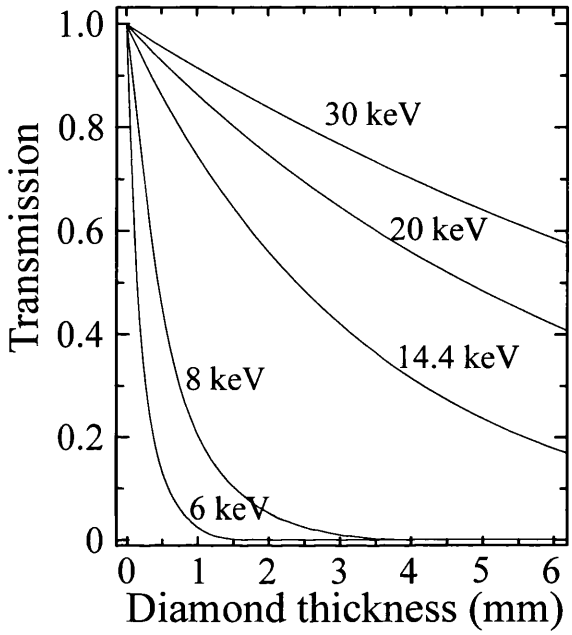

Figure 2-8 Diagram showing the amount of diamond absorption as a function of diamond thickness and energy (from Dadashev et al. [100]).

We calibrate the energy range covered by the detector using the emission lines of radioactive sources and by tuning the gain and the shaping time on the amplifier. Then we collect the diffraction pattern of a standard sample, for example, the tungsten wire from the alignment cross hair, in order to calibrate the 2θ angle. The tungsten diffraction peaks allow calculation of the angle very accurately.

The interpretation of an energy dispersive X-ray spectrum presents several issues. In particular, it is not recommended to perform structure refinement (e.g. Rietveld refinement) because the sample may be textured (e.g. preferential orientations, can cause very dramatic changes in the relative intensities). As the diffraction pattern is not collected throughout the diffraction cones, the operator do not observe if the sample is textured. In a 2D diffraction pattern, the spottiness of the pattern show if the sample has texture problems. In that case, the integration of the full rings average the diffraction pattern and correct the texturing problem to an certain extent. Furthermore, we only have an approximate knowledge of the beam energy profile and the X-ray

absorption by the diamonds at high pressure. In order to minimise the texturing problems, a motorised stage rotated the cell around the X-ray axis, therefore providing a better averaging of the relative intensities (Figure 2-3). However, the rotation does not always allow collecting all the reflections.

2.2.1.5. Angular dispersive X-ray diffraction

In order to perform an angular dispersive experiment in a diamond anvil cell it is important to have a high photon flux as this type of experiment requires a monochromatic X-ray beam. We performed angular dispersive X-ray diffraction (EDXRD) experiments on sector 13 GeoSoilEnviro Consortium for Advanced Radiation Sources Collaborative Access Team (GSECARS-CAT) at Advanced Photon Source (APS) at the Argonne National Laboratory (ANL) south of Chicago (Illinois, USA) and at the Synchrotron Radiation Source (SRS) in Daresbury (UK) beamline 9.1.

As shown above, the X-rays produced by the synchrotron are not monochromatic (figure 2-6 and figure 2-7). A monochromator, either channel-cut monocrystal (typically silicon (220) or (111)) or a double crystal (typically made of 2 single crystals i.e. silicon or diamond) (figure 2-9), renders the white beam monochromatic. The "white" X-ray beam enters the monochromator at a set angle. The beam comes out of the monochromator after two reflections. The monochromatic output beam is parallel to the input white beam but has a different height. The angle between the crystal and the incoming white X-ray beam determines the energy of the monochromatic beam exiting the monochromator.

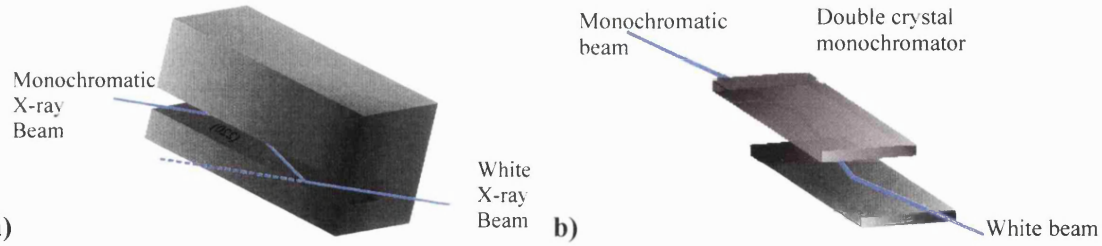

Figure 2-9 Illustration of (a) channel-cut crystal monochromator and (b) double crystal monochromator.

We collect the diffraction pattern with an X-ray sensitive area detector. In a first approximation, the X-ray wavelength, the distance between the sample and the imaging detector, and the spatial resolution of the detector determine the resolution of the diffraction pattern. We used two types of detectors: CCD detectors and image plates. The image plate has a better resolution and covers a larger area than the CCD. Table 2-1 helps to make a choice between CCD detector and image plate. For example, it may be better to use a CCD detector for studies of phase transitions at

high temperature when one collects a lot of spectra. However, for a fine structure analysis one may prefer the use of an image plate, even though the image plate requires a longer reading time.

The main advantages of using a CCD detector are the speed, the good spatial and geometrical correction. However, one should not use a CCD detector for long collection time (more than a few minutes) as it has a small dynamic range (number of intensity levels) and is likely to saturate or induce some electronic noise. The image plate is excellent for long exposure times well over an hour. Thus, it is more appropriate to use the image plate for weakly scattering samples. The spatial distortion correction of image plates with online readers is excellent. Image plates read using an independent reader can give rise to non reproducibility in the reading of the image plate. However, in some cases, the reader is particularly accurate and gives rise to an exceptionally good correction (like in the case of the reader used at Daresbury by the Edinburgh group).

	CCD detector	Image plate
Detector size	100 x 100 mm	200 x 300 mm
Pixel size	88 μm	100 μm
Typical distance from the sample	200 mm	300 mm
Reading time	Few seconds	Several minutes
Spatial and geometrical corrections	Good	See above
Requires opening of the hutch for each new diffraction spectrum	NO	YES

Table 2-1 Comparison between instrumental parameters of CCD detector (Bruker 1K) and image plate used at GSECARS-CAT (APS).

The monochromatic beam is fairly large (in the order of 1 x 1 mm) and it is important to keep as many photons as possible in order to obtain good quality spectra. So it is often imperative to focus the beam using for example Kirkpatrick-Baez mirrors [101] (K-B mirrors). K-B mirrors allow the focusing down to beam sizes of less than 30 μm. In order to stop any beam shape imperfections, we also use cleanup slits which in some cases also reduce the size of the beam.

In the experiments performed on the superconducting wiggler beamline 9.1 at the SRS, we did not use a focused beam. A pinhole defined the beam size. Therefore, the incident X-ray beam was significantly weaker than on the bending magnet beamline 13 BM-D at APS/GSECARS which provides a focused beam.

2.2.1.6. X-ray diffraction data processing

The processing of angular dispersive data is very important. The image plate, or CCD detector, do not have a perfect geometry. Therefore, we must correct the distortion. We place a regularly perforated mask in front of the detector and collect the image of the mask. From this image, we calibrate the distortion of the detector and the unwarping matrix. Finally, we apply the unwarping matrix to correct the data distortion. The next step is the calibration of the data prior to integration. We must determine the sample – detector distance as well as the tilt and the position of the detector with respect to the X-ray beam. To obtain these parameters, we collect the spectrum of a standard material like CeO_2 (figure 2-10). Finally, we integrate the data along the rings in order to transform the pattern from two dimensional to one dimensional (figure 2-10).

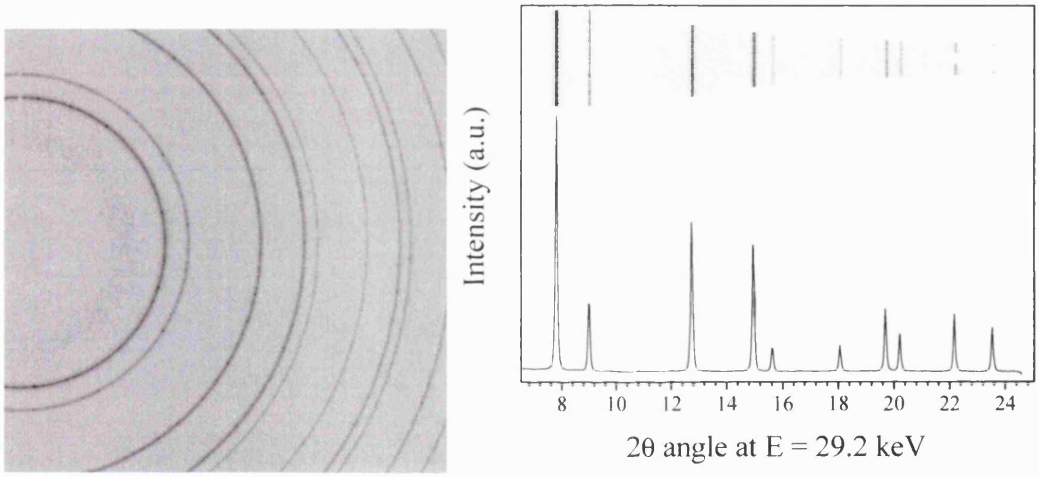

Figure 2-10 2D diffraction pattern of CeO_2 on the left and integrated diffraction patterns on the right The top inset in the integrated pattern shows an intermediate step in the pattern where each of the radius of the 2D pattern are juxtaposed vertically. This intermediate step is important to observe any error in the integration and the deviation of the diffraction rings from perfect circles.

We performed this procedure using the software Fit2D [102] for the data collected at the APS and using the software EDIPUS (from the University of Edinburgh) for the data collected at the SRS (UK). We calibrated the data collected at the SRS and APS using respectively a Zr foil and CeO_2 powder.

2.2.2. Raman spectroscopy

2.2.2.1. The Raman effect

Two groups, CV Raman and K.S. Krishnan in India, and G. Landsberg and L. Mandelstam in Germany [103-105] first described the Raman effect in 1928. The Raman effect results from the inelastic interaction of light with matter. Scientists commonly use Raman spectroscopy to study gases, liquids and solids. In most cases, Raman spectroscopy is a non destructive analysis tool for a sample as small as a few micrometers, unless the sample burns, decomposes or transforms under the laser.

When an electromagnetic wave interacts with matter, some energy exchanges occur. The material absorbs some of the energy. The energy excites the material into a virtual energy level. The released energy is quantised and depends upon the possible vibrations of the atoms within the material. However, not all the vibrations give rise to a Raman peak. A phonon can only give rise to a Raman signal if it induces a change in polarisability. In order to be Raman active, the vibration has to obey the selection rules [106].

The frequency and intensity of the Raman scattering depends upon the exciting wavelength. Furthermore, the Raman frequency for a specific vibration is independent of the exciting wavelength.

The classical description of the Raman scattering (described for a diatomic molecule) results from an electromagnetic wave (E_0) interacting with the material and inducing a dipole moment (μ_{ind}):

$$\overrightarrow{\mu_{ind}} = \alpha \vec{E} \tag{7}$$

with α the polarisability tensor.

$$E = E_0 \cos[2\pi \nu^* t] \tag{8}$$

$$\alpha = \alpha_0 + \alpha_1 \cos[2\pi \nu_i t] \tag{9}$$

with ν^* the frequency of the incident electromagnetic wave and ν_i the frequency of vibration, α_0 in the equilibrium polarisability tensor and α_1 the derived polarisability.

$$\mu_{ind}(t) = \alpha_0 E \cos(2\pi \nu^* t) + \tfrac{1}{2}\alpha_1 E_0 \cos(2\pi(\nu^* + \nu_i)t) + \tfrac{1}{2}\alpha_1 E_0 \cos(2\pi(\nu^* - \nu_i)t) \tag{10}$$

Rayleigh Raman anti-Stokes Raman Stokes

A vibration (phonon) results in a Raman peak only if the polarisability changes during the vibrational displacement. For example, it only depends upon the deformation induced in the crystal. Typically, highly symmetric vibrations are the most Raman active.

Figure 2-11 presents a quantum way to describe the Raman effect. The phonon excites an electron into a virtual level. Consequently, there is photon emission at a different energy. If the electron was in an excited state, the emitted energy is larger than that of the incoming photon and creates an anti-Stokes band. If the electron was not in an excited state, the emitted photon has a lower energy than the incoming photon and creates a Stokes-shifted peak in the spectrum of the scattered light. At any temperature above 0 K, the Raman effect generates both anti-Stokes and Stokes bands (figure 2-12) and equation 11 gives the ratio of their intensities as a function of temperature.

$$\frac{I_{anti-stokes}}{I_{Stokes}} = \left(\frac{\nu^* + \nu_i}{\nu^* - \nu_i}\right)^4 \exp\left(\frac{-\hbar\nu_i}{kT}\right) \qquad (11)$$

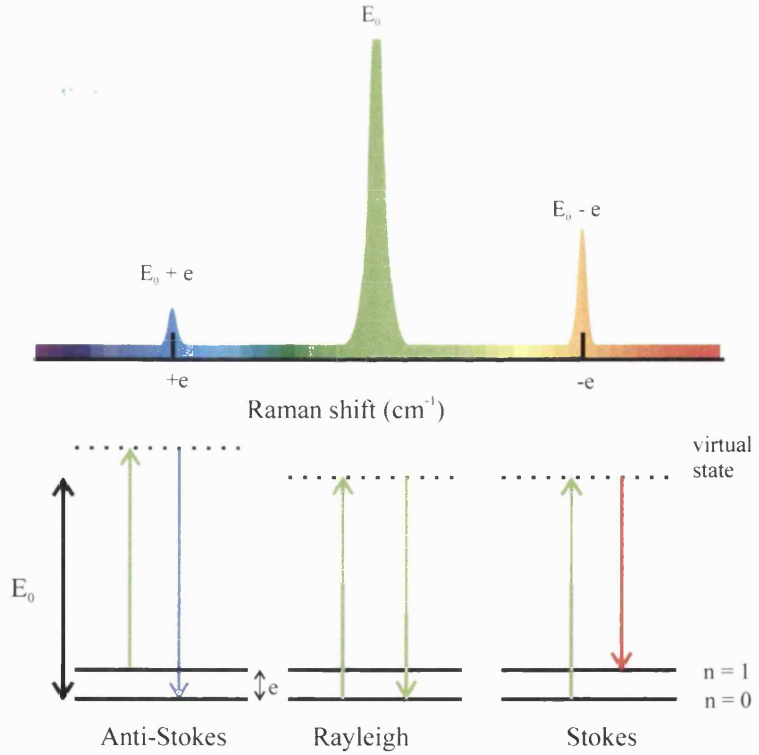

Figure 2-11 Schematic representation of the Raman effect.

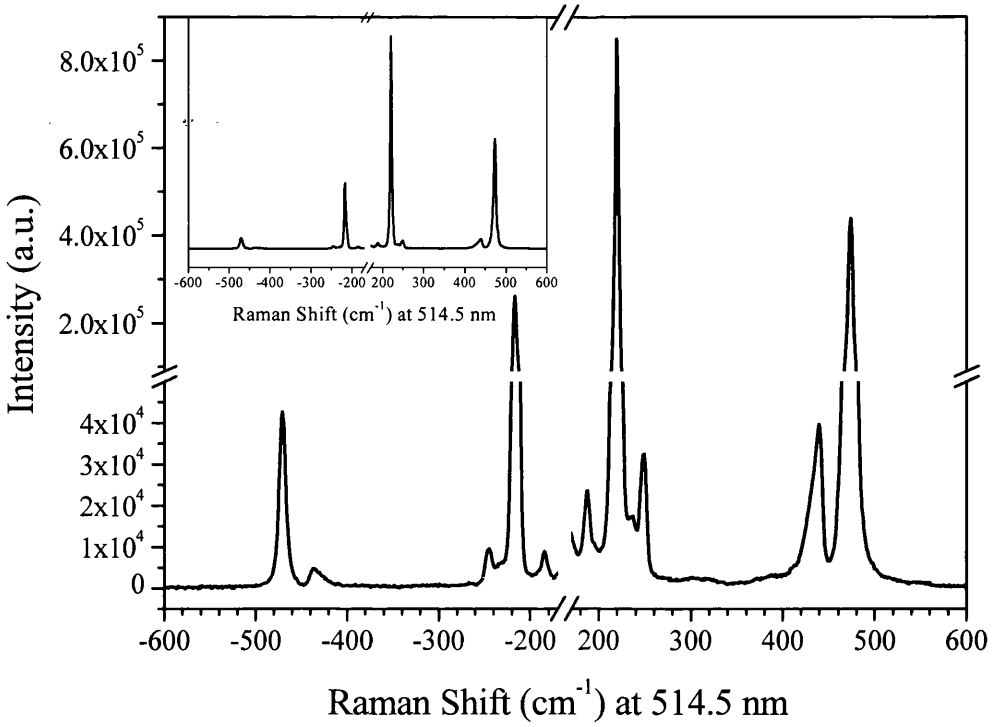

Figure 2-12 Example of Raman spectrum showing the Stokes and anti-Stokes bands of a sample of sulphur collected at room temperature. We cut and rescaled the intensity axis in order to emphasise the low intensity peaks. The top left corner inset presents the spectrum without the intensity truncation. We also cut the spectrum between -170 and 170 cm^{-1} where the notch filter cuts the signal of the straight through laser line.

2.2.2.2. The Raman system

As described above, the Raman effect results from the excitation of a sample with light. The intensity of the scattering resulting from the Raman effect is six orders of magnitude weaker than the intensity of the exciting light. The intensity is also dependant upon the wavelength of the exciting light, with a relation $I \sim I_0/\lambda^4$ where I is the Raman scattering intensity, I_0 the intensity of the exciting light and λ the wavelength of the exciting light. However, the Raman shift is independent of the exciting wavelength. In order to perform a Raman spectroscopy experiment, one requires several elements:

- intense monochromatic exciting light (laser)
- a way to filter the laser line after excitation of the sample (notch filter or pre-monochromator)
- a high resolution spectrometer to disperse the wavelengths
- a very sensitive detector to collect the weak signal

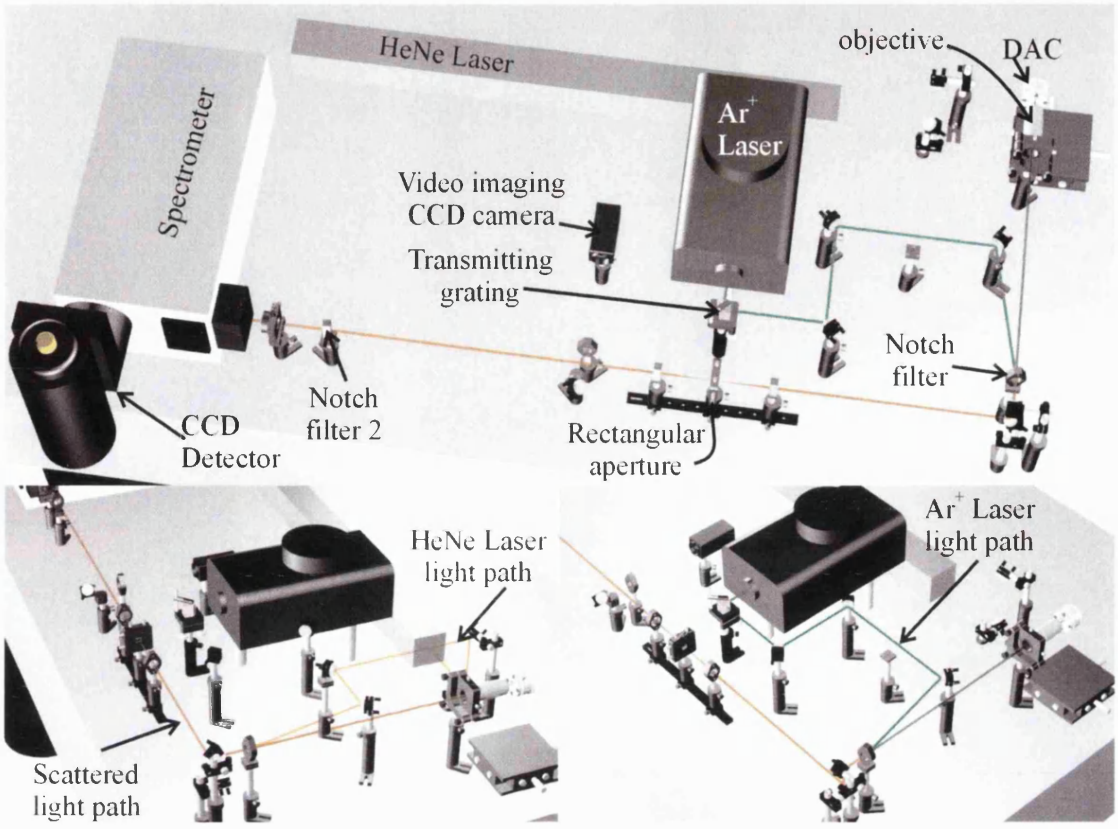

Figure 2-13 Custom built Raman system at UCL, on the left system using the HeNe laser and on the right system using the Ar^+ laser. The orange line indicates the path of the HeNe laser, the green line indicates the path of the Ar^+ laser and the red line indicates the path of the scattering signal from the sample.

I built the micro-Raman spectroscopy system (figure 2-13 and figure 2-14) using a multi line air cooled Ar^+ laser (150M Laser physics®) and a high power HeNe laser (Melles Griot). The Ar^+ laser provides 50 mW of laser light at 514.5 nm and 488 nm which are the two strongest lines. The HeNe laser provides 35 mW at 633 nm. However, one must use a plasma line filter in order to cut the strong and numerous plasma lines from that laser. The plasma line filter cut about 40 to 50 % of the laser power leaving only less than 20 mW of available power. The power lever of the HeNe laser is fixed, so we vary the laser power sent to the sample by placing neutral density filters at the laser output.

We select the laser line of the Ar^+ using a Kaiser® transmitting grating (holographic grating mounted between two prisms). The grating transmits the s polarised (polarisation parallel to the grating) laser line at a 90 ° angle figure 2-15. The grating disperses the wavelengths, and makes their selection possible.

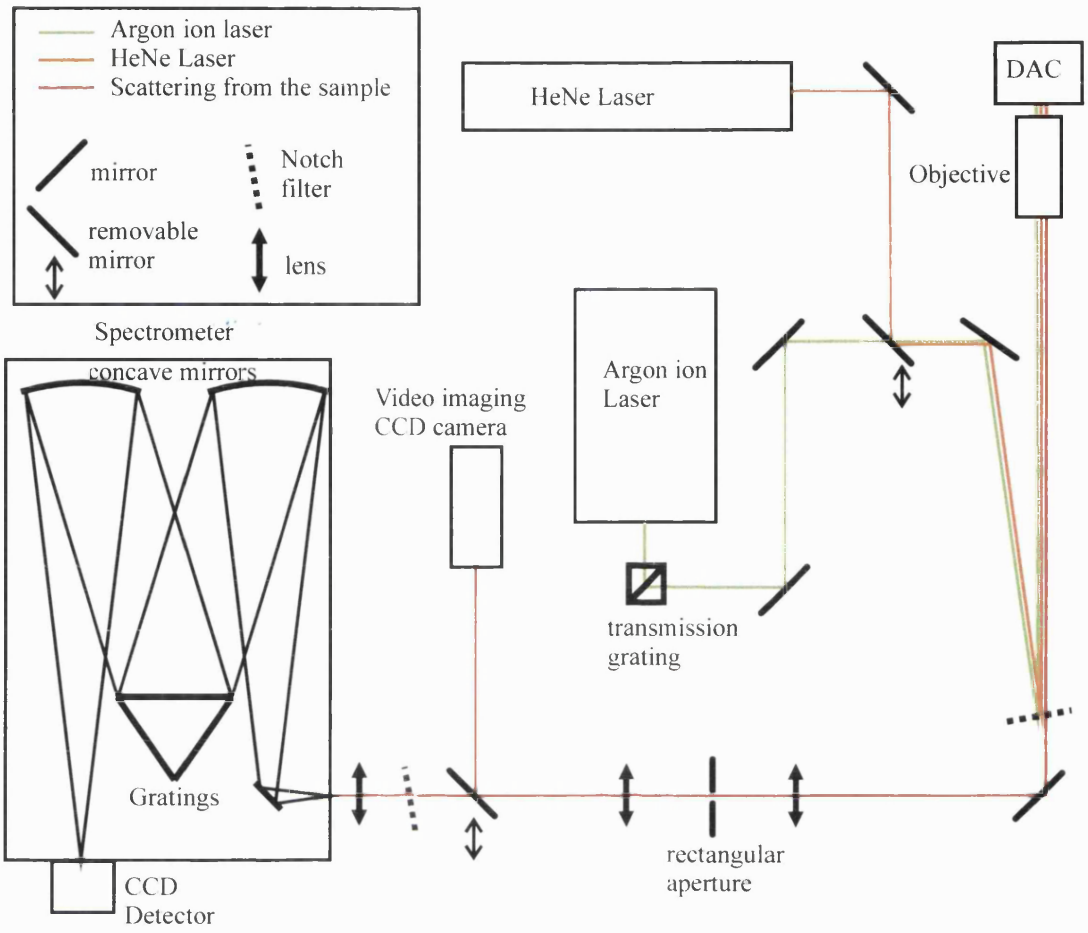

Figure 2-14 Schematic representation of the custom built Raman spectroscopy system at UCL. We shifted the lines representing the various light paths in order to clarify the diagram.

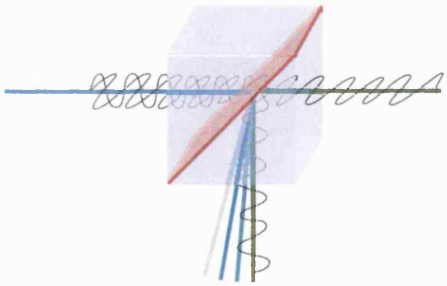

Figure 2-15 Schematic representation of the Kaiser® transmission grating. The grating sends each wavelength at a different angle.

Broadband enhanced Al coated mirrors ($\lambda/10$) steer the laser beam from the laser output to the notch filter. Those mirrors have an average reflectance of 88 % between 400 and 700 nm. At this stage, there is always sufficient laser power so that it is acceptable to have some losses, thus reducing the cost of the optical elements. Finally, a Kaiser® SuperNotch-Plus™ holographic filter at an incidence angle of less than 5 ° sends the incoming beam into the objective and to the sample. The notch filter acts as a mirror for the selected laser line (514.5 nm or 632.8 nm) and

transmits all other wavelengths. This notch filter is different from the transmission grating as it reflects rather than transmits the specific wavelength and is not part of a prism. An infinitely corrected Mitutoyo super long working distance objective SL50 with a 50x magnification focuses the beam onto the sample. The working distance of this objective is 21 mm. The angle of the notch filter is the most critical part of the system as it determines whether or not the laser line is steered into the objective along its optical axis.

We collect the scattered light signal in a backscattered geometry. Thus, the objective collecting the Raman signal is the same as that focusing the beam onto the sample. We then filter the reflected beam and the Rayleigh light using the Kaiser® SuperNotch-Plus™ filter previously used as a mirror. At this stage, it is important to collect as much of the weak scattered signal as possible. Therefore, we use highly efficient mirrors to steer to beam from the notch filter to the spectrometer and detection system. The mirrors are broadband dielectric mirrors with a 99 % reflectivity between 488 and 694 nm. We first steer the beam downward in order to reach the height of the spectrometer entrance slits. It is important to note that none of the optics used in the system polarises the Raman scattering from the sample. Therefore, the polarisation state of the Raman signal is not changed.

In order to discriminate the signal from the sample from Raman scattering or luminescence from the diamond, windows of our high pressure cell, we use a confocal spatial filtering system. A 100 mm focal length achromatic doublet lens focuses the beam onto a rectangular aperture. The continuously variable rectangular aperture spatially selects the desired beam diameter of the signal. Then a second 100 mm focal length achromatic doublet lens collimates the beam. Typically, the aperture is set to select a 5 x 5 μm area on the sample.

Then, the beam passes through a second Kaiser SuperNotch™ filter in order to discriminate further against the incident laser line (usually 514.5 nm). Experience showed that "leakage" can occur along the light path or from stray diffuse or specular reflections with the laboratory, which could result in swamping the weak Raman signal incident on the detector. It is particularly necessary to use of the second notch filter for studies of weakly scattering metallic samples such as the transition metal nitrides studied here. In the case of such samples, there is little penetration of the incident beam into the sample. Therefore, the sample reflects a large portion of the elastically scattered light along the main beam path. Thus, there is much more laser light to discriminate from the weak Raman signal. We do not use any secondary notch filter with the HeNe laser excitation, as the first notch filter appears to remove enough of the laser light for useful spectroscopy.

Finally, a 31.8 mm focal length achromatic doublet lens focuses the beam onto the entrance slit of the spectrometer. We carefully selected the focal length of that lens in order to provide

maximum coverage of the diffraction grating inside the spectrometer, thus providing maximum resolution. The focal length of the spectrometer is f_1 = 500 mm. The size of the gratings is a square of 68 mm x 68 mm. The radius of the beam is $a \sim 2$ mm. With these data, one can calculate the optimum focal length for the lens (f_2) using simple geometry.

$$f_2 = \frac{a}{0.5 \times 68} \times f_1 = \frac{2}{34} \times 500 = 29.4 \text{ mm}$$

A slightly longer focal length ensures the preservation of the totality of the signal since it reduces the size of the beam at the spectrometer grating. Therefore, we selected a 31.8 mm focal length lens.

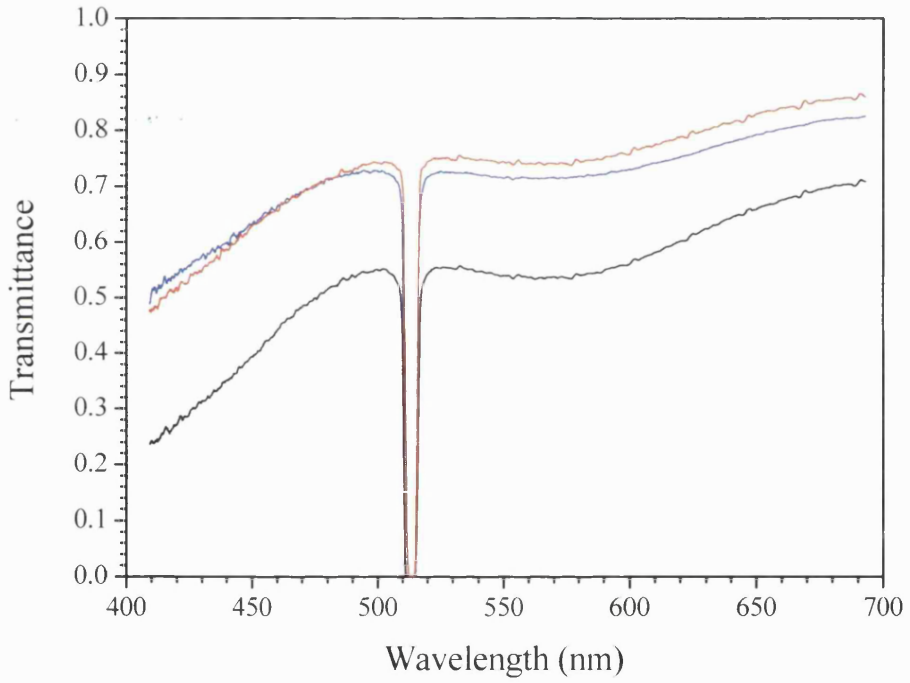

Figure 2-16 Absorption curve of the Kaiser® SuperNotch™ filters used in the Raman system. In blue for the first filter, in red for the second filter and in black for the combination of both filters.

Figure 2-16 shows the absorption curve of a typical notch filter. Such notch filters provides an extremely high throughput combined with rejection of the incident laser light when compared to a traditional triple spectrometer system. However, the quality of the notch filter determines the low relative wavenumber (Rcm^{-1}) detection limit of the system. In our experience, it is very difficult to obtain interpretable Raman signals at less than 100 Rcm^{-1} with a notch filter system. That point is the major inconvenience of the notch filter system, compared to a double or triple grating spectrometer system. However, it allows for the first time the collection, in situ in the diamond anvil cell, of spectra of very weakly scattering solids such as metals. In our system,

using two notch filters, it is possible to detect Raman shifts as close as 45 cm^{-1} of the laser line, with samples that are of good optical quality; i.e. that do not reflect too much of the laser line. In that case, we fix the position of one of the notch filter and slightly rotate the other one off its optimum angle in order to adjust the low-frequency cut-off, figure 2-17.

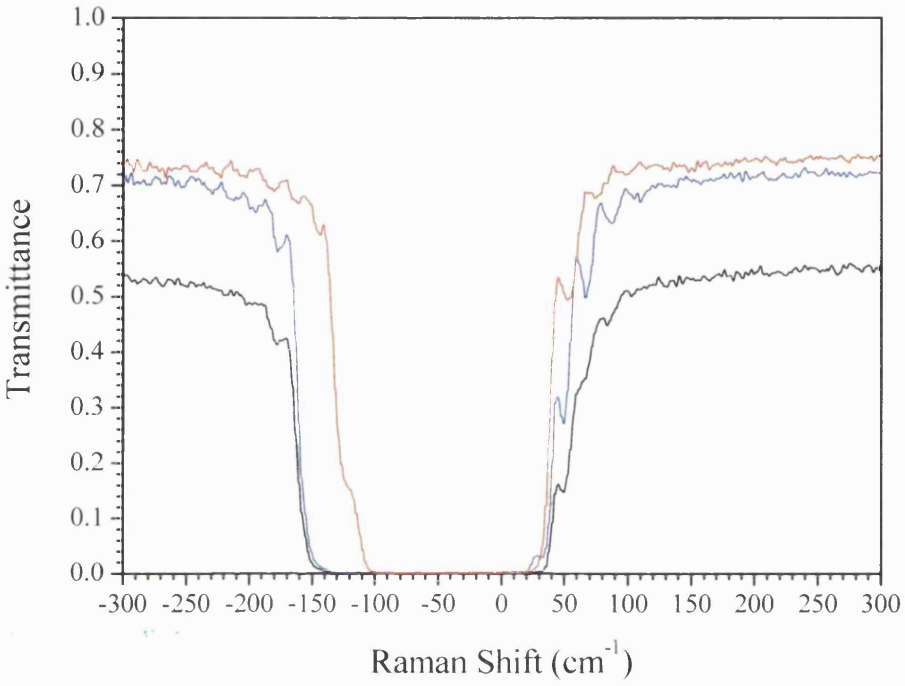

Figure 2-17 Schematic representation of the notch filters optimisation. By rotating the notch filter, the edge of minimum in the transmission curve moves either towards higher or lower wavenumbers.

The spectrometer used is an Acton Research SpectraPro® 500i spectrometer with a focal distance of 500 mm, an aperture ratio λ/6.5 with a imaging Czerny-Turner arrangement using aspheric mirrors. The spectrometer includes a choice of three interchangeable diffraction gratings (600, 1200, 2400 grooves/cm) mounted on a rotateable turret. The chosen range of gratings allows interplay between the desired spectral resolution and the spectral range as shown in table 2-2. The detector is a back-illuminated silicon CCD detector Princeton Instruments Spec10:100B of 1340 x 100 pixels with a pixel size of 20 x 20 µm.

	600 $g.cm^{-1}$	1200 $g.cm^{-1}$	2400 $g.cm^{-1}$
Spectral Range (cm^{-1})	2500	1400	800
Resolution (cm^{-1})	~ 3.0	~ 1.0	~ 0.5

Table 2-2 Spectral range and resolution of the spectrometer for each grating centred at 520 nm.

2.3. High pressure synthesis techniques

2.3.1. Diamond Anvil Cell (DAC)

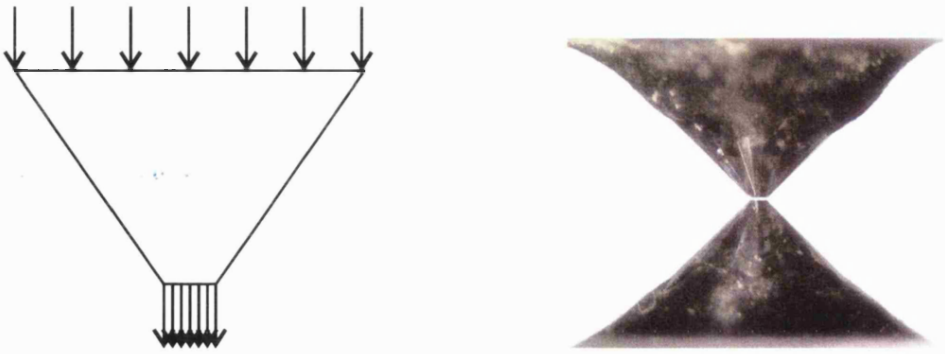

Figure 2-18 Left: Illustration of a tapered anvil and the principle of pressure multiplication into the sample volume by reduction of the anvil area. The pressure is given by P = F/A, where F is the applied force, and A is the cross-sectional area normal to the direction of applied force. Right: in an opposed anvil device, we place the sample between the small anvil faces of two opposed anvils and compressed by application of force to the external flat faces. In the case of the DAC, the anvils are single crystalline diamonds.

The diamond anvil cell (DAC) is a miniaturised version of the "opposed anvil" device, that was developed in the early days of modern high pressure research [107, 108]. In such instruments, we place the sample between two opposing anvils. An external force is applied to the anvils and drives them together (figure 2-18). The tapered form of the anvils multiplies the pressure. The samples reach high pressure following the principle of area reduction between the outer and inner anvil faces. In "large volume" opposed anvil devices, machined pieces of hard alloys such as tungsten carbide (used in the form of sintered polycrystalline material) form the anvils. In the case of the diamond anvil cell, cut gemstone quality single crystalline diamonds are the anvils.

Diamond is an excellent window for numerous types of experiments ranging from infrared, Raman and X-ray diffraction. However, it is opaque to ultraviolet electromagnetic radiation (from ~ 5 eV up to ~ 10 keV (X-ray) figure 2-8).

2.3.1.1. Choice of the diamonds: The "four C's"

Because single crystal diamond is the anvil material, the choice of the diamonds is one of the major components of the experiment. The diamond has to sustain extremely high strain. Although one selects the stones for high pressure experiments rather than as jewellery pieces, the same four C's (colour, clarity, cut and carat) used in the diamond grading industry remain useful criteria. The four C's suitable for an experiment depend upon the experiment.

2.3.1.1.1. Clarity

The position and amount of inclusions in the diamond define the clarity of the stone. The inclusions are mainly small graphite spots, fluids, or small cracks. We require flawless (FL) (no flaws visible with a 10 x magnification), internally flawless (IF), or very very slightly included (VVS) and in some cases, very slightly included (VS) diamonds for high pressure experiments. The FL and IF stones are extremely rare and expensive thus it is not often possible to use such diamonds for a high pressure experiment. So, most of the diamonds used in the experiments presented in the thesis are VVS and VS. The VS stones are in fact about 15 to 20 % cheaper than the VVS stones. Thus, the price difference is significant enough to consider when preparing an experiment. Although the VS stones have some inclusions the inclusions are neither on the vertical axis from the culet nor on the culet itself. Such inclusions would jeopardise the success of the experiment. Since the inclusions are away from the highly stressed parts of the diamond, mainly the centre of the diamond culet, they do not present any concerns.

2.3.1.1.2. Colour

Diamonds exists in a large variety of colours. The colours range from perfectly colourless to light yellow and brownish for the most common stones. However, in particular for spectroscopy, the colour of the diamonds is a critical point of the experiment. Any background fluorescence from the anvil would soon overwhelm the signal from the sample. The colour of diamonds required for the experiment depends upon the region of the electromagnetic spectrum used to probe the sample (IR or visible).

Good Raman spectroscopy experiments at high pressure, using visible or near infrared light necessitate low fluorescence diamonds (Type IA). A "low fluorescence" diamond as determined by the diamond industry is a diamond which only displays a low fluorescence under ultraviolet (UV) light. Raman spectroscopy experiments do not generally involve any UV light, thus this determination is not suitable for our purpose. The fluorescence involved in the Raman spectroscopy experiment is in the visible range. If the exciting wavelength is in the blue or the green, the diamond fluorescence must not cover those regions or the lower energy region (*e.g.* yellow, orange, red and infrared). Thus, the colour of the stone is extremely important. Only colourless diamonds are suitable for a Raman spectroscopy experiment. The Gemmological Institute of America symbols for the suitable stones vary from D to G, D qualifies the most colourless stone and G the less colourless stone. All of those stones appear completely colourless when observed individually.

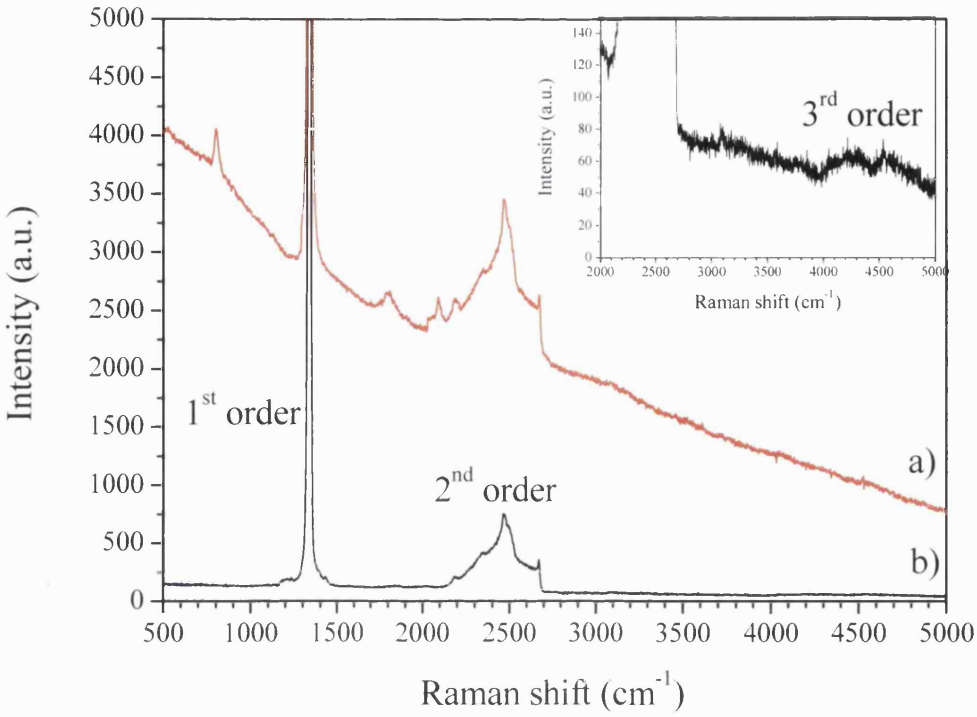

Figure 2-19 Raman spectra of typical Type Ia diamonds: a) a slightly yellow stone with a steeply sloping fluorescence background, that would not be suitable for Raman spectroscopy and b) a colourless diamond with little fluorescence background (2nd order peak: background ratio 10:1). We measure the strong first order Raman phonon at 1332 cm^{-1}.

In order to test if a stone is suitable for Raman spectroscopy experiments one should measure its second order Raman spectrum. We systematically test all of our stones before purchasing them. As shown on figure 2-19, the bottom spectrum is typical for an excellent diamond for Raman spectroscopy. The background must be perfectly flat and the second order Raman spectrum should be intense when compared to the background. Figure 2-19, in the lower spectrum, the signal to background ratio is in the order of 10:1 for the peak of the second order Raman spectrum of diamond. On figure 2-19, the top spectrum shows the same region of the spectrum for a diamond not suitable for Raman spectroscopy experiments. The background is very intense and does not allow efficient measurement of the second order Raman spectrum of diamond. Although this criterion is usually sufficient, one must always check the background in the lower Raman shift region in case the diamond exhibit any unwanted features.

Experience shows that the D and E coloured stones with "low fluorescence" are often the most suitable stones for Raman spectroscopy experiments.

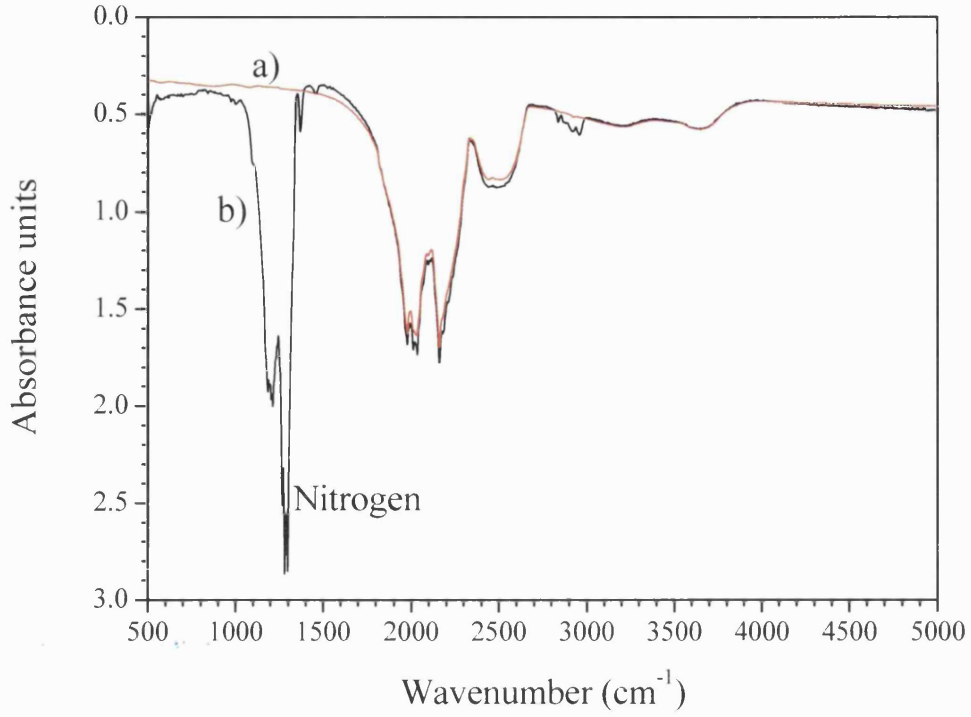

Figure 2-20 Infrared absorption spectra of diamonds. a) is a Type IIa "nitrogen-free diamond") that is essentially IR transparent in the region of interest for most experiments, and b) is rich in nitrogen "platelets", that give rise to strong absorption features between 1000 and 1400 cm^{-1}.

Nitrogen "free" diamonds (type IIa) are necessary in order to achieve good results in an infrared (IR) spectroscopy experiment. IR diamonds are often brownish or yellowish in colour which make them part of the most common family of diamonds. However, only very few yellow or brown diamonds are suitable for IR experiments. They must have a very low content in nitrogen. The only way to ensure a diamond is suitable for the IR experiment is to physically test it using the IR spectrometer. The bands we are interested in are between 1000 and 1500 cm^{-1} and are characteristic of nitrogen. As shown on figure 2-20, the diamond peaks are between 1600 and 2700 cm^{-1}. The top spectrum on figure 2-20 displays a spectrum characteristic for a "nitrogen free" diamond. The bottom diamond spectrum displays strong peaks between 1000 and 1400 cm^{-1} which make the diamond not suitable for IR experiments.

Finally, for an X-ray diffraction experiment, the colour of the diamond does not matter. The electromagnetic energy range of the X-rays is much higher than that covered by the colour of the diamond. The main issue about X-ray diffraction in a diamond cell experiment is the choice of the X-ray wavelength. The X-ray energy must be high enough for the diamonds to be at least partially transparent (figure 2-8).

2.3.1.1.3. Carat weight; size

The size of the diamond determines the limitation in sample volume and maximum pressure during an experiment. Larger diamonds give rise to larger pressure and larger sample sizes. However, diamond is a very expensive material. Thus, most of the stones used for the experiments are in the order of 1/3 of a carat (1 carat = weight of a Carob seed which is about 0.2 g).

2.3.1.1.4. Cut

The cut of the diamond also determines the pressure range accessible in a given experiment. The diamonds most often used for DAC experiments have a "brilliant" cut, which is one of the styles most commonly used in jewellery for round stones (figure 2-21). The large flat facet is termed the "table" and the point of the diamond is the "culet face" (usually absent in a well cut jewellery diamond). In a diamond anvil cell experiment, the culet faces of two opposing diamonds press on the sample. The widest perimeter around the diamond is the "girdle" or "crown". We mainly use stones which have a modified brilliant cut. In the modified brilliant cut, the table is ground down towards the girdle in order to increase the area to which we apply the initial force. For DAC studies, the parallelism between the table and culet faces is absolutely critical: any non-parallelism will cause the diamonds to fail, at even modest pressures. Furthermore, it is also preferred when the culet is directly at the vertical of the centre of the table in order to preserve the symmetry of the anvil; it is not always the case in the diamonds used in jewellery. For a brilliant cut diamond of a starting weight around 0.3 carats, the diameter of the crown is about 4.5 mm, the table is polished to a diameter between 3.8 and 4 mm and the culet to a diameter of 300 μm, for typical experiments. As a result, the ratio between the table and the culet area is about 160 to 180. We use those diamonds at pressures up to 50-60 GPa. We also used diamonds with a smaller culet of about 200 μm for the experiments performed at higher pressures, up to 80 GPa.

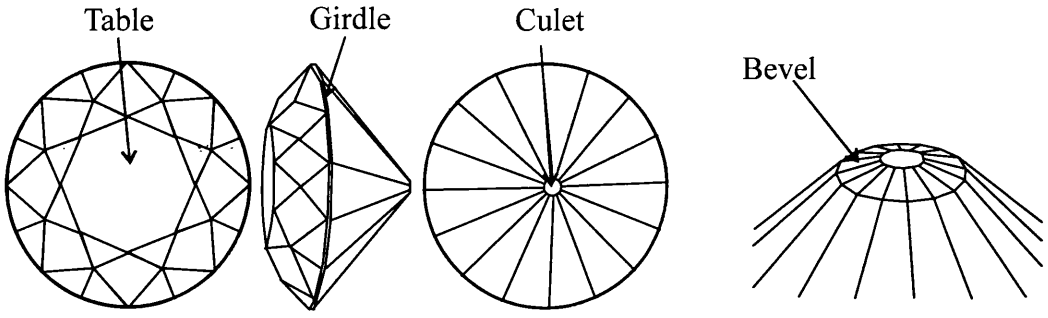

Figure 2-21 Diamond cut showing from left to right a view of the table, a side view, a view from the top where the culet is and a closer view of a bevelled culet. The pictures are on scale with a culet of 300 μm and a full diameter of 4.5 mm.

However, for experiments into the megabar range, it is usual to introduce a bevel into the culet, to produce a smaller culet face. The bevel angle is typically between 2 and 10 ° (figure 2-21). Bevelling the culet allows the diamond to deform at very high pressure without cutting into the gasket, thus preventing the destruction of the anvils (figure 2-22) [109].

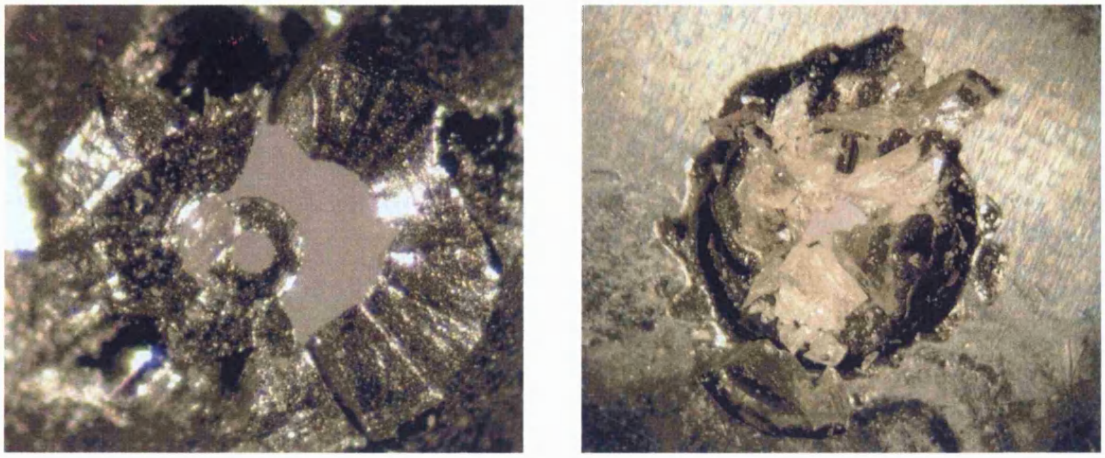

Figure 2-22 The pictures illustrate a failed experiment where the diamonds have cut through the soft stainless steel gasket (on the left) after leaving the sample at 55 GPa overnight. On the right photograph, we show the remaining pieces of one of the diamonds shattered after making contact with the other diamond upon gasket failure at high pressure.

2.3.1.2. Preparation of a diamond anvil cell experiment

We performed Raman spectroscopy, laser heating and X-ray diffraction experiments in the diamond anvil cell. Thus, the chosen cell design had to be suitable for those experiments. For angular dispersive X-ray diffraction, we require a wide opening angle with, preferably, a conical aperture. For the double sided laser heating experiment, the size of the DAC must be small providing a distance from the objective to the sample shorter than 21 mm on each side. Finally, there are no further requirements for the Raman experiments other than the choice of diamond previously discussed.

For a tungsten carbide seat, the opening angle and the diameter of the conical aperture in the backing plate define the maximum 4θ angle (4θ corresponds to the opening angle of the diffraction cone) accessible during an angular dispersive diffraction experiment. However, if the opening diameter is too large the diamond support is not sufficient and the anvil may fracture. If the diamond is too tall it will also reduce the 4θ angle as shown in figure 2-23. If one uses a beryllium backing plate, the DAC frame itself determines the maximum angle.

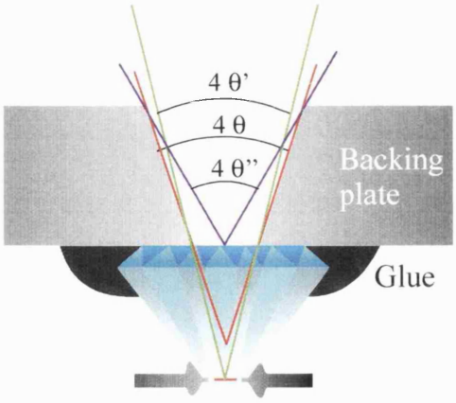

Figure 2-23 Picture showing the possible diffraction angles through the backing plate. The 4θ angle is the opening angle of the conical aperture of the backing plate, the angle 4 θ' is the maximum diffraction angle that can be measured and 4 θ'' is the theoretical maximum diffraction angle.

2.3.1.2.1. Type of diamond anvil cell: small cylindrical Mao type cell

The "Mao-type" cell is a very compact and versatile cell design that is most useful for laser-heating experiments. We apply pressure by turning four screws with opposite threading. The design is convenient for cryogenic loading of pressure media. The length of the cell in the pressurisation direction is about 35 mm. The short distance allows easy focusing of the infrared heating lasers inside the cell. The location of the sample at the centre of the cell, readily implements the possibility of double sided laser heating experiments. The cylindrical shape of the DAC allows the rotation around the cell axis during X-ray diffraction data collection in order to have a better averaging of the powder. Figure 2-24 presents a representation of the Mao cell.

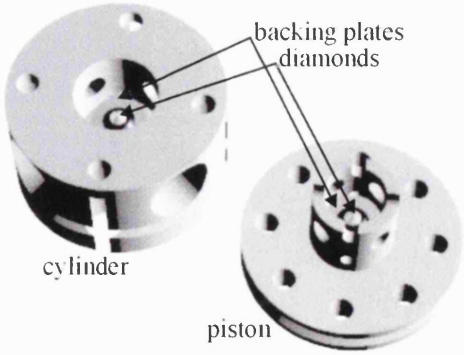

Figure 2-24 Schematic 3-D drawing of a laser heating diamond anvil cell. The cell diameter is about 50 mm.

2.3.1.2.2. Preparation of the cell

2.3.1.2.2.1. Mounting of the diamonds

We glue the diamonds on to their "backing plates", prior to subsequent alignment. In most cases, the backing plates are made of tungsten carbide (or of beryllium very low X-ray absorption). We first clean the backing plate thoroughly in order to remove any traces of dust. We clean the table of the diamond in the same way. Then we place the table of the diamond on the backing plate and centre it in order to have the conical aperture of the backing plate in the same axis as the centre of the culet face of the diamond. We then glue the diamond in place while pressing slightly on it in order to prevent the sealing material flowing between the diamond and the plate (figure 2-25). For most experiments, it is suitable to use an epoxy such as Stycast® (specially designed for cryogenic temperature conditions).

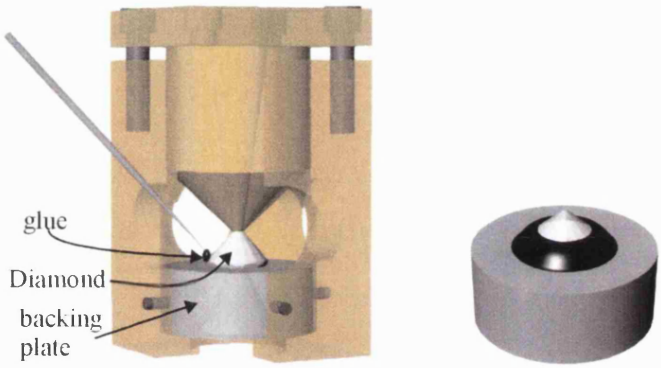

Figure 2-25 A diamond mounting jig (often made of brass). We centre the diamond on the backing plate and hold it in place with the top part pressing down on it (a small indentation is made in the brass cone to fit the diamond culet). We then apply some glue around the diamond to fix it to the backing plate using a needle. On the right is a picture of a diamond glued on to its backing plate (Stycast® sets black as shown).

Once we have glued the diamonds to their backing plates, the subsequent alignment procedure is perhaps the most important part of the cell preparation. We must align the diamonds in the cell respectively to each other so that the two culets are facing each other perfectly. Any misalignment will cause the diamonds to fail at high pressure. Once the culets are matching perfectly, it is important to check that the two culets are parallel by carefully bringing both diamonds together, to have the two culets touching. This can be a "dangerous" procedure (at least for laboratory budgets): we are bringing the hardest material known in contact with another sample of the hardest material, and the result could be catastrophic failure of both pieces before any experiment has begun! In order to prevent damaging the diamonds, it is usual to rub a finger on one of the diamonds in order to place a fine layer of grease on the culet face: the grease then acts as a cushion between the culets. The culets are perfectly parallel if there are no interference fringes (coloured fringes) appearing on the culet once they are in contact (figure 2-26). If there

are some fringes remaining, one must improve the parallelism by either checking that the backing plates are seating properly or by slightly rotating one of the backing plates. Lacks of adequate parallelism along with the lateral alignment are some of the major reasons for anvil and gasket failure.

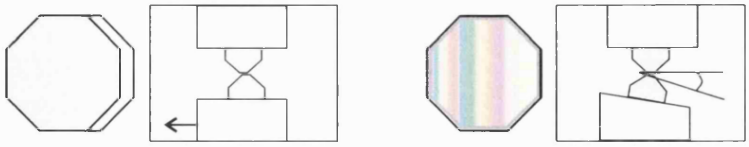

horizontal alignment tilt alignment

Figure 2-26 Diagram showing diamond alignment and centring procedures. On the left is a diagram of the horizontal alignment procedure of the diamonds: the aim is to match the position of the two culets looking from the side of the DAC and then re-check by looking down through the top diamond. The diagram on the right presents the tilt alignment: there, the aim is to make all the fringes disappear. The fringes present in this diagram indicate that the two culets are not parallel.

2.3.1.2.2.2. Gasket preparation

Diamond is the hardest material known, but it is also very brittle. Even a small shock applied between two diamonds in contact will break at least one of them. In order to prevent the destruction of the diamonds in DAC experiments, one places a gasket between the anvils. The gasket material is generally a metal. A hole with a diameter smaller than the culet diameter (usually ~ 50 % of the culet diameter) drilled through the metal gasket forms the sample chamber. The gasketed DAC (Figure 2-27) arrangement permits the study of fluid samples at high pressures, along with the phenomena of crystallisation and the glass transition, and it allows the surrounding of solid samples with a hydrostatic or quasi-hydrostatic medium that provides a homogeneous pressurisation environment.

The gasket is usually a disk of metal cut from a 250-300 μm thick foil of metal such as stainless steel, rhenium, or tungsten, all of which are highly absorbing in the X-ray energy range, or Be which has a low X-ray absorption coefficient. One chooses the gasket material according to the type of experiment. In order to reach the highest pressures, the gasket material should be as hard as possible but it has to remain sufficiently compressible in order to allow the increase of pressure. For experiments below 40 GPa, it is common to use T301 steel, which is quite strong and relatively deformable – it is also cheap and easy to handle. However, one should not use stainless steel for experiments above 50 GPa with non-bevelled diamonds, as the sharp edges at the rim of the culet will cut the gasket and create diamond – diamond contacts that will result in anvil failure (figure 2-22). It is common to use metals like tungsten or rhenium in high pressure experiments. Furthermore, with their high melting points (>3000°C), they are the most useful

metals for high P-T experiments. Tungsten is particularly useful for diffraction experiments as it has a *bcc* (body centred cubic) structure, thus has only a few X-ray diffraction peaks. Rhenium is *hcp* (hexagonal compact packing) and it has more X-ray diffraction lines, which can overlap with those of the sample. However, tungsten is more prone to breakage during the experiment than rhenium, in particular when performing cryogenic loadings. In order to perform "side diffraction" experiment (i.e., involving passage of the incident and diffracted X-ray beams through the gasket), one requires an X-ray "transparent" gasket material such as beryllium or boron–epoxy composite. Beryllium is not suitable in most heating experiments, as it becomes very soft at high temperature (melting point is 1283°C).

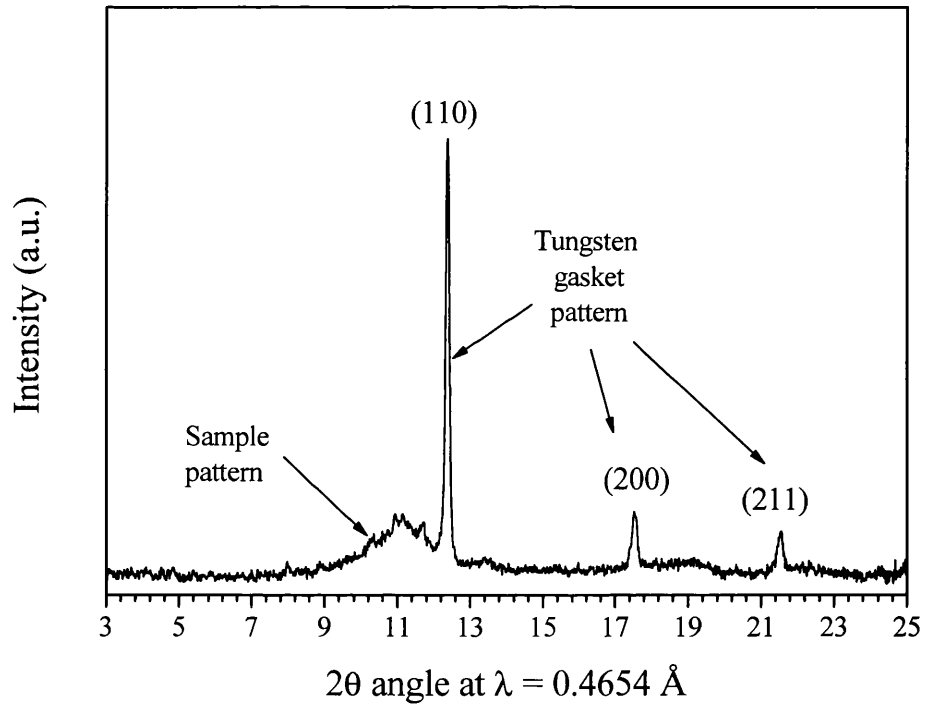

Figure 2-27 Illustration of a weak diffraction pattern at high pressure using a tungsten gasket. The sample of amorphous germanium nitride only display a broad feature centred on 11 °. The tungsten gasket displays one strong reflection and two weaker peaks.

A very important step in the cell preparation is the pre-indentation of the gasket, down to a thickness of about 50 to 30 μm (requiring pressurisation to approximately 20 GPa) before drilling the hole. The pre-indentation step will reduce the flow of gasket material away from the sample chamber volume during the experiment, and the subsequent risks of "blow-out" of the gasket hole.

We used an electro-erosion device to drill the hole in the gaskets. The centring of the hole is critical for a successful experiment. If the hole is too close to the edge of the pre-indent, the hole

might migrate during the experiment, and result in a "blow out" - the gasket fails, and the anvils may fracture. For a 300 μm culet, useful hole diameters typically range between 165 and 90 μm.

2.3.1.2.3. Sample preparation and loading

Once we have mounted and aligned the diamonds in the cell, and prepared and drilled the gasket, we are ready to mount the sample along with its pressure-transmitting medium and an appropriate pressure sensor into the chamber. In order to obtain a good quality sample loading using powdered materials, it is important to have a well-compacted sample. If the sample is already in the form of chips of dense polycrystalline grains that are of a suitable size for the diamond cell loading, no further preparation is necessary. However, if the sample is in the form of a loose powder, one should press the material in order to obtain a compact solid for loading. We commonly press the powdered samples between plates of hard materials such as WC, diamond anvils or moissanite anvils. For X-ray diffraction experiments, it is important to ensure that the sample thickness is as large as possible (i.e., about half of the pre-indent thickness of the gasket) in order to maximise the signal. However, if the sample is too thick, it will tend to "bridge" between the diamonds, and thus result in a highly non-hydrostatic environment that can lead to spurious compressibility results, and even observation of unexpected phase transformations.

The pressure medium is necessary in order to obtain a (nearly) isotropic stress environment around the sample, and also to prevent the gasket hole from collapsing around the sample. In order to have a perfectly hydrostatic medium surrounding the sample, a material that remains a fluid throughout the entire pressurisation range should envelope the sample. In practice, we never achieve this situation. No pressure-transmitting medium is ever "perfect". One should always make compromises depending upon the pressure range investigated, the nature of the sample, the properties under study, and also the capabilities of the laboratory and the experiment one is attempting. In any case, no matter the nature of the pressurisation medium, if the sample is polycrystalline, then grain – grain contacts within the solid material will determine much of the pressurisation environment.

One of the easiest pressure media to load, and one that is useful for many diffraction studies, is an alcohol-based mixture such as 4:1 methanol: ethanol. One adds this medium using a syringe into the sample chamber during loading: it remains fluid and hydrostatic to 10 GPa, and it does not contribute to the diffraction signal. By approximately 12 GPa, the mixture has solidified to the extent that it no longer provides a hydrostatic environment. However, methanol: ethanol is not a suitable medium for laser heating experiments as it decomposes at high temperatures.

The simplest pressure media to load are soft solid media such as sodium chloride or cesium iodide. These give rise to strong but simple diffraction patterns which are also used as pressure indicator. Although these are solids and hence cannot provide a hydrostatic pressurisation environment, they are softer (i.e., have a weak resistance to shear) than many minerals and ceramics studied at high pressure, so they can be useful. Solid media are also particularly convenient in laser heating studies, because they form a thermal insulation between the sample and the diamonds. Furthermore, laser heating generally relaxes the differential strains around the sample. Loading a solid medium is simple. We first press a small chip of the medium and then place it into the gasket hole. Then, we set the sample on top of it. It is better to slightly under fill the hole with medium: the complete filling of the hole can result in its expansion upon pressurisation, resulting in gasket failure.

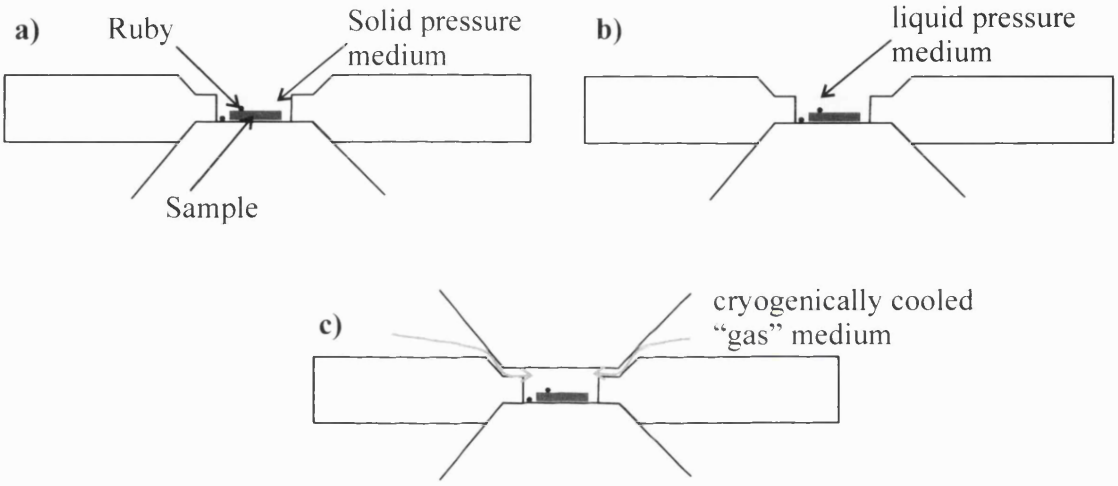

Figure 2-28 Diamond anvil cell loading a) in a solid medium, b) in 4:1 methanol: ethanol and c) cryogenic loading.

It is common to use liquefied gases such as argon and nitrogen as pressure-transmitting media. We can readily load these cryogenically. In this case, we first load the cell with the sample and then close it, leaving a gap of a few microns between the top diamond and the gasket. The "loading chamber" is a polystyrene recipient. We place the cell in this device, and slowly add liquid nitrogen allowing the cell to reach liquid nitrogen temperature before the level of nitrogen reaches that of the gasket. If the cell is not cold enough when the liquid nitrogen reaches the level of the gasket, the vaporising nitrogen will blow the sample out of the gasket hole. Then, we raise the level of nitrogen up to the top of the DAC and leave it there for several minutes. We finally close the cell, remove it from the nitrogen bath and allow it to warm up (at this stage, the cell is completely frosted due to atmospheric condensation). At this stage, if the pressure in the cell is more than 0.5 GPa, the loading was successful. If not, the operator must restart the loading. In the case of argon loading, we place a small recipient (e.g., a plastic cup) inside the

liquid nitrogen bath, and place the cell inside it. Directing the argon gas from the cylinder through the surrounding liquid nitrogen and into the cold recipient using copper tubing liquefies it. In that case, the level of liquid argon rises slowly enough for the cell to cool down.

In order to perform a successful laser heating experiment, one has to thermally insulate the sample from the diamonds, as diamond is an excellent thermal conductor (800 W $m^{-1}K^{-1}$ for the less conducting type). We commonly carry out two types of loadings. In the first type, we load the sample between two thin layers of NaCl and place some ruby chips on the side in order to measure pressure. The second way to load the sample is to place it on top of a few ruby chips or smaller sample chips, then add some ruby chips on top of the sample and partially close the cell. We finally load the cell cryogenically with nitrogen or argon. The liquid flows below and above the sample creating an insulating layer all around the sample.

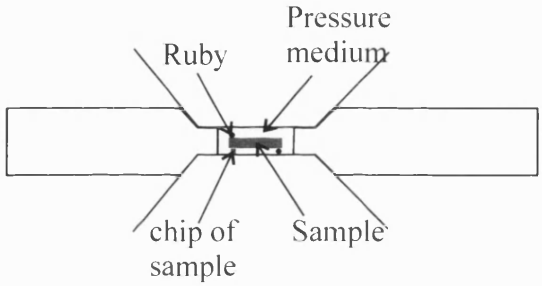

Figure 2-29 Diagram showing the type of diamond anvil cell loading required for a laser heating experiment.

2.3.1.2.4. Pressure measurement in the diamond anvil cell

In a diamond anvil cell one can determine the pressure using spectroscopy or using X-ray diffraction. In most cases, we established the pressure using ruby fluorescence spectroscopy and in fewer cases using the equation of state of gold.

Piermarini *et al.* first introduced the "Ruby Sharp-Line Luminescence" technique in 1972 [110] in order to determine the pressure inside the DAC. This method soon became the main way of determining the pressure in the DAC. After several calibrations [77, 111, 112] of the R1 and R2 lines of ruby, it is a relatively accurate pressure measurement tool. Figure 2-30 presents examples of ruby fluorescence spectra at two pressures in the DAC.

The equation followed by the ruby fluorescence lines shift with pressure, results from a calibration of that shift against the equation of state of several metals originally determined using shock experiments. Thus, the ruby calibration cannot be more accurate than the original shock data as it is a secondary pressure scale. The shift of the fluorescence lines is not only dependent upon pressure. There is also a large shift with temperature. Therefore, ruby is not suitable for pressure measurement at high temperature.

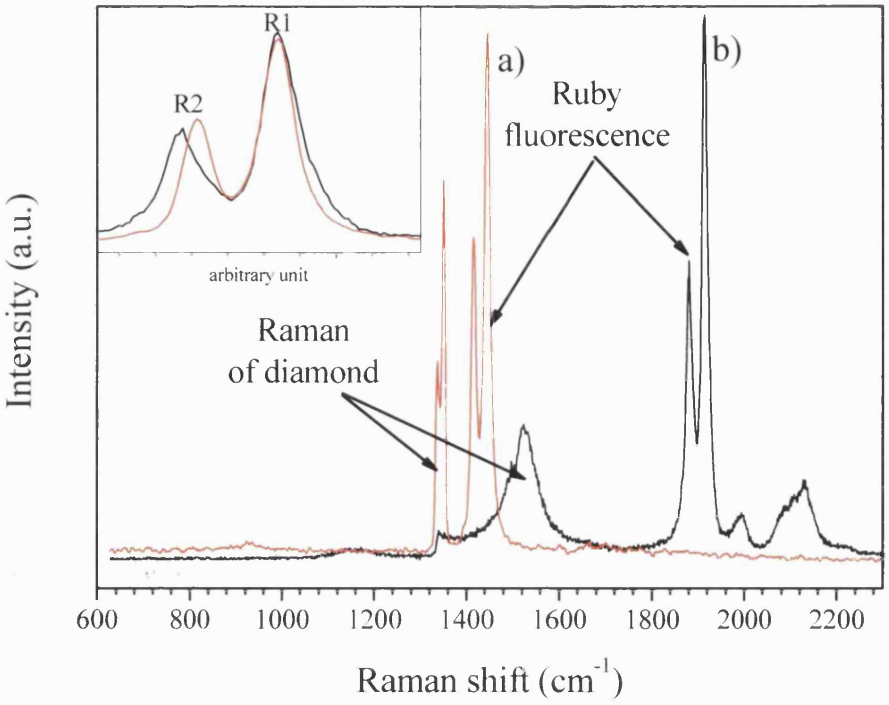

Figure 2-30 Examples of ruby fluorescence spectra collected for 0.01 second for an experiment performed in an argon pressure medium a) at 6 GPa and b) 80 GPa using a HeNe laser (λ = 633 nm). The top left inset presents the same two spectra with one of the spectra translated in order to compare the width and separation of the peaks. The width of the ruby fluorescence lines do not change between the low pressure and high pressure spectrum. Only the difference in energy between the R1 and R2 lines increases slightly. This difference indicates the presence of some small amount of non-hydrostaticity. In a non hydrostatic environment, the ruby lines would not show any separation and would be extremely broad. The first order Raman peak(s) of diamond display a doublet at low pressure and cover a wide range of wavenumber at high pressure. The width of the first order Raman signal dramatically increased because the system probes all the way through the diamond; therefore, we observe the variation of strain throughout the diamond along the laser path. At low pressure the pressure outside the cell and inside the cell are close, resulting in two sharp peaks covering a small range of wavenumbers. At high pressure, the stress conditions outside the cell and at the centre of the culet are quite different, resulting in a very large range of "pressure" values recorded throughout the diamond. Therefore, we observe a broad Raman signal.

Equation 12 gives the relation between the pressure and the wavelength shift of the R1 fluorescence peak at room temperature.

$$P = \frac{19.4}{5}\left[\left(\frac{\lambda_0 + \Delta\lambda}{\lambda_0}\right)^5 - 1\right] \quad (12)$$

P is the pressure and λ_0 is the wavelength of the ruby R_1 fluorescence line at 10^5 Pa.

As previously mentioned, we also measured pressure using the equation of state of gold. In that case, we measure the pressure using a primary scale (originally determined using shock experiments) thus pressure should in theory be more accurate. However, this technique is only available when carrying out experiments at the synchrotron. Furthermore, it is not always convenient since the 0 GPa lattice parameter of the pressure probe must be measured, therefore adding extra data collection.

2.3.2. Heating in a diamond anvil cell

There are several reasons why one would require heating a sample at high pressure. Among those examples are the determinations of phase diagram, synthesis of new phases, determination of melting curves, and study of high temperature properties of materials [92, 93, 96, 97]. The technique first arose in order to solve geological problems [113]. Those problems include determination of the melting curve of iron (and other metals) which remains a debated problem. The determination of the phase diagram in the system forsterite – spinel – perovskite + MgO is another example of an open problem. In order to gain new knowledge on these problems and many others, it is necessary to reach pressures up to several hundreds of GPa and temperatures well above 3000 K. Therefore, specific techniques are necessary.

There are several ways to heat a sample placed *in situ* at high pressure inside the diamond anvil cell. The first way is to use a resistive technique where the heater is creating a hot environment around the sample. In this case, the temperature is limited to about 1500 °C at best. In such experiments, a reducing atmosphere surrounds the gasket and diamonds in order to prevent their oxidation. A thermocouple placed in the back of the diamond records the temperature. In a preliminary experiment, the correlation curve between the temperature in the back of the diamond and that at the sample position is correlated using two thermocouples, one at the sample position and one on the back of the diamond.

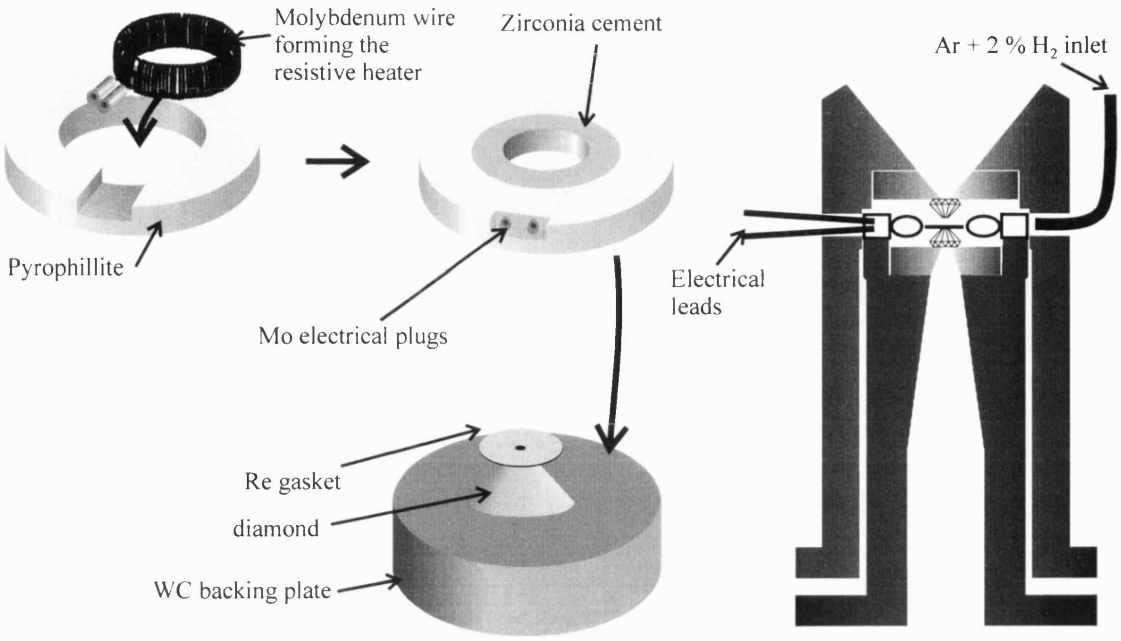

Figure 2-31 Schematic representation of a resistive heating experiment with the description of the heater, the assembly and the experimental setup. Zirconia cement seals the Mo heater in place and short Mo tubes form plugs for the electrical leads. Two small screws hold the heater assembly in place around the diamond.

The second way to heat a sample is using interaction between the sample and an electromagnetic wave, in our case a laser. Depending upon the wavelength of the laser, the electromagnetic wave interacts with the sample in various ways.

The first report of laser heating in a diamond anvil cell is that of Bassett *et al.* who observed the disproportionation of Fe_2SiO_4 in to 2 FeO + SiO_2 at 25 GPa and 3000 °C [113]. In this experiment, Bassett *et al.* used a pulsed ruby laser in order to achieve the high temperature. Today, most laser heating experiments are performed using continuous lasers with a near infrared Nd:YAG (Nd^{3+} doped Yttrium Aluminium Garnet) or Nd:YLF (Nd^{3+} doped Yttrium Lithium fluoride) laser or a mid-infrared CO_2 laser.

The sample absorbs the near-IR laser (E = 1.2 eV) via several processes such as light scattering by grain boundaries and lattice defects, both of which are very weak mechanisms. Another absorption process is charge transfer mechanisms in metallic and certain semiconductor samples which give strong absorption. The use of near IR laser is not suitable for most insulators. Therefore, Boehler *et al.* [114] introduced the use of CO_2 lasers in order to heat mineral samples such as olivine in the DAC. During a CO_2 laser heating experiment (λ = 940 cm^{-1}), the electromagnetic wave has a wavelength of the order of that of the phonon frequencies. Therefore, the heating results from the resonant absorption of the radiation by the lattice vibrations. CO_2 lasers are also a standard tool in the metal cutting industry where the laser can

cut steel pieces thicker than 15 mm in most standard machines (for reference, a list of north American company names are available at: *www.macuttingsystems.com/links.html*).

2.3.2.1. Nd:YAG laser heating: double sided

The Nd:YAG laser is a solid state laser that emits at a wavelength of 1064 nm (1.16 eV). We employed two types of near-IR laser heating systems to carry out the experiments presented in this thesis. The system built at UCL and NSLS [115] only involve one multimode Nd:YAG laser. The system built beamline 13ID-D at the APS uses two 25 W Nd:YAG lasers with two different beam profiles: TEM_{00} Gaussian mode and TEM_{01}^* ("doughnut" mode). Those two lasers are then combined into one beam in order to obtain a "flat" beam profile [116]. We only describe the system designed and built at UCL below. References [115, 116] describe the other systems used in the experiments.

In each of these systems, the optical layout is very similar. The optics split the laser beam into two beams of equal intensity. We steer the beams toward each side of the sample going through one beam splitter and using mirrors, and focus them onto the sample using two identical objectives. The size of the beam at the sample position is typically smaller than 15-20 μm in diameter. With an increase of laser power, the laser heats both sides of the sample.

Near-infrared (N-IR) lasers only interact with the sample surface due to the low penetration depth in sample suitable for N-IR laser heating experiments. Therefore, it is preferable to heat the sample from both sides in order to prevent any considerable temperature gradient within the sample along the pressurisation axis. Such gradients would result in a heterogeneous sample in the same direction. In particular, we require a uniform heating when we analyse the sample with X-ray diffraction, as in that case the X-rays probe the entire depth of the sample.

We collect the thermal emission from the sample using the same objectives used to focus the IR beam and analyse it using a spectrometer coupled with a CCD detector. The types of optics used for the near infrared laser are the same as the one used for the visible laser. Although, it is often preferred to use dielectric mirrors, or even notch filter, specifically designed to reflect 99.8 % at 1.064 μm. The dielectric mirrors are semi transparent to the visible light and allow the collection of the thermal emission of the sample through the same mirrors.

2.3.2.2. CO_2 laser heating: single sided

The CO_2 Laser has a wavelength of 10.6 μm (940 cm^{-1}). The use of a CO_2 laser heating system requires special types of optics since the materials commonly employed in lenses (SiO_2 glass) absorb the infrared light at that wavelength. Therefore, it is common to focus the CO_2 laser on the sample using a ZnSe lens [117].

A CO_2 laser heating system heats the sample only from one side unlike in the case of Nd:YAG laser heating. The laser heating community trusts that single side heating is sufficient in order to obtain a reasonable temperature gradient in the pressurisation axis since the laser has a much deeper penetration depth, more than the thickness of the sample. In the system we designed and built at UCL, it is possible to focus the laser beam down to an area of 50 μm in diameter on the sample. The main advantage of single sided experiment is the simplicity of the system. The system allows the implementation of the Raman system without optical components on the Raman spectrometer side of the system. Such a system is more compact than a double sided laser heating system and one could easily add it to an X-ray diffraction station at a synchrotron. Furthermore, the larger heating spot is a major advantage for in situ X-ray diffraction as it allows a larger X-ray beam within the hot spot therefore increasing the number of X-ray photons collected on the detector. Finally, high power CO_2 laser are extremely standard and compact items which make them cheaper than most high power near infrared lasers.

As shown previously, not all the diamonds are qualified as infrared "transparent" [118, 119]. In fact, only type IIa (less than 1 ppm of nitrogen) diamonds have a very low absorbance in the infrared radiation between 1000 and 1400 cm^{-1}. The laser heating community claims that one must use type IIa diamonds in order to perform a CO_2 laser heating experiment. However, experience shows that it is not necessary. In fact, type I diamonds have very little absorption around 940 cm^{-1}. Thus there is no need to use type IIa diamonds that are about twice as expensive as the type I diamonds.

2.3.2.3. Laboratory laser heating systems at UCL

In order to perform the laser heating experiment in the UCL laboratory, we have designed and built a very versatile system. The aim was to be able to change over from a near IR to a mid-IR laser heating experiment and back without any major realignment procedure. The purpose of the system was to use the micro-Raman spectroscopy system before during and after laser heating, with both CO_2 or Nd:YAG heating experiment. Therefore, we tested and optimised numerous configurations and optic mounts in order to find the optimum setup.

We have presented above the specially designed Raman system. Here we describe the laser heating part of the system which forms a whole with the Raman system.

The heating system comprises two lasers. One CO_2 laser from Synrad® which provides 50 W of TEM_{00} laser light at 10.6 μm and one custom built Nd:YAG laser from Quantronix® which provides 100 W of laser light when used in multi-mode and about 25 W when used in TEM_{00} at a wavelength of 1.064 μm. The Nd:YAG laser can have three different beam profiles depending upon the diameter of the pinhole in front of the 100 % reflection mirror in the back of the laser.

The choice of beam profile also changes the size of the beam and therefore the size of the heating spot in the diamond anvil cell. Thus, one chose the beam profile in accordance with the pressure range and the type of experiment.

2.3.2.3.1. The CO_2 laser heating system

Silver coated mirrors steer the CO_2 laser to a ZnSe lens which focuses the laser beam onto the sample inside the diamond anvil cell. We align the system using a red diode (λ = 645 nm) tracking laser mounted on the head of the CO_2 laser. We preliminarily adjust the diode laser so that it is perfectly coaxial with the CO_2 laser. Then we align of the CO_2 laser heating system using the tracking diode laser.

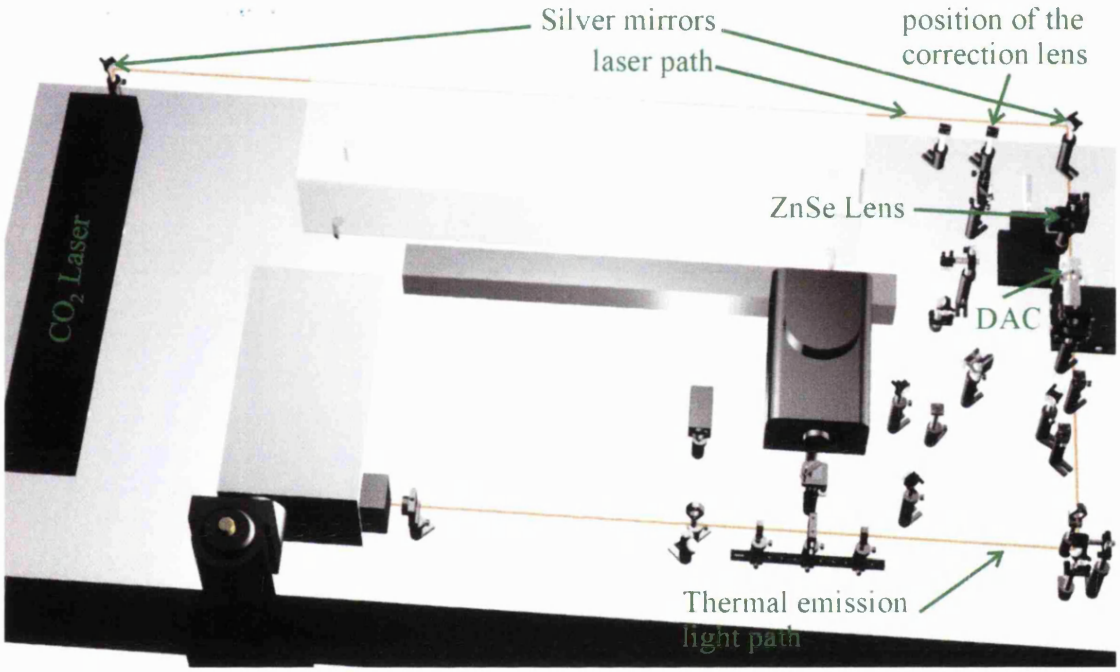

Figure 2-32 3-D drawing of the CO_2 laser heating system. The orange line indicates the path of the laser before the DAC and of the thermal emission from the hot sample after the DAC.

However, we encounter one major problem when aligning the system. There is a large difference between the focal length of the ZnSe lens for the CO_2 laser and for the red laser. The ZnSe lens is a single convex concave lens with a focal length of 63 mm for the CO_2 laser. However, the focal length in the visible is significantly different, because of the variation of the ZnSe refractive index as a function of wavelength. Therefore, we added a "correction lens" on the path of the tracking laser in order to make the focal point of the tracking laser and that of the CO_2 laser coincide. We mounted the correction lens on a magnetic kinematic base since we must remove it when the CO_2 laser is in use. If one forgets to remove the extra lens, the CO_2 laser is 100% absorbed by the lens and no heating occurs! The proper positioning of the correction lens is a crucial tool for the alignment of the CO_2 laser.

During the CO_2 laser heating experiment, we can easily analyse the sample using Raman spectroscopy providing the temperature is not too high and the thermal emission from the sample does not overwhelm the Raman signal. We also use the Raman spectroscopy system to measure the temperature as shown below.

2.3.2.3.2. The Nd:YAG laser heating system

A small red diode laser (λ = 670 nm) mounted in front of the Nd:YAG laser shows the path of the near-IR laser beam. A dichroic mirror then steers the diode laser to make it coaxial with the Nd:YAG laser. The dichroic mirror is transparent to the Nd:YAG laser therefore we never have to remove that mirror. We align the Nd:YAG laser system using the small diode laser.

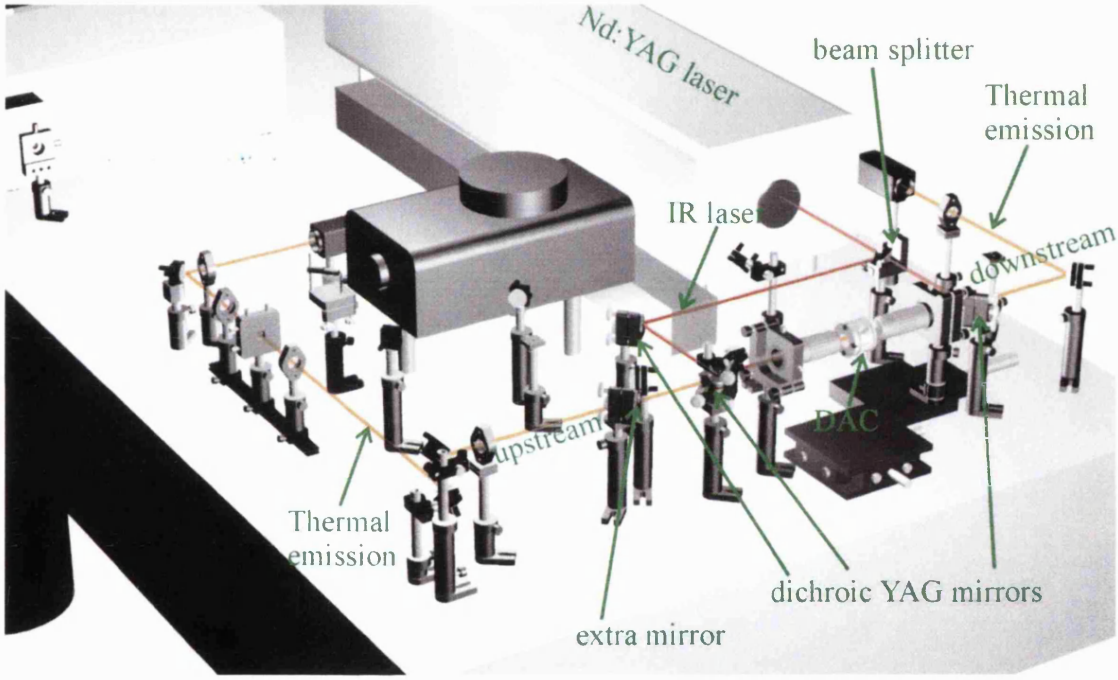

Figure 2-33 3-D representation of the Nd:YAG laser heating system. The red line indicates the infrared laser and the orange line indicates the thermal emission. We only use the extra mirror to correct the position of the optical axis after the light travels through the dichroic mirror and undergoes a horizontal translation due to the thickness of the mirror.

First, a high-power resistant and polarisation independent cube shaped beam-splitter of ½" x ½" splits the laser beam into two beams of the same intensity. We used a prism stage, which allows very accurate alignment, to hold the beam splitter. One half of that beam passes straight through the cube. The cube reflects the other half and steers it at a 90 ° angle. A dichroic mirror (a different dichroic mirror from that used to steer the diode laser) steers the straight beam toward the downstream (CO_2 laser side) objective. The Nd:YAG laser dichroic mirrors have a 99.8 % reflectance at the 1.064 μm wavelength. However, they only reflect the red laser partially on the front surface and on the back surface. Thus, during alignment with the red laser one must ensure

that the alignment laser beam is the one coaxial with the infrared laser and not one reflected on the back of a dichroic mirror.

Two dichroic mirrors steer the second Nd:YAG beam twice at a 90 ° angle before reaching the upstream (Raman system side) objective.

We focus the near-IR laser onto the sample using two 10 x Mitutoyo objectives with a working distance of about 31 mm. The objectives work with both the visible and the near-IR wavelengths.

We mounted the downstream objective on the same kinematic base as the ZnSe lens of the CO_2 laser heating system in order to make the interchange very reproducible.

2.3.2.4. Temperature measurements

The temperature measurement is a critical feature in a laser heating experiment. With the constant improvement in the quality of lenses and other optical parts available, the design of a "good" temperature measurement system is becoming fairly simple.

We measure the emission from the sample in a wavelength range from 400 to 950 nm in most cases. A grey (equation (13)) or black (equation (14)) body fit of the radiation from the sample to the Planck radiation law allows the determination of the temperature [101].

$$L_\lambda = \frac{\varepsilon(\lambda)C_1}{\lambda^5}\frac{1}{e^{C_2/\lambda T}-1} \tag{13}$$

$$L_\lambda = \frac{\varepsilon(\lambda)C_1}{\lambda^5}\frac{1}{e^{C_2/\lambda T}} \tag{14}$$

where

$C_1 = 2\pi hc^2 = 3.7417749 \cdot 10^{-16}\,\mathrm{W\,m2}$

$C_2 = \frac{hc}{k} = 0.01438769\,\mathrm{m\,K}$

$\varepsilon(\lambda) = 1.0$ for a blackbody

with L(λ) the intensity as a function of wavelength.

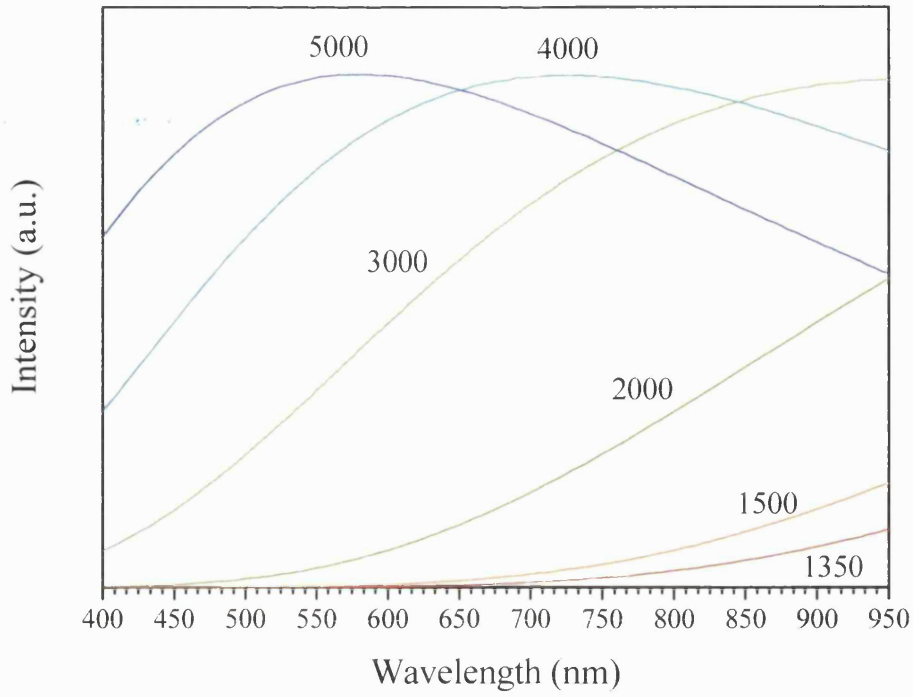

Figure 2-34 Black body emission as a function of wavelength. The temperatures indicated on the figure are in K and the maxima of the radiation are normalised in order to make the comparison easier.

Figure 2-34 presents the blackbody emission as a function of wavelength for temperature ranging from 1350 to 5000 K. The maxima shift from far infrared at low temperature to visible and ultraviolet at high temperature.

Most lenses are made from a single uniform material. As the focal length depends on the wavelength, one should fabricate the lens using materials with a refractive index independent of the wavelength or with a combination of lenses. Until very recently, it was not possible to purchase very efficient achromatic lenses with a sharp focal point. Therefore, one had to use reflective optics to obtain a sharp focal point. Although reflecting optics are still better than achromatic lenses, transmitting optics only generate negligible errors when compared with other errors occurring during the measurement of the sample temperature. For example, the radial temperature distribution of the sample displays dramatic gradients. The temperature gradients inside the cell are extreme. Within a few micrometers, the temperature changes from a few thousands of degrees to just a few hundreds of degrees or even almost room temperature.

In order to obtain an accurate measure of temperature, we calibrate the temperature measurement system using a pre-calibrated tungsten lamp. The pre-calibration of the system allows the determination of the response curve of the system. Once we have determined the response curve, it is possible to access, in a first approximation, the black body emission curve of the sample from the signal collected by the spectrometer as shown on figure 2-35.

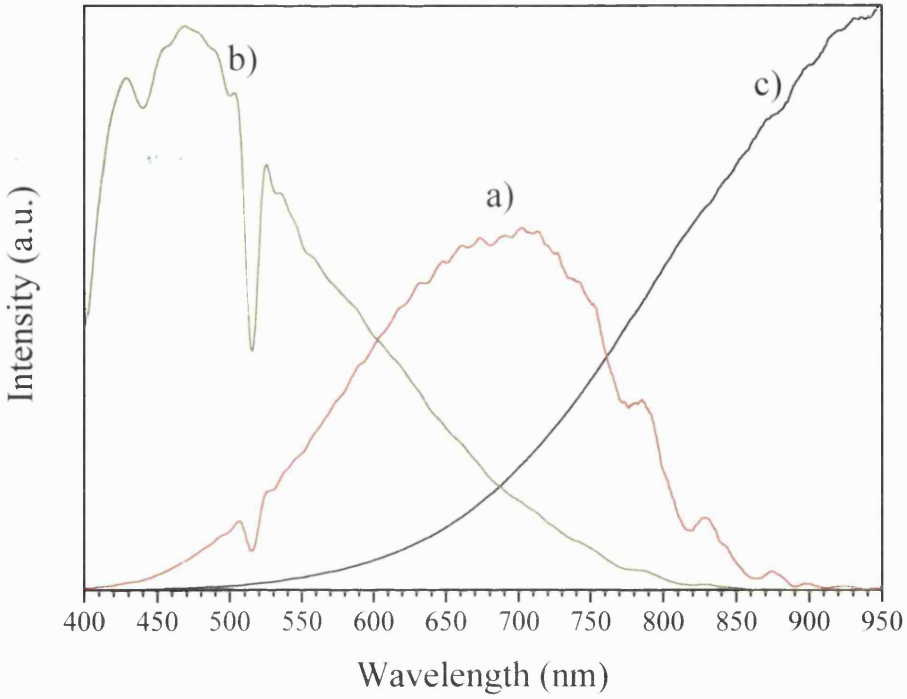

Figure 2-35 Temperature measurement using thermal emission; a) spectrum collected by the system, b) intrinsic response curve of the optics and spectrometer system and c) corrected spectrum of the thermal emission (grey-body curve) from the sample.

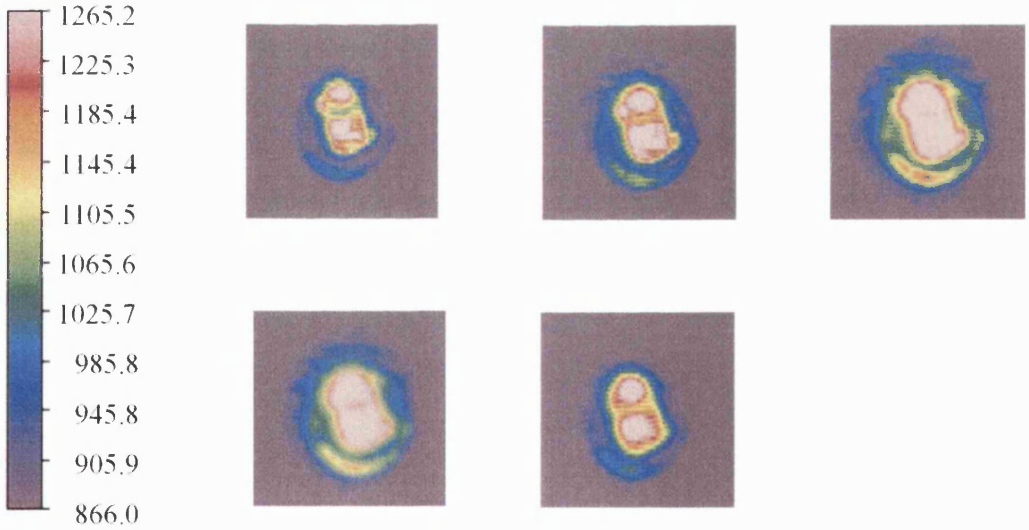

Figure 2-36 Example of images of an Al_2O_3 sample heated with the CO_2 laser, recorded using the thermal imaging camera. The large variation in colour indicates the steep temperature gradients.

We have also performed some temperature measurement using a thermal imaging camera. The camera is sensitive in the near infrared and pre-calibrated in order to give the temperature. Figure 2-36 presents some of the images we recorded on a sample of alumina in the diamond anvil cell.

2.3.3. Multi-anvil press synthesis

The sample size in a diamond anvil cell experiment is extremely small. We sometimes require a larger sample size in order to facilitate its characterisation, i.e. laboratory X-ray diffraction, neutron diffraction, electron probe characterisation. The pressure is a force per area, thus in order to synthesis a larger sample (larger area) one needs a much larger force. The apparatus employed in the synthesis of our large samples is a multi-anvil press. We performed all of the large volume sample syntheses at Arizona State University (ASU) in collaboration with Dr. Kurt Leinenweber.

The name of the two presses we used for the experiments are "Big Blue" and "Red" (Paul F. McMillan and John R. Holloway at ASU constructed little blue which is identical to red. Little blue is now in a re-building phase at the Royal Institution in the Davy Faraday Research Laboratory in London, for future experiments). These have respectively a ram diameter of 17" and 18" inches and can achieve a force of 1100 and 300 tonnes. The press is a Walker type multi anvil [120, 121]. It is based on a split cylinder geometry with three wedges at the bottom and three on top (figure 2-37). We place the sample within a cylinder inside an octahedron (figure 2-38). We place the octahedron in an assembly of eight cubes which have a truncated corner (figure 2-37).

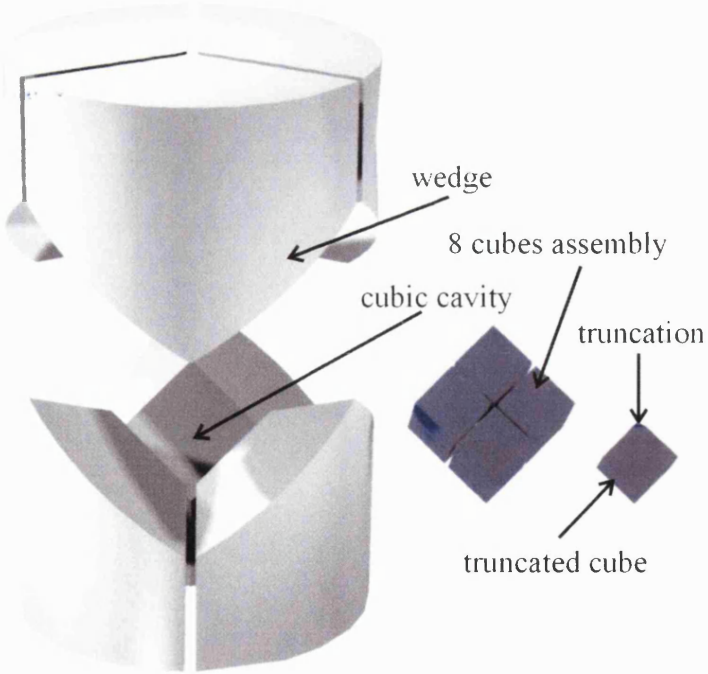

Figure 2-37 Schematic representation of the multi anvil press with the split cylinder, the cube assembly inside of which lies the octahedron and a truncated cube.

The size of the cube truncation determines the pressure range accessible for a specified press. Thus, in order to perform experiments at various pressures, we use several sizes of WC cube

truncations and different sizes of pressure transmitting/sample containment octahedra. The two sizes used for the experiments are 14-8 (14 mm edge for the octahedron and 8 mm triangle edge for the truncation) which allows the reach of pressures up to 12 GPa in Big Blue and 9 GPa in Red. The second size is the 8-3 which is only used in Big Blue and allows the reach of pressures up to 27 GPa although the highest pressure reached during our experiments is about 20 GPa. Reaching the high temperatures necessary for the synthesis constitutes a separate problem.

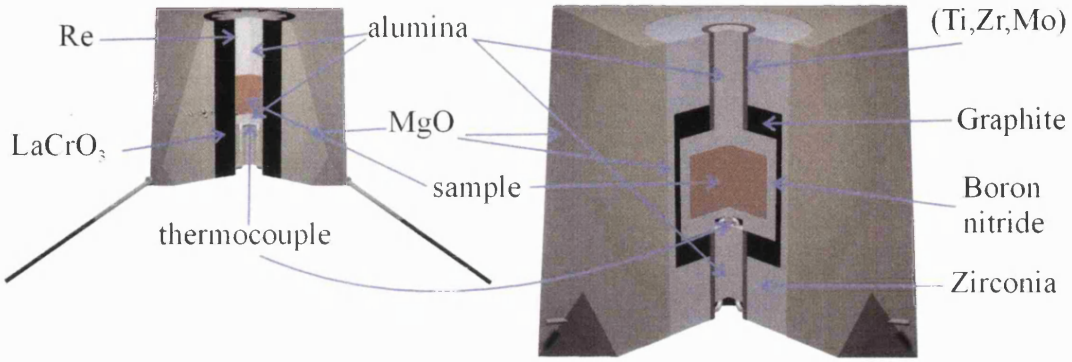

Figure 2-38 Scaled representation of the octahedron assembly on the left, 8-3 assembly and on the right 14-8 assembly.

The Bayerisches Geoinstitut in Bayreuth Germany originally developed the 14 mm octahedron assembly that we use in our experiments [122]. In order to prepare the octahedron, we place the sample within a platinum capsule itself surrounded with an MgO sleeve around which we place a graphite heater. We measure the temperature using a type S thermocouple which sits under the sample capsule. A thin MgO disk insulates the thermocouple from the capsule (figure 2-38).

Fei [123] developed the 8 mm octahedron assembly which allows the reach of much higher pressures. In this assembly, we place the sample between two rhenium disks inside a tube formed with a rhenium foil which acts as a heater. A thick $LaCrO_3$ sleeve surrounds the Re. In some cases, one can also use $LaCrO_3$ (in the absence of Re) as a heater up to the highest pressure as it does not undergo any high pressure transition into an insulation material unlike graphite. We measure the temperature using a type C thermocouple placed right below the sample. A very thin Al_2O_3 disk insulates the thermocouple from the rhenium capsule. We also place an alumina plug on top of the sample in order to maintain the sample position at the centre of the octahedron (figure 2-38).

2.4. Thermodynamics of high pressure phase transitions

A large part of the experiments presented in this thesis involved the exploration and the discovery of new phases at high pressure. Therefore, a brief discussion of the thermodynamics of high pressure and high temperature phase transitions is necessary. Furthermore, we have performed several equation of state measurements for nitride materials during the course of the experiments. Thus, it is necessary to present an introduction to the relevance, measurement and analysis of the equation of states V(P) (at constant temperature) or V(P,T), and in particular the Birch-Murnaghan formalism. We used this formalism in most of the fitting procedures.

2.4.1. Phase transitions

First order solid – solid phase transitions occur when the application of high pressure and/or high temperature drives one phase beyond its stability field, and provides enough thermal energy to transform that phase into a more stable phase. The new phase possesses a higher density or entropy. From a thermodynamic point of view, the phase transition occurs once the sample crosses the boundary in the T – P field from one phase to another. However, we often observe that the phase transition does not actually occurs at that exact point. The transition can occur once the conditions are well into the stability field of the second phase or even never occur like it the case of the diamond to graphite transition. Diamond exists at ambient conditions even though the thermodynamically stable phase is graphite. The phenomenon resulting in this behaviour is the kinetics. The kinetics play an important role in most phase transitions in particular when the transition takes place at low temperatures.

There are several definitions of a phase transition. In this study, we will use the Ehrenfest classification. In this classification, there are two types of phase transitions: first order and second order. In theory, other orders are also possible.

At the equilibrium pressure (or temperature) of a phase transition, the two polymorphs have the same Gibbs free energy (G).

$$\Delta G = \Delta H - T\Delta S = 0 \qquad \text{with} \qquad H = U + PV$$

where H is the enthalpy, T the temperature, S the entropy, U the internal energy, P the pressure and V the volume.

By definition, a first order phase transition occurs when there is a discontinuity in the first derivative of the free energy.

$$\left(\frac{\partial G}{\partial T}\right)_P = -S \qquad \text{and} \qquad \left(\frac{\partial G}{\partial P}\right)_T = V$$

For example, it is very easy to detect a volume discontinuity using X-ray diffraction.

By definition, a second order phase transition occurs when there is a discontinuity in the second derivative of the free energy, hence in the heat capacity (C_P), thermal expansion (α) or compressibility (β):

$$\left(\frac{\partial^2 G}{\partial P^2}\right)_T = \left(\frac{\partial V}{\partial P}\right)_T = -V\beta$$

$$\left(\frac{\partial^2 G}{\partial P \partial T}\right) = \left(\frac{\partial V}{\partial T}\right)_P = Va$$

$$\left(\frac{\partial^2 G}{\partial T^2}\right)_P = \left(\frac{\partial S}{\partial T}\right)_P = -\frac{C_P}{T}$$

Experience shows that kinetics usually controls the first order phase transitions (figure 2-39) at low temperature. In contrast, kinetics never drives a second order phase transitions.

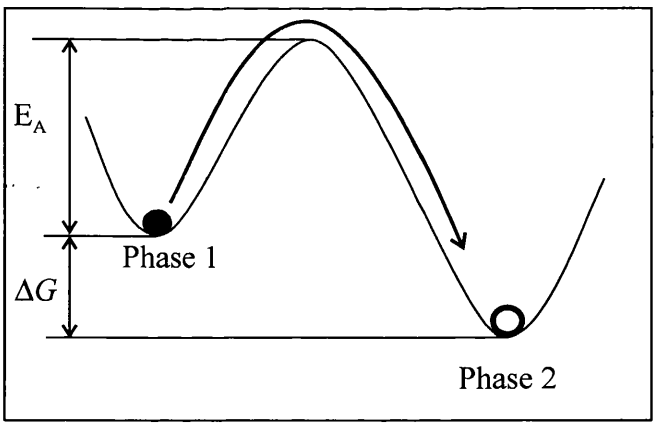

Figure 2-39 Energy diagram displaying the energy barrier encountered during a first order phase transition. E_A represent the activation energy of the transition. The P – T conditions are in the stability field of phase 2.

One can display a phase diagram several ways. Three examples are enthalpy as a function of pressure, enthalpy versus volume and pressure versus temperature phase diagram (figure 2-40).

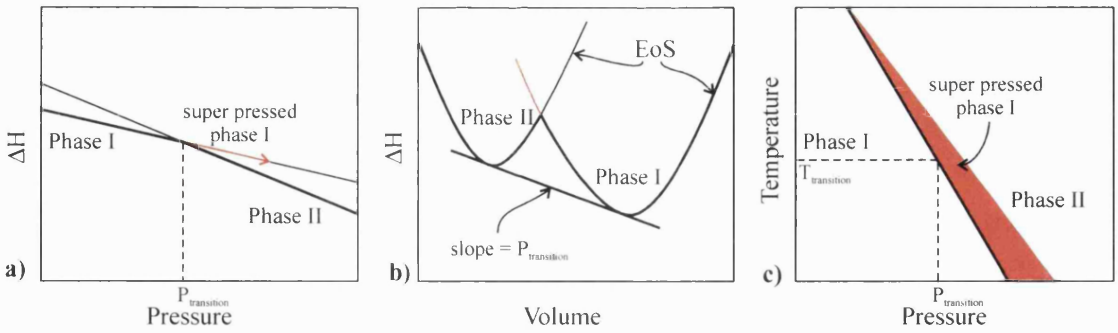

Figure 2-40 Three representation of phase diagrams a) enthalpy as a function of pressure the red arrow indicates the path followed when the sample is metastably compressed, b) enthalpy versus volume diagram, each parabola represent the isothermal equation of state of each phase, the slope of the common tangent to the two parabola is the pressure of the thermodynamic phase transition, again in red the path followed during the metastable compression of the sample, c) pressure – temperature phase diagram with in red the field where phase I exists metastably.

2.4.2. Equations of state

The equation of state determines the thermodynamic state of an elastic solid under hydrostatic pressure, at absolute temperature. The equation of state determines the relation between V, P and T.

According to Hooke's law, the isothermal equation of state under hydrostatic pressure P has the form:

$$P = -K_0 \frac{\Delta V}{V_0}$$

Where K_0 is the bulk modulus, V_0 is the room pressure volume.

However, at high pressure the linear Hooke's law is no longer valid as the bulk modulus changes with pressure. Therefore, it is necessary to introduce an equation of state based on a finite strain.

There are several forms of equation of state depending upon the choice of finite strain definition. For example, the change in distance between neighbouring points during deformation defines the Eulerian strain approach and gives rise to the Birch-Murnaghan equation of state at the third order [124-126]:

$$P(V) = 3K_0 f(1+2f)^{5/2}\left(1+\frac{3}{2}(K_0'-4)f\right)$$

with the Eulerian strain $f = \frac{1}{2}\left[\left(\frac{V_0}{V}\right)^{2/3} - 1\right]$

Another way to express the equation of state is by using interatomic potentials. This give rise to the Vinet equation [127]:

$$P(V) = 3K_0\left(\frac{V_0}{V}\right)^{1/3}\left(1-\left(\frac{V_0}{V}\right)^{1/3}\right)e^{\frac{2}{3}(K_0'-1)\left(1-\left(\frac{V_0}{V}\right)^{1/3}\right)}$$

In the thesis we only used the Birch-Murnaghan equation of state in the fitting of the data. We used the software EosFit from R. Angel to fit all the data.

Finally, in most of the equation of state studies, we are also presenting the data in terms of Eulerian strain as a function of normalised pressure *F*

$$F = P\left(3f\left(1+2f\right)^{5/2}\right)^{-1}$$

This representation of the data gives a better representation and emphasises any error in the fitting procedure or any wrong data point. We also plot the errors on the data. The diagrams will show that the errors dramatically increase at low strain values as we divide the data by a smaller and smaller $\left[\left(V_0/V\right)-1\right]$.

We present the error analysis below:

$$f = \frac{1}{2}\left(\left(\frac{V}{V_0}\right)^{-2/3} - 1\right)$$

$$[f] = -\frac{1}{2}\left(\frac{V}{V_0}\right)^{-2/3} \times \left(-\frac{2}{3}\right)\frac{\left[\frac{V}{V_0}\right]}{\frac{V}{V_0}} = \frac{1}{3}\left(\frac{V}{V_0}\right)^{-5/3} \times \left[\frac{V}{V_0}\right]$$

$$F = P\left(3f\left(1+2f\right)^{5/2}\right)^{-1}$$

$$[1+2f] = \sqrt{2} \times [f] = \mathbf{A}$$

$$\left[(1+2f)^{5/2}\right] = (1+2f)^{5/2} \times \frac{5}{2} \times \frac{\mathbf{A}}{1+2f} = \mathbf{B}$$

$$\left[3f(1+2f)^{5/2}\right] = 3f(1+2f)^{5/2} \times \sqrt{\left(\frac{\sqrt{3}\times[f]}{3f}\right)^2 + \left(\frac{\mathbf{B}}{(1+2f)^{5/2}}\right)^2} = \mathbf{C}$$

$$\left[\left(3f(1+2f)^{5/2}\right)^{-1}\right] = \frac{-1\times\mathbf{C}}{3f(1+2f)^{5/2}} = \mathbf{D}$$

$$\left[P\left(3f(1+2f)^{5/2}\right)^{-1}\right] = F\sqrt{\left(\frac{[P]}{P}\right)^2 + \frac{\mathbf{C}}{\left(3f(1+2f)^{5/2}\right)^{-1}}} = \mathbf{D}$$

2.5. Conclusion

In summary, in this chapter we presented various techniques: X-ray diffraction, Raman spectroscopy, high pressure tools and laser heating systems used in order to perform the experiments presented in the following chapters.

We also introduced a few thermodynamic tools including the Birch-Murnaghan equation of state formulation. We will refer to these few tools in the following chapters.

Chapter 3.

Group IV Spinel Nitrides

3.1. Introduction

The first spinel nitride, Si_3N_4, Ge_3N_4 and Sn_3N_4 were synthesised in 1999 [41, 42, 44, 46, 47, 49, 128]. Several groups have carried out the syntheses of Si_3N_4 and Ge_3N_4 at high pressure and high temperature (10-15 GPa and 1500-2000 K). One group also synthesised for the first time a Sn_3N_4 phase, which has a spinel structure, using a room pressure synthesis route.

Due to the very recent synthesis of the group IV nitrides, there is very little knowledge of their properties and their chemistry. In this chapter, we will first present the synthesis using laser heated diamond cell methods from the stoichiometric β-Si_3N_4 phase and bulk modulus measurement study on the spinel form of Si_3N_4. Somayazulu *et al.* previously reported the bulk modulus of Ge_3N_4 spinel as mentioned in the first chapter [48, 49].

In a second part, we will show the study at high pressure of the Si_3N_4 – Ge_3N_4 system. We first carried out the study using laser heated diamond anvil cell techniques. Then, we used large volume press techniques to obtain larger sample volumes. The aim of this study was the synthesis of the first ternary spinel nitride phases with compositions $Si_xGe_yN_4$ with $x + y = 3$.

3.2. γ-Si_3N_4 spinel nitride

3.2.1. Experimental methods

We loaded commercially obtained α-Si_3N_4 (containing ~5-10% β- Si_3N_4) into a "cylindrical" design diamond anvil cell for double-sided laser heating studies, with 300 μm culet diamond anvils. We drilled a 100 μm hole in a rhenium gasket to form the sample chamber and loaded the cell cryogenically with pure nitrogen that would work as the pressure transmitting fluid. We measured the pressure using the ruby fluorescence scale. Previous experiments have shown that Si_3N_4, a white material does not couple with the Nd:YAG laser. Therefore, in order to bypass this difficulty the samples were loaded with ~1% amorphous boron powder to efficiently absorb the laser energy. We pressurised the materials to approximately 20 GPa and laser heated them

up to around 2000 K. We collected energy dispersive X-ray diffraction patterns at the superconducting wiggler beam line station X17-B1 of the National Synchrotron Light Source (NSLS) at a diffracting angle $2\theta = 12.0000°$.

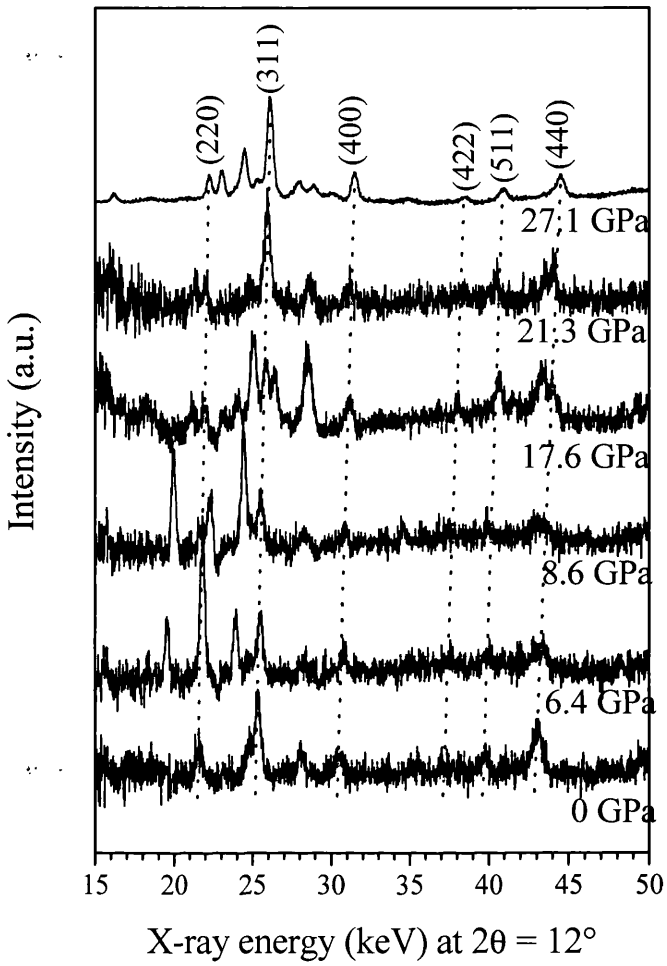

Figure 3-1 Changes in the energy dispersive X-ray diffraction pattern of γ-Si_3N_4 as a function of decreasing pressure following synthesis in the laser heated DAC at ~20 GPa. We observed some peaks due to unreacted α-Si_3N_4 (starting material) in all of the spectra. Those peaks correspond to regions of the sample not laser heated but sampled by the X-ray beam. The dotted vertical lines indicate the peaks belonging to the spinel pattern. We can assign the other peaks to α-Si_3N_4.

After synthesis at 20 GPa, we further pressurised the sample to 35 GPa and then decompressed. The further compression gives a wider range a pressure allowing a better fit for the equation of state.

We performed a second set of experiments at the APS beamline 13 BM-D (bending magnet beamline) using a monochromatic X-ray beam at E = 29.2 keV. In those experiments, we

compressed the sample up to 19 GPa and then laser heated using a Nd:YAG laser. Finally, we collected the X-ray diffraction patterns upon decompression to room pressure.

3.2.2. Results and discussion

In figure 3-1, we plot selected energy dispersive X-ray diffraction patterns for γ-Si_3N_4 as a function of pressure during decompression following synthesis at a pressure of 20 GPa. Before laser heating, the pattern shows only peaks corresponding to α-Si_3N_4. Following laser heating, the diffraction patterns present a new set of peaks corresponding to the (220), (311), (400), (333) and (440) reflections of the $Fd\bar{3}m$ cell of γ-Si_3N_4 (spinel phase). However, the patterns still present some peaks of α-Si_3N_4 from untransformed regions of the sample.

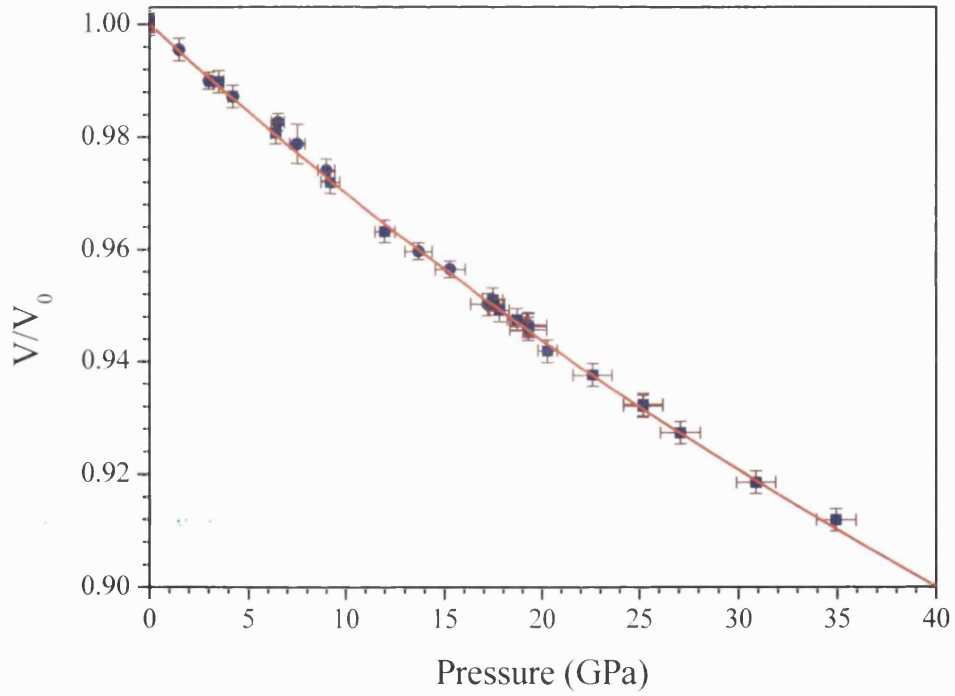

Figure 3-2 Pressure dependence of the unit cell volume of γ-Si_3N_4 measured between 0 and 35 GPa at room temperature. Full squares represent the EDX data and full circles represent the ADX data. The line represents the fit of the data to the Birch-Murnaghan equation of state.

As previously reported [41], one can recover the spinel-structured γ-Si_3N_4 phase upon decompression to ambient pressure and temperature. Spectra taken *in situ* during further compression to 35 GPa and during decompression to ambient pressure allows the determination of the pressure dependence of the unit cell volume. The spectra collected in the DAC at room pressure in two separate sets of experiments gave the ambient pressure cell edge (a_0) at 7.742(9) Å leading to an ambient pressure volume (V_0) of 8.29(3) $Å^3$ / atom. Figure 3-2 shows the

variation of cell volume with pressure. Using the Birch-Murnaghan equation of state and plotting the data in a normalised pressure – Eulerian strain diagram (figure 3-3), a least squares best fit to our data yields K_0 = 308 (5) GPa and K_0' = 4.0 (2) (table 3-1).

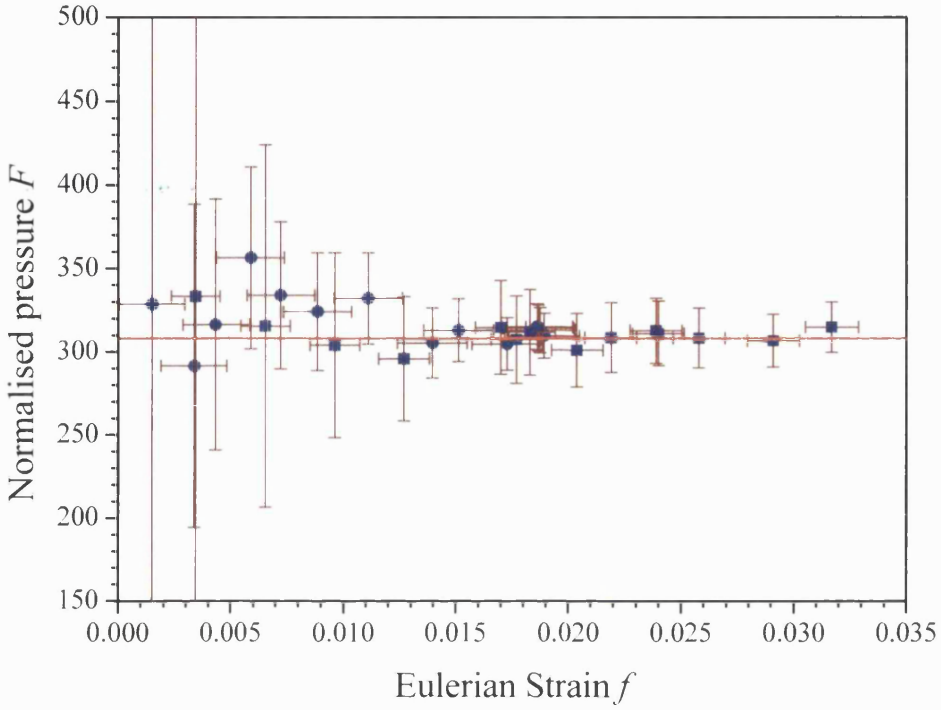

Figure 3-3 Reduced variable F-f representation of the data. A linear least squares best fit gave K_0 = 308(5) GPa and K_0' = 4.0(2).

γ-Si_3N_4	V_0 (Å^3/atom)	K_0 (GPa)	K_0'
Experiment	8.29(3)	308(5)	4.0 (2)
Theory (LDA)[51]	8.142	308	3.9
Theory (GGA)[51]	8.450	284	3.9

Table 3-1 Summary of the high pressure parameters from a Birch-Murnaghan equation of state analysis.

	V_0 (Å^3/atom)	K_0 (GPa)	K_0'
α-Si_3N_4 [39]	10.429	228.5	4.0
β-Si_3N_4 [51]	10.411	270	4.0
γ-Si_3N_4	8.286	308	4.0

Table 3-2 Summary of bulk moduli determined experimentally for Si_3N_4.

The measured bulk modulus of the silicon nitride spinel phase is significantly higher than that of the low pressure phase of silicon nitride (table 3-2). As one would expect, the densely packed spinel-structured phases are much less compressible than the less dense phases which are stable or metastable at room pressure. The densification of Si_3N_4 across the α-γ transition is 20.4 %,

and this value is close to the one found for the β-γ transition in Ge_3N_4 [49]. The physical and chemical similarity of the two materials suggests that solid solutions may exist between γ-Si_3N_4 and γ-Ge_3N_4 (see below), as found in spinel-structured Si- and Ge-bearing oxides prepared at high pressure [129].

3.3. Ge_3N_4 – Si_3N_4 spinel system

3.3.1. Introduction

The two new spinel nitrides Si_3N_4 and Ge_3N_4 have the same structures. In the field of oxide spinels, there is a large number of ternary phases. Since ternary phases exist among the spinel oxides, one would expect that ternary spinel nitrides could exist as well. Therefore, in the following paragraphs, we are investigating the Si_3N_4 – Ge_3N_4 system at high pressure. In the first part of the study, we performed the experiments using laser heated diamond anvil cell techniques coupled with synchrotron X-ray diffraction. In the second part, we change the synthesis tools to large volume presses in order to obtain larger sample volumes and have a better characterisation of the samples.

3.3.2. Synthesis of ternary spinel nitrides using laser heated diamond anvil cell

3.3.2.1. Experimental methods

We designed the present experiments in order to explore the formation and stability of ternary nitride phases in the γ-$(Si,Ge)_3N_4$ system. In the case of nitrides, we loaded the starting mixture of elements (Si and Ge) or compounds (Si_3N_4 and Ge_3N_4) into the cell with nitrogen, which acted as a pressure medium and provided a high nitrogen activity around the sample during heating. The high nitrogen activity prevented the sample from decomposing at high temperature and facilitated the synthesis of new nitrides. We carried out three sets of experiments using 1:2, 1:1, and 2:1 starting mixtures of α-Si_3N_4 and β–Ge_3N_4. We loaded the samples into a "cylindrical" design DAC with 300 μm culet diamonds. We formed the sample chamber by drilling a 100 μm hole into a rhenium (or occasionally stainless steel) gasket. We recorded the pressure using the ruby fluorescence technique and pressurised the samples to ~20 GPa before heating. We collected energy dispersive X-ray diffraction patterns *in situ* at high pressure (we also collected some patterns at high temperature) at a diffraction angle of $2\theta = 12.008(7)$ °. We laser heated the sample to 2000 K.

Upon initial compression, the X-ray diffraction pattern of the α-Si_3N_4 starting material was difficult to observe in the presence of the much stronger lines of the β-Ge_3N_4 phase; this was because of the difference in atomic numbers. However, above ~19 GPa, the Ge_3N_4 phase became disordered and its X-ray diffraction peaks broadened and decreased in intensity (see chapter 4) [48, 49], so that the Si_3N_4 spectrum became visible. Upon laser heating, the sample transformed immediately into the stable spinel phase(s) (figure 3-4).

3.3.2.2. Results and discussion

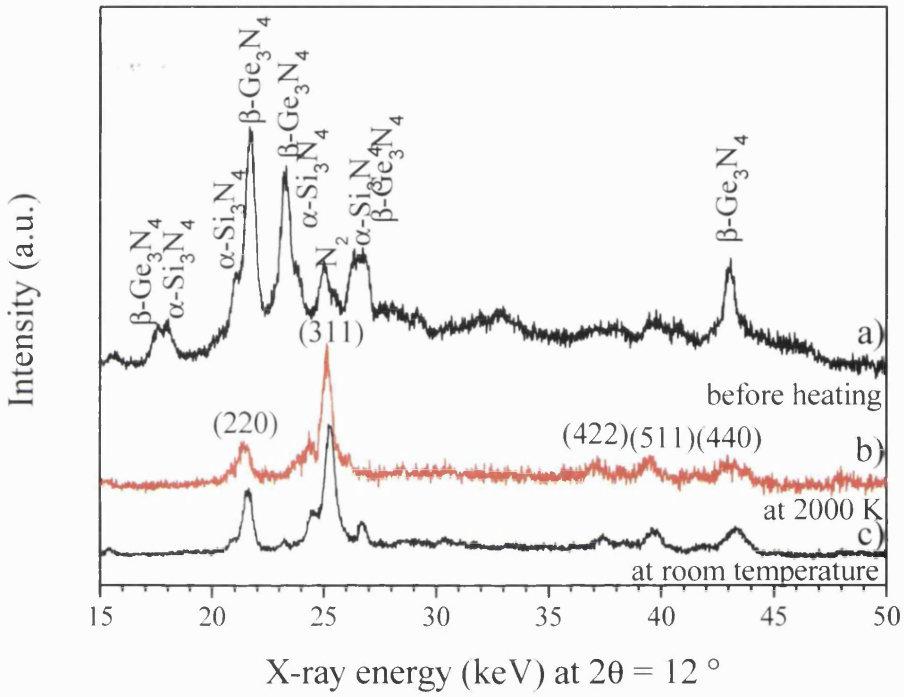

Figure 3-4 Energy dispersive X-ray diffraction patterns for a mixture of 2 α-Si_3N_4 + 1 β-Ge_3N_4 at P ~ 20 GPa a) at room temperature before laser heating, b) at high temperature during heating at around 2000K and c) at room temperature following heating and quench.

Figure 3-4 presents a typical energy dispersive X-ray diffraction pattern of a 2:1 α-Si_3N_4 + β-Ge_3N_4 mixture before, during and after laser heating. Once laser heating begins, the peaks from the low pressure phases disappear, giving rise to a spinel-type pattern. The results obtained were similar for all three mixtures. Examination of the X-ray patterns shows the splitting of each spinel peak into two components in all cases (figure 3-5). Thus, the heating experiment synthesised not one but two spinel phases, from each of the three starting compositions.

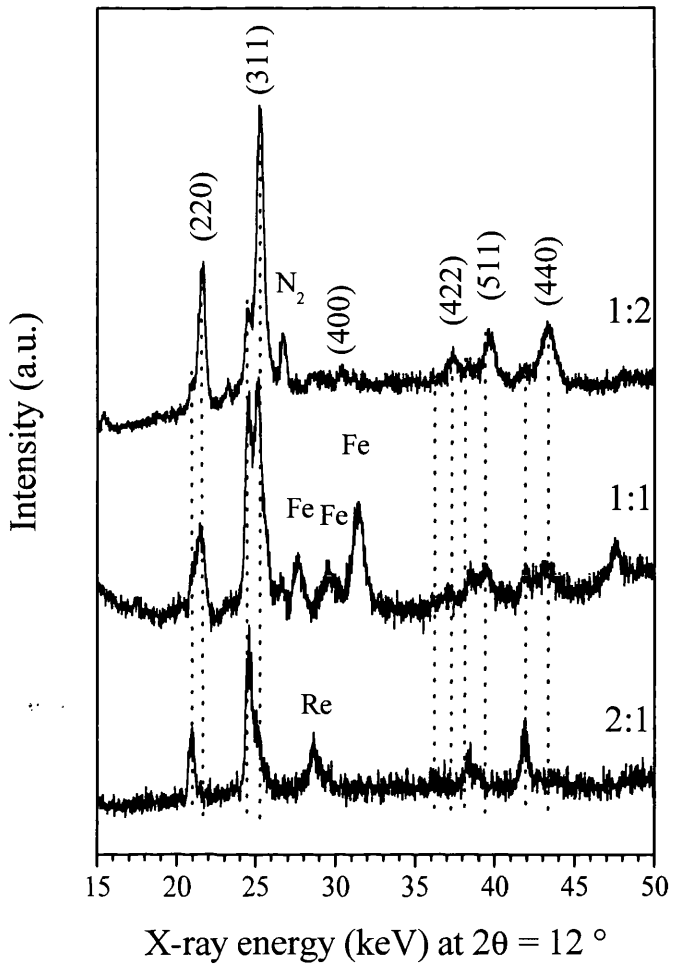

Figure 3-5 Energy dispersive X-ray diffraction patterns at P ~ 20 GPa and room temperature (RT) after laser heating three different mixtures of α-Si_3N_4 and β-Ge_3N_4, in the respective ratios 2:1, 1:1, and 1:2. All of the peaks in the spinel diffraction pattern are doubled. The two components do not change in position but vary systematically in relative intensities as a function of bulk composition, indicating the presence of two spinel phases at all compositions.

The collection of the energy dispersive X-ray diffraction patterns was performed while rotating and oscillating the diamond anvil cell. Therefore, the relative intensity of the diffraction peaks should be relatively reliable. The overall intensities of the X-ray diffraction patterns for the two spinels are comparable, indicating that the heavy element germanium is present in substantial amounts in both spinels (unlike in the case of the starting mixture of α-Si_3N_4 and β-Ge_3N_4). In particular, the 1:1 mixture shows the same intensity for both spinels in particular for the (311) reflection. The positions of the diffraction peaks in the patterns of the two spinels do not change when the bulk composition varies (figure 3-5). Instead, the relative intensities of the characteristic peaks for each spinel (e.g., the prominent (220) and (311) reflections) vary systematically with Si_3N_4 / Ge_3N_4 ratio. As a result, instead of a spinel solid solution being

present throughout the composition range, there are two co-existing spinels with fixed unit cell parameters.

starting composition	temperature	spinel A (Å)	spinel B (Å)
1 α-Si_3N_4 + 2 β-Ge_3N_4	HT	7.99	7.78
1 α-Si_3N_4 + 2 β-Ge_3N_4	HT	8.04	7.79
1 α-Si_3N_4 + 2 β-Ge_3N_4	RT	7.97	7.78
1 α-Si_3N_4 + 1 β-Ge_3N_4	HT	8.01	7.79
1 α-Si_3N_4 + 1 β-Ge_3N_4	RT	7.99	7.78
1 α-Si_3N_4 + 1 β-Ge_3N_4	RT	7.99	7.77
2 α-Si_3N_4 + 1 β-Ge_3N_4	HT	8.04	7.79
2 α-Si_3N_4 + 1 β-Ge_3N_4	HT	7.98	7.80
2 α-Si_3N_4 + 1 β-Ge_3N_4	RT	8.00	7.74
γ-Ge_3N_4	RT	8.03	
γ-Si_3N_4	RT	7.57	

Table 3-3 Results from the cell parameter refinement of spinel patterns at 20 GPa during laser heating in situ at high temperature(HT) and after temperature quench at room temperature and high pressure (RT) mixtures of α-Si_3N_4 and β-Ge_3N_4. We fit the lattice parameters with an uncertainty of approximately ± 0.03 Å. We calculated the lattice parameters for the end members γ-Si_3N_4 and γ-Ge_3N_4 from their measured ambient pressure volumes and bulk modulus [6, 10, 15] using a Birch-Murnaghan equation of states.

starting composition	spinel A	spinel B
2 α-Si_3N_4 + 1 β-Ge_3N_4	~ 0 $Ge_{3-x}Si_xN_4$ x<0.5	~ 1 $GeSi_2N_4$
1 α-Si_3N_4 + 1 β-Ge_3N_4	~ 1 $Ge_{3-x}Si_xN_4$ x<0.5	~ 3 $GeSi_2N_4$
1 α-Si_3N_4 + 2 β-Ge_3N_4	~ 1 $Ge_{3-x}Si_xN_4$ x<0.5	~ 1 $GeSi_2N_4$

Table 3-4 Idealised estimated ratio and composition of spinel products from the starting material and the lattice parameter measured.

Table 3-3 presents the refined cell parameters for each of the two spinels "A" and "B". Table 3-4 presents a summary of the results from table 3-3 interpreted in term of compositions. Figure 3-6 display the data and shows the unit cell parameter refined for both A and B spinels at each of the three Si / Ge composition ratios. Table 3-3 and figure 3-6 compare the mixed $(Si,Ge)_3N_4$ values with those of the end member spinels γ-Si_3N_4 and γ-Ge_3N_4. We extrapolated the lattice parameter of the end members to 20 GPa using the measured compressibility for these phases [46, 48]. In figure 3-6, the straight line drawn between the γ-Si_3N_4 and γ-Ge_3N_4 end members at 20 GPa gives an estimate of the lattice constant expected for a $(Si_xGe_{1-x})_3N_4$ alloy with Si and Ge atoms distributed randomly on tetrahedral and octahedral sites (Vegard's law). The data plotted in figure 3-6 confirm that there is no variation in lattice constant within each of the two spinels with different Si/Ge ratio in the starting mixture.

For all starting compositions examined here, one of the reaction products consists of a spinel with a lattice parameter very close to that of γ-Ge_3N_4. The second spinel phase is much richer in Si_3N_4 component. Vegard's law gives a first estimate for the composition of the Si-rich spinel

phase from the intersection of the observed lattice parameter values with the ideal mixing line. The result indicates a spinel composition close to 60 mol % Si_3N_4, or $(Ge_{0.40}Si_{0.60})_3N_4$.

In figure 3-4, the diffraction pattern b shows that the two spinels are already clearly visible at high temperature. Thus, there is no closure of the solid solution up to the synthesis temperatures (~2000 K). It also appears that the lattice parameter of the silicon rich nitride is the same (within experimental error) at high and room temperature. Thus, the new ternary nitride must have a small thermal expansion coefficient.

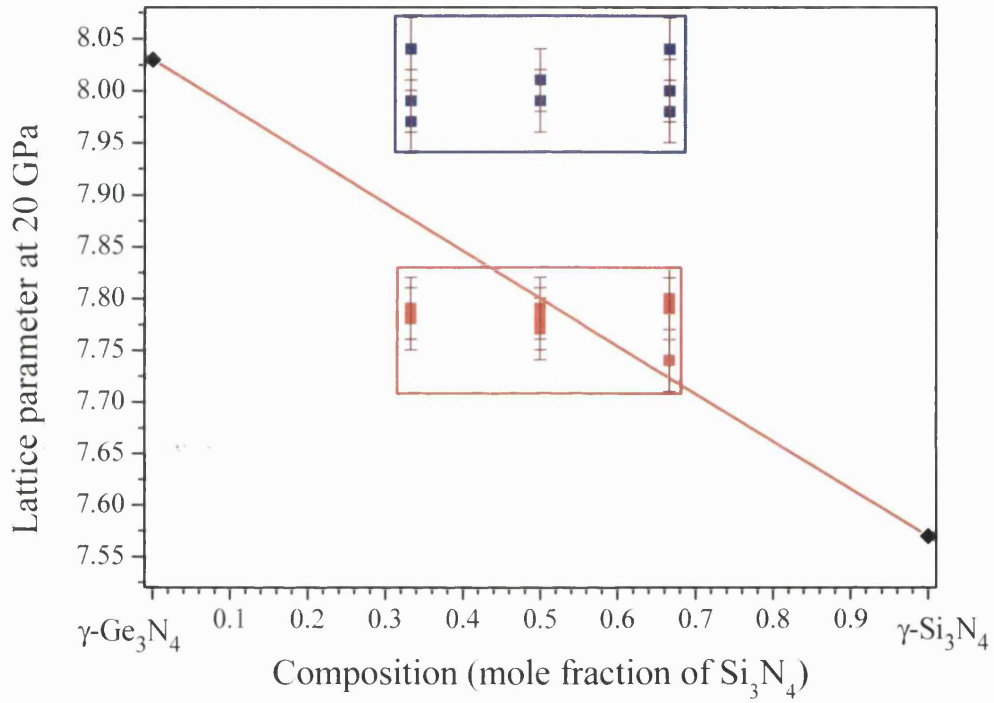

Figure 3-6 Spinel lattice parameters as a function of starting composition. Each pair of points, one in the top box and the other in the bottom box, correspond to lattice parameters refined for the two spinel phases identified in each energy dispersive X-ray diffraction pattern. The solid line shows Vegard's law (average lattice constant) for a random $(Si_xGe_{1-x})_3N_4$ alloy, drawn between the end members γ-Ge_3N_4 and γ-Si_3N_4, with their lattice parameters extrapolated to P = 20 GPa and room temperature.

In order to find out if the newly synthesised ternary spinel is the normal or inverse spinel type, we generated the X-ray diffraction patterns, using PowderCell 2.3, for both cases and compared them with the measured X-ray diffraction patterns. Figure 3-7 shows the calculated X-ray diffraction patterns for the normal and inverse spinels. One can compare those with the uppermost trace of the experimental spectra (Figure 3-5) of the mixtures, because the Si-rich phase dominates this pattern with a nominal composition 2:1 Si_3N_4:Ge_3N_4. The calculated pattern for the normal spinel has the (220) reflection much more intense than (400), as it is

observed experimentally (for the pure Ge_3N_4 spinel, the (400) reflection is approximately half as intense as (220)). In the inverse spinel, the (220) reflection is extremely weak compared to the (400) peak. Clearly, the inverse spinel pattern does not match the pattern shown in figure 3-5. Furthermore, the calculated pattern shows the intensity for the (422) reflection comparable to those of the (151) and (440) reflections, like it is observed in the measured pattern. The theoretical pattern for the inverse form has (422) much weaker than the other two peaks. From the above observations, we conclude that the newly synthesised phase is a normal spinel: i.e., the Si^{4+} ions occupy octahedral sites, and Ge^{4+} ions preferentially occupy tetrahedral positions. The result appears initially counterintuitive, as Ge^{4+} ions (0.55Å) are considerably larger than Si^{4+} (0.40Å). However, *ab initio* calculations confirmed this result [130].

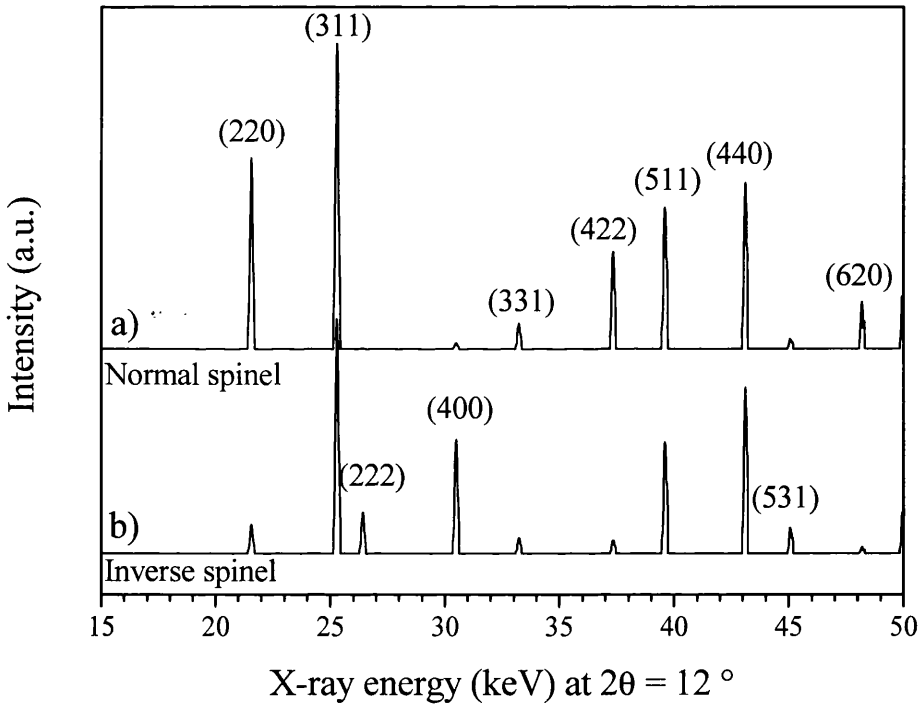

Figure 3-7 Calculated X-ray diffraction patterns for (a) normal spinel $GeSi_2N_4$ (idealised from the observed composition $(Ge_{0.40}Si_{0.60})_3N_4$) with Ge ordered on tetrahedral sites and Si ordered on octahedral sites (b) inverse spinel $Si^{iv}(SiGe)^{vi}N_4$.

The synthesis pressure and temperature for the new ternary nitride spinel are within the range attainable by large volume press techniques. The experiments also indicate that the new phase is recoverable to ambient conditions. In consequence, the next paragraph will focus on the synthesis of larger samples of the new ternary nitride spinel in a large volume press.

3.3.3. Synthesis of ternary spinel nitrides using multi-anvil press techniques

Following the very interesting discovery of a new ternary spinel nitride phase using diamond anvil cell techniques, we decided that it would be useful to obtain a larger sample of the new phase. Thus, we moved from the diamond anvil cell to the large volume press techniques.

3.3.3.1. Experimental methods

We performed the experiments at Arizona State University using the Big Blue press previously described and a 3-8 assembly. We originally only confined the sample within the rhenium furnace with a small rhenium disk above and below. In a second set of experiments, we further enclosed the sample into a boron nitride capsule. The experimental conditions were 20 GPa (4950 psi of oil pressure in the press) and temperatures ranging from 1500 °C to above 2300 °C. In most cases, we measured the temperature using a type C thermocouple. However, in some cases the thermocouple failed upon pressurisation. Therefore, we had to use the power curve obtained during the successful runs in order to estimate the temperature.

The sample used during the synthesis experiments were ground mixtures of α-Si_3N_4 + α-β-Ge_3N_4. We mixed and ground the starting samples with two WC cubes.

3.3.3.2. Results and discussion

In the first run, we used a 2:1 mixture of Si_3N_4 and Ge_3N_4, and heated the sample to 1500 °C for 2 hours. The X-ray diffraction pattern of the quench sample shows very little reaction between silicon nitride and germanium nitride. The resulting pattern shows the X-ray diffraction pattern of γ-Si_3N_4 + γ-Ge_3N_4. Therefore, we decided to increase the temperature in order to increase the kinetics. We performed the following experiments at 20 GPa and 2000 °C.

We loaded four mixtures of silicon nitride and germanium nitride; 1:4, 1:2, 1:1 and 2:1. Figure 3-8 presents the X-ray diffraction patterns of the samples resulting from those syntheses. The extra peaks in the pattern are from an undetermined phase of rhenium alloying with the germanium in the sample (Figure 3-9).

The patterns clearly show that there is no complete reaction between the silicon nitride and germanium nitride even though we heated the sample for two hours. The only sample displaying a single spinel pattern is that of the sample synthesised from a mixture of 4 Ge_3N_4 + 1 Si_3N_4. The lattice parameter and Rietveld refinement of the pattern give a composition $(Ge_{0.9}Si_{0.1})_3N_4$ with all the Si atoms in octahedral sites. The difference between the starting composition and the product composition is most likely due to the large errors in the starting composition as we

only sample a very small amount of the weighted sample. Although this result appears in contradiction with the DAC experiments, the errors in compositions measurement in the DAC experiments can easily encounter for the difference. The lattice parameter of the spinel considered to be "Ge_3N_4" in the DAC synthesis is not exactly that of germanium nitride therefore it could have a composition including a small amount of silicon. Therefore, the results are in fact consistent to this extent.

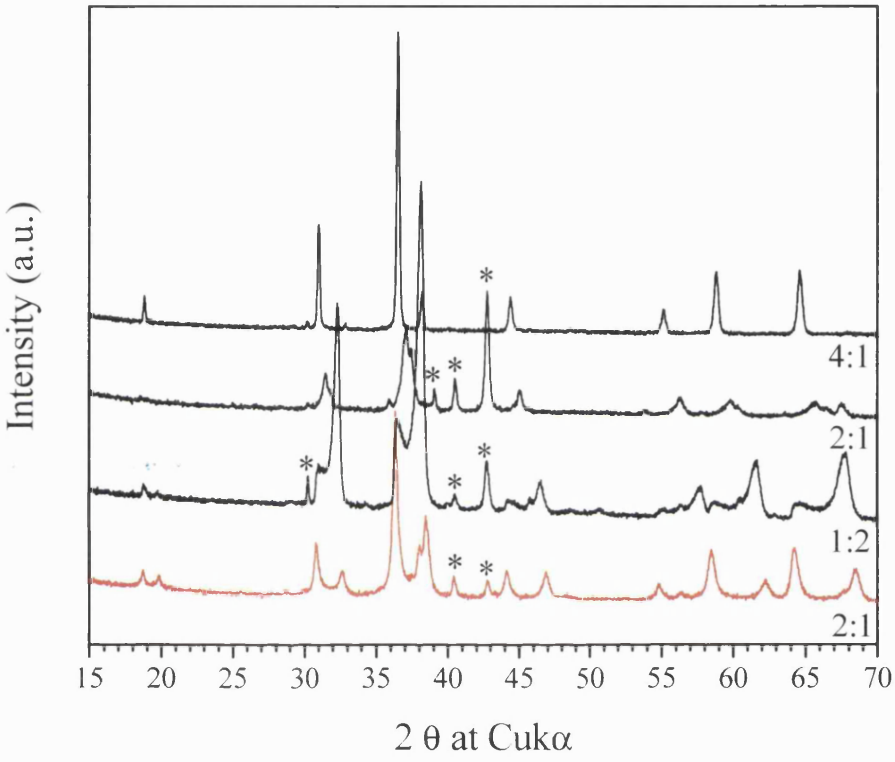

Figure 3-8 X-ray diffraction patterns of spinel nitrides synthesised from three mixtures of germanium nitride + silicon nitride heated at 2000 °C and 20 GPa in the multi-anvil press. The lowest spectrum in red is that of the synthesis performed at 1500 °C and 20 GPa.

In order to observe the phase relationship between the spinels synthesised at high pressure, we observed the sample using scanning electron microscopy (SEM) with the backscattered electrons detector. Therefore, the images show a "compositional map" of the sample. Figure 3-9 shows some of the observed images of the sample. We clearly see that the sample is multi phased. There are several shades of grey indicating a variation in the composition. The shades of grey also indicate that the sample is not at equilibrium. Therefore, the experimental conditions have to be modified.

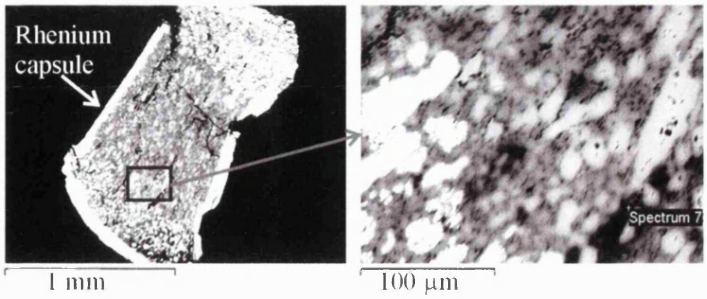

Figure 3-9 Backscattered SEM pictures of one of the samples synthesised in the multi-anvil press. The white grains are drops of rhenium within the sample. The composition of those grains is not pure Re. There is a range of composition with various amount of Ge up to 50% in some cases. The grey grains are the silicon germanium nitride spinels with a range of compositions.

We performed one final set of experiments where we ground the sample even thinner and increased the temperature to 2300 °C. Those experimental conditions are very extreme and we could only sustain the temperature between 10 and 60 minutes as the furnace often melted. In the previous set of runs, the capsule material was diffusing and reacting with the nitrides. In order to attempt to prevent this reaction, we placed the sample inside a small boron nitride capsule within the rhenium capsule. This resulted in a significantly smaller sample size. Nevertheless, the size was still dramatically larger than that obtained in a diamond anvil cell experiment and allowed an easy sample preparation for electron microscopy studies.

Figure 3-10 presents the X-ray diffraction pattern of the sample from a 2:1 mixture of Si_3N_4 – Ge_3N_4. The sample was also analysed using electron probe and the SEM (figure 3-11). In this case, the sample shows a uniform composition except for the drops of rhenium present in the sample. The boron nitride capsule did not prevent the rhenium from diffusing into the sample. Nevertheless, rhenium does not diffuse into the spinel grains as shown in the three high magnification electron micrographs. The rhenium stays within the grain boundaries. The sample grain size is about 5 µm. The backscattered electron photographs show that there is no significant change in composition from grain to grain unlike in the case of the previous syntheses at 2000 °C. The sample is more uniform although there is still a lot of rhenium with the bulk of the sample.

Using the lattice parameter obtained from the X-ray diffraction pattern (a = 7.95 Å) and Vegard's law, we obtain a composition $GeSi_2N_4$. Using electron probe, we obtain the exact same composition as well. Therefore, we have evidence for a new ternary spinel nitride with the composition $GeSi_2N_4$.

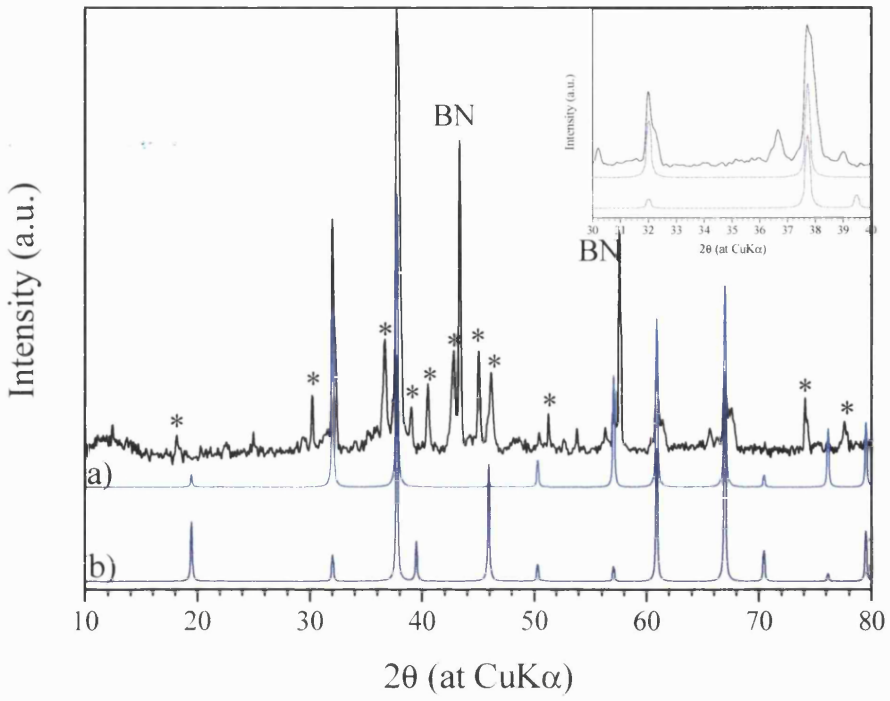

Figure 3-10 X-ray diffraction pattern of a sample synthesised at 20 GPa and 2300 °C from a mixture of 2 Si_3N_4 + 1 Ge_3N_4. The peaks indicated with * correspond to a Re_xGe_y phase and the peaks with BN correspond to left over super hard cubic boron nitride from the capsule material ground with the sample. Below the measured spectrum, we present two calculated spectra a) for a normal spinel and b) for an inverse spinel.

We carried out the investigation of the relative peaks intensity of the $GeSi_2N_4$ spinel. However, due to the presence of an unidentified Re_xGe_y phase in the pattern, we were not able to carry out a good Rietveld refinement. Nevertheless, we previously showed that there is a dramatic change between the relative intensity of the peaks from a normal to an inverse spinel. The comparison of the calculated spectra with that measured for $GeSi_2N_4$ presented figure 3-10 clearly shows that the sample is a normal spinel.

We performed the experiment at 2300 °C using several starting compositions however, we obtained $GeSi_2N_4$ spinel every time. It appears that the rhenium acts as a sink for Si and Ge in excess from the $GeSi_2N_4$ composition at that temperature. Therefore, we will have to carry out the experiments using a Re free assembly in order to further characterise the Si_3N_4 – Ge_3N_4 spinel phase diagram.

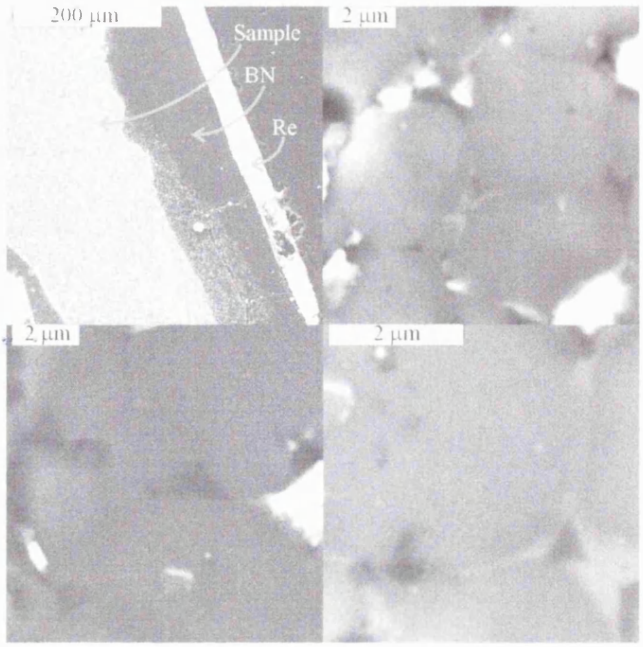

Figure 3-11 SEM photographs of one of the samples synthesised at 20 GPa and 2300 °C from a mixture of 2 Si_3N_4 + 1 Ge_3N_4. All the pictures but the bottom left one are collected using the secondary electron detector. The bottom left picture was collected using the back scattered detector.

3.3.4. Raman spectroscopic study of the Ge_3N_4 – Si_3N_4 spinel system

The Raman spectra of silicon nitride spinel although reported in the literature is not understood. The spectra previously reported have an incorrect peak assignment with a large number of extra peaks [45]. Therefore, we will start by presenting the Raman spectra of the two pure phases of Si_3N_4 and Ge_3N_4 spinels. Then, we will study the spectra of the intermediate phases. In any case, factor group analysis only predicts five Raman active modes: 3 T_{2g} + 1 E_g + 1 A_{1g}. However, as we describe below, in most cases, we observe more than these five peaks in the spectra.

3.3.4.1. Raman spectra of γ-Si_3N_4

We synthesised the sample of spinel silicon nitride using laser heated diamond anvil cell techniques at pressures from 14 to 20 GPa. We varied the synthesis temperatures from 1500 K up to 3500 K.

Kroll predicted the position of the Raman bands of γ-Si_3N_4 [131] (table 3-5). Figure 3-12 presents some polarised and unpolarised spectra of γ- silicon nitride. The polarised Raman spectroscopy experiment on powdered sample is acceptable to the extent that the polarisation is averaged to all the orientations of the crystallites, e.g. only the totally symmetric modes like A_{1g} disappear in cross polarised experiments. All the other modes can only undergo a decrease in intensity.

The spectra show that two of the T_{2g} modes are extremely weak and are not observed in most cases. The A_{1g} mode is also very weak and extremely broad. The two strong modes are the E_g and the T_{2g} modes. The A_{1g} modes are generally expected to be very intense and the very weak intensity in this case is not yet explained.

	γ-Si_3N_4 [131]	γ-Ge_3N_4 [131]	γ-Ge_3N_4 [51]
T_{2g}	413	244	245
T_{2g}	500	574	576
E_g	518	471	467
T_{2g}	838	719	710
A_{1g}	946	831	830

Table 3-5 Predicted Raman peak positions for γ-Si_3N_4 and γ-Ge_3N_4 from LDA/GGA calculations of Dong et al. [51] and Kroll [131].

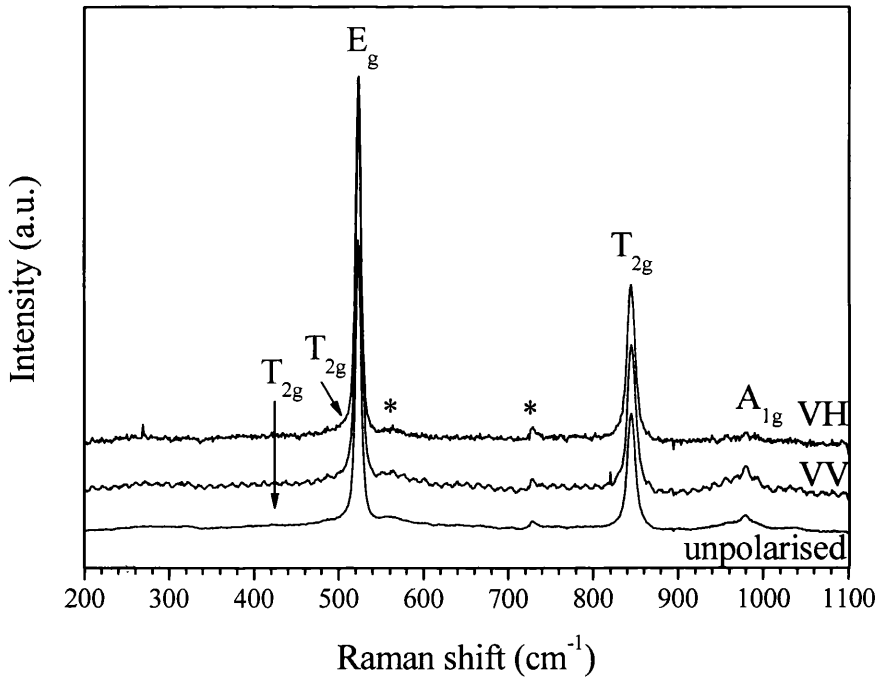

Figure 3-12 Polarised and unpolarised Raman spectra of γ-Si_3N_4 at room pressure after synthesis at 16 GPa and 1500 K. We assigned the peaks by comparison with Kroll's theoretical data. The two peaks with a * are not identified at present. Although those extra peaks are not expected, they are present in all the spectra.

Although the spectra presented above are relatively simple and easy to analyse, in most cases, the spectra are more like those presented figure 3-13. In that case, we synthesised the sample of silicon nitride spinel at a much higher temperature in the diamond anvil cell using laser heating techniques. We can attribute the dramatic change in the spectrum to the creation of nitrogen vacancies in the spinel structure. At high temperature, the activity of nitrogen decreases and the sample of silicon nitride becomes non-stoichiometric.

The appearance of extra features in the spinel Raman spectrum was previously reported among oxides [132-135]. In fact, the Raman spectra of spinels are mostly dependent upon the nitrogen (or oxygen) motions. Therefore, any changes in the nitrogen content and creation of vacancies will result in dramatic changes in the pattern.

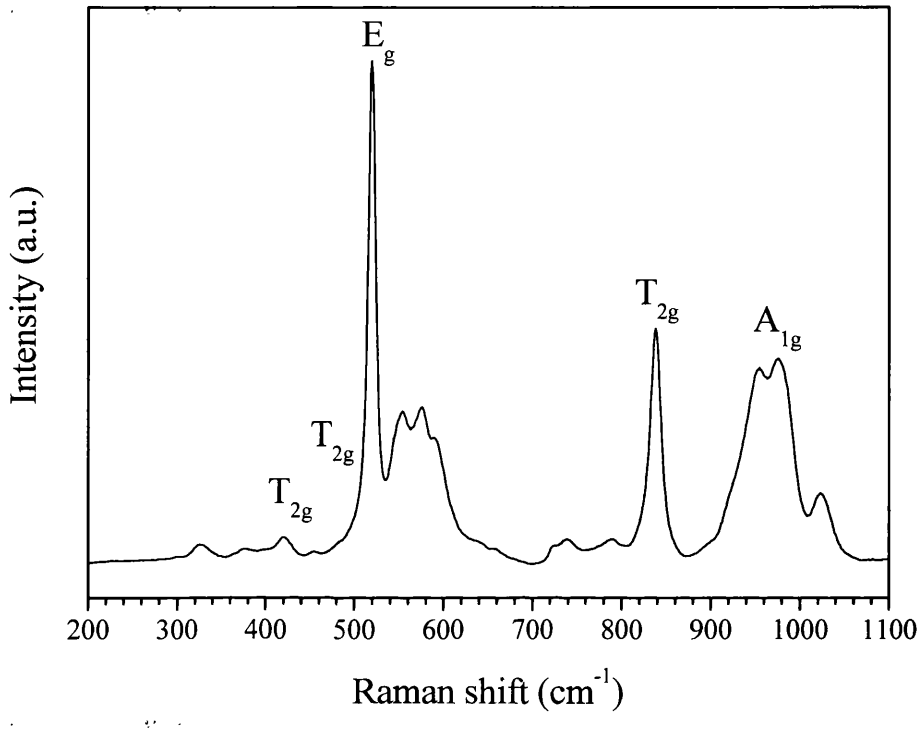

Figure 3-13 Raman spectra of γ-Si_3N_4 at room pressure after laser heating synthesis at 20 GPa and 3000 K. The spectra display strong features around 550 – 600 cm^{-1} and 900 – 1050 cm^{-1}. Those features can be associated nitrogen vacancies in the sample.

3.3.4.2. Raman spectra of γ- Ge_3N_4

Deb *et al.* [50] have previously reported the Raman spectrum of γ-Ge_3N_4. In their study, they synthesised the sample using multi anvil techniques. The study from Deb *et al.* showed an excellent agreement with the peak position calculated by Dong *et al.* [51] except for the low frequency T_{2g} peak which was 100 cm^{-1} above the expected position. The peak that Deb *et al.* reported at 325 cm^{-1} could also result from elemental Ge which is present in the sample in small amount. We collected a Raman spectrum on the same γ-Ge_3N_4 sample this time trying to sample as little Ge as possible in the spectrum. Figure 3-14 present the Raman spectrum and shows that it is possible to collect spectra where the peak at 324 cm^{-1} has almost no intensity. Therefore, it is highly probable that the 324 cm^{-1} peak is only due to elemental germanium.

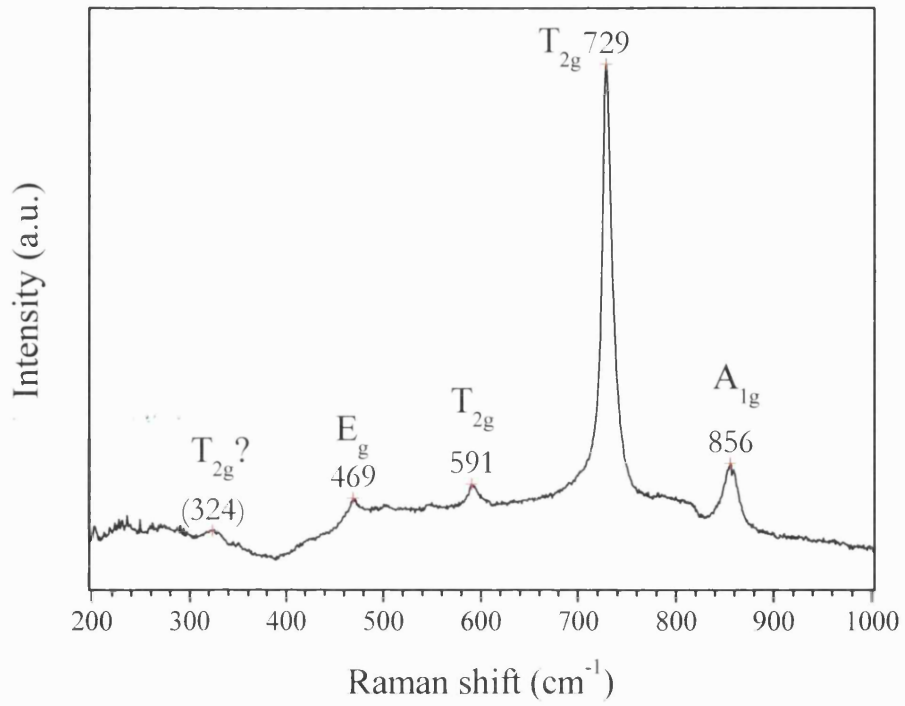

Figure 3-14 Raman spectrum of γ-Ge_3N_4 synthesised using a multi-anvil device at 12 GPa and 1400 K.

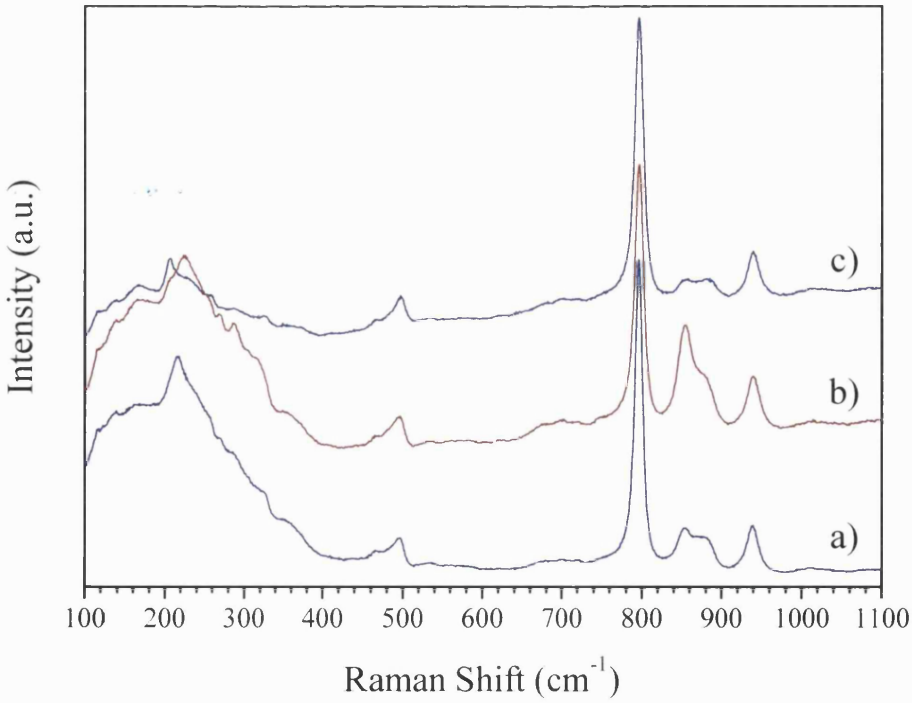

Figure 3-15 Room temperature Raman spectra of γ-Ge_3N_4 successively synthesised in one DAC experiment at 18 GPa and variable temperatures: a) 1700 K b) 2500 K c) 1700 K.

We also collected Raman spectra on samples in a nitrogen pressure medium, synthesised using laser heated diamond anvil cell (figure 3-15). We laser heated the samples at pressure between 9 and 25 GPa and temperature ranging from 1500 to 3000 K. The broad feature below 400 cm^{-1} is characteristic of nitrogen present in the cell as the pressure medium. The spectra show an extra feature between 700 and 900 cm^{-1}. We first heated the sample to 1700 K then to 2500 K and finally reheated the sample at 1700 K. The intensity of the extra feature changed dramatically with temperature. The higher the synthesis temperature the more intense the extra feature was. Therefore, like in the case of silicon nitride, the extra peak is resulting from nitrogen vacancies created at high temperature as the nitrogen activity decreases in the sample chamber.

3.3.4.3. Raman spectra of spinels in the Si_3N_4 – Ge_3N_4 system

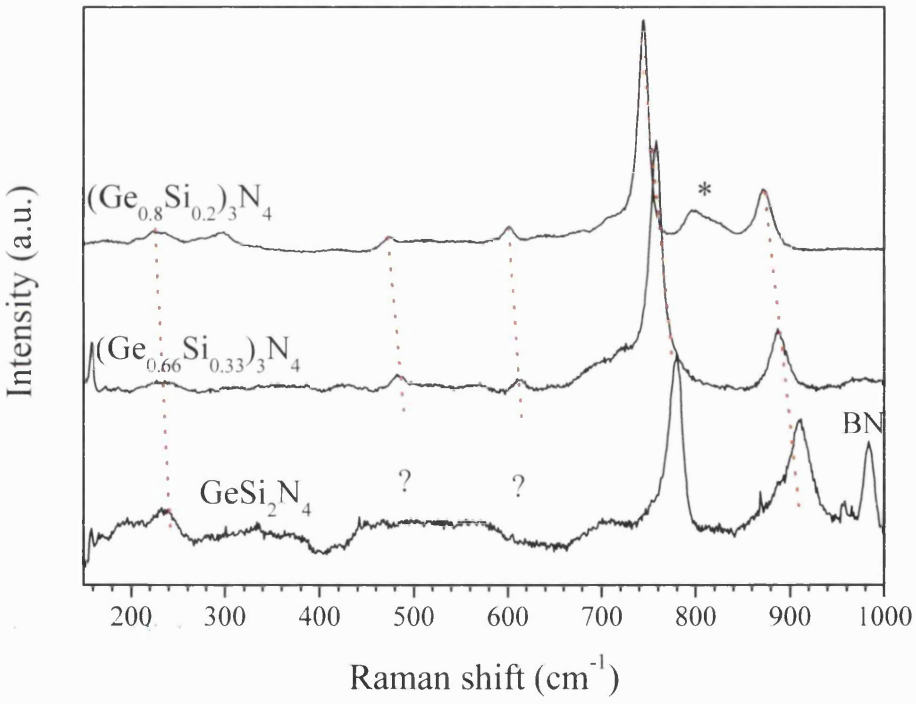

Figure 3-16 Raman spectra of three ternary spinel nitride compositions. We determined the composition using the electron microprobe. BN indicates the Raman peak of cubic boron nitride. The * indicates a peak resulting from the nitrogen vacancies.

We collected Raman spectra on the samples synthesised using the multi anvil (figure 3-16). The spectra were typical of the now familiar spinel nitride Raman spectrum. In particular, they are extremely similar to that of germanium nitride. The phonon frequencies change as a function of composition and have frequencies intermediate between that of silicon nitride and germanium nitride. It appears that the peak position is strongly dependent upon the composition. In some of the very non-uniform samples, it was possible to measure very large peak shifts between two positions in the sample. The advantage of using Raman spectroscopy rather than X-ray

diffraction, in that case, is that the area probed with the laser is only in the order of a few micrometers. In the case of laboratory X-ray diffraction analysis, the X-ray beam probes a large part of the sample at once. Therefore, Raman spectroscopy allows a smaller sample and a finer analysis of the compositional variation within the sample.

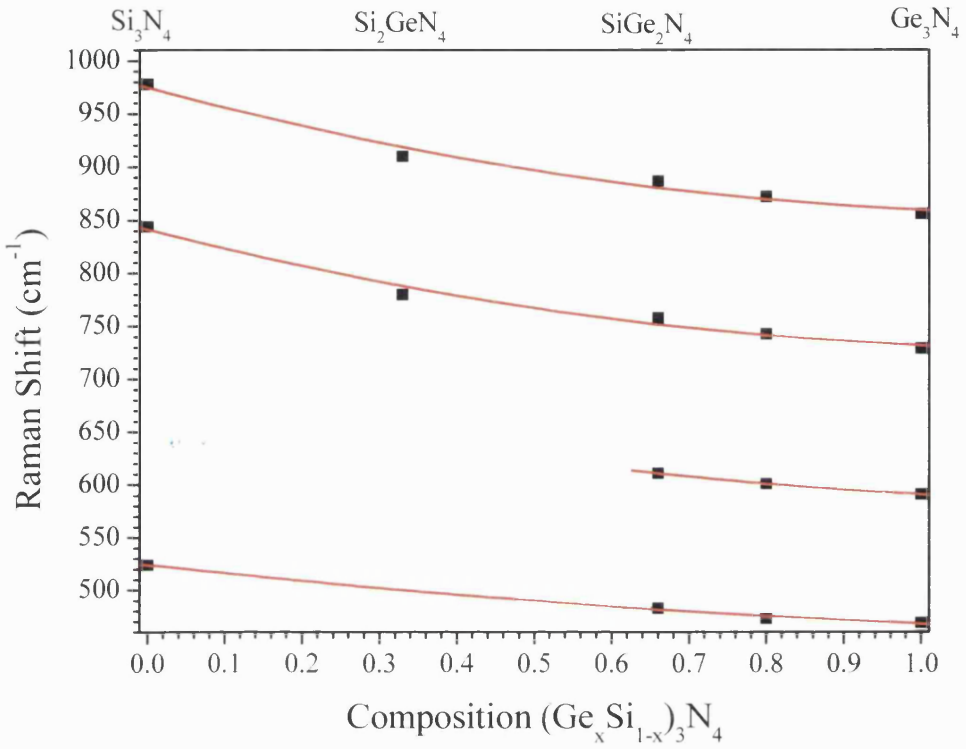

Figure 3-17 Raman shift of Ge – Si nitride spinels as a function of composition. Composition of the spinel measured using electron microprobe on various parts of the samples.

Figure 3-17 shows a summary of the results on the Raman spectroscopy study of the ternary spinel nitride with a diagram of the Raman shift as a function of composition. The peak shift change regularly as a function of composition. Therefore, we can use Raman spectroscopy in a first approximation in order to determine the composition of the ternary spinel nitride in the system $Si_3N_4 - Ge_3N_4$.

3.3.5. Summary

From the data collected using the diamond anvil cell and the multi anvil press, we have evidence of the synthesis of the first ternary spinel nitride with the composition $GeSi_2N_4$. The relative intensity of the peaks in the X-ray diffraction pattern allowed us to determine that Ge atoms are in the tetrahedral sites and Si atoms are in the octahedral sites. This result is consistent with that determined by Dong *et al.* [130]. They explain the surprising site preferences by looking at the nitrogen environment. The tetrahedral site formed by the three octahedrally coordinated metal atoms and one tetrahedrally coordinated metal atom around the nitrogen atom

are much more symmetrical with ^{IV}Ge and ^{VI}Si than in the inverse spinel case. Therefore, the normal spinel is more stable than the inverse spinel at the composition $GeSi_2N_4$.

The experimental results from diamond anvil cell and multi anvil synthesis bring some input on the Si_3N_4 – Ge_3N_4 spinel phase diagram. The phase diagram at high temperature shows some solid solution between Ge_2SiN_4 and Ge_3N_4 as we could synthesise the sample with the composition $Ge_{2.7}Si_{0.3}N_4$. Furthermore, the results also showed that there was no solid solution between Ge_2SiN_4 and $GeSi_2N_4$. The only compositions synthesised between those compositions were the results of synthesis where the sample did not reach equilibrium. However, the presence of rhenium reacting with the sample as a sink for Ge was an inconvenience during the experiments and could lead to partially inaccurate conclusions in the multi-anvil syntheses.

Finally, we performed a Raman spectroscopic study on both the end members and the intermediate phases in the system γ-Si_3N_4 – γ-Ge_3N_4. The results show that creation of a significant amount of nitrogen vacancies in the spinel structure at temperature above 2000 K. Furthermore, there is a regular decrease in phonon frequencies from silicon nitride to germanium nitride. Therefore, in a first approximation, it is possible to determine the composition of the ternary spinel nitrides.

Chapter 4.

Pressure Induced Phase Transition in β-Ge_3N_4

4.1. Introduction

The recent discovery of new silicon and germanium nitride phases synthesised at high pressure and high temperature lead to a renewed interest in the study of their polymorphism [41, 47, 49] (see chapter 3). Si_3N_4 and Ge_3N_4 show identical polymorphism at low pressure (see chapter 1).

The α- and β-forms of Si_3N_4 and Ge_3N_4 contain tetrahedrally-coordinated Si and Ge. The N atoms are at the centre of a triangle formed by three Si or Ge atoms in the β-phase. In the α-phase the N atoms are slightly out of the triangles. The high-density spinel structures contain Si and Ge in both octahedral and tetrahedral coordination to nitrogen, and the N atoms are coordinated to four Si or Ge. γ-Ge_3N_4 is the only solid state compound to date that contains Ge in octahedral coordination to nitrogen.

In this chapter, we investigate the polymorphism that occurs in β-Ge_3N_4 during metastable compression at ambient temperature, using a combination of energy-dispersive (ED) and high-resolution angle-dispersive (AD) X-ray diffraction of powdered materials. We carried out the experiments at the NSLS beamline X-17C, and at Daresbury SRS beamline 9.1.

We initiated this study following the experiments that led to the synthesis of γ-Ge_3N_4 [49]. In the ED synchrotron run, we found that we could follow the diffraction peaks from metastably compressed β-Ge_3N_4 to P = 40 GPa, although the character of the pattern changed above P = 20 GPa (figure 4-1) [49]. Here, we analyse the variation in unit cell parameters obtained from these ED synchrotron runs, along with AD diffraction data. The V(P) plots reveal a large density decrease (5-7%) occurring at P = 20-24 GPa, consistent with the occurrence of a phase transition in metastably compressed β-Ge_3N_4. *Ab initio* calculations and Raman spectroscopy also confirm the occurrence of that phase transition [136], [51].

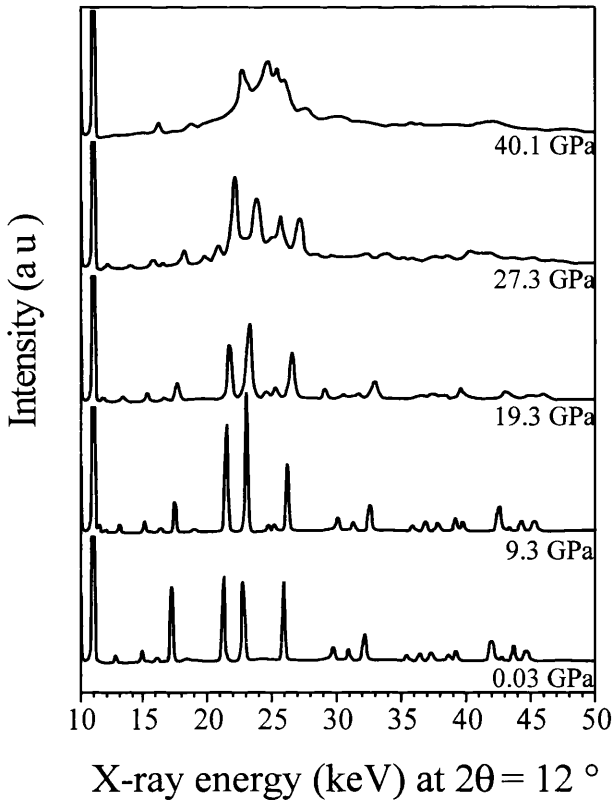

Figure 4-1 Energy dispersive X-ray diffraction of β-Ge_3N_4 at high pressure.

Following our initial experimental observations, J. Dong *et al.* [51] performed *ab initio* density functional calculations within the local density approximation (LDA) to examine the polymorphism that might occur within β-Ge_3N_4 compressed at low T. They concluded that metastable phase transitions are expected in the pressure range P = 20-30 GPa. The phase transition involves N atom displacements away from special symmetry positions within the $P6_3/m$ structure. Dong *et al.* first analysed the data in terms of displacement patterns considering all unit cells in phase; i.e., Γ point ($q = 0$) instabilities. They predicted the occurrence of two second order phase transitions, at 20 and 28 GPa, that reduced the symmetry first from $P6_3/m$ to $P\bar{6}$, and then to P3 (figure 4-2). The E(V) curve showed inflection points at these pressures. McMillan *et al.* recently studied the metastable transitions in β-Ge_3N_4 by Raman scattering spectroscopy [136]. The data confirm that a phase transition occurs at P = 20 GPa. The number of peaks observed at pressures above the transition greatly exceeds that expected for the $P\bar{6}$ structure, but they correspond generally to those predicted for the P3 structure. They concluded that the $P6_3/m$–P3 transition occurred directly in a first-order manner, bypassing the predicted intermediate $P\bar{6}$ phase.

In the theoretical study, Dong *et al.* already recognised that the $P6_3/m$-P3 transition could occur directly *via* a first order process, at a predicted transition pressure $P_{tr} \sim 23$ GPa, because the calculated energy barrier for the first order β-δ transition was small, on the order of 0.01 eV/atom (10.6 kJ/mol) (figure 4-2). The transition pressure corresponds to the common tangent

between the minima on the calculated E(V) curve. McMillan *et al.* have termed the new "post-phenacite" phase δ-Ge_3N_4, to distinguish it from previously known α-, β- and γ-polymorphs [136].

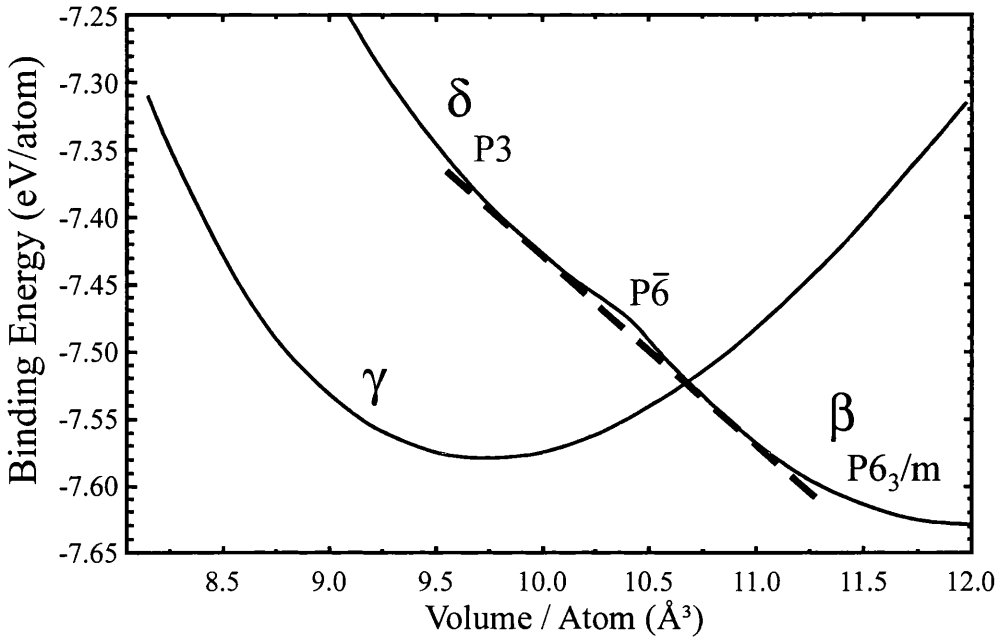

Figure 4-2 Energy versus volume diagram adapted from Dong et al. [51].

In the present work, we have continued the investigation of the metastable compressional behaviour of both β- and α-Ge_3N_4 polymorphs, using synchrotron X-ray diffraction techniques in the diamond anvil cell. We report analyses of the ED data to obtain unit cell volumes for pure β-Ge_3N_4, and to demonstrate the onset of the phase transition. The AD technique gives much higher resolution than energy-dispersive studies, so that accurate cell parameters can be determined as a function of pressure through the transition. We carried out the AD study using a mixture of α- and β-Ge_3N_4 phases, in order to compare their compressional behaviours. We calibrated the behaviour of the β-Ge_3N_4 polymorph in the mixture against the refined data for the pure phase from our previous runs. We observed that both results are identical. The AD XRD method permits the clear identification and distinction of the diffraction features from the α- and β-Ge_3N_4 phases within the sample, so that we can refine their cell parameters independently. The AD technique also permits one to identify occasional diffraction features that result from random crystallites still present in samples at high pressure (figure 4-17). This discrimination is important in studying the onset of amorphisation in the Ge_3N_4 materials at very high pressure.

4.2. Experimental methods

We originally obtained the Ge_3N_4 samples used in the experiments from Aldrich® (44,755-2) in >99.99 % chemical purity. X-ray diffraction indicated that the sample was a mixture of α- and β-Ge_3N_4 phases (approximately 1:2) (figure 4-3).

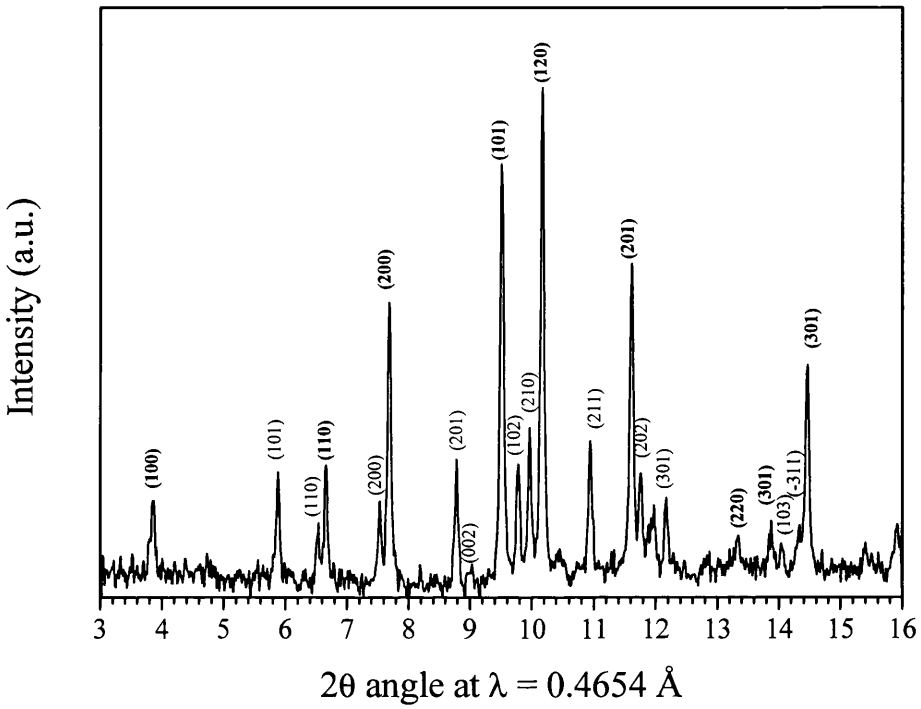

Figure 4-3 X-ray diffraction pattern of the α- and β-Ge_3N_4 starting material, the bold labels indicate the reflections from the β-phase, the other reflections are from the α-phase.

We used that material for the AD diffraction experiments carried out at SRS Daresbury. We obtained nearly pure samples of β-Ge_3N_4 polymorph (usually containing 1-3% of elemental Ge) for the Brookhaven ED runs by treating the mixture at 8 GPa and 900 °C in a multi-anvil device using a 14-8 assembly (see chapter 2). We pressed aliquots of the germanium nitride samples into discs (~2-3 μm thick, 40 μm across), and loaded them into the sample chambers in the diamond anvil cell. We carried out the ED experiments in Ar, loaded cryogenically into the cell [41, 47, 49]. In the angular dispersive diffraction experiments, the diamonds had 300 μm culet and we pre-indented a 250 μm-thick tungsten gasket to a thickness of 30 μm.

In the AD runs we used a 4:1 methanol/ethanol mixture as pressure medium. That medium remains fluid and provides a hydrostatic environment to approximately 10 GPa. Although it solidifies above this pressure, it remains much softer than the ceramic nitrides studied here, so that we do not expect the non-hydrostatic effects induced by the pressure medium to influence the results.

We measured pressure using the ruby fluorescence method, on several grains distributed throughout the cell. The pressure gradient within the medium never exceeded 10% of the average pressure, and was generally less than 5%, as determined by recording pressures from several different ruby grains within the sample chamber, even at the highest pressures. In fact, in such experiments on polycrystalline samples, the main deviations from a hydrostatic pressurisation environment occur because of grain-grain contacts. In a multi-phase assemblage, such as that studied here, a phase transition occurring in one phase can be detected in the mechanical response of the other phase. In fact, the high resolution of the AD XRD data permitted the observation of such subtle effects in the α-/β-Ge_3N_4 mixture studied here. We discuss this observation within the text.

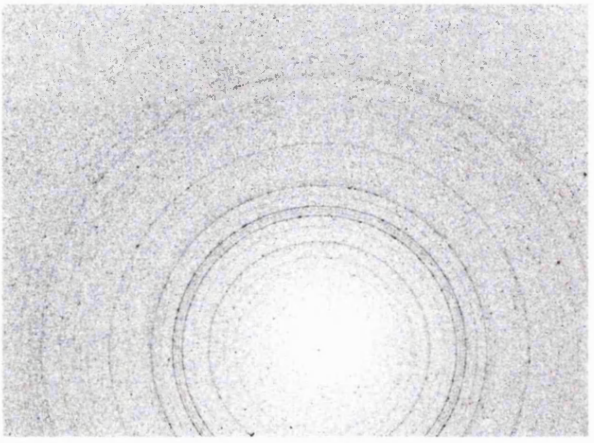

Figure 4-4 2-D diffraction pattern of germanium nitride at room pressure in the diamond anvil cell before compression.

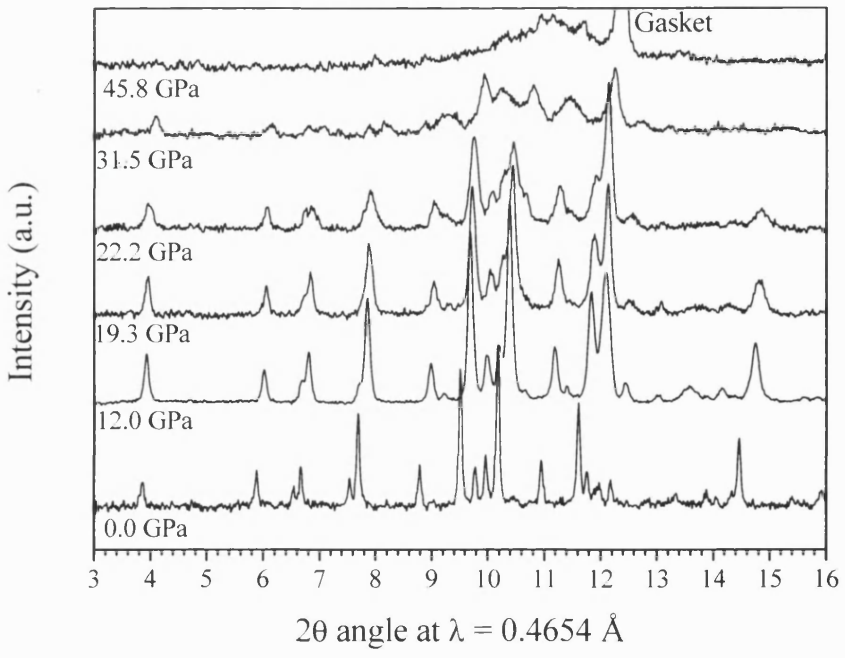

Figure 4-5 integrated patterns of germanium nitride as a function of pressure.

We obtained angle-dispersive X-ray diffraction patterns using monochromatic radiation (λ = 0.4654 Å). The X-rays incident on the sample were collimated and defined by a 75 μm diameter pinhole placed in front of the cell. We used an image plate detector to record the diffraction patterns. We performed the integration of the 2-D data using the software EDIPUS, that R.J. Nelmes and M. McMahon (University of Edinburgh) made available to us. Figure 4-4 shows a typical 2-D data set for a polycrystalline sample taken within the cell. Figure 4-5 presents the integrated 1-D diffraction patterns.

We collected the energy-dispersive data at a scattering angle $2\theta = 12^{\circ}$ (figure 4-1) [48, 49]. We fitted the ED data using the LeBail extraction technique. We subtracted the background due to Compton scattering from the diamonds manually. Then we refined the lattice parameters and peak shapes. The LeBail extraction procedure does not consider the structure explicitly, but places peaks at each of the diffracting energies and fits the peak intensity and shape at that position. This allows the extraction of lattice parameters with good precision when we cannot easily obtain structural information, as in the case of the EDX studies. It also eliminates the need for the arbitrary removal of spurious peaks, because of the high degree of redundancy of the fit for high-symmetry materials (i.e., we generally fit >15 peaks reliably in the present study, for only 2 lattice parameters: *a* and *c*).

4.3. Results and discussion

Figure 4-6 show the combined V(P) data for β-Ge_3N_4 from all data sets. The data show a rapid decrease in volume (~5-7%) between P = 22-23 GPa (figure 4-6). The volume drop indicates the occurrence of a large structural change in the material, and it is most likely associated with a phase transition. The volume change in also associated with a large change in the c/a ratio (Figure 4-16).Due to the weakening of the ED spectrum above 15-17 GPa, coupled with the possible presence of spurious reflections from untransformed regions of the sample, we could not resolve the detailed behaviour of *c* and *a* parameters throughout the transition from the ED data.

In order to study the phase transition in greater detail, we performed the experiment using high resolution angular dispersive experiments (figure 4-3 and figure 4-4). Figure 4-6 combines refined V(P) values from the AD data for β-Ge_3N_4 with the ED data. We observed the reproduction of both the low pressure compressional data and the occurrence of a phase transition associated with a 5-7 % volume drop between 22-24 GPa in both types of experiment.

We carried out the AD experiments for a mixture of α- and β-Ge_3N_4. Because of the differences in space group symmetry and lattice parameters between the two structures, and also the high resolution of the AD technique, we clearly distinguished the peaks from the α- and β- phases within both the 2-D (figure 4-4) and the integrated 1-D diffraction patterns (figure 4-5). We could also fit the lattice parameters of the two phases independently. In particular, the fitting procedure systematically rejected any peak overlap between both phases in order to prevent any wrong assignments and resulting error in the fit. Comparison of the β-Ge_3N_4 data between the AD and ED studies allowed us to determine that no changes in the V(P) behaviour occurred because of the mixed-phase nature of the sample. The AD study of the mixed-phase sample allowed us to compare the compressional behaviour of α- and β-Ge_3N_4. In particular, the flattening of the compression curves of both α- and β-Ge_3N_4 are discussed below along with the β- to δ- phase transition.

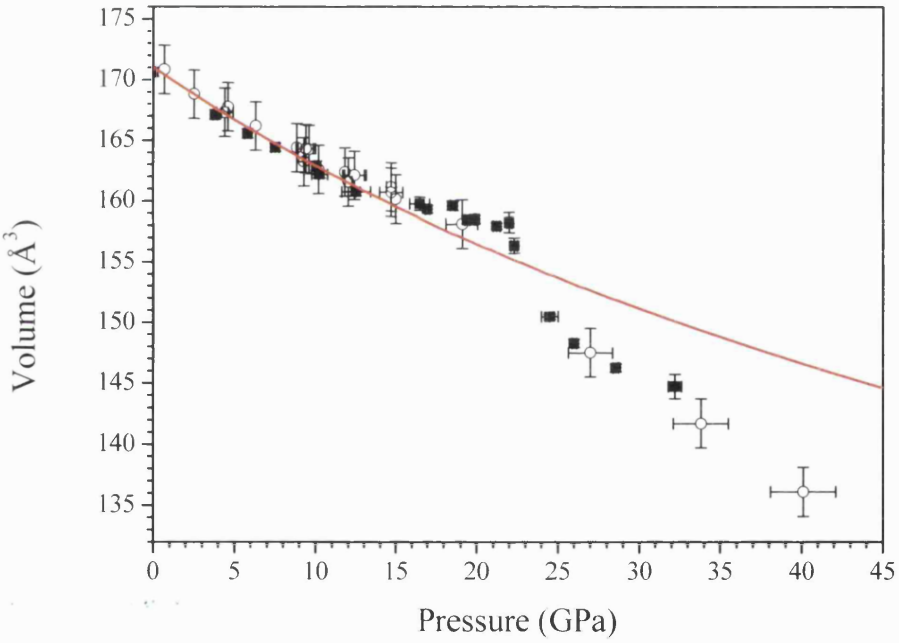

Figure 4-6 Volume data as a function of pressure from all the β-Ge_3N_4 data sets. The full squares represent the AD data and the circles represent the ED data. The line indicates the Birch-Murnaghan equation of state fit of the low pressure data. Above 22 GPa, the data show a clear deviation from the equation of state.

4.3.1. α-Ge_3N_4 under high pressure

Figure 4-7 presents the variation in the unit cell volume of α-Ge_3N_4 as a function of pressure. Below P = 15 GPa, the V(P) data show a regular decrease that we fitted using a third-order Birch-Murnaghan equation of state, to obtain values for the zero pressure bulk modulus (K_0) and its pressure derivative K'. Figure 4-8 also presents the normalised pressure (F) and Eulerian strain (f) representation of the data.

We excluded points above 15 GPa from the fit, because the V(P) relation behaves anomalously in this region (see below). The F-f plot is nearly a horizontal line, indicating that K' must lie close to 4. In a first estimate, we assumed K_0' = 4: this yielded K_0 = 163(2) GPa. A least squares fit to the data set yielded K_0 = 165(10) GPa, for a fitted value of K_0' = 3.7(4). These values are in excellent agreement with theoretical predictions [51] (table 4-1). We observed a substantial broadening of the α-Ge_3N_4 diffraction peaks above P = 30 GPa. The diffraction peaks of α-Ge_3N_4 can no longer be distinguished from a broad amorphous signal above P ~ 35-40 GPa (figure 4-5).

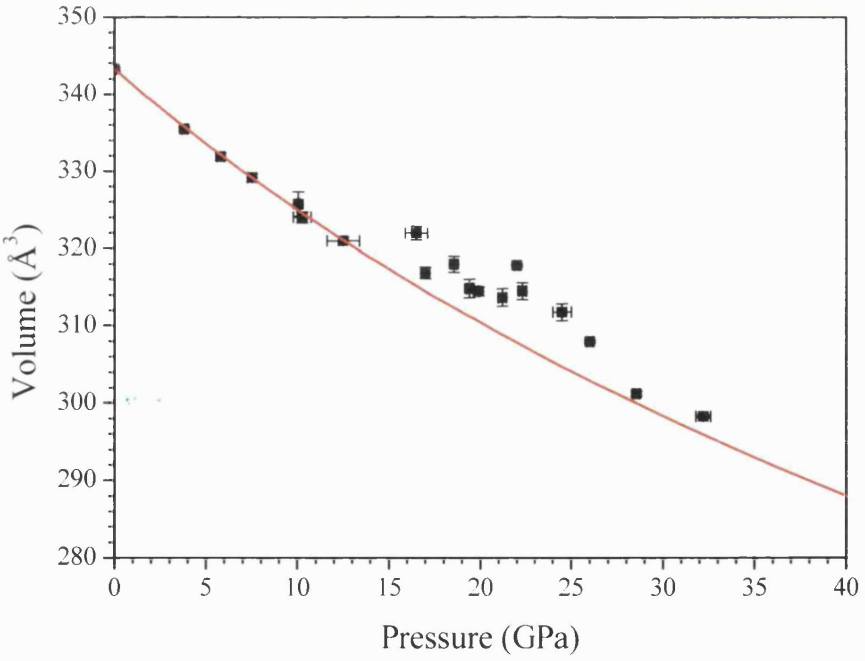

Figure 4-7 Volume of α-Ge_3N_4 as a function of pressure. The red line is the Birch-Murnaghan equation of state fit of the data.

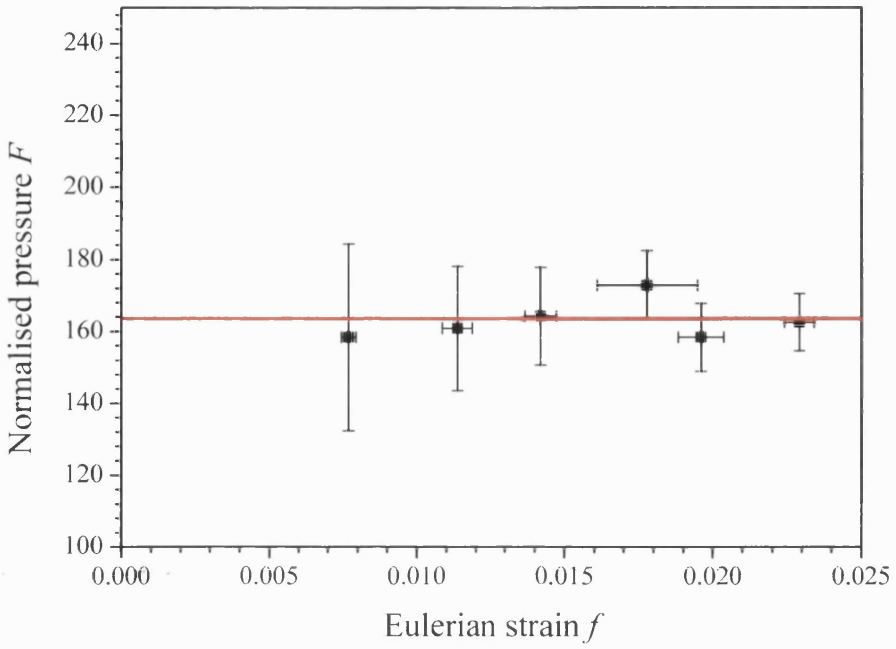

Figure 4-8 Normalised pressure as a function of Eulerian strain diagram for α-Ge_3N_4.

	K_0 (LDA)[51]	K_0' (LDA)[51]	K_0 (exp.)	K_0' (exp.)
α-Ge_3N_4	178	2.1	165(10)	3.7(4)
β-Ge_3N_4	185	3.7	185(10)	4.4(5)
γ-Ge_3N_4	240	4.5	295(5)[48]	3.8(2)[48]

Table 4-1 Theoretical prediction (LDA) and experimental (exp.) bulk modulus values for three germanium nitride phases.

The V(P) data for α-Ge_3N_4 exhibit a slight "upward bulge" in the 15-25 GPa region, indicating that the volumes are slightly larger (1-2%) than the normal compressibility trend would predict. We can suggest several possible origins for this feature. First, one could suggest that it results from a "stiffening" of the methanol-ethanol pressure medium above 10 GPa. However, this is unlikely because the onset of the "upturn" in V(P) occurs approximately 5 GPa above the solidification of the pressure medium (see also discussion below for β-Ge_3N_4). Second, a structural transformation might occur within the α-Ge_3N_4 phase, which could be analogous to the β-δ phase transition described for β-Ge_3N_4 (below). However, the mechanical weakening and subsequent "hardening" visible in figure 4-7 bring the V(P) relation back to the low pressure trend by 25 GPa: also, the *c*/*a* ratio (figure 4-16) does not show the same behaviour across the transformation region as does that for β/δ-Ge_3N_4 (see also below). However, the observation of the anomalous V(P) data indicate that the high pressure behaviour of α-Ge_3N_4 might require further investigation. The preferred interpretation is that the α-Ge_3N_4 sample is sensitive to the β-δ transition occurring within the β-Ge_3N_4 sample, in which it is embedded as a minority component. There is a 5-7 % volume reduction associated with the β/δ phase transformation,

along with an onset of mechanical weakening within the β-Ge_3N_4 polymorph above P = 15 GPa. The α-Ge_3N_4 phase will thus experience a reduction in external (pressure) constraints and may relax its volume to a larger value than expected from the intrinsic compressibility relation. Upon completion of the first-order β-δ transition within the "matrix" majority phase, the α-Ge_3N_4 polymorph will again experience the full pressure from the external pressurisation medium, and its V(P) relation returns to the low-pressure curve (figure 4-7).

4.3.2. β-Ge_3N_4 under high pressure

The variations with pressure of the β-Ge_3N_4 cell volume and lattice parameters are quite different to those recorded for α-Ge_3N_4 (figure 4-6). A previous study by Raman spectroscopy clearly indicated that a phase transition occurs within the sample at P = 20-22 GPa, and that some mechanical weakening associated with phonon mode broadening and loss of Raman intensity may exist above P = 15 GPa [136] (figure 4-9). This result is consistent with results of previous *ab initio* (LDA) calculations, that indicate that a sequence of $P6_3/m$ - $P\bar{6}$ - P3, or a direct first-order $P6_3/m$ – P3 transition, might occur in the 20-25 GPa range (figure 4-2). The Raman spectroscopic results indicate that the latter possibility is more likely, during ambient temperature compression [51, 136].

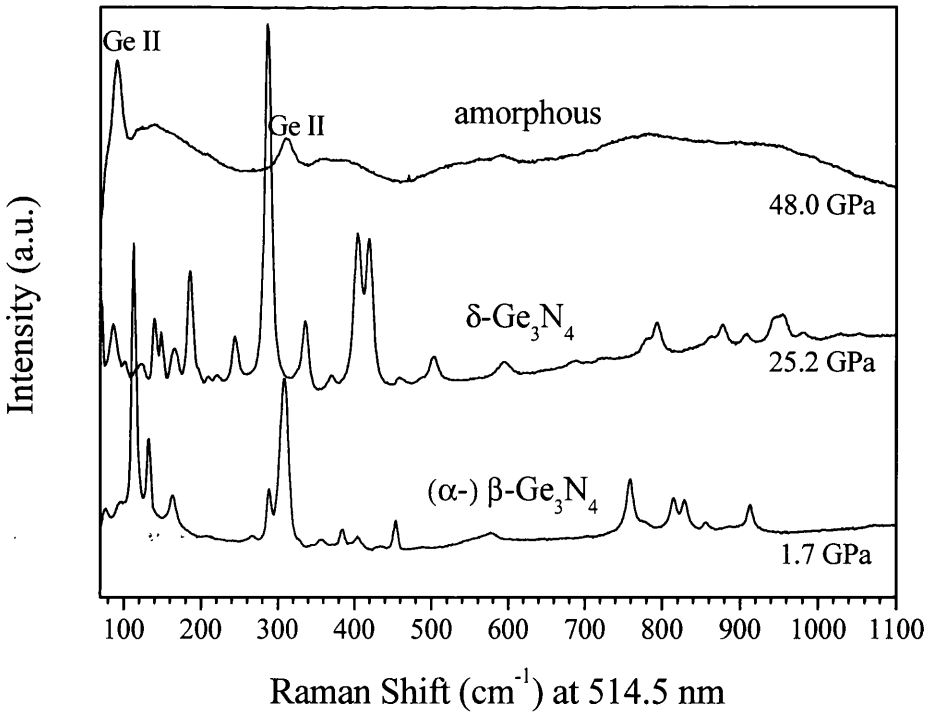

Figure 4-9 New set of Raman spectra of β-Ge_3N_4 at high pressure.

The changes observed in the X-ray diffraction patterns and the V(P) plots, from both the ED and AD XRD studies, confirm the occurrence of a phase transition resulting in a 5-7 % volume

decrease above P = 22 GPa. There is a smooth decrease in the cell volume up to P = 15 GPa, that permits an estimation of the bulk modulus of the low pressure β-Ge_3N_4 polymorph. Figure 4-10 shows a reduced variable *F-f* plot, as for α-Ge_3N_4, constructed using the determined V(P) data and the zero-pressure volume V_o. The second-order Birch-Murnaghan solution with K' = 4 is shown as a horizontal line on the plot. This assumption gave K_0 = 187(6) GPa. A third-order Birch-Murnaghan fit gave K_0 = 185(10) GPa, for a fitted K_0' = 4.4(5). These values are again in excellent agreement with *ab initio* calculations [51, 52, 74] (table 4-1).

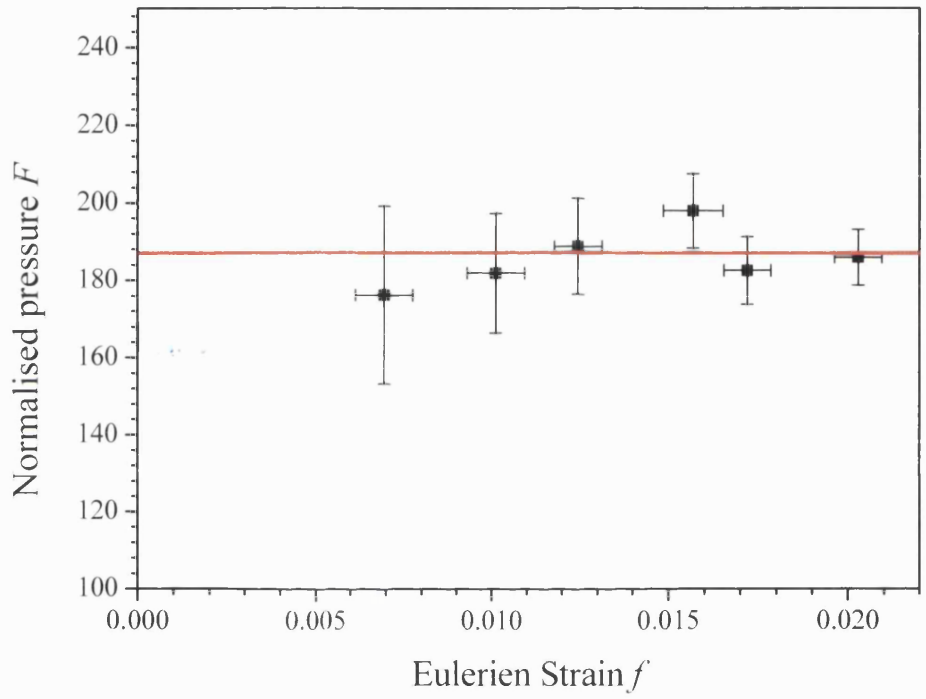

Figure 4-10 β-Ge_3N_4 normalised pressure as a function of Eulerian strain relation.

Between 21-23 GPa, there is a large (5-7 %) drop in the volume in β-Ge_3N_4, that we do not observe for the α-Ge_3N_4 phase (figure 4-7). This volume drop occurs for both the ED data obtained for the pure β-Ge_3N_4 phase, and in the AD runs on the mixed α- and β-containing sample (figure 4-6). The Raman spectroscopic study of metastably compressed β-Ge_3N_4 (figure 4-9), shows that a large number of new peaks appear in the spectrum above P = 21 GPa, that signal a phase transition occurring into a newly-described δ-Ge_3N_4 polymorph [136]. From the observed Raman data compared with predictions from the previous theoretical studies, we concluded that the high pressure phase had P3 symmetry, with a structure related to β-Ge_3N_4 by small displacements of the N atoms [51, 136]. We propose that the volume drop observed for β-Ge_3N_4 here is associated with the β-δ phase transition.

The predicted X-ray diffraction pattern for the δ-Ge_3N_4 phase differs only slightly from that of β-Ge_3N_4 (figure 4-11). The main difference is the increased intensity of the (111) reflection, near 2 θ = 11.4 ° (at λ = 0.4654 Å). However, that peak coincides with a reflection from the α-Ge_3N_4 phase present within the sample studied by angle-dispersive techniques (figure 4-11). Furthermore, by 25 GPa, the Raman spectra show clearly that the β-Ge_3N_4 sample has transformed completely into δ-Ge_3N_4 (figure 4-9). The X-ray pattern then consists of peaks from δ-Ge_3N_4, most of which are common to reflections of the β-Ge_3N_4 phase, but one of which coincides with a peak of α-Ge_3N_4, which coexists with the δ-Ge_3N_4 in the sample and does not undergo any analogous phase transition (figure 4-11).

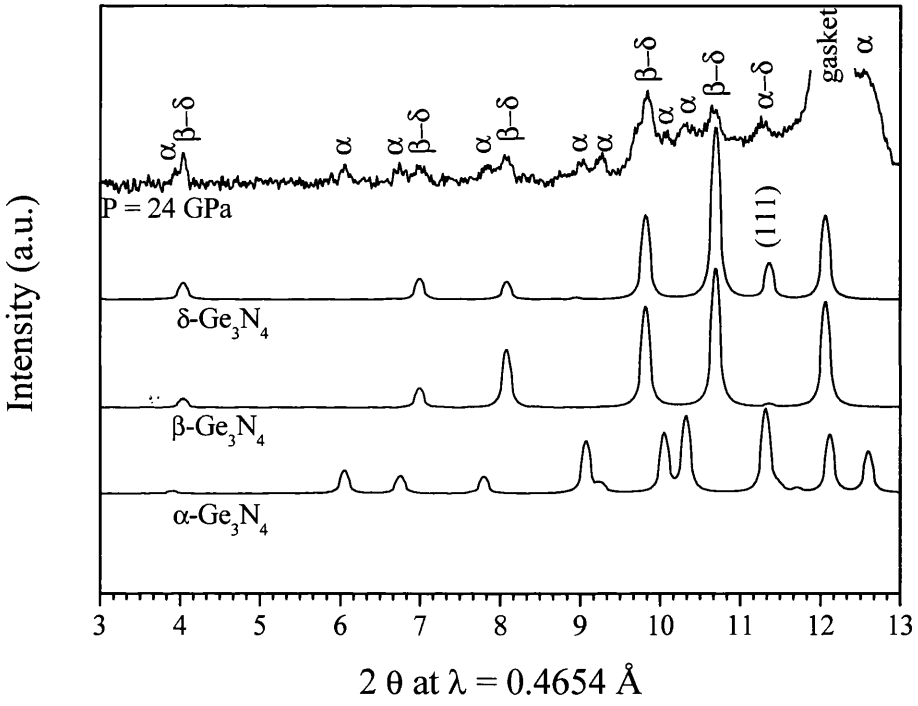

Figure 4-11 Calculated X-ray diffraction patterns of α- β- and δ-Ge_3N_4 at 24 GPa, compared with an observed pattern in the same pressure range.

Just below the transition, beginning at P ~ 15 GPa, the V(P) data for β-Ge_3N_4 show a slight upward deviation from the compressibility curve. We observed a similar effect for α-Ge_3N_4. This effect is not due to the pressure medium, because it was observed in ED and AD data for samples pressurised in MeOH/EtOH and in argon, for pure β-Ge_3N_4 and the α-β mixture. The difference with the α-Ge_3N_4 data is that the β/δ-Ge_3N_4 data do not return to the V(P) curve of the low pressure phase following the transformation region. We propose that this is associated with the onset of the β-δ transition. Although the β-δ ($P6_3/m$ – P3) phase transformation is formally first-order, it is closely linked to soft vibrational modes within the β-Ge_3N_4 sample, that begin to be manifested at lower pressure [51, 136]. In the Raman spectroscopic study, the

Raman peaks begin to broaden and lose intensity at P ~ 15 GPa, well below the transition [136]. This will result in a larger K' than expected within the β-Ge_3N_4 phase.

As the β-δ transition begins to occur, certain regions of the sample will occupy a 5-7 % smaller volume than before. This will result in a positive volume relaxation in surrounding regions (Figure 4-12), which correspond to untransformed α-Ge_3N_4 or β-Ge_3N_4. Upon completion of the transition, above P = 24 GPa, the V(P) relation of the α-Ge_3N_4 sample returns to that observed at low pressure. The V(P) relation of the other phase corresponds to that of the δ-Ge_3N_4 polymorph. In particular, between 15 and 21 GPa, the c/a ratio do not show any variation as the errors in the pressure measurement are cancelled by the division of one parameter by the other if the effect in the same on both parameters. Therefore, the deviation is most likely due to an "error" in the pressure measurement. During the onset of the transition the pressure within the sample and that within the pressure medium are not equal. Therefore, the data plotted as a function of pressure in the medium show some discrepancy.

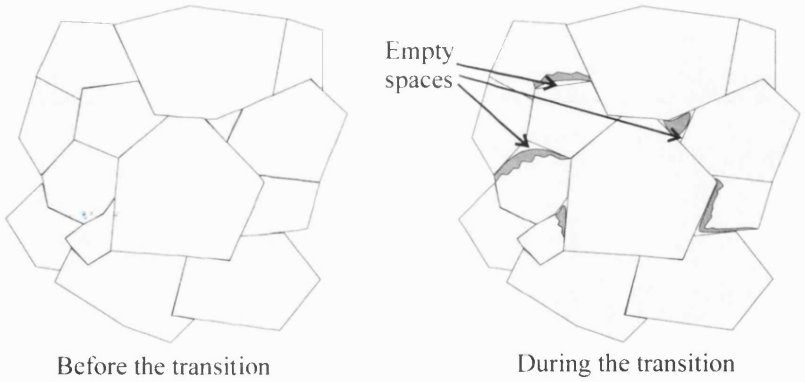

Figure 4-12 Visual representation of the volume relaxation occurring during the phase transition at the grain boundaries.

Using the data points between 24-37 GPa, we fitted the V(P) data using a second order Birch-Murnaghan EoS formalism, assuming K' = 4, to obtain a bulk modulus estimate for the δ-Ge_3N_4 polymorph as K = 161(20) GPa (note: this is a bulk modulus referred to a reference volume point at 24 GPa, i.e., K_{24GPa}, rather than "K_0") (figure 4-13). It is not strictly correct to extrapolate this value down to ambient pressure, nor to extrapolate that for β-Ge_3N_4 up to above the β-δ transition. Although the transition is first order in nature, it is only slightly so, and mode softening that affects the compressibility occurs within the two phases, that can not exist much above or below the transition pressure [51, 136]. We do note that the bulk modulus value of the high pressure δ-Ge_3N_4 phase is 15 % smaller than that of the low-pressure β-Ge_3N_4 phase, close to that of the α-Ge_3N_4 polymorph. Usually, we expect high-pressure, higher-density phases to have lower compressibility than their low-P, low-density counterparts. However, the δ-Ge_3N_4 form is derived from β-Ge_3N_4 by relaxation of the N atom positions away from their special

positions within the phenacite structure: this gives rise to additional degrees of freedom for structural relaxation during compression, and it is normal that the compressibility should be greater, and similar to that of α-Ge_3N_4.

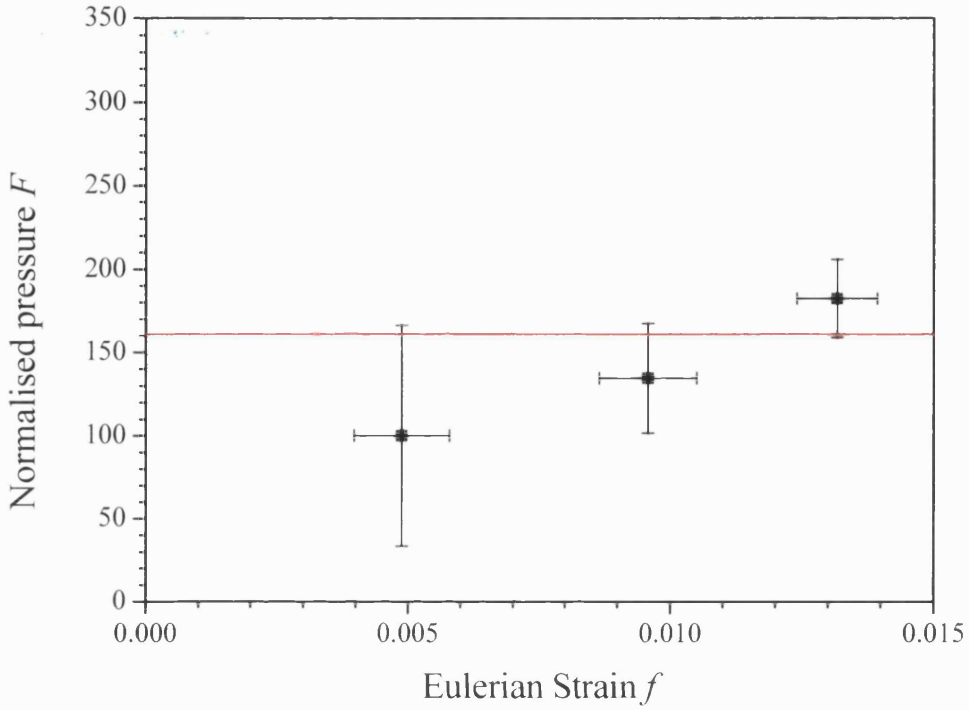

Figure 4-13 Normalised pressure as a function of Eulerian strain diagram relation for δ-Ge_3N_4.

In order to record further crystallographic details and better define the nature of the phase transition, we also refined the *a* and *c* lattice parameters for the α-, β-, and δ-Ge_3N_4 polymorphs from our high resolution AD data. The α-Ge_3N_4 data show a monotonic decrease with increasing pressure (figure 4-14). The *c*(P) values do show a small anomaly in the vicinity of the β-δ transformation; this can be analysed as discussed above for the V(P) relations.

The data for β-Ge_3N_4 reveal a 2.5% reduction in the *a*-axis parameter at the transition pressure, that does not occur in the *c* dimension (figure 4-15). This implies that the β-δ transition results from a contraction in the *a* axis, or in the plane normal to *c*. This result is consistent with the structural mechanism for the transformation suggested by the atomic displacement patterns obtained from *ab initio* calculations [51]. Both the *a* and *c* parameters exhibit a slight "upturn" between 15-25 GPa, as we have previously discussed for the V(P) data.

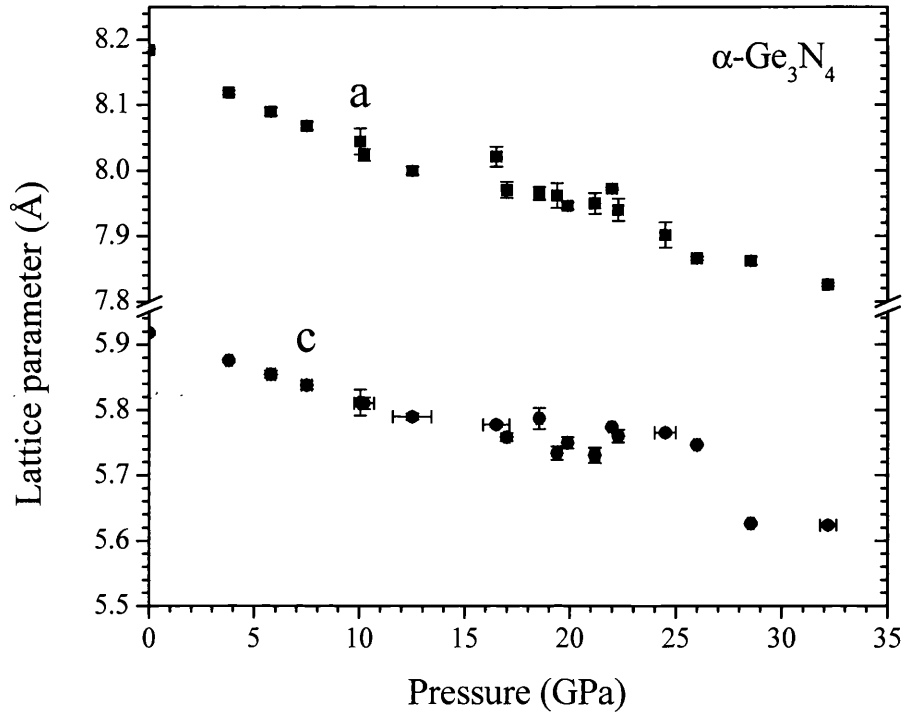

Figure 4-14 a and c lattice parameters of α-Ge_3N_4 as a function of pressure.

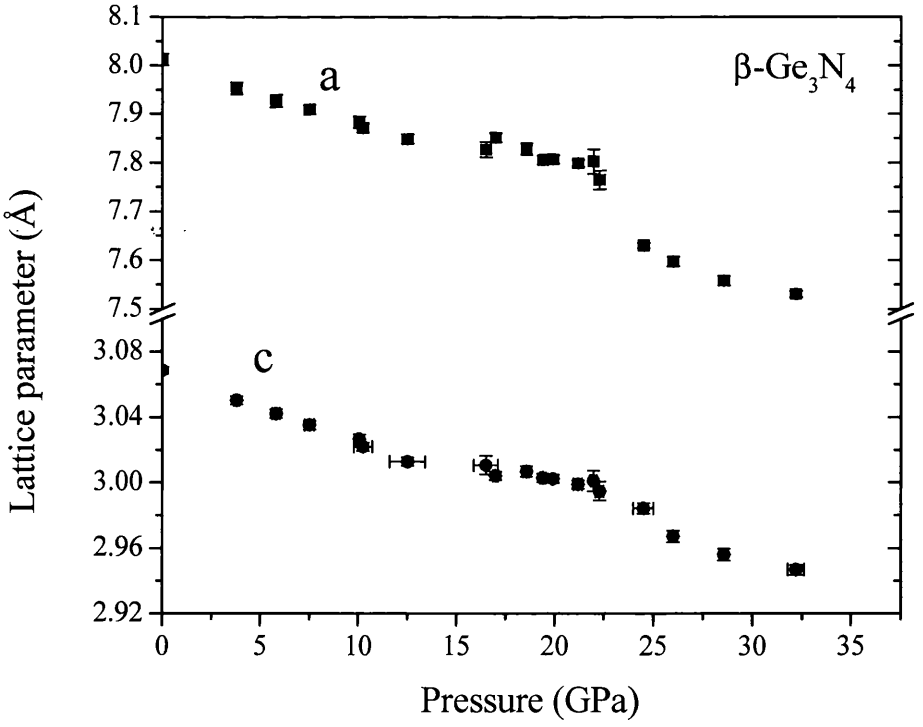

Figure 4-15 a and c lattice parameters of β-Ge_3N_4 as a function of pressure.

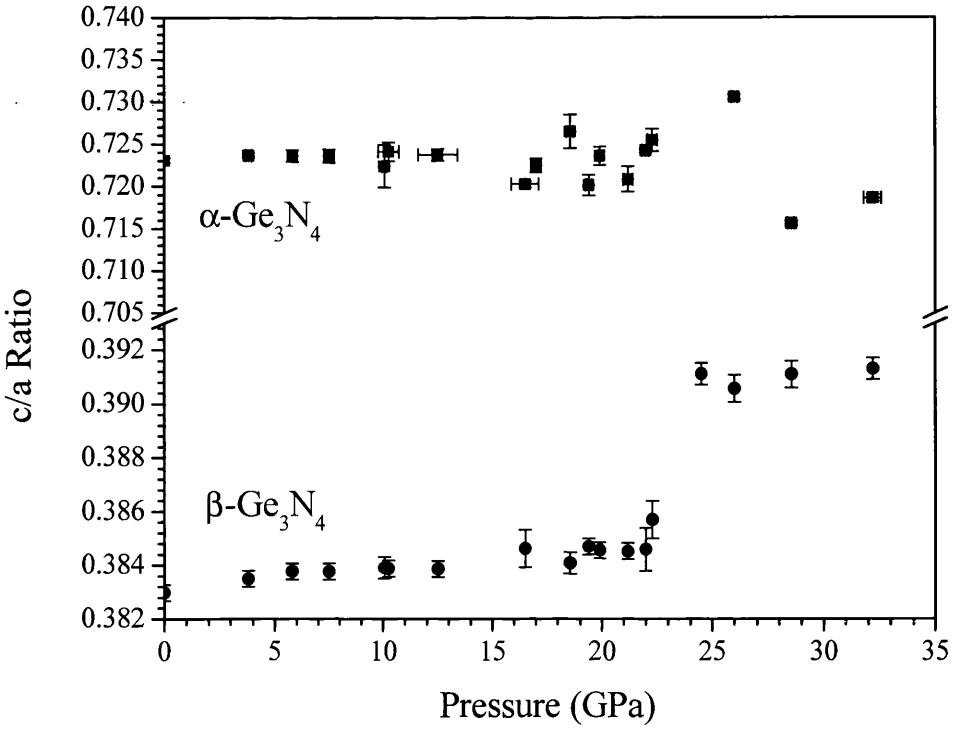

Figure 4-16 c/a ratio as a function of pressure for α-Ge_3N_4 (full squares) and β-Ge_3N_4 (full circles); the β-Ge_3N_4 c/a ratio data display a jump at the transition pressure which proved once more that the phase transition is first order.

To eliminate such "global" effects, we have plotted the *c/a* ratios for the α- and β-phases as a function of pressure through the transition region (figure 4-16). The *c/a* for the α-Ge_3N_4 polymorph carries across the transition without change: that for β-Ge_3N_4 jumps abruptly from 0.383 to 0.391 at the β-δ transition (i.e., ~2% change), marking the collapse in structural constraints normal to the *c*-axis. The sudden jump in the c/a ratio is another evidence of the first order nature of the phase transition.

The V(P) and unit cell axis data for metastably compressed β-Ge_3N_4 are consistent with the occurrence of a β-δ phase transition, as McMillan *et al.* recently observed by Raman spectroscopy [136]. In the previous theoretical study, Dong *et al.* proposed that a sequence of second-order displacive phase transitions driven by zone centre soft modes involving displacements of the N atoms away from special symmetry sites could occur within the structure, in a symmetry sequence $P6_3/m - P\bar{6} - P3$ [51]. However, McMillan *et al.* concluded in the experimental Raman scattering study, that the $P6_3/m - P3$ (i.e., β-δ) transition occurred directly, due to the number of peaks observed above the phase transition pressure. Therefore, they determined that the phase transition was first order in character. However, it is likely that vibrational mode softening occurs within the β-Ge_3N_4 phase prior to the phase transition, reminiscent of the underlying second-order nature of the phase transition predicted at $q = 0$ and

T = 0 K, that results in mechanical weakening of the sample at pressures below the phase transition, above P = 12-15 GPa. There was no observation of any soft vibrational modes in the Raman study, because these are expected to be spectroscopically inactive [51]. In the Raman spectroscopic study, the characteristic peaks of the β-Ge_3N_4 phase did begin to broaden above 10-12 GPa, indicating the presence of dynamical disordering or mechanical weakening within the sample, prior to the phase transition at 20-22 GPa [136].

Thus, the X-ray data are consistent with the occurrence of a first order β-δ phase transition in Ge_3N_4 upon compression. The V(P) jump reaches completion within 2-3 GPa of the transition pressure, rather than spread out over 8-10 GPa, as would occur in the case of two sequential second-order displacive phase changes. We conclude that the transition is first order in nature, in agreement with the Raman scattering study.

The theoretical work, initially investigated the soft modes at the Brillouin zone centre (Γ point). However, a previous calculation on related β-Si_3N_4 using empirically-derived force constants had suggested that mode instabilities might also occur away from $q = 0$, but parallel to the c-axis (i.e., along 00ζ) [137]. In subsequent LDA calculations, J. Dong *et al.* showed that no such (00ζ) mode softening occurred for β-Ge_3N_4 [51]. In the Raman scattering study from Deb et al. as well as the new data presented Figure 4-9, it is possible to account for most of the modes observed at high pressure within the P3 symmetry predicted for δ-Ge_3N_4. However, we observed a family of additional weak peaks in the spectrum, which indicated the presence of a larger true unit cell than expected, within perhaps a "disordered" or "incommensurate" structure, involving condensation of phonon modes away from the Γ point, or the involvement of some order-disorder process during pressurisation.

In the present study, we observed a large decrease in the a-axis parameter of Ge_3N_4 at the β-δ transition, but not in the c-parameter (figure 4-15). This result indicates that the β-δ transition is associated with a sudden structural contraction in the plane normal to c, associated with N atom displacements in the (00x) plane, as predicted by theory. Before and after the transition the c/a ratio is constant (figure 4-16), indicating that a transition between structurally distinct polymorphs has occurred, and the data confirm that the transition occurs over a narrow pressure range. The α-Ge_3N_4 phase, that we studied simultaneously within the same pressure chamber, does not show any such changes in the a- and c- parameters over the same pressure range (figure 4-14), indicating that the β-δ transition only occurs within the phenacite-structured polymorph. This polymorph contains channel-like voids extending parallel to the c axis: these voids are absent within the α-Ge_3N_4 polymorph (see chapter 1). It is the presence of those voids that allows the N atoms to move away from their initial symmetric positions in the β-Ge_3N_4

structure [51]. In the α-phase, a similar set of movements would require substantial bond breaking and displacements of Ge and N atoms to occur, although it is not impossible.

The diffraction peaks of both α- and β/δ- Ge_3N_4 polymorphs become broader and weaker above P = 24 GPa (figure 4-5). We made the same observation in our previous ED studies (figure 4-1) [48, 49]. For example, the distinctive (301) reflection of β/δ-Ge_3N_4 near 14.5° 2θ (λ = 0.4654 Å) is no longer distinguishable from the background by the time the pressure reaches 31.5 GPa (Figure 4-5). These results indicate that there is an increase in the magnitude of the changes in atomic position around their average positions within the high pressure phase. At very high pressures, we only observe an "amorphous" diffraction pattern in the 2-D and integrated 1-D patterns at 45.8 GPa (figure 4-17 and figure 4-5). This is consistent with the broad amorphous bands observed in the Raman spectrum at the same pressure (figure 4-9). We observe in the 2-D AD image (figure 4-17) that weak crystalline peaks also observed in the ED spectra above 40 GPa (figure 4-1) result only from several small crystallites present within the sample, and that diffuse amorphous diffraction rings characterise most of the sample. The results indicate that, above 35-40 GPa, both α- and β-/δ-Ge_3N_4 polymorphs have become so disordered on an atomic scale that they have lost all structural and vibrational coherence: i.e., "pressure induced amorphisation" has occurred [138, 139]. This disorder cannot involve Ge or N diffusional processes because of the low temperature; however, local bonding rearrangements can occur, while the atoms remain close to their original positions.

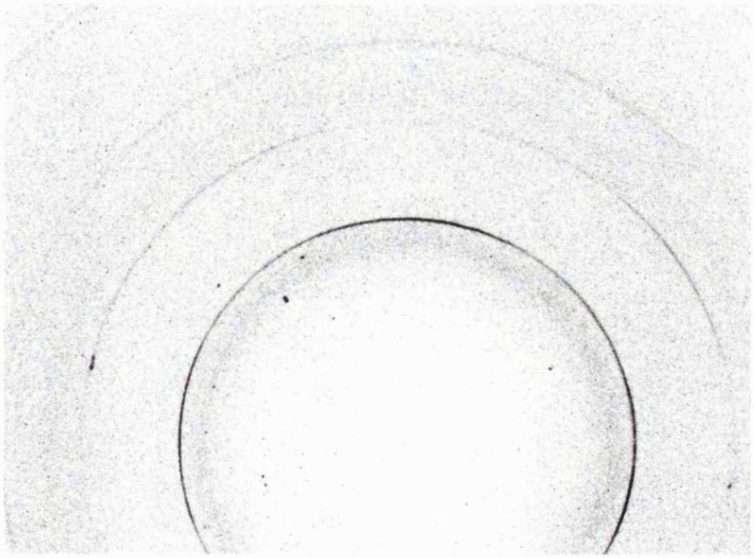

Figure 4-17 2-D diffraction pattern of germanium nitride at 47 GPa. The diffraction from the sample now only exists as a diffuse amorphous rings indicating the occurrence of pressure induced amorphisation. The strong sharp rings observed in the pattern are due to the diffraction lines of the tungsten gasket.

J Dong *et al.* suggested a mechanism for the amorphisation phenomenon from their theoretical results [51]. J. Dong *et al.* found that 5-fold coordinated Ge environments would appear within the δ-Ge_3N_4 structure at very high densities, formed in a displacive manner *via* close approach of 3-coordinated bridging N atoms to adjacent GeN_4 tetrahedra [51]. By P = 35 GPa, the volume of the δ-Ge_3N_4 phase is tending toward that of spinel-structured γ-Ge_3N_4 (figure 4-18), although the metastably-compressed tetrahedrally-coordinated polymorph has become highly metastable with respect to the stable high density spinel phase. The spinel polymorph contains 2/3 of its Ge atoms in octahedral coordination (GeN_6 species) as well as 1/3 tetrahedrally-coordinated GeN_4 groups, and its formation from the low-pressure polymorphs involves a major structural reorganisation that involves a high activation energy barrier (0.08 eV/atom: 85 kJ/mol) (figure 4-2). This is why it is possible to compress metastably the tetrahedrally coordinated polymorphs at ambient temperature. We can understand the occurrence of Ge_3N_4 amorphisation in terms of development of local coordination instabilities developed within the low-pressure structures at high density. Formation of 5-fold coordinated GeN_5 groups (or, equivalently, formation of NGe_4 polyhedra) will result in lengthened and weakened Ge-N bonds, lowering the energy barriers towards structural relaxation within the sample towards the more stable dense form. However, the low (ambient) temperature of the compression experiments precluded the nucleation and growth of the stable high pressure crystalline phase (γ-Ge_3N_4): the result is an amorphous form of Ge_3N_4.

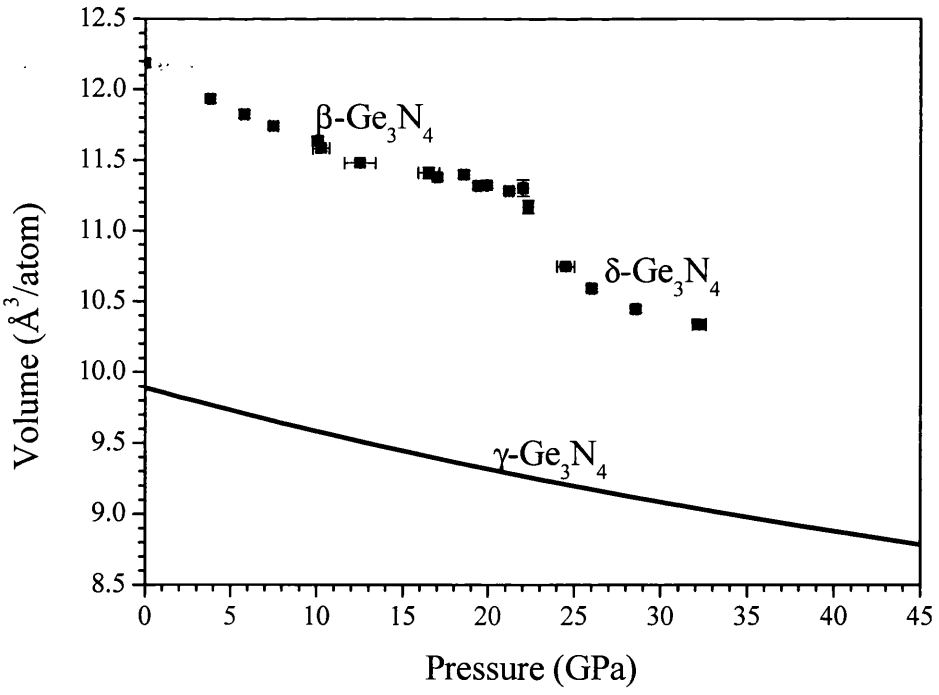

Figure 4-18 V(P) diagram comparing the relative volumes of the β-, δ- and γ- phases of germanium nitride. The units are in Å/atom in order to allow a useful comparison between the volumes of phases with different number of formula units per cell.

A. Zerr has recently reported a new phase of Si_3N_4, which appears upon metastable compression of β-Si_3N_4 at ambient temperature. He has termed that new phase "δ-Si_3N_4", and also proposed that it is a "post-spinel" polymorph [140]. It is useful to examine the possible connection between this new form of Si_3N_4, and the new δ-Ge_3N_4 polymorph described here. Zerr has proposed that the new δ-Si_3N_4 phase corresponds to a "post-spinel" structure, which necessarily contains high-coordinate Si atoms [41, 141]. However, Zerr presents some Raman spectra for δ-Si_3N_4. Those spectra are similar in form to those obtained in our recent study for the post-phenacite phase δ-Ge_3N_4. Examination of the published diffraction data indicates that one can assign all but two of the peaks to a Si_3N_4 polymorph with the δ-Ge_3N_4 structure, which has a similar diffraction signature to the β-Si_3N_4 phase (figure 4-11). We conclude that Zerr in fact observes the occurrence of a β-δ polymorphic phase transition in Si_3N_4, analogous to that described here for Ge_3N_4. The new δ-Si_3N_4 polymorph is then isostructural with δ-Ge_3N_4, and corresponds to a "post-phenacite" rather than a "post-spinel" structure, and contains only four-coordinated Si atoms.

4.4. Conclusions

We have confirmed by analysis of energy-dispersive and high resolution angle-dispersive synchrotron X-ray diffraction studies that β-Ge_3N_4 undergoes a metastable phase transition at approximately 22 GPa, into a new polymorph termed "δ-Ge_3N_4". The phase transition is characterised by a reduction of approximately 5-7 % in the cell volume. It is also associated with a discontinuity in the compressional behaviour of the *a* axis but not the *c* axis parameter. In particular the compressional behaviour of the axes is emphasised by the plot of the c/a ratio as a function of pressure which display a sudden increase at the transition pressure. The results are consistent with theoretical predictions by Dong *et al.* [51] as well as with a recent Raman spectroscopic study [136]. The transformation involves a first order $P6_3/m$ – P3 phase transition. The high pressure δ-Ge_3N_4 polymorph is structurally derived from β-Ge_3N_4, and the two are related by small cooperative displacements of the N atoms. Both phases contain Ge in tetrahedral coordination to nitrogen. It is likely that a newly-described δ-Si_3N_4 polymorph is analogous to δ-Ge_3N_4, based upon comparison of the X-ray diffraction and Raman data with those of Ge_3N_4. The transition into the δ-phase does not occur for α-Ge_3N_4, because of the different crystal stacking of GeN_4-connected layers. However, both α- and β/δ-Ge_3N_4 exhibit pressure-induced amorphisation at P > 30-35 GPa, because of Ge-N bond lengthening and weakening associated with incipient formation of GeN_5 (NGe_4) species in the structures. This phenomenon results in a lowering the activation energy barriers toward highly-coordinated configurations.

Chapter 5. Transition Metal Nitrides: Determination of Compressibilities

5.1. Introduction

Transition metal nitrides provide important refractory materials, such as "superhard" cermets for mechanically-resistant coatings, force-transmitting elements, and as useful magnetic and conductive materials, including high-T_c superconductors [3, 7]. Throughout the years, the scientific community has measured many of the relevant material properties of transition metal nitride compounds and composites, such as the hardness, shear moduli, superconducting transition temperature. However, there is little information on the bulk modulus of the pure materials, which gives direct information on the volume compressibilities of the nitride compounds, that one can correlate with their electronic properties, and especially the cohesive energy [3, 7]. In this chapter we present compressibility measurements for five transition metal nitrides that constitute important materials (δ-MoN, γ-Mo_2N, TaN, TiN and Cr_2N), using in situ X-ray structure determinations using synchrotron radiation in the diamond anvil cell. Industry already uses all of these nitrides as "super-hard" coating materials because of their high hardness properties and their chemical stability. However, the volume compressibility remains unknown even though it is an important parameter.

We performed the compressibility studies of TiN, TaN, Cr_2N and γ-Mo_2N at the APS in Argonne National Laboratory south of Chicago on the bending magnet beamline 13 BM-D.

We loaded the samples in a diamond anvil cell with 300 μm diameter culet diamonds and a 100 μm diameter hole. We measured the pressure using ruby fluorescence for the TiN and Cr_2N experiments, and diffraction of Au particles added to the sample for the TaN experiment. The pressure medium was nitrogen for the TiN, Cr_2N and γ-Mo_2N experiments, and the soft solid NaCl for the TaN experiment.

At APS, we collected the data using a Bruker CCD detector and integrated around the rings using the Fit2D software package. We calibrated the patterns using a CeO_2 standard sample mounted on a glass fibre.

In all cases, we performed a careful analysis of the 2D diffraction patterns. The aim was to determine if there was any deviatoric stress in the patterns which would result in an incorrect measurement of the bulk modulus. The patterns were integrated into a 2D pattern as shown figure 2-9. The vertical bands were always perfectly straight meaning that there was no deviatoric stress at least along the compression axis. Therefore, the bulk modulus measurement presented below should be very accurate.

5.2. Synthesis and compressibility study of δ-MoN phases

5.2.1. Synthesis of hexagonal MoN phases

Chapter 1 already discussed the phase diagram of the Mo – N system. The Mo-N system contains two principal phases: δ-MoN (hexagonal) and γ-Mo_2N (cubic).

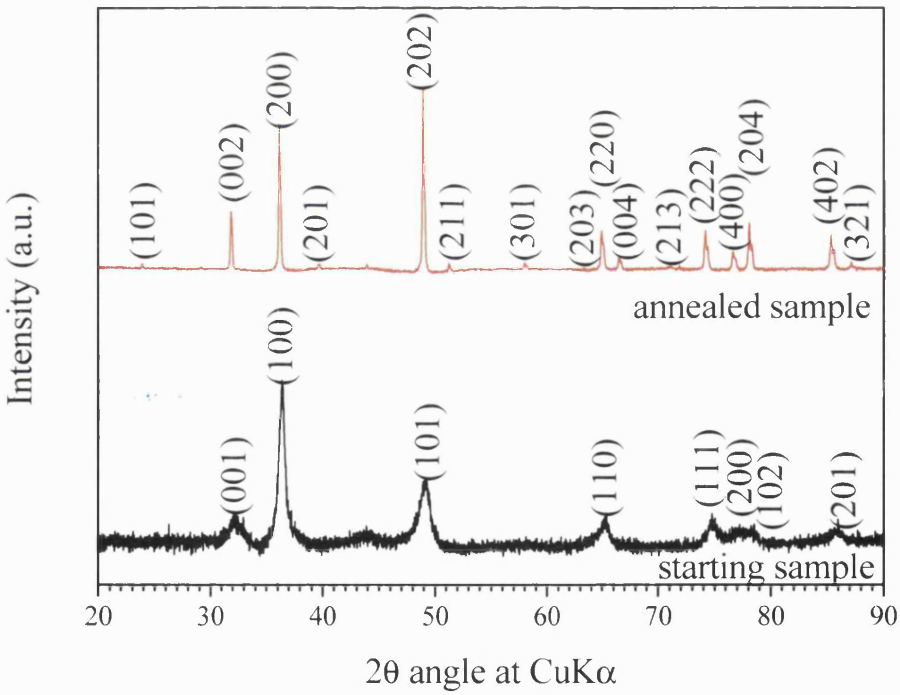

Figure 5-1 X-ray diffraction pattern of disordered δ-MoN (bottom) and ordered δ-MoN (top) obtained after high pressure annealing.

We synthesised δ-MoN (hexagonal), which has a WC structure in the "disordered" structure (see chapter 1) from the reaction of $MoCl_5$ + NH_3 at high temperature and room pressure. The variation of temperature changes the ratio δ- to γ- phase [142]. The higher the temperature the more γ-Mo_2N is synthesised along with some δ-MoN. The synthesis also generates some NH_4Cl as a by-product along with the molybdenum nitride. We can remove the ammonium chloride by

sublimation above 350 °C under flowing dry N_2. Bezinge *et al.* [88] previously described this synthesis process.

As shown by Bezinge, the synthesis at room pressure gives rise to a sample of δ-MoN with a relatively poor crystallinity. Figure 5-1 presents the X-ray diffraction of the sample obtained that way.

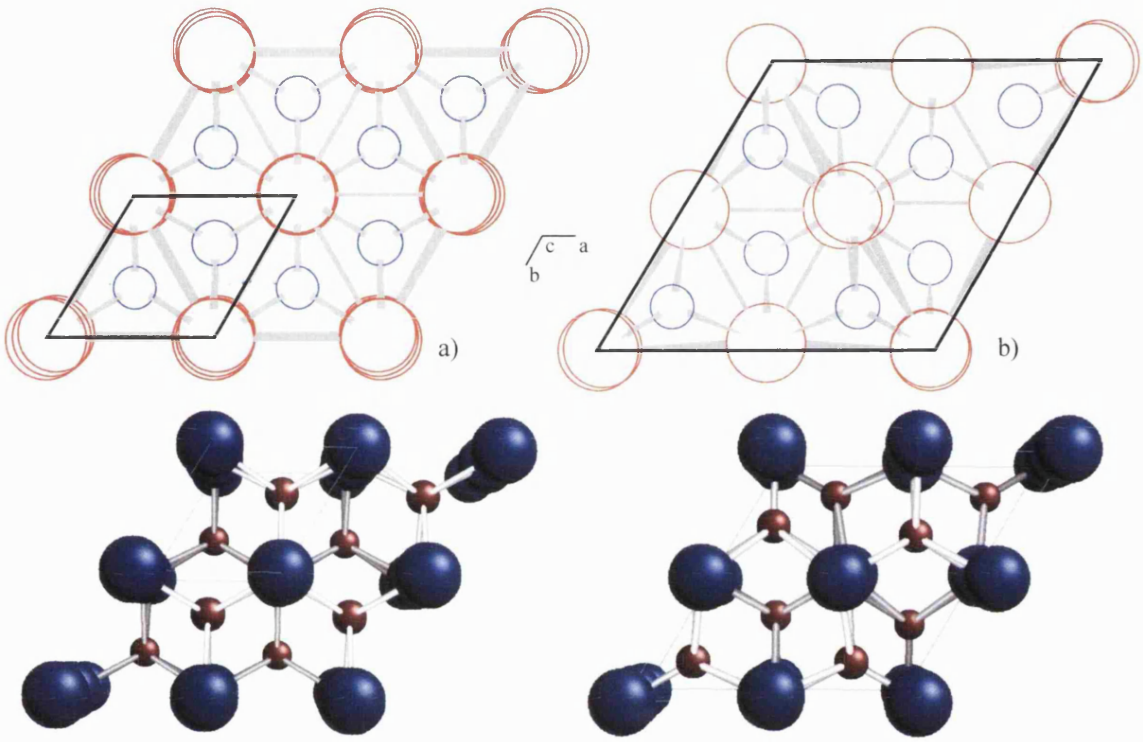

Figure 5-2 Schematic representation of the disordered δ-MoN (a) and ordered δ-MoN (b) structures. The small difference lay in the small change in the N and Mo atoms. The small circles or spheres represent the N atoms and the larger circles or spheres represent the Mo atoms.

Bezinge also showed that upon high pressure annealing at 6 GPa and 1500 °C, one can recrystallise the sample of disordered δ-MoN into a well crystalline ordered δ-MoN with a very similar structure. We reproduced the second synthesis step which is more an annealing process than a proper synthesis as the aim is to heat the sample without losing nitrogen in order to recrystallise it. We performed the annealing in a 14-8 mm assembly (described chapter 2) in the multi-anvil. For the synthesis, we used an octahedron of Cr:MgO (from Mino Yogio), pressed the sample into a dense disk and placed it into a boron nitride capsule. Finally, we heated the sample by mean of a graphite furnace while an S type thermocouple recorded the temperature.

Figure 5-1 presents the δ-MoN diffraction pattern obtained in this study. The pattern shows the existence of new diffraction peaks. The new peaks indicate that the hexagonal lattice must have undergone a doubling in order to allow the new reflections. The doubling of the unit cell is an

indication of the structural ordering. The structural ordering resulting in the doubling of the unit cell is that of the nitrogen atoms.

In fact, in 2000 Zhao *et al.* [87] suggested a structure for δ-MoN based on alternating layers of Mo and N atoms with very short Mo-N bond (1.4 Å) along the c axis. That structure possessed the same lattice parameter previously reported. This structure is in fact not physically possible according to results from the recent calculations performed by F. Cora at the Royal Institution [143].

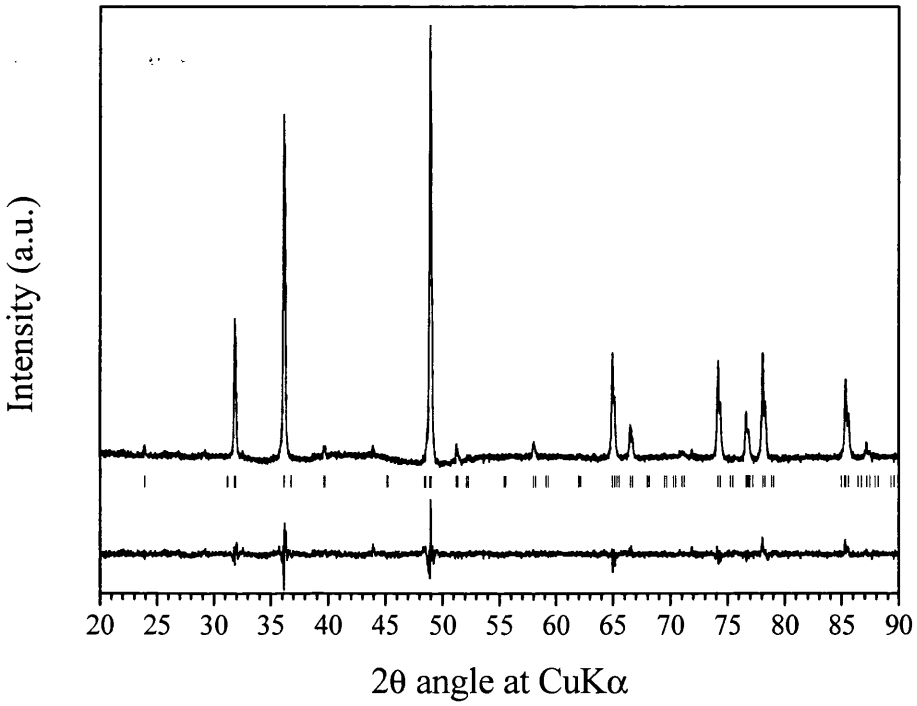

Figure 5-3 Rietveld structure refinement of the ordered δ-MoN phase from the X-ray diffraction data. The decrease of the background intensity around 50 ° is due to a saturation of the detector due to the extremely intense (202) diffraction peak. We represent in black the experimental data, in red the fit of the data and in blue the difference between the data and the fit.

Figure 5-3 presents the results of a structure refinement performed on the ordered phase (δ-MoN). We tested the two structures and the refinement clearly showed that the structure suggested by Zhao *et al.* [87] was clearly not appropriate. In fact, the correct structure was the one that Bezinge *et al.* [88] previously proposed.

a = 5.7401(9) Å; c = 5.6202(7) Å

Atoms	x	y	z	Wyckoff indices	Occupancy	Thermal parameter
Mo1	0.00	0.00	0.6195(1)	2 a	0.75(6)	0.0177(1)
Mo2	0.4891(1)	0.5108(8)	0.5600(5)	6 c	1.0(5)	0.0254(2)
N2	1/3	2/3	0.7938(7)	2 b	1.0(2)	0.0022(1)
N2	0.1479(9)	0.8520(1)	0.2644(4)	6 c	0.89(4)	0.0314(1)

WRp = 0.0377 (3.8 %)

R_p = 0.0284 (2.8%)

χ^2 = 2.05

Table 5-1. Structural data of the ordered δ-MoN from the Rietveld refinement results in the space group $P6_3mc$ (No. 186).

5.2.2. Equation of state of δ-MoN

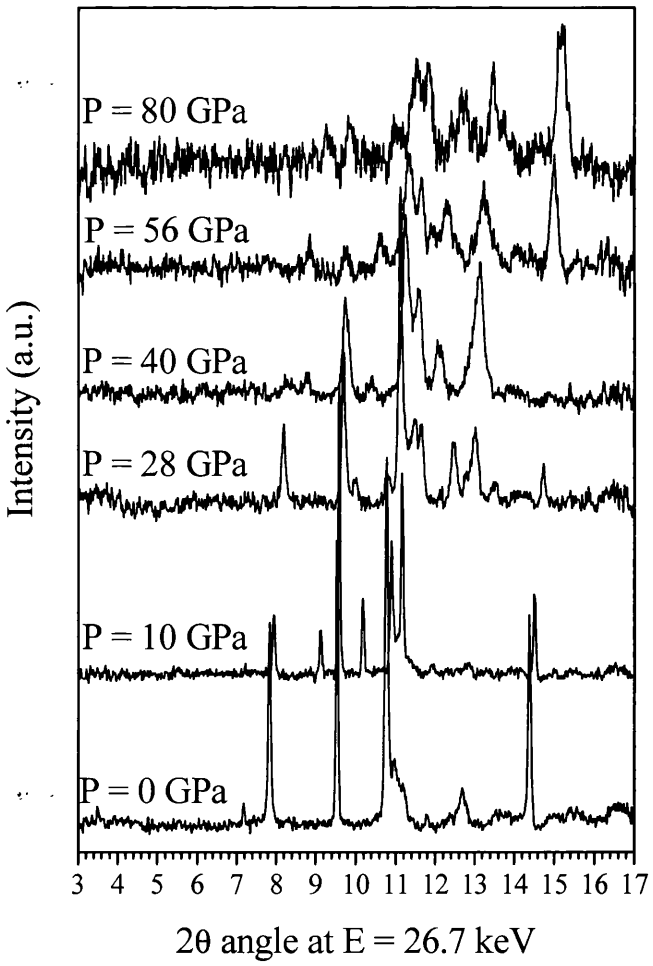

Figure 5-4 X-ray diffraction patterns of δ-MoN collected at the SRS at a wavelength λ = 0.4654 Å as a function of pressure.

There is very little data on the ordered δ-MoN phase due to the complex synthesis process. Furthermore, there is no information on the compressibility of that phase. We performed a

compressibility study of δ-MoN using X-ray diffraction in the diamond anvil cell. We loaded a sample of disordered δ-MoN into the diamond anvil cell and laser heated at 5.6 GPa to 2000 °C using the laboratory Nd:YAG laser heating system in order to transform the sample into the ordered δ-MoN phase. Then, we collected X-ray diffraction pattern of the sample at the SRS (UK) beamline 9.1 using angular dispersive diffraction at a wavelength $\lambda = 0.4654$ Å (Cd edge). The diamond had a culet diameter of 200 μm and the sample chamber in a rhenium gasket had a diameter of 90 μm. We integrated the data around the rings using the EDIPUS software and calibrated them with a Zr foil.

We increased the pressure up to 80 GPa using steps of about 5 GPa. We discontinued the experiment upon anvil failure at 85 GPa. We re-loaded the sample, and repeated the experiment up to about 50 GPa using a second diamond anvil cell. We also collected the diffraction at room pressure in order to have a good V_0 in the starting model for the bulk modulus refinement. Figure 5-4 shows selected diffraction patterns.

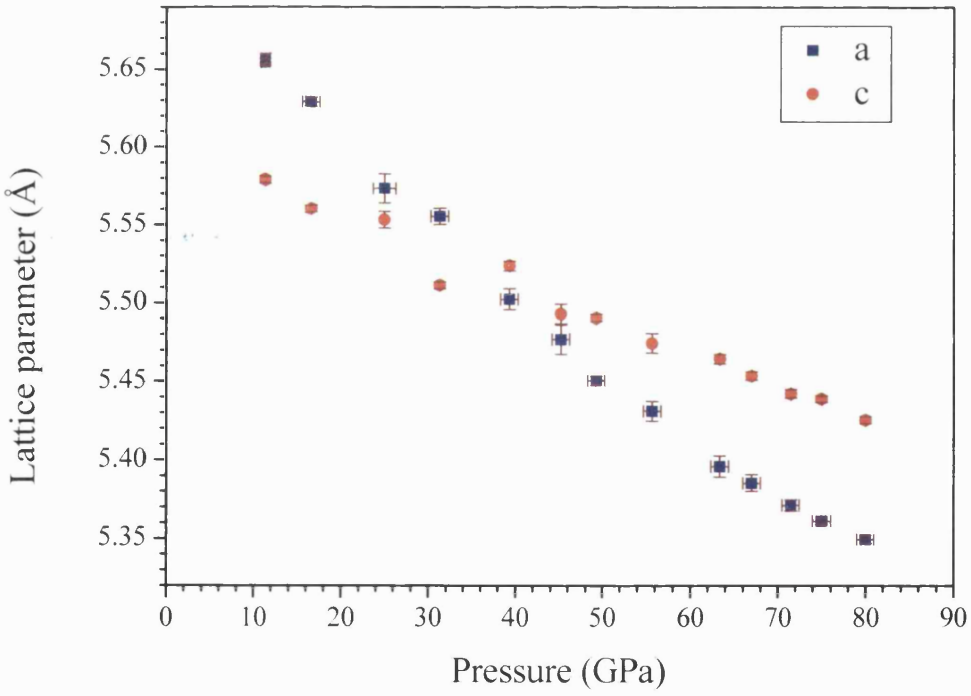

Figure 5-5 Plot of the a and c lattice parameters as a function of pressure for δ-MoN.

Fitting to the X-ray diffraction patterns at each pressure led to the determination of the lattice parameters (figure 5-5) and volume (figure 5-7) of δ-MoN as a function of pressure. The measured c/a ratio (figure 5-6) always remained close to unity, although it increased slightly as a function of pressure, showing that the δ-MoN is slightly more compressible along the *a* axis than along *c* (figure 5-5). Below 40 GPa, *a* is slightly longer than *c*, and above 40 GPa, *a* becomes the shortest axis (figure 5-6).

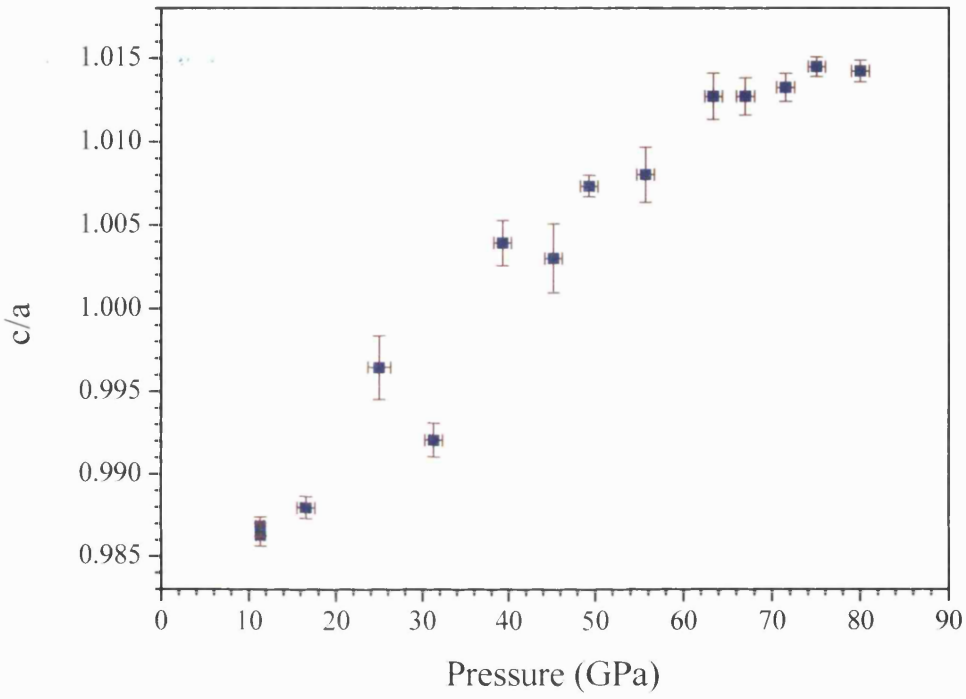

Figure 5-6 Plot of the experimentally measured c/a ratio for δ-MoN as a function of pressure, showing the structural stability of this phase upon compression.

The average bond distance compression from room pressure to 80 GPa is just above 6 %. The bonds between Mo atoms in the (00x) plane are more compressible than that between atoms of different layers. The Mo-Mo compression from room pressure to 80 GPa is 6.8 % for the bonds in the (00x) plane and 3.6 % for the other bonds. We calculated those compressions assuming that the relative atomic positions remain the same at high pressure. However, it is likely that the atoms will move in order to minimise the reduction in interatomic distances.

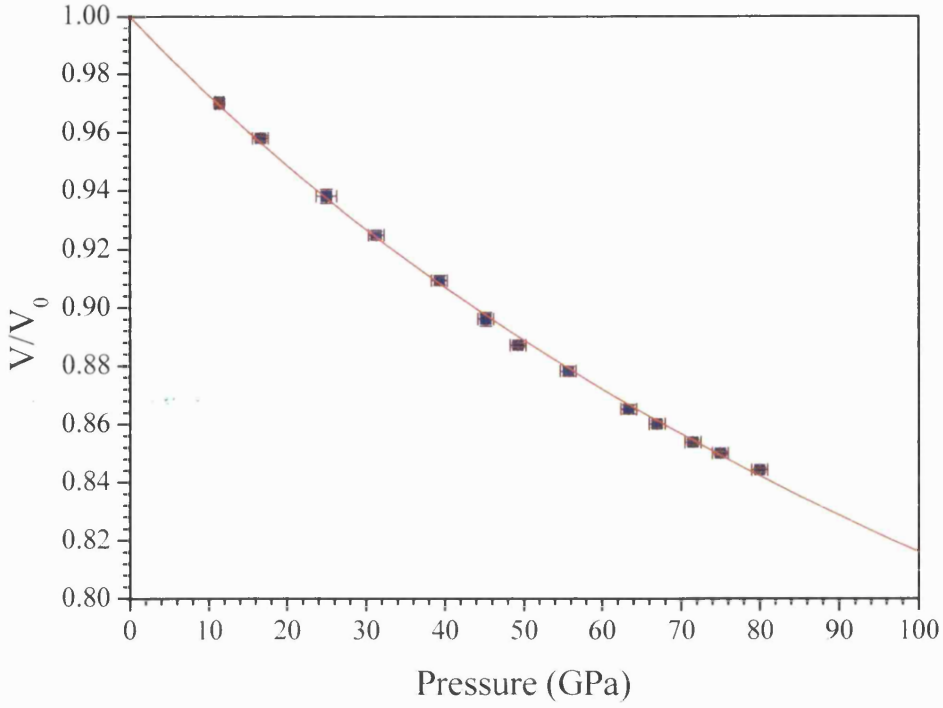

Figure 5-7 Plot of V/V_0 data for δ-MoN as a function of pressure with the fit of the Birch-Murnaghan equation of state for K_0 = 345(9) GPa and K_0' = 3.5(3).

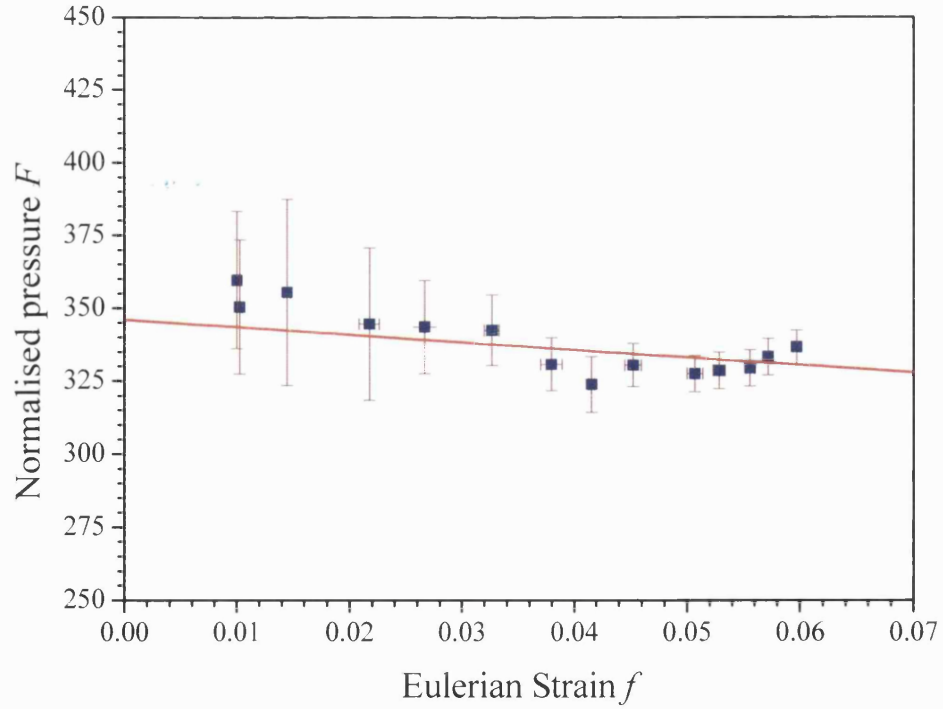

Figure 5-8 Plot of the normalised pressure (F) as a function of Eulerian strain (f) showing a slight slope of the data points consistent with the deviation of K_0' from 4 observed when fitting.

Figure 5-7 shows V/V_0 as a function of pressure. Fitting the data to the Birch-Murnaghan equation of state gives K_0 = 345(9) GPa with K_0' = 3.5(3). Representing the data in terms of the Eulerian strain parameter (f) and normalised pressure (F), allows us to clearly show the slight negative slope which demonstrates that $K_0' < 4.0$ (figure 5-8). The bulk modulus measured for δ-MoN is extremely high and among the highest reported to date. This indicates a very high value of the cohesive energy [20].

5.3. Synthesis and compressibility study of γ-MoN_{1-x}

5.3.1. Structural and compositional characteristics

As previously described, γ-MoN_{1-x} has a B1 structure. Z. Zhang and K. Leinenweber synthesised the sample of cubic MoN_{1-x} at Arizona State University using high pressure techniques.

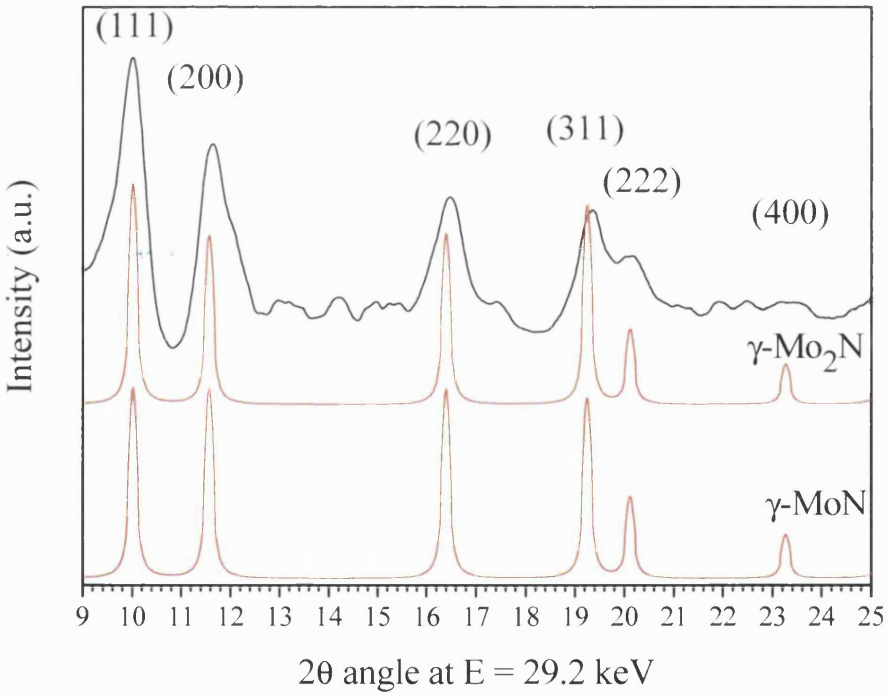

Figure 5-9 Angular dispersive pattern of the cubic MoN_{1-x} starting material measured on beamline 13BM at APS (Chicago). The red line represents a calculated pattern for the cubic phase of MoN and Mo_2N. The relative intensity of the (111) and (200) reflections are almost equal for the MoN composition. At the Mo_2N composition, the (111) diffraction peak is about 30 % more intense than the (200) reflection.

They pressurised a mixture of $MoCl_3$ + Zn_3N_2 to P ~ 1 GPa and heated it to T = 700 °C in a piston cylinder device. The reaction gave two products: $ZnCl_2$ and molybdenum nitride. Figure 5-9 presents the X-ray diffraction pattern of MoN_{1-x}.

The diffraction pattern shows an extreme broadening of the diffraction peaks. The peak width results from both the small crystallite size and the poor crystallinity of the sample. Using the Scherrer equation (1), we estimated the crystallite size from the peak width and the system resolution to be about 10 nm.

$$d = 0.9\lambda \frac{1}{FWHM \cos\theta} \quad (1)$$

With d the crystallite size, λ the X-ray wavelength, *FWHM* the full width at half maximum of the diffraction peak and θ the diffraction angle.

The peaks also show a significant amount of asymmetry also resulting from the poor crystallinity and strain within the crystallites. The poor crystallinity likely to be related to the phonon instability reported by Hart *et al.* [90]. Furthermore, the lattice parameter and relative intensity of the diffraction peaks are related to the composition of MoN_{1-x} ($0 < x < 0.5$). Marchand *et al.* showed that the relative intensity of the cubic molybdenum nitride X-ray diffraction peaks changes as a function of composition from Mo_2N up to MoN_2. In fact, the results are only meaningful in the composition range Mo_2N - MoN because any composition richer in N than MoN is not structurally consistent with the B1 structure as the N atoms fill all the available octahedral sites at the MoN composition.

The relative intensity of the (111) and (200) reflections are extremely close for the MoN composition. The (111) reflection is about 30 % more intense than the (200) peak for the Mo_2N composition. The second case is the most consistent with the data shown figure 5-9. Thus, we estimate that the composition of the sample is close to Mo_2N from the relative intensities.

5.3.2. Compressibility study

In order to determine the compressibility of the cubic starting material γ-Mo_2N, we loaded a sample into a diamond anvil cell. We cryogenically loaded the sample into a nitrogen pressure medium. We then determined the pressure using the ruby scale described in chapter 2. We chose Re as the gasket material and the diamond culet diameter was 300 μm in diameter with a sample chamber of 130 μm diameter. We performed the experiment at the bending magnet beamline 13 BM-D at GSECARS-CAT at the APS using angular dispersive techniques at λ = 0.4246 Å and at the NSLS beamline X17B1 using energy dispersive X-ray diffraction at a 2 θ angle of 12 °.

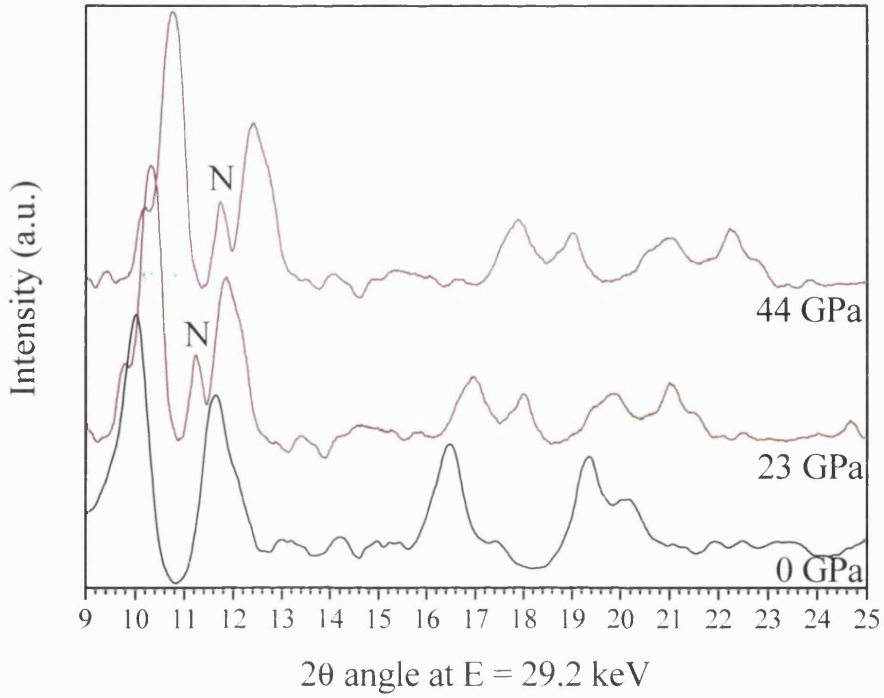

Figure 5-10 X-ray diffraction spectra of MoN_{1-x} in the cubic B1 phase. The spectrum at room pressure is the one presented in figure 5-9. We collected the spectra at 23 and 43.8 GPa in energy dispersive at NSLS (Brookhaven NY) at a diffraction angle of 12.000° and converted the scale to match the angular dispersive spectrum.

We collected the X-ray diffraction patterns as a function of pressure. Figure 5-10 presents selected X-ray diffraction patterns. A close look at the diffraction patterns shows that there are some distortions in the structure resulting into a splitting of the (111) reflection at high pressure. However, the low resolution of the pattern did not allow a clear determination of the new structure. The distortion can result from several parameters. First, it may be intrinsic of γ-Mo_2N. Otherwise, it could be a result from some anisotropy in the pressure within the sample chamber resulting in large shear stress. The shear stress could result into some significant amount of distortion in the cubic lattice.

We observed the rocksalt like (B1) structure of Mo_2N up to 50 GPa at room temperature. The structure persists as long as the sample is not laser heated as shown on figure 5-10. From the numerous experiments, we could use the few spectra of the B1 phase at various pressures in order to estimate the bulk modulus. Figure 5-11 shows the plot of the normalised volume as a function of pressure measured from the X-ray diffraction data. The fit of the data from figure 5-11 to the Birch-Murnaghan equation of state gives a bulk modulus K_0 = 301(7) GPa for a pressure derivative set at 4. The value of the bulk modulus is relatively high indicating that the B1-Mo_2N is likely to be a relatively hard material.

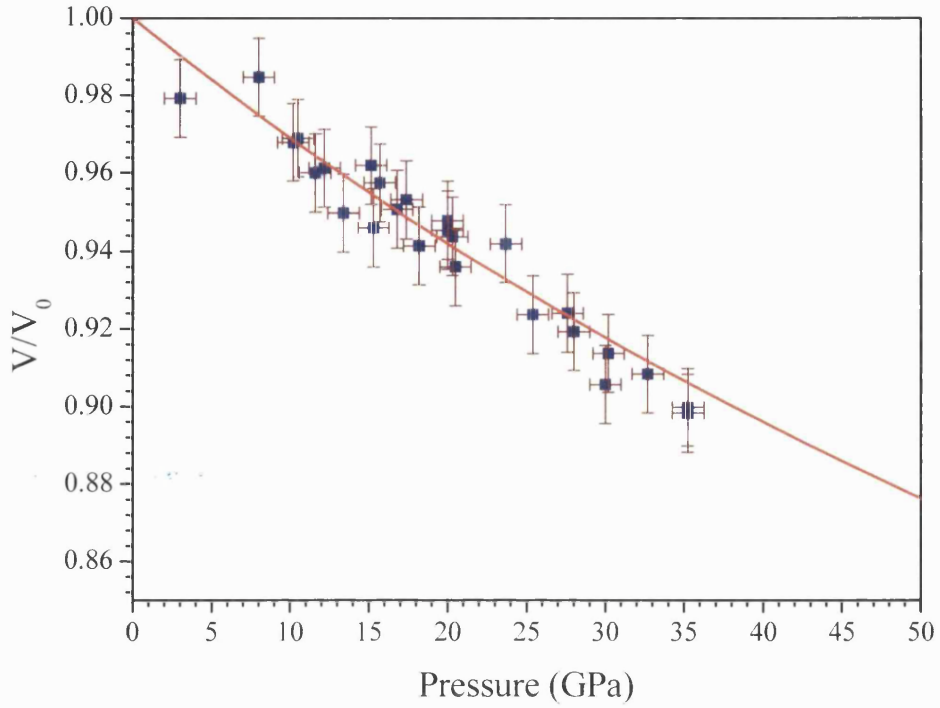

Figure 5-11 Plot of V/V_0 for the γ-Mo_2N sample as a function of pressure with the fit of the Birch-Murnaghan equation of state for K_0 = 301(7) GPa and K_0' = 4.

5.4. Compressibility study of ε-TaN

Tantalum nitride is one of the hardest nitrides and one of the materials with the highest melting point (3093 °C [7]). In fact the carbide counterpart TaC is the material with the highest melting point with a melting point at 3983 °C at room pressure [7]. There are reports of several phases for tantalum nitride..The phase studied in the compression experiment is the hexagonal phase ε-TaN. Compared with TiN and Cr_2N, TaN has a very strong X-ray diffraction spectrum due to Ta which is a very heavy element and consequently has a large X-ray scattering factor.

We collected angular diffraction patterns of TaN from room pressure up to 40 GPa using very small pressure steps (figure 5-12). We also repeated the experiment several times in order to get a large number of data points. Figure 5-13 presents a plot of tantalum nitride reduced volume as a function of pressure. We fitted the data to a Birch-Murnaghan equation of state in order to obtain the bulk modulus and pressure derivative. The results of the fits are K_0 = 358(8) GPa and K_0' = 2.3(4) with a fitted V_0 = 68.25(3) Å.

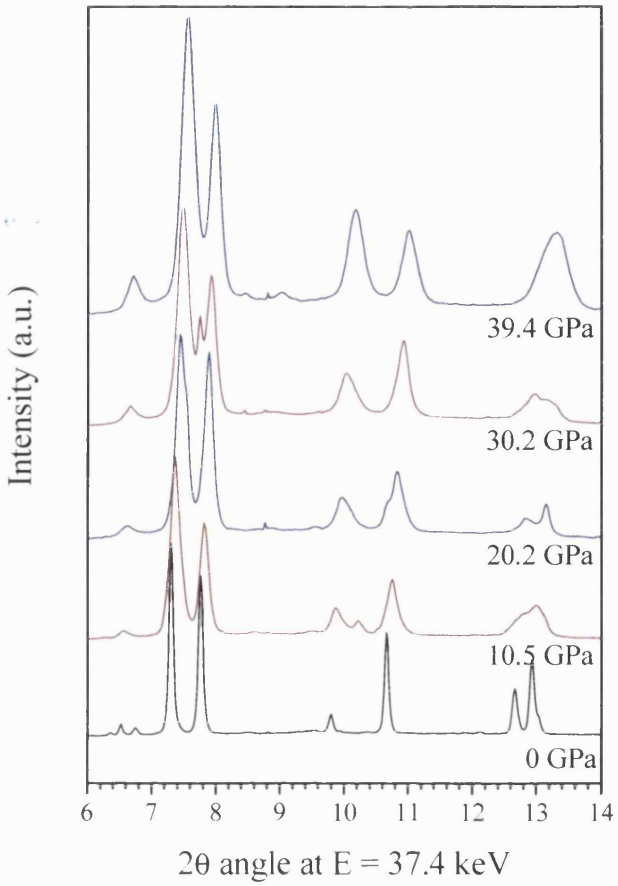

Figure 5-12 Angular dispersive X-ray diffraction patterns of ε-TaN at high pressures.

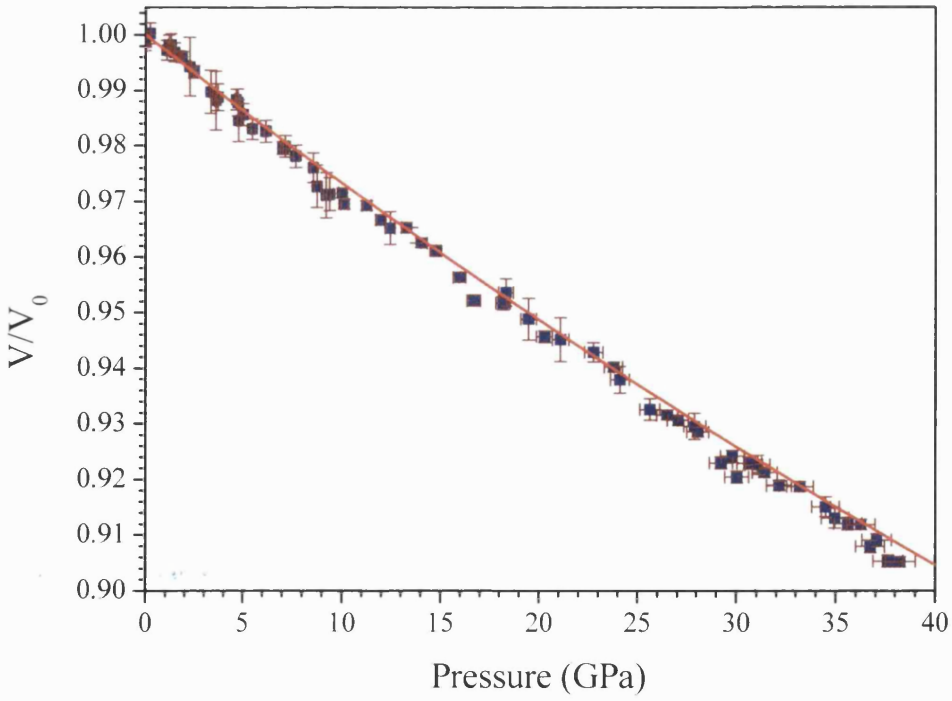

Figure 5-13 V/V_0 as a function of pressure for ε-TaN.

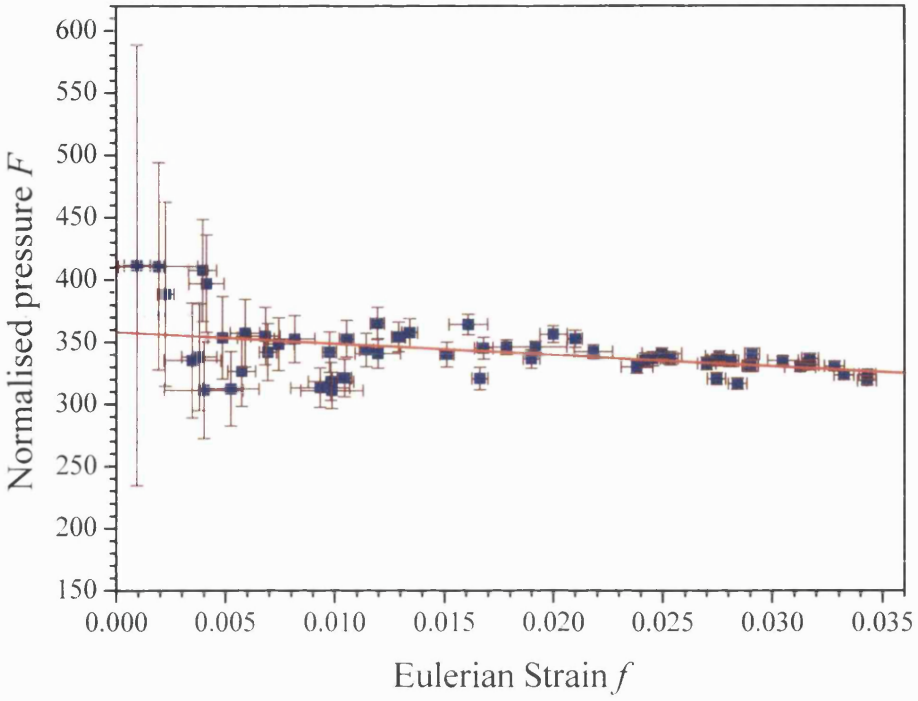

Figure 5-14 Normalised pressure F versus Eulerian strain f diagram of the tantalum nitride data.

Figure 5-14 shows a representation of the data in a normalised pressure as a function of Eulerian strain diagram. The data display a slight negative slope confirming that the K_0' is less than 4.0 as shown with the fit of the data. The example of ε-TaN is a good equation of state measurement example for a highly incompressible material using powder X-ray diffraction. The data on the *F(f)* plot show a large increase of the error bars as the strain tends toward 0. This large increase of the error is due to the fact that we normalise the data to the room pressure volume. Thus, as the data tents toward 0, we divide them by a smaller and smaller V/V_0 as shown in chapter 2. Furthermore, the F(f) plot shows that it is not necessary to collect data at extremely high pressure as above about 25 GPa, the scattering and errors are small enough to obtain an excellent fit . High bulk modulus does not necessarily means that one must carry out the experiment up to megabar pressures.

We can examine the variation of the lattice parameters of ε-TaN as a function of pressure in order to ensure that there is no onset of a phase transition like it was the case in the germanium nitride study. Figure 5-12 presents selected X-ray diffraction patterns of ε-TaN at high pressure and figure 5-15 shows the fitted lattice parameters. The X-ray diffraction pattern of TaN becomes broader as pressure increases. The broadening can result either from the pressure medium which in this case is NaCl or from an intrinsic destabilisation of the ε-structure. Sodium chloride is a very stiff pressure medium at 40 GPa and could give rise to the increase in peak

width. However, the diffraction peaks from gold do not display any significant broadening. Thus, one can conclude that TaN is undergoing a small structural disordering at high pressure. The average position of the atoms remain the same however, their positions vary more than at lower pressure.

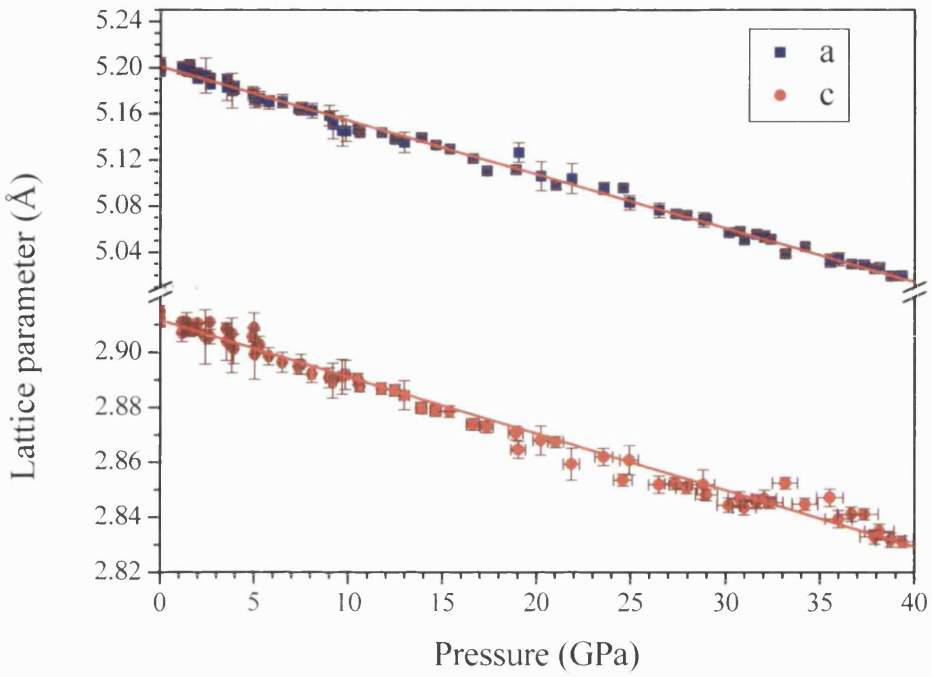

Figure 5-15 Lattice parameters a and c for TaN as a function of pressure.

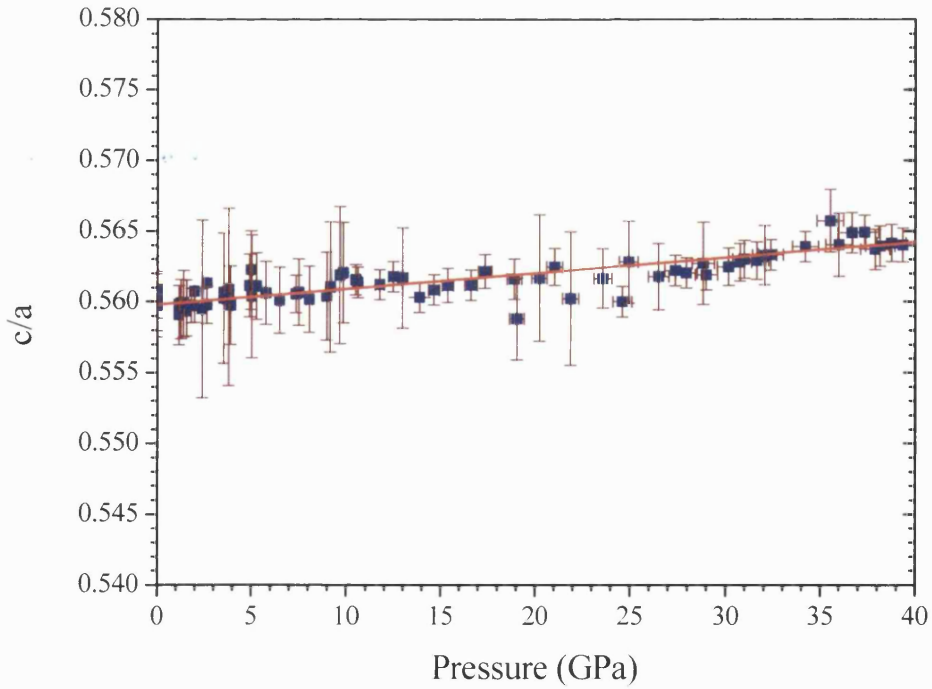

Figure 5-16 c/a as a function of pressure for TaN

If the tantalum nitride structure is becoming unstable, there could be some evidence of it in the variation of the lattice parameters as a function of pressure. Figure 5-15 shows the plot of the lattice parameters as a function of pressure and reveals that there is no change in the behaviour of the lattice parameters as pressure increases. The slight deviation for the straight line drawn by the data on the c axis is due to some errors in the fitting and is unlikely to be due to a real change in the c axis.

In summary, ε-TaN is extremely incompressible. The compressibility of tantalum nitride is comparable to that of δ-MoN measured in the previous chapter. However, the structures of the two materials are rather different as shown in the first section. Once again, we can relate the large value of the bulk modulus to the high cohesive energy and hardness of the nitride material. Furthermore, the structure of ε-TaN is stable up to at least 40 GPa upon room temperature compression. However, TaN undergoes a small disordering upon pressurisation.

5.5. Compressibility study of TiN

TiN is a B1 structured material. There is a large variation of composition in the Ti-N system and depending upon the composition, the physical properties will vary sometime very significantly. Thus, we probed the sample of TiN from Alpha Aesar used in the experiment using electron probe technique in order to ensure that the composition is TiN within experimental errors. In fact, the lattice parameter of titanium nitride is strongly dependent upon the nitrogen content as shown figure 5-17. The lattice parameter of the sample a = 4.24 Å also matches very well the lattice parameter measured for TiN.

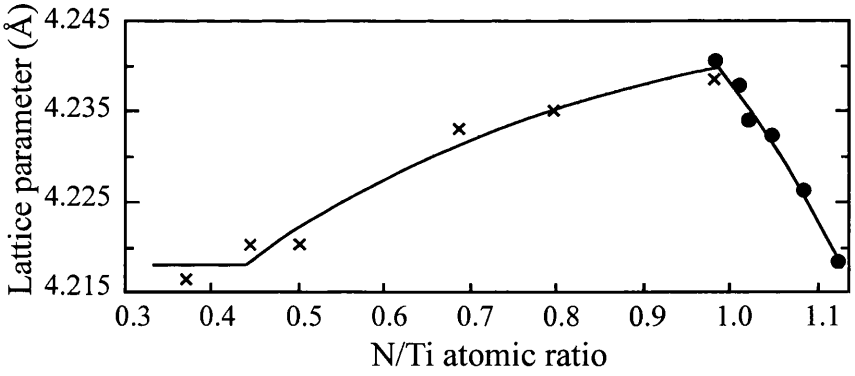

Figure 5-17 Variation of TiN_x lattice parameter as a function of the nitrogen content, figure adapted from Toth [7].

We pressed the sample into a very compact platelet and loaded it into the diamond anvil cell. The pressure range of the experiment was from room pressure up to 20 GPa. Due to the high symmetry of titanium nitride, which has a B1 structure, only very few peaks were available for the fit. We only fitted three peaks at all pressures in order to determine the lattice parameter and

volume. However, as there is only one lattice parameter, the redundancy is sufficient to obtain good quality fits.

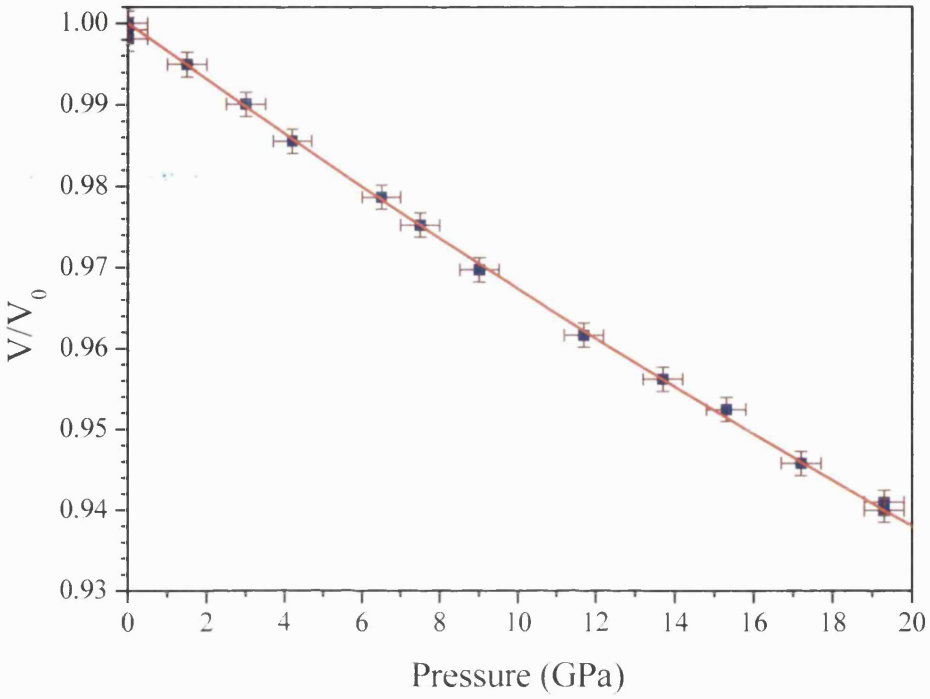

Figure 5-18 V/V_0 as a function of pressure measured for TiN along with the Birch-Murnaghan equation of state fit of the data.

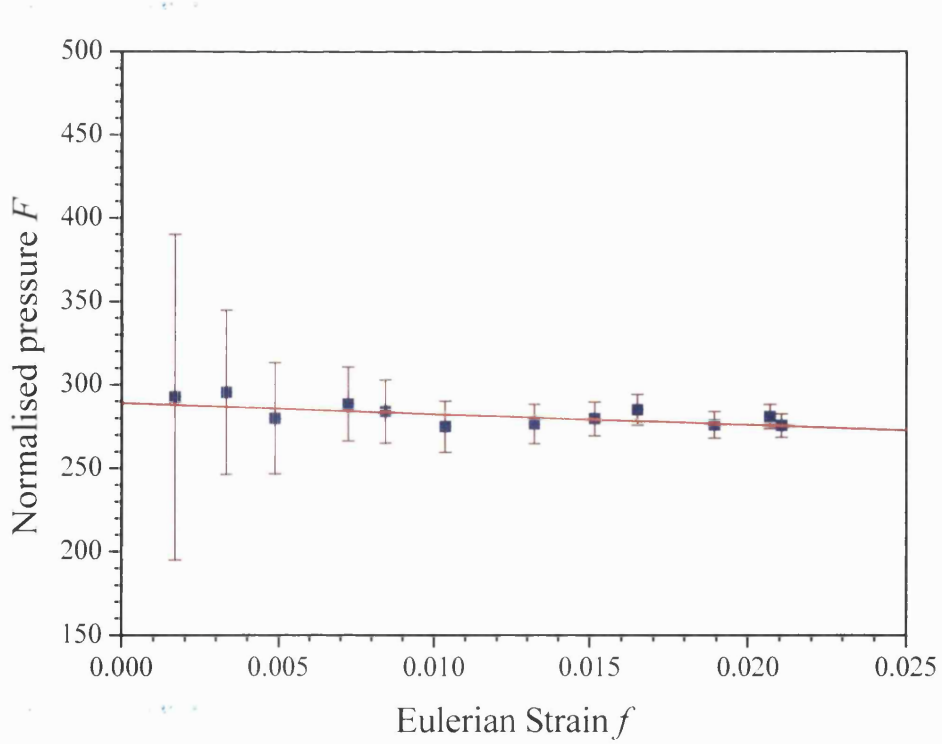

Figure 5-19 Normalised pressure as a function of Eulerian strain for TiN.

Figure 5-18 presents the normalised volume as a function of pressure for TiN. We measured the V_0 value and also subsequently fitted it when fitting the data to the Birch-Murnaghan equation of state. Figure 5-18 presents the equation of state fit of the data as a line.

The measured bulk modulus is K_0 = 289(7) and K_0' = 2.5(8) when using the measured V_0 = 76.223 $Å^3$. The results of the fitting procedure are almost the same when fitting the room pressure volume: K_0 = 290(17), K_0' = 1.4(7) and V_0 = 76.219(72) Å. A plot of the normalised pressure versus Eulerian strain presented figure 5-19 shows that K_0' is lower than 4 as there is a small negative slope of the data.

5.6. Compressibility study of Cr_2N

Chromium nitride exists in several phases. The phase studied in the compressibility experiment is the hexagonal Cr_2N phase. Chapter 1 presented the Cr_2N structure. The Cr_2N phase is the most common chromium nitride phase. Its main application is as a coating for tools. We performed the compression experiment at pressures from 0 up to just below 25 GPa. As the phase of chromium nitride we are interested in is hexagonal, the diffraction pattern is more complex. At each pressure we used 6 peaks in order to refine the a and c lattice parameters.

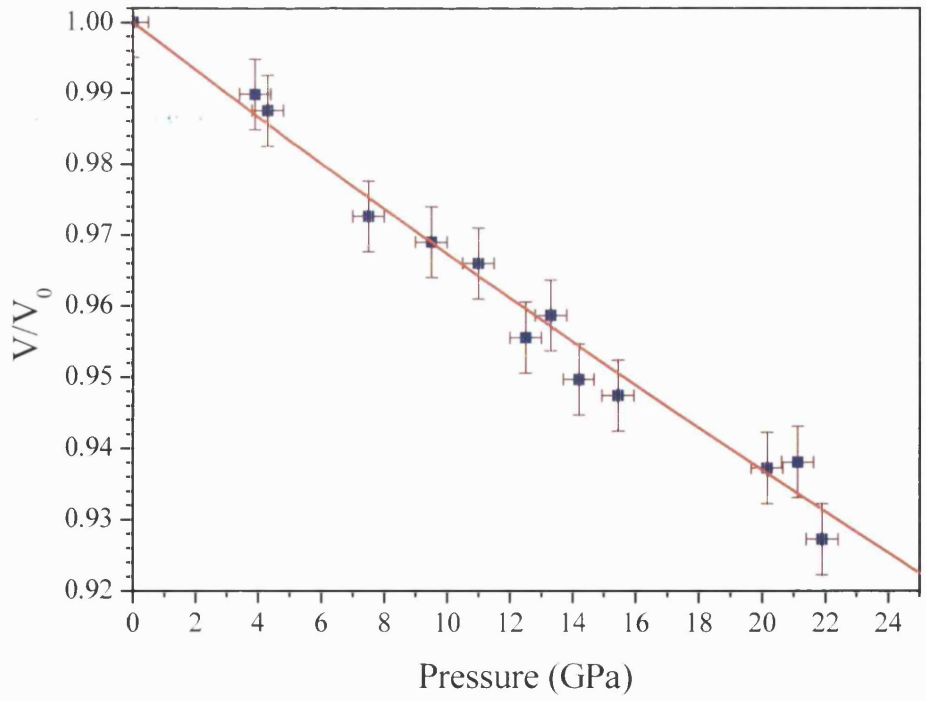

Figure 5-20 V/V_0 as a function of pressure for Cr_2N.

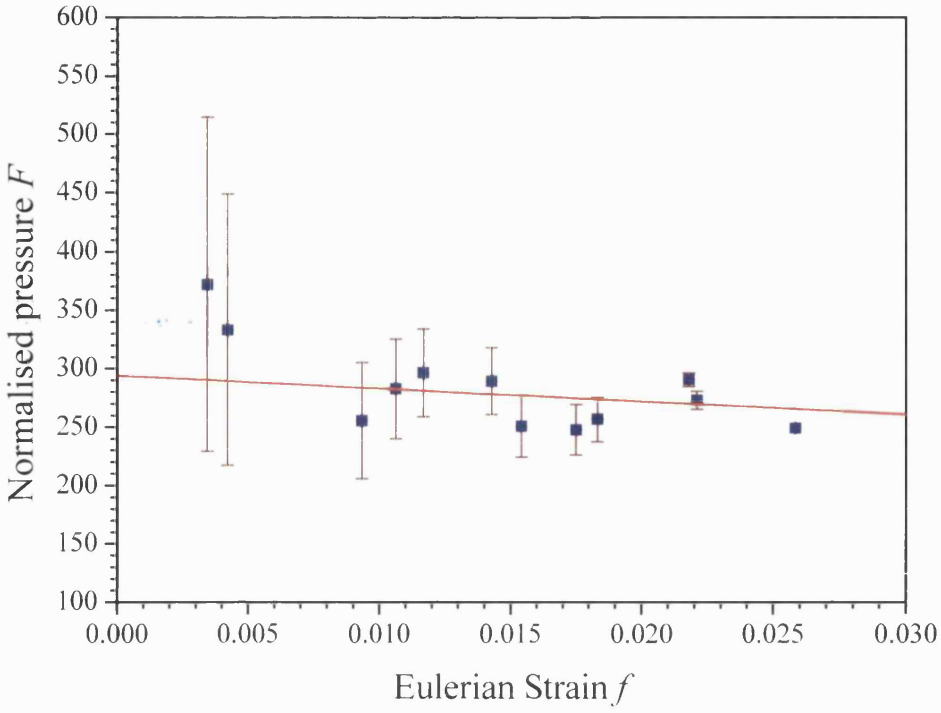

Figure 5-21 Normalised pressure (F) versus Eulerian strain (f) diagram of the Cr_2N compression data.

Even though there is some scattering in the data, we could fit the observed volumes (figure 5-20) to a Birch-Murnaghan equation of state and obtained K_0 = 294(23) for K_0' = 1.5(20) with a fixed V_0 = 89.428 Å measured. The large error in the fitted value of the K_0' comes from the large scattering of the data. In order to confirm the small value of the pressure derivative, figure 5-21 presents a plot of the data in a normalised pressure versus Eulerian strain diagram. The diagram confirms that the data have a slight negative slope. Thus the fitted value of the pressure derivative is less than 4 and probably around 2 as estimated by the Birch-Murnaghan fit.

The value of the bulk modulus measured for Cr_2N is in the same range as TiN although the two materials have very different structures and nitrogen content.

5.7. Discussion

From the experimental data, we observed that the bulk modulus of transition metal nitrides varies from one nitride to the other even within the same structural group (hexagonal or cubic). The variation in bulk modulus is due to two main reasons. First, the structures are different. Thus, the electronic density of states is different and depending upon the position of the Fermi level with respect of the bonding and anti-bonding states, the cohesive energy / bulk modulus increases or decreases. Secondly, the chemical composition changes between the materials

therefore changing the number of valence electron and the energy of the Fermi level. Figure 5-22 illustrates both of those concepts.

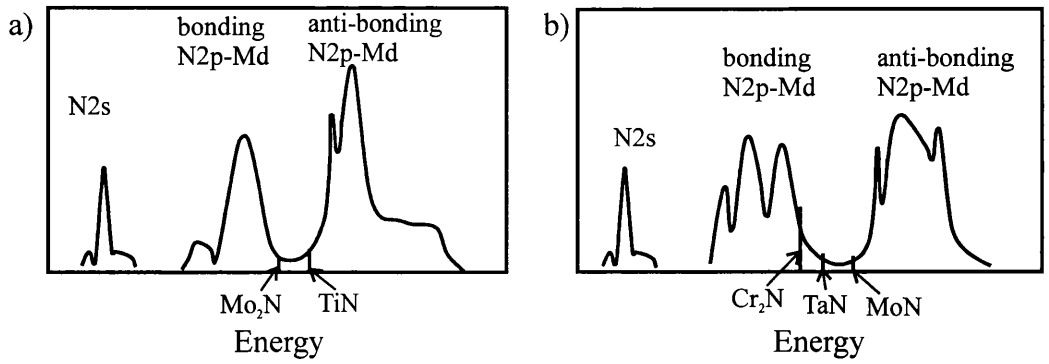

Figure 5-22 Diagrams showing a general trend of the density of states for cubic B1 (a) and hexagonal (b) transition metal nitrides. the vertical straight lines indicate the position of the Fermi level. Figure adapted from Lévy et al. [18].

Within the cubic structure, TiN has (4 + 5)/2 = 4.5 valence electrons and Mo_2N has (6 + 2.5)/2 = 4.25 valence electrons. Within the hexagonal structures, TaN has (5 + 5)/2 = 5 valence electrons, MoN has (6 + 5)/2 = 5.5 valence electrons and Cr_2N has (6 + 2.5)/2 = 4.25 valence electrons.

$$K_o = c\frac{E_c}{V_m} \tag{2}$$

(E_c is the cohesive energy, V_m is the molar volume, K_o the zero-pressure bulk modulus: c a constant between 2-4)[20].

From the valence electron counting and the shape of the density of states, Mo_2N should have a slightly higher cohesive energy than TiN, because TiN starts to slightly fill the anti-bonding levels and Mo_2N has a Fermi level just below the anti bonding energy levels. Equation 2 relates the cohesive energy to the bulk modulus. Thus, one could have expected that TiN would have a slightly lower bulk modulus than Mo_2N as shown by the experimental data.

From the valence electron counting and the shape of the electron density of states of hexagonally structured transition metal nitrides, TaN and MoN should have a very similar bulk modulus and Cr_2N should have a much lower bulk modulus. In Cr_2N not all of the bonding level are filled unlike in the case of MoN and TaN. Thus, the cohesive energy of Cr_2N is significantly lower. Consequently, one could have expected that TaN and MoN would have extremely high and very similar bulk moduli and Cr_2N would have a lower value of bulk modulus.

5.8. Conclusions

In conclusion, we have determined the bulk modulus of a number of transition metal nitrides (table 5-2). The bulk moduli are extremely high and indicate that the hardness of those materials are likely to be particularly high as well, according to Teter [144].

Phase	Bulk modulus (GPa)	Pressure derivative
δ-MoN	345(9)	3.5(3)
ε-TaN	358(8)	2.3(4)
Cr_2N	294(23)	1.5(20)
γ-Mo_2N	301(7)	4.0 (assumed)
TiN	290(17)	1.4(7)

Table 5-2 Bulk modulus and pressure derivative of transition metal nitride phases.

Chapter 6. Raman Spectroscopic Studies of Transition Metal Nitrides.

6.1. Introduction

Chapter 6 presents a Raman spectroscopic study of several important transition metal nitrides. Raman spectroscopy is a very sensitive technique for phase transition as shown previously. Furthermore, there is very little information available and often no report at all, on the vibrational spectra of transition metal nitrides, even at ambient conditions. In particular, the knowledge of those spectra would allow the use of Raman spectroscopy as a finger printing technique in the case of the extremely small samples studied in the DAC at high pressure, or for example prepared by CVD synthesis, where X-ray diffraction is not always a useful characterisation technique.

At ambient conditions it is extremely difficult to collect good quality Raman spectra of transition metal nitrides. Nitrides tend to oxidise upon heating under the laser in air. Transition metal nitrides are semi-metallic and are very dark in colour, they tend to absorb or reflect most of the laser light, and they heat up under high laser power. It is often easier to collect the Raman spectrum in the diamond anvil cell where the sample is contained within an inert atmosphere, and is less likely to oxidise or decompose.

Here we present the first Raman spectra collected for several transition metal nitrides. The crystallinity of the nitrides studied in these investigations was extremely good when analysing the samples with X-ray diffraction (i.e., the diffraction lines were sharp, and all expected reflections were observed). However, the Raman bands were often very broad, except in the case of ε-TaN. We discuss the reasons for this observation below. We divided the discussion into two parts, depending upon the structure of the transition metal nitride. The first part describes the hexagonal nitrides ε-TaN and δ-MoN. The second part presents the B1 structured transitions metal nitrides TiN_{1-x}, VN_{1-x} and γ-Mo_2N. These materials should have no allowed first-order Raman spectra: any features are then disorder-induced due to the presence of defects on the anion sites, or due to second order scattering.

When using visible exciting light, the Raman effect only interacts with vibrations at the centre of the Brillouin zone, as the wavelength of the visible light is much greater than that of the unit cell dimension. However, this statement only holds if the crystal is "perfectly" ordered, and contains no structural defects that might remove the coherence of vibrational waves travelling through the crystal. Consequently, excitations across the entire Brillouin zone are sampled when collecting a Raman spectrum from a "defective" or disordered solid. The Raman spectrum then resembles the phonon density of states (DOS). The Raman spectrum is then expected to be comparable with the vibrational DOS obtained using inelastic neutron scattering techniques. We have observed this phenomenon in our studies of nitrides.

6.2. Hexagonal transition metal nitrides

Two examples of Raman spectroscopic studies of hexagonal transition metal nitrides are presented in this paragraph. First, is presented a study of tantalum nitride followed by a study of δ-MoN. The two compounds have a hexagonal structure, but the metal packing and N site occupancies are quite different; therefore, we expect some general similarities but differences in detail in their Raman spectra. For each study we start by carrying out a factor group analysis in order to determine the number of expected Raman active modes, before investigating the observed Raman spectra.

6.2.1. Raman spectroscopic study of ε-TaN

Prediction of Raman peaks activity of ε-TaN

Space group: $P\bar{6}2m$ (D_{3h}^3)

Structure $Z = 3$
Ta1: 1a (D_{3h})
Ta2: 2d (C_{3h})
N: 3f (C_{2v})

Number of expected modes:
$N = 3n - 3 = 3 \times 6 - 3 = 15$ (with 3 acoustic modes corresponding to translations in the crystal)

D_{3h}	E	$2C_3$	$3C_2$	σ_h	$2S_3$	$3\sigma_v$		
A_1'	1	1	1	1	1	1		$\alpha_{xx}+\alpha_{yy}, \alpha_{zz}$
A_2'	1	1	-1	1	1	-1	R_z	
E'	2	-1	0	2	-1	0	(T_x, T_y)	$(\alpha_{xx}-\alpha_{yy},\alpha_{xy})$
A_1''	1	1	1	-1	-1	-1		
A_2''	1	1	-1	-1	-1	1	T_z	
E''	2	-1	0	-2	1	0	(R_x,R_y)	$(\alpha_{xz},\alpha_{yz})$

C_{3h}	E	C_3	C_3^2	σ_h	S_3	S_3^5		$\varepsilon=e^{2\pi i/3}$
A'	1	1	1	1	1	1	R_z	$\alpha_{xx}+\alpha_{yy}, \alpha_{zz}$

E'	1 1	ε ε*	ε* ε	1 1	ε ε*	ε* ε	(T_x, T_y)	$(\alpha_{xx}-\alpha_{yy}, \alpha_{xy})$
A''	1	1	1	-1	-1	-1	T_z	
E''	1 1	ε ε*	ε* ε	-1 -1	−ε −ε*	−ε* −ε	(R_x, R_y)	$(\alpha_{xz}, \alpha_{yz})$

C_{2v}	E	C_2	$\sigma_v(zx)$	$\sigma_v(yz)$		
A_1	1	1	1	1	T_z	$\alpha_{xx}, \alpha_{yy}, \alpha_{zz}$
A_2	1	1	-1	-1	R_z	α_{xy}
B_1	1	-1	1	-1	T_x, R_y	α_{xz}
B_2	1	-1	-1	1	T_y, R_x	α_{yz}

D_{3h}	C_{3h}	C_{2v}
A_1'	A'	A_1
A_2'	A'	B2
E'	E'	A_1+B_2
A_1''	A''	A_2
A_2''	A''	B_1
E''	E''	A_2+B_1

Ta (C_{3h}):

C_{3h}	→	D_{3h}
E'	→	2E'
A''	→	A_1''
A''	→	A_2''

Ta (D_{3h}):
E'

N (C_{2v}):

C_{2v}	→	D_{3h}
A_1	→	A_1'
A_1+B_2	→	2 E'
B_2	→	A_2'
B_1	→	A_2''
B_1	→	E''

$\Gamma_{total} = A_1' + A_2' + A_1'' + 3\ A_2'' + 5\ E' + E''$
$\Gamma_{acoustic} = E' + A_2''$
$\Gamma_{optic} = A_1' + A_2' + A_1'' + 2\ A_2'' + 4\ E' + E''$
$\Gamma_{Raman} = A_1' + 4\ E' + E''$
2 or 3 E' modes from Ta
A_1' + E'' + 1 or 2 E' modes from N motions
Thus, there are 6 Raman active modes.

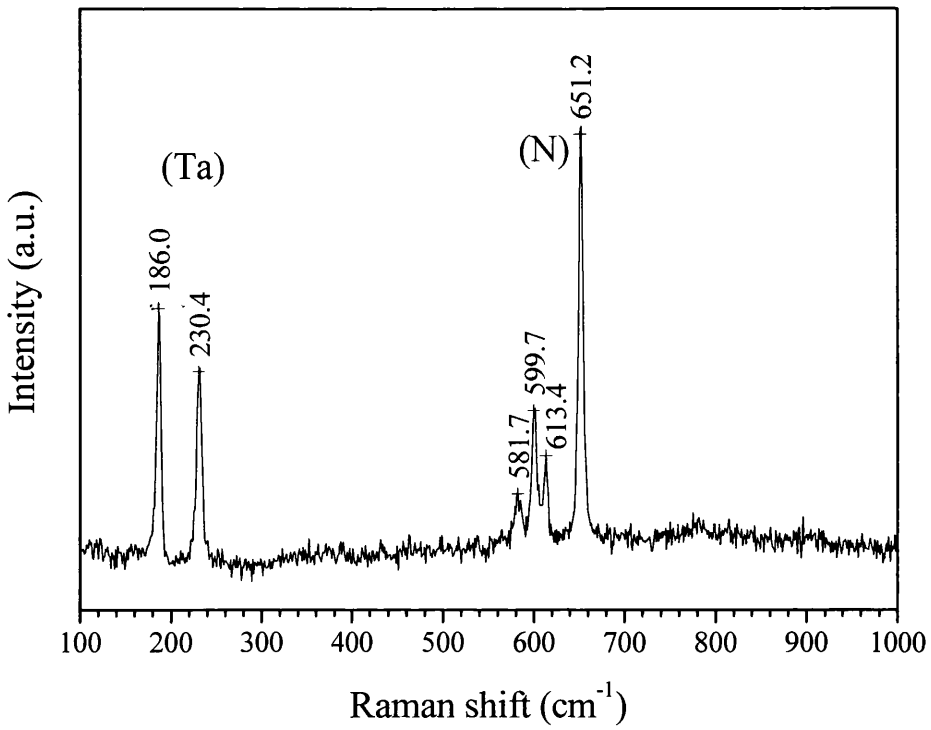

Figure 6-1 Raman spectrum of ε-TaN collected using a 514.5 nm excitation line.

The Raman spectrum of ε-TaN presented figure 6-1 displays six sharp lines, as expected. Two occur at low wavenumbers indicating that they are mostly due to the motion of the heavier element: Ta. Thus we can easily assign the peaks at 186 and 230 cm^{-1} to have E' symmetry vibrations. Four bands are at higher wavenumbers between 500 and 700 cm^{-1} indicating that they are mainly due to the motion of the lighter element: N.

In order to determine the symmetry of the vibrations in the high wavenumber region, it is required to perform a polarised Raman experiment. In cross polarised Raman spectrum, the peak intensity component of the α_{xx}, α_{yy} and α_{zz} is zero. Therefore, a cross polarised Raman experiment would dramatically change the intensity of the A_1' peak as it results from the $\alpha_{xx}+\alpha_{yy}$, α_{zz} polarisability tensor. The E' modes should also show some decrease in intensity in the cross polarised spectra compared to the parallel polarised pattern due to the $\alpha_{xx} - \alpha_{yy}$ component of the vibration. However, the E'' peaks should not display any change in intensity.

Figure 6-2 present a polarised Raman study on a powder sample ε-TaN. The differences in the spectra (compared with figure 6-1) are due to the change in the exciting wavelength from 514.5 nm to 633 nm. The difference between the VV (vertically polarised laser and vertically polarised signal) and the VH (vertically polarised laser and horizontally polarised signal) is due to the symmetry of the vibrations.

The two spectra are normalised to the 600 cm^{-1} peak. As expected, the two modes at low wavenumbers show a noticeable decrease in intensity since they have an E' symmetry. The 651 cm^{-1} peak displays a dramatic intensity drop therefore it must have the A_1' symmetry. The two small peaks on either side of the 600 cm^{-1} band are barely noticeable. However, the spectra were normalised to the 600 cm^{-1} mode and all the peaks other than that one show a decrease in intensity. Thus that peak is the E'' mode which according to its symmetry should not show any intensity decrease from VV to VH. Consequently, the remaining two peaks on either side of the 600 cm^{-1} band have a E' symmetry.

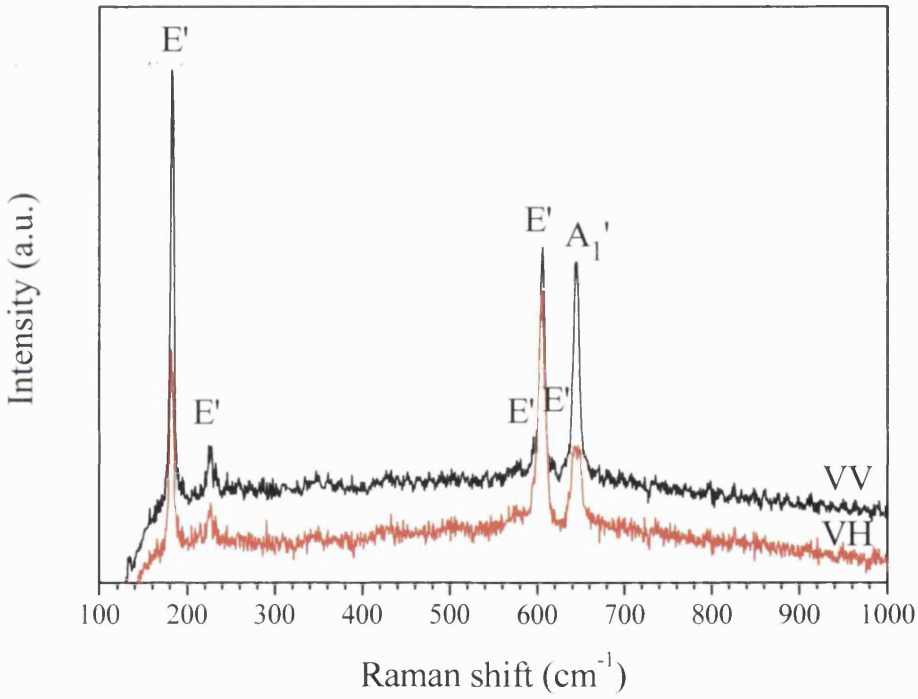

Figure 6-2 Polarised Raman spectra of ε-TaN collected using a 633 nm wavelength. The top spectrum in black was collected with the incident laser vertically polarised and the scattering was collected in the vertical polarisation. The bottom spectrum (in red) was collected with an incident laser vertically polarised and only the horizontally polarised signal was collected.

6.2.2. Raman spectroscopic study of δ-MoN

Prediction of Raman peaks activity of δ-MoN

Space group: $P6_3mc$ (C_{6v}^4)

Structure: $Z = 8$
Mo1: 2a (C_{3v})
Mo2: 6c (C_s)
N_1: 2b (C_{3v})
N_2: 6c (C_s)

Number of expected modes:

$N = 3n - 3 = 3 \times 16 - 3 = 45$ (with 3 acoustic modes corresponding to translations in the crystal)

C_{6v}	C_{3v} (σ_v)	C_S (σ_v)
A_1	A_1	A'
A_2	A_2	A''
B_1	A_1	A'
B_2	A_2	A''
E_1	E	A'+A''
E_2	E	A'+A''

2 x 6 atoms in C_s :

C_s	E	σ_h		
A'	1	1	T_x, T_y, R_z	α_{xx}, α_{yy}, α_{zz}, α_{xy}
A''	1	-1	T_z, R_x, R_y	α_{xz}, α_{yz}

C_s		C_{6v}						
A'	→	A_1	2	2	1	1	2	2
	→	B_1	2	2	2	2	1	1
A''	→	A_2	2	1	1	2	1	2
	→	B_2	2	1	2	1	2	1
A'+A''	→	E_1	1+1	2+1	2+1	3	3	3
	→	E_2	1+1	2+1	1+2	3	3	3

The red column indicates the chosen combination among all the possible combinations.
thus : $4 A_1 + 4 B_1 + 2 A_2 + 2 B_2 + 6 E_1 + 6 E_2$ (N and Mo contributions)

2 x 2 atoms in C_{3v} :

C_{3v}	E	$2C_3$	$2\sigma_v$		
A_1	1	1	1	T_z	$\alpha_{xx}+\alpha_{yy}$, α_{zz}
A_2	1	1	-1	R_z	
E	2	-1	0	(T_x, T_y); (R_x, R_y)	($\alpha_{xx}+\alpha_{yy}$, α_{xy}), (α_{xz}, α_{yz})

C_{3v}		C_{6v}
A_1	→	A_1
	→	B1
E	→	E_1
	→	E_2

Thus : $2 A_1 + 2B_1 + 2 E_1 + 2 E_2$ (N and Mo contributions)

C_{6v}	E	$2C_6$	$2C_3$	C_2	$3\sigma_v$	$3\sigma_d$		
A_1	1	1	1	1	1	1	T_z	$\alpha_{xx}+\alpha_{yy}$, α_{zz}
A_2	1	1	1	1	-1	-1	R_z	
B_1	1	-1	1	-1	1	-1		
B_2	1	-1	1	-1	-1	1		
E_1	2	1	-1	-2	0	0	(T_x, T_y); (R_x, R_y)	(α_{xz}, α_{yz})
E_2	2	-1	-1	2	0	0		($\alpha_{xx}+\alpha_{yy}$, α_{xy})

Total:

$\Gamma_{total} = 6 A_1 + 6 B_1 + 2 A_2 + 2 B_2 + 8 E_1 + 8 E_2$

$\Gamma_{acoustic} = A_1 + 2\ E_1$

$\Gamma_{optic} = 5\ A_1 + 6\ B_1 + 2\ A_2 + 2\ B_2 + 6\ E_1 + 8\ E_2$

$\Gamma_{Raman} = 5\ A_1 + 6\ E_1 + 8\ E_2$

Thus, there are 19 Raman active modes expected.

As shown above, there are 19 predicted Raman active modes for δ-MoN. The spectra recorded do not show that many (figure 6-3). We can resolve 8 peaks, including the low wavenumber peak recorded at around 160 cm^{-1} using the green laser (λ = 514.5 nm). There are significant variations in the peak relative intensities as a function of the exciting wavelength. These differences are due to the fact that the 514.5 nm incident light is vertically polarised and the 633 nm light is horizontally polarised. Therefore, due to the strong polarisation effect of the spectrometer gratings, some strong changes in intensity can occur. The combination of spectra collected with the green Ar^+ laser and red HeNe laser allows the identification of more peaks (figure 6-5).

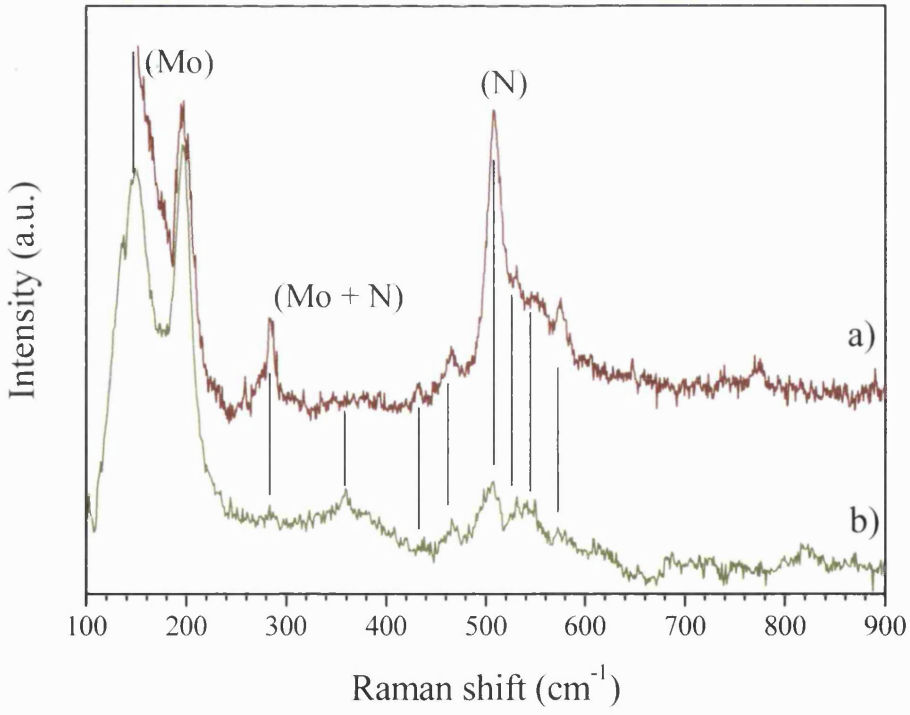

Figure 6-3 Raman spectra of δ-MoN at 3.0 GPa using a) the HeNe (λ = 633 nm) laser and b) the Ar^+ (λ = 514.5 nm).

The pattern display a doublet in the low wavenumber region and four peaks in the high wavenumber region. Therefore, from this extend, the pattern is very similar to that of tantalum

nitride. Consequently, we assign the modes in the low wavenumber region to mostly Mo motions and the modes in the high wavenumber region to mainly N motions. The peaks between 300 and 500 cm^{-1} result from motions involving both Mo and N motions. Unlike in the TaN example, all the modes can come from either Mo or N as both atoms have the same local symmetry. Therefore, a peak assignment is not readily possible from a powder sample. Furthermore, the peaks are not sharp unlike in the TaN pattern.

The low wavenumber doublet is composed of one very broad peak centred at 150 cm^{-1} and a sharp peak at 200 cm^{-1}. Those two peaks are mainly resulting from the Mo motions.

The rest of the spectrum is extremely weak in the patterns collected with the 514.5 nm wavelength, but it is more intense using the 633 nm wavelength. The third peak occurs just below 300 cm^{-1}. That peak is the last one that can be assigned to mainly Mo motions. In the high wavenumber part of the spectrum, the patterns display a weak sharp peak at 430 cm^{-1} which does not change in wavenumber with applied pressure. Although this peak is observed in all the patterns collected with the HeNe laser it might not come from the sample, as it shows no shift with pressure. Finally, the pattern shows a succession of four unresolved peaks. Those peaks show a large shift with pressure (figure 6-4). These vibrations are most likely to result from N motions.

In summary, the δ-MoN Raman spectrum is extremely broad and not resolved for most part. The broadness is due the metallic character of the sample. Furthermore, the pattern shows some similarities with that of TaN with two groups of peaks at high and low wavenumbers.

6.2.2.1. Study of δ-MoN at high pressure

As previously shown by X-ray diffraction, the cold compression of δ-MoN does not result in any phase transition or structural modification up to 80 GPa. This observation was repeated using Raman spectroscopy in the diamond anvil cell. In order to perform Raman spectroscopy on the semi metallic molybdenum nitride sample at high pressure it was necessary to use a Raman transparent pressure medium such as argon. Thus, the experiment was performed with a sample a δ-MoN within an argon pressure medium cryogenically loaded into the DAC. The gasket was made of rhenium and the gasket hole was about 90 μm. It was possible to collect Raman spectra of the sample up to 80 GPa.

The Raman scattering of δ-MoN is extremely weak and required long collection time from 30 to 60 minutes using the 633 nm wavelength of the HeNe laser. Some selected spectra a presented figure 6-4.

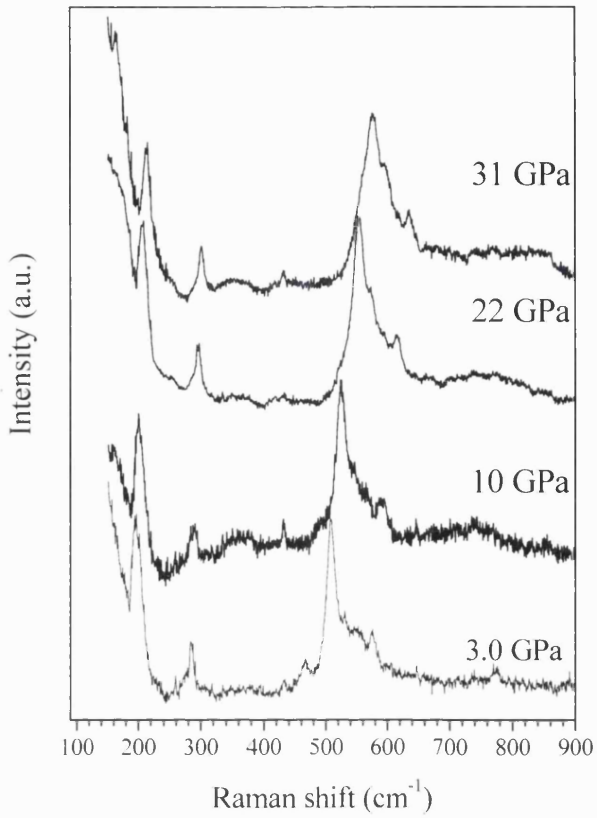

Figure 6-4 Raman spectra of δ-MoN at high pressure collected using a red (λ = 633 nm) HeNe laser excitation line.

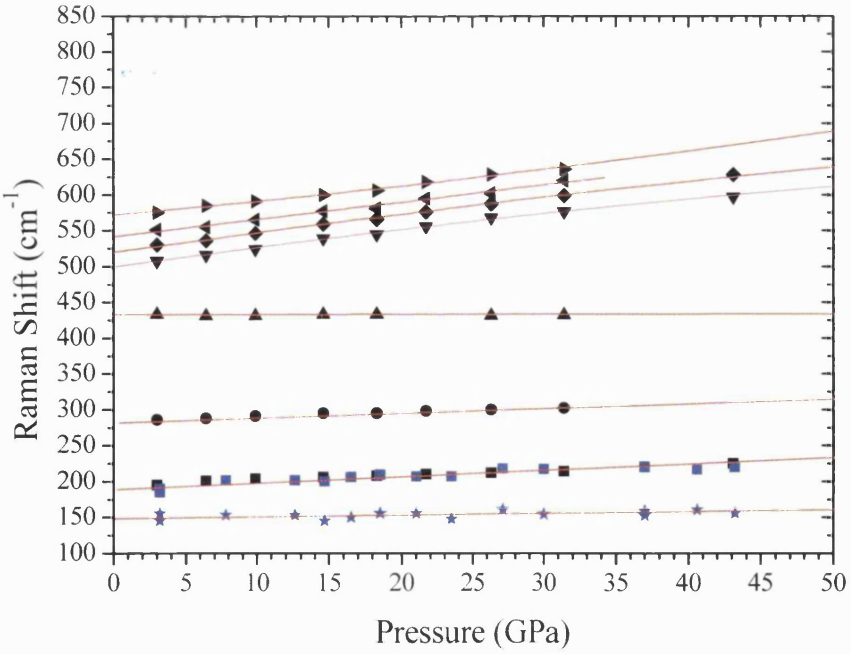

Figure 6-5 Raman shift of δ-MoN as a function of pressure. We display in black the data collected in the experiments performed using the HeNe laser (λ = 633 nm) and in blue are the data collected using the Ar^{+} laser (λ = 514.5 nm).

6.2.2.2. Study of δ-MoN after laser heating at high pressure

We collected some Raman spectra of the sample after laser heating. The spectra show no significant difference apart from a slight sharpening of the Raman peaks (figure 6-6). Thus no structural changes occurred in this case.

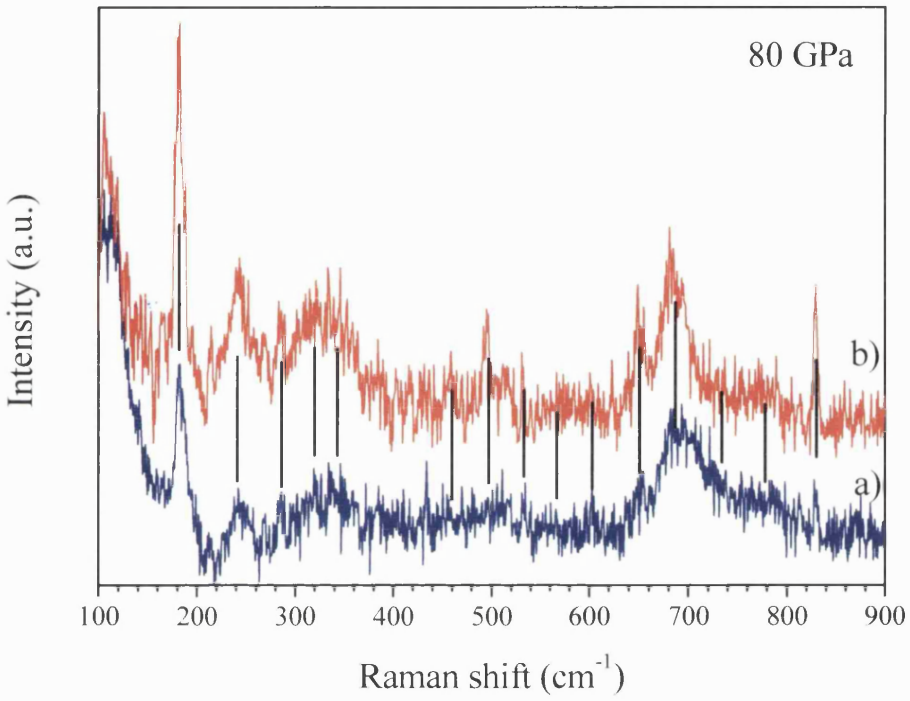

Figure 6-6 Raman spectra of δ-MoN before (in black) and after laser heating (in red) at 80 GPa.

6.3. Cubic transition metal nitrides

The cubic B1 structured transition metal nitrides are a large class of widely used materials. However, the factor group analysis predicts that B1 structured material should not have any Raman active mode. Nonetheless, transition metal nitrides and in particular titanium nitride and vanadium nitride are usually deficient in nitrogen. The presence of non-crystallographically ordered vacancies breaks the vibrational coherence resulting in the observation of the phonon density of states in the Raman scattering.

Factor group analysis of B1 structured transition metal nitride MN

Space group: Fm3m (O_h^5)

Structure Z = 4
M: 4a (O_h)
N: 4b (O_h)

Number of expected modes:
N = 3n -3 = 3*2 – 3 = 3 (with 3 acoustic modes)

O_h	E	$8C_3$	$3C_2$	$6C_4$	$6C_2'$	i	$8S_6$	$3\sigma_h$	$6S_4$	$6\sigma_d$		
A_{1g}	1	1	1	1	1	1	1	1	1	1		$\alpha_{xx}+\alpha_{yy}, \alpha_{zz}$
A_{2g}	1	1	1	-1	-1	1	1	1	-1	-1		
E_g	2	-1	2	0	0	2	-1	2	0	0		$\alpha_{xx}+\alpha_{yy}-\alpha_{zz}, \alpha_{xx}-\alpha_{yy}$
T_{1g}	3	0	-1	1	-1	3	0	-1	1	-1	(R_x,R_y,R_z)	
T_{2g}	3	0	-1	-1	1	3	0	-1	-1	1		$\alpha_{xy}, \alpha_{xz}, \alpha_{yz}$
A_{1u}	1	1	1	1	1	-1	-1	-1	-1	-1		
A_{2u}	1	1	1	-1	-1	-1	-1	-1	1	1		
T_u	2	-1	2	0	0	-2	1	-2	0	0		
T_{1u}	3	0	-1	1	-1	-3	0	1	-1	1	(T_x, T_y,T_z)	
T_{2u}	3	0	-1	-1	1	-3	0	1	1	-1		

Γ_{optics} $= 2\ T_{1u} - 1\ T_{1u}$
$= T_{1u}$
Γ_{Raman} = none

Thus there are 0 Raman active modes.

6.3.1. Raman spectroscopic study of titanium nitride

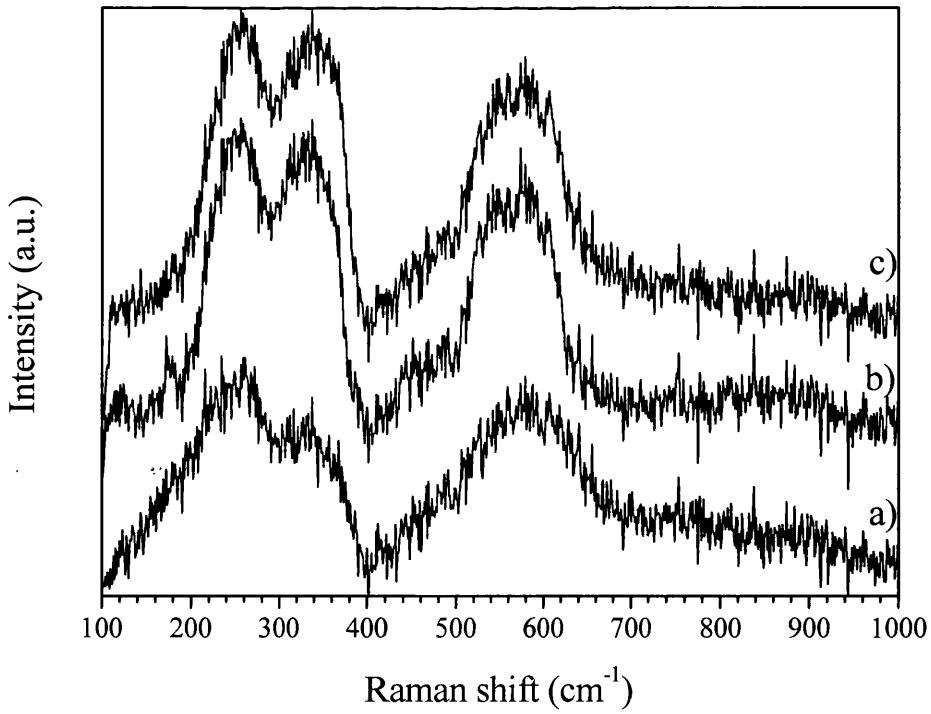

Figure 6-7 Raman spectra of titanium nitrides with three nitrogen contents. From the bottom to the top: a) $TiN_{0.59}$, b) $TiN_{0.80}$ and c) $TiN_{0.88}$.

Figure 6-7 Raman spectra of titanium nitrides with three nitrogen contents. From the bottom to the top: a) $TiN_{0.59}$, b) $TiN_{0.80}$ and c) $TiN_{0.88}$. present the Raman spectrum of three compositions of titanium nitride ranging from $TiN_{0.59}$ to $TiN_{0.88}$. The sample were generously sent to us by M. MacKenzie from the university of Glasgow. The samples are sintered and can withhold more laser power than the powdered sample bought form Alpha Aesar. The spectra were collected for 1 hour using the 514.5 nm wavelength of a Ar^+ laser with a power of about 1 mW.

There are phonon density of state reported in the literature for TiN (figure 6-9) [145]. A close comparison of the phonon density of states measured using inelastic neutron scattering with the Raman spectra collected on titanium nitride samples shows a very similar pattern. In fact the not only the shape of the pattern is similar but also the energy of the phonons.

For example, the phonon density of state of TiN measured using neutron shows a broad peak from 200 up to 350 cm^{-1} followed by a gap and then a peak centred on approximately 570 cm^{-1}. The first broad feature corresponds to the transverse and longitudinal acoustic modes (TA and LA respectively) and the second feature corresponds to the transversal and longitudinal optical modes (TO and LO respectively)[145]. The Raman spectrum of $TiN_{0.88}$ display a broad feature with two maxima from 200 up to 370 cm^{-1} followed by on broad peak centred at 570 cm^{-1}. Thus not only the shapes of the two spectra are extremely similar but also the positions of the peaks are identical. In conclusion, the spectra recorded using Raman spectroscopy techniques are in fact the phonon density of state of titanium nitrides. However, the acoustic modes show a more defined separation between the translational and longitudinal modes in the Raman spectra than in the neutron scattering experiment.

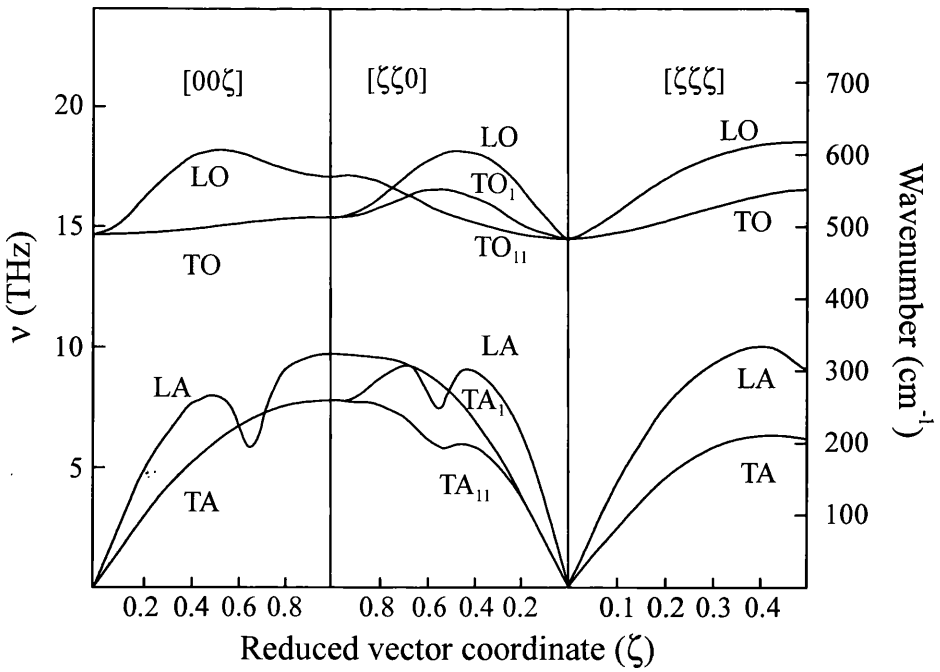

Figure 6-8 TiN phonon dispersion curves. Diagram adapted from reference [146]

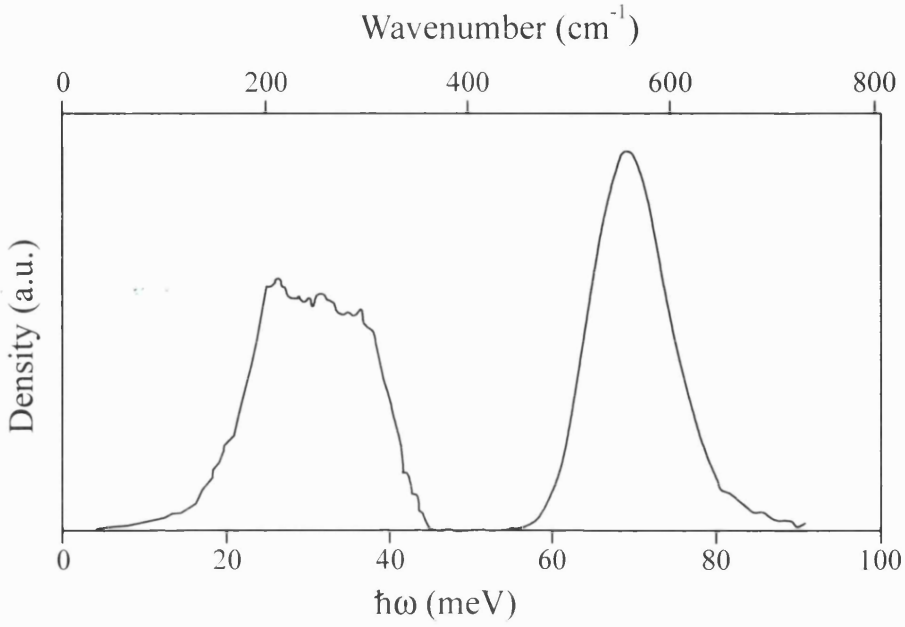

Figure 6-9 Phonon density of states of TiN measured using inelastic neutron scattering by Rieder and Drexel [145]. They subtracted the two-phonon interactions from acoustic – acoustic and optical – optical modes.

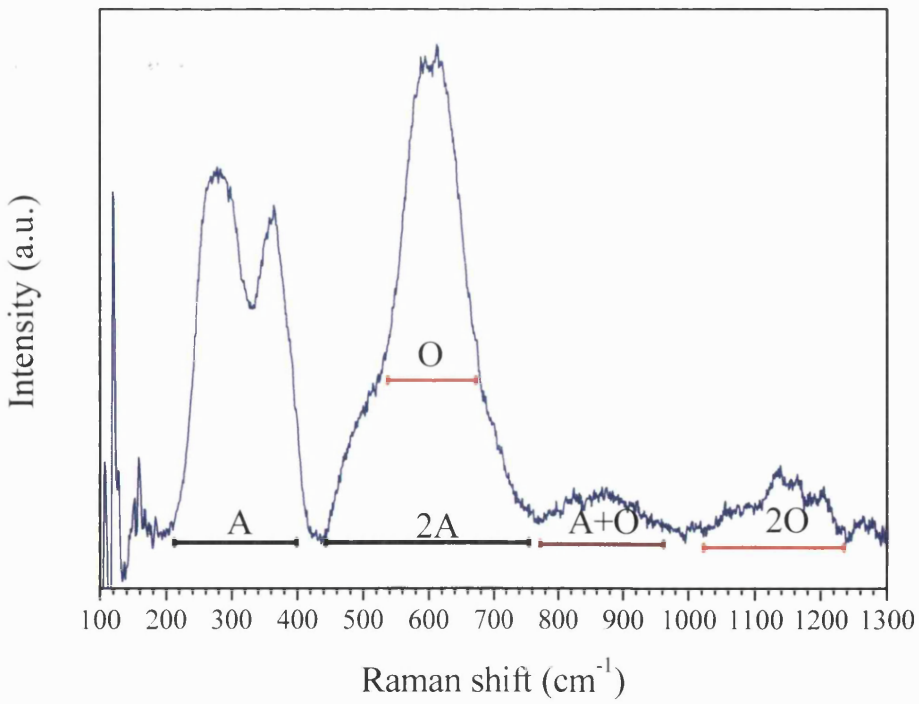

Figure 6-10 Raman spectrum of TiN at 1.7 GPa (same spectrum as in figure 6-11) with subtracted background showing the detail of the peaks assignment. A indicates the acoustic modes and O indicated the optical modes.

A closer look at the spectra of titanium nitride at three different compositions shows that there are some slight changes. First of all, the spectra of $TiN_{0.88}$ to $TiN_{0.80}$ are perfectly identical. A significant broadening occurs at the $TiN_{0.59}$ composition. At that composition almost 40% of the nitrogen sites are vacant resulting in a disordering of the structure.

The presence of other features in the spectra in particular between the acoustic and optical modes can be understood in several ways. Rieder and Drexel explain the feature as coming from surface modes [145], Spengler and Kaiser explain it as a two phonon interaction [147]. The later explanation is illustrated figure 6-10. Nevertheless, the presence of the extra peaks could also be the result from significant amount of oxygen impurity in the sample. In particular, if the extra features in Raman spectrum are from a two phonon interaction, the intensity is dramatically increased from the neutron scattering experiment to the Raman spectrum.

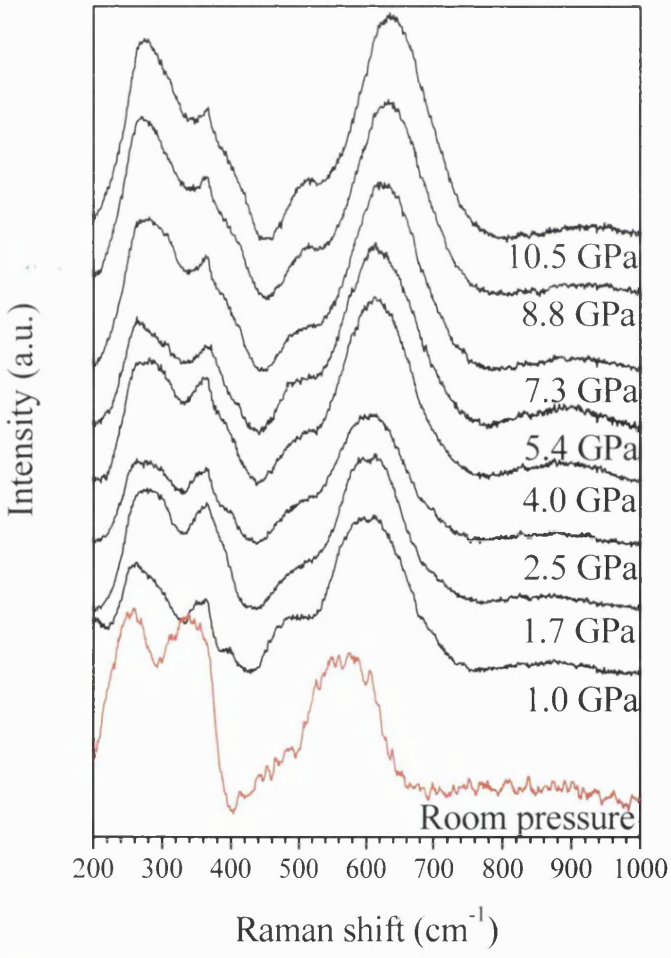

Figure 6-11 Raman spectra of TiN at high pressure. The spectra in red is that of the powdered sample taken at room pressure outside the DAC.

The observation of the spectra of titanium nitride at high pressure (figure 6-11) was performed in a diamond anvil cell in a argon pressure medium. The sample was pressed from a powder

sample from Alpha Aesar. The compacted sample was loaded in the cell ensuring that the sample was perfectly smooth and very parallel to the culet of the diamond. The orientation and the roughness of the sample surface were optimised in order to maximise the Raman signal. In fact, the experiment showed that the sample could withstand much higher laser power once in the diamond anvil cell without decomposing or oxidising. Spectra were collected from room pressure up to just above 10 GPa.

The frequencies of the TA-LA branches do not seem to be affected by pressure; however, there is a regular positive shift with pressure of the optical branches. The shift is also accompanied with a significant sharpening of the peak. The sharpening can result from a recrystallisation of the sample with migration of the defects toward the grain boundary, thus sharpening the optical modes. The positive shift indicates a Ti-N vibration hardening. In fact, as shown in the previous chapter, the Ti-N bond is compressed with increase of pressure as the volume of TiN decreases.

6.3.2. Raman spectroscopic study of vanadium nitrides.

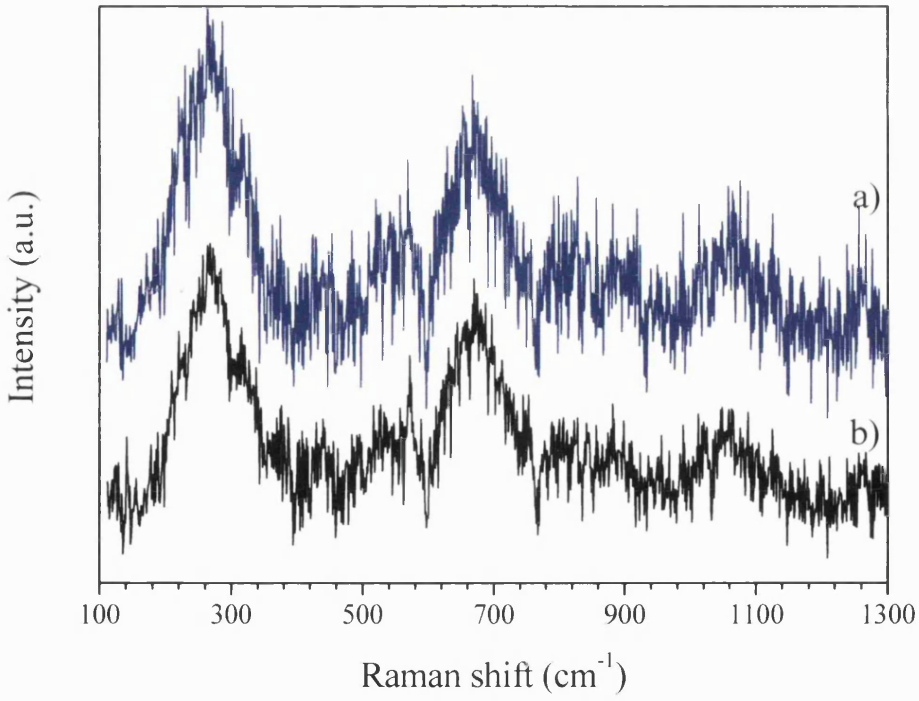

Figure 6-12 Raman spectra of vanadium nitride at two compositions; $VN_{0.97}$ (a) and $VN_{0.93}$ (b).

Vanadium nitride is extremely similar in properties and structure to titanium nitride. We performed Raman spectroscopy on two compositions of vanadium nitride provided by by M. MacKenzie from the university of Glasgow. The Raman spectra are presented figure 6-12. The spectra are extremely similar to that of titanium nitride. However, there is not report of the

phonon density of state for vanadium nitride thus we cannot compare the spectra to it as previously performed for titanium nitride. Nevertheless, as the structure of vanadium nitride and titanium nitride are identical, it is useful to compare the spectra recorded for vanadium nitride to the phonon density of state of titanium.

First of all the spectra of vanadium nitride are much weaker than that of TiN. A linear background subtraction was performed on the spectra in order to render the diagram readable. Each spectrum was collected for two hours at about 1 mW of Ar^+ laser power at $\lambda = 514.5$ nm in order to obtain a usable Raman spectrum.

The Raman spectra figure 6-12 display two main peaks. The peak centred at 270 cm^{-1} correspond to the TA and LA branches and the peak centred at 670 cm^{-1} can be assigned to the TO and LO branches. A closer look at the 270 cm^{-1} feature shows a shoulder on the high wavenumber side at 320 cm^{-1}. The two peaks correspond to the two peaks observed for titanium nitride (TA and LA). In the titanium nitride spectrum the two peaks have the same intensity. In the vanadium nitride spectrum the TA peak centred at 265 cm^{-1} is 30 % more intense than the LA peak centred on 320 cm^{-1}. Thus the shape of the acoustic branches of vanadium nitride is slightly different to that of titanium nitride. The LA branch appears to have a shallower slope than that of titanium nitride. This difference could result in a difference on the sound velocity between titanium nitride and vanadium nitride.

The optical modes of vanadium nitride are very similar to that of titanium nitride although they are shifted 100 cm^{-1} higher. On the contrary, the acoustic modes do not display any measurable shift from titanium nitride to vanadium nitride. The shift between the acoustic and optical modes is related for one part to the difference in weight between the two atoms. The weight of Ti and V are extremely similar, therefore the large shift is not solely related to the increase in the atomic weight difference. The width of the gap is also strongly correlated to the oxidation state of the metal. The number of bonding and anti-bonding electrons changes the width of the gap as it change the amount of correlation between the phonons and the electronic levels.

Like in the titanium nitride spectrum, the vanadium nitride spectra display a feature between the acoustic and optical modes. Those extra features have the same origins.

6.3.3. Raman spectroscopic study of γ-Mo_2N

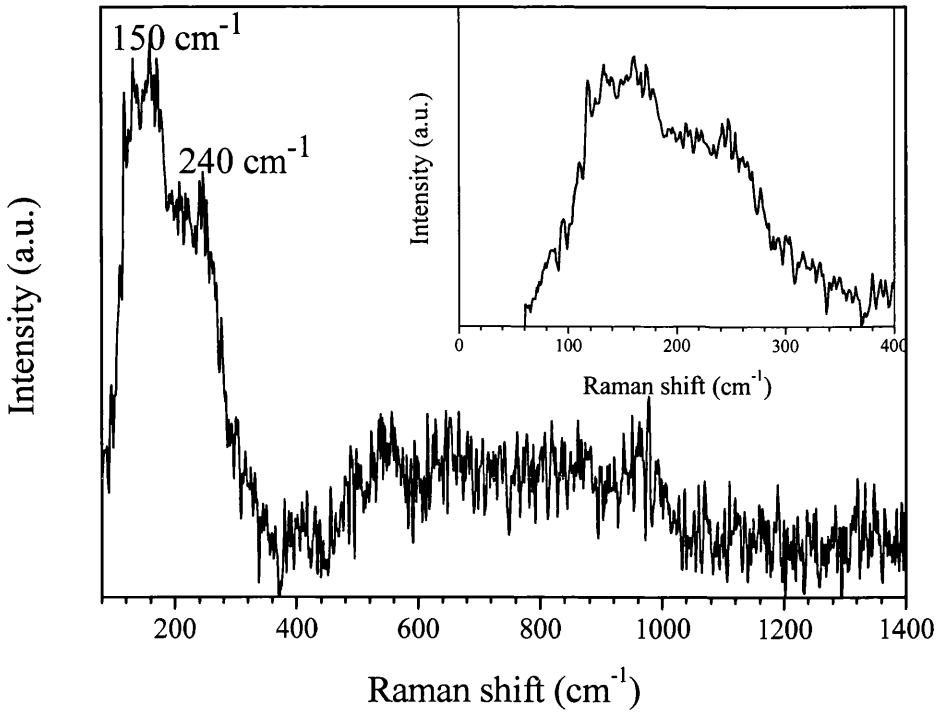

Figure 6-13 Raman spectrum of molybdenum nitride from Alpha Aesar. The broad feature between 500 and 1000 cm^{-1} is a combination of the second order acoustic modes and the first order optical modes.

Figure 6-13 presents a Raman spectrum taken on the as bought sample of molybdenum nitride from Alpha Aesar. The sample consists in a mixture of γ-Mo_2N and Mo. The Raman spectrum mainly shows one large broad feature with a second broad feature appearing as a shoulder. The first feature is centred on 150 cm^{-1} and the second one is centred on 230 cm^{-1}. Next to those intense peaks is a very weak and broad feature between 530 and 980 cm^{-1}.

The broad features are characteristic of a density of states like spectrum. In fact, the shape of the Raman spectrum clearly shows the density of states of a B1 structured material in particular in the low wavenumber region. Although there is no report of phonon density of states for γ-Mo_2N, there are reports of phonon density of states for δ-NbN_{1-x} which has the same B1 type structure with a range of compositions depending upon the amount of N vacancies. Consequently, the phonon density of states for both those materials should be very similar. The data on the niobium nitride density of states are only available in the low energy region, below 40 meV (below 350 cm^{-1}). Niobium nitride phonon density of states presents two broad features centred on 150 cm^{-1} and 210 cm^{-1} (figure 6-14). A comparison between the spectrum figure 6-13 and figure 6-14 shows that the two materials have extremely similar density of states.

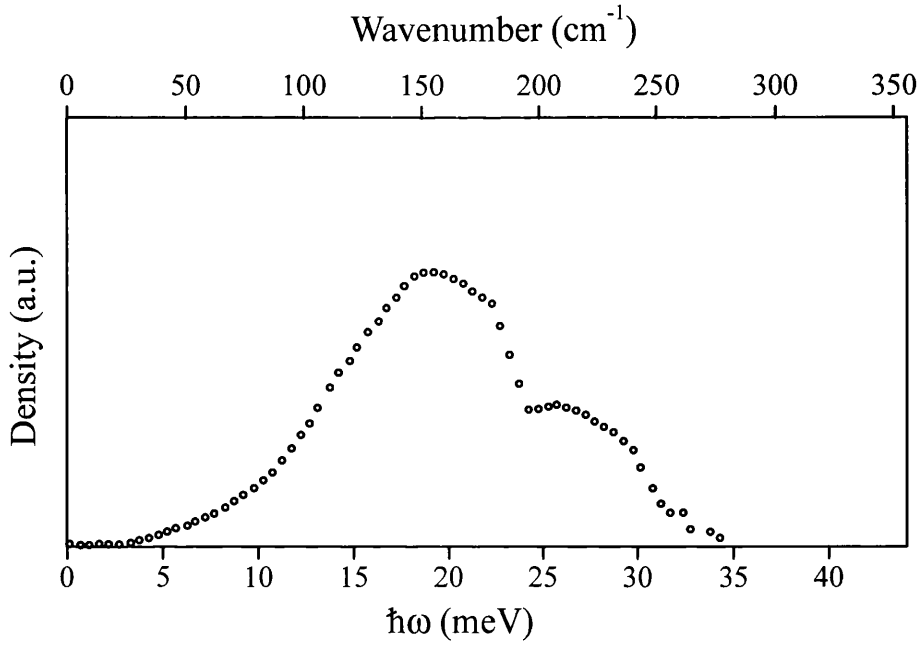

Figure 6-14 Phonon density of states for δ-$NbN_{0.84}$ [146].

In fact, the phonon density of states of niobium nitride is only represented for the acoustic modes and not the optical modes. The Raman spectrum of γ-Mo_2N shows both the acoustic and optical modes. Comparatively to the previous two transition metal nitrides where the optical modes were displaying a sharp strong peak, γ-Mo_2N presents a very broad peak in the optical modes region. This indicates that the optical branches show more dispersion in energy than in the previous nitrides.

6.4. Conclusions

In summary, we have seen that it is possible to collect Raman spectra of most transition metal nitrides even at high pressure. The data also show strong similarities between the spectra of hexagonal transition metal nitrides where there is a small group of vibrations at low wavenumbers (below 300 cm^{-1}) and a larger group of vibration at higher wavenumbers (above 500 cm^{-1}). The low energy vibrations are characteristic of the metal motions and the high energy vibrations are characteristic of the nitrogen motions. We also performed a polarised Raman study on a powder sample of ε-TaN in order to successfully assign all the vibrational modes.

In the second part, we performed Raman studies on rocksalt structured transition metal nitrides. The results showed that the spectra of titanium nitride, vanadium nitride and γ-Mo_2N are extremely similar and are in fact density of states. In the case of titanium nitride, it was showed that the spectrum starts to display a significant amount of broadening at composition of $TiN_{0.59}$. The compressional study on TiN showed that the acoustic modes do not shift with pressure and

the optical modes show a small positive shift. Therefore, there is a hardening of the Ti – N bond upon pressurisation.

Finally, the study of γ-Mo_2N showed that the shape of the phonon density of state is preserved even at very low nitrogen content. In particular the acoustic part is still displaying an intense doublet. However, the optical part of the spectrum has become extremely weak and significantly broader. Thus, there are some significant changes occurring in the structure of the optical branches.

Chapter 7. General Conclusions

7.1. Group IV nitrides

At high pressure, both silicon nitride and germanium nitride transform into a spinel phase upon heating at a pressure above 12-15 GPa and temperature above 1500 °C. The compressibility study of silicon nitride showed that γ-Si_3N_4 is highly incompressible and has a bulk modulus K_0 = 308(5) GPa and a pressure derivative K_0' = 4.0(2). The large value of the bulk modulus indicates that silicon nitride spinel is likely to be a high hardness material.

Since the high pressure phases of silicon nitride and germanium nitride are identical, we also investigated the possibility of intermediate phases in the γ-Ge_3N_4 – γ-Si_3N_4 system. The synthesis experiments led to the preparation of the first ternary spinel nitride compound, $GeSi_2N_4$. This is a normal spinel with Si and Ge atoms respectively octahedrally and tetrahedrally coordinated to the N atoms. We also observed a Ge-rich solid solution close to $Ge_{2.7}Si_{0.3}N_4$. Although results are not yet sufficient to fully determine the phase diagram of the Ge_3N_4 – Si_3N_4 system in the spinel structure, we have determined that there is a domain where $GeSi_2N_4$ and a germanium rich nitride coexist.

The laser heating diamond anvil cell study of the end members of this system using Raman spectroscopy showed that there are variations in the spinel nitride stoichiometry as a function of temperature. The results from syntheses at temperature above 2000 K at about 15 GPa indicate that the synthesis product is often nitrogen deficient. The Raman spectra of nitrogen deficient spinels display extra features, and the intensity of those features increases with the amount of nitrogen vacancies.

We also studied the behaviour of β-Ge_3N_4 at high pressure upon metastable compression at room temperature. The previous theoretical work from Dong *et al.* suggested that either one first order phase transition or two second order phase transitions would occur at pressures around 20 GPa. The X-ray diffraction study showed a 5-7 % volume drop at a pressure of about 20 GPa. At that pressure there is a large decrease in the value of the a parameter and no change in the length of the c parameter. The transition corresponds to atomic displacements within the hexagonal basal plane. The changes related to the phase transition are movement of the nitrogen atoms away from the centre of the triangle formed by the Ge atoms in a direction orthogonal to the plan formed by those Ge atoms. The phase transition was also observed using Raman

spectroscopy. We have termed the new phase δ-Ge_3N_4. Finally, we also compared those results with the ones Zerr [140] recently published on cold compression of β-Si_3N_4 and concluded that the behaviour of both β-Ge_3N_4 and β-Si_3N_4 are identical. The original interpretation presented by Zerr in his article suggesting that β-Si_3N_4 transformed into a post-spinel phase is in fact erroneous; it is most likely that the high pressure form of Si_3N_4 is identical to the δ-Ge_3N_4 polymorph studied here.

Finally, upon further compression above 45 GPa, δ-Ge_3N_4 and α-Ge_3N_4 become amorphous. We observed the amorphisation using both X-ray diffraction and Raman spectroscopy. At that pressure, the structure is based on Ge atoms tetrahedrally coordinated to N atoms. At 45 GPa, this coordination scheme can no longer accommodate the compression and a significant amount of bond breaking occurs to possibly form denser GeN_5 units. However, the system only reaches the amorphous state when the amount of energy available in the system is too low (no heating) to allow the transformation of germanium nitride into the spinel phase.

7.2. Summary of the results on transition metal nitrides

In the second part of the research, chapter 5 and 6, we studied some examples of transition metal nitrides at room pressure and high pressure. The examples were two molybdenum nitride phases, δ-MoN and γ-Mo_2N, TiN, TaN, Cr_2N and VN.

In a first part, we determined the bulk modulus of δ-MoN, γ-Mo_2N, TiN, TaN and Cr_2N. We determined that δ-MoN and TaN have extremely high bulk modulus values with $K_0 \sim 350$ GPa. Those materials are among the least compressible materials known. The compression studies also showed that TiN, γ-Mo_2N and Cr_2N also have very high bulk moduli, with values around 300 GPa. We also showed that upon room temperature compression, those nitrides do not undergo any phase transition in the pressure range of the experiments.

In a second part, we performed the first Raman spectroscopic study of two hexagonal nitrides: TaN and δ-MoN and three B1 structured nitrides: TiN, VN and MoN. These studies demonstrated strong similarities in the vibrational spectra of the two hexagonal materials even though they have different structures. We could assign all the Raman peaks in the TaN Raman spectrum. The hexagonal nitrides display a group of two peaks at low wavenumbers below about 300 cm^{-1} which results from mainly metal motions, and a group of a larger number of modes above 500 cm^{-1} which are resulting from mainly nitrogen motions. In the case of TaN, we did not observe any vibrational mode between those two regions. However, in the case of δ-MoN we observed additional weak features in that intermediate region. We observed the compressional behaviour of MoN using Raman spectroscopy and did not observed any phase

transition. Finally, we also performed a laser heating experiment at high pressure. Upon laser heating in an Ar pressure medium at 79 GPa, δ-MoN did not undergo any phase transition.

B1-structured materials do not possess any Raman active modes. Therefore, we did not originally expect to observe a first order Raman spectrum for those materials. However, Raman features are rendered active because of the presence of N defects. The B1 structured nitrides that we studied, TiN, VN and γ-Mo_2N, displayed a broad phonon density of states spectrum. The density of states obtained using Raman spectroscopy technique was identical to that previously measured using inelastic neutron scattering. We determined the pressure shift of the bands, and we observed no phase transitions, consistent with X-ray diffraction experiments.

References

[1] N. E. Brese, M. Okeeffe, Struct. Bond., ***79***, 307 (1992)
[2] F. J. DiSalvo, Science, ***247***, 649 (1990)
[3] S. T. Oyoma, *The chemistry of Transition Metal Carbides and Nitrides*, Blackie Academic & Professional, Glasgow, **1996**.
[4] O. Ambacher, J. Phys. D: Appl. Phys., ***31***, 2653 (1998)
[5] R. Niewa, F. J. DiSalvo, Chem. Mater., ***10***, 2733 (1998)
[6] R. Marchand, F. Tessier, F. J. DiSalvo, J. Mater. Chem., ***9***, 297 (1999)
[7] L. E. Toth, *Transition metal carbides and Nitrides, Vol. 7*, Academic Press, New York ; London, **1971**.
[8] J. Häglund, A. Fernández Guillernet, G. Grimvall, M. Körling, Phys. Rev. B, ***48***, 11685 (1993)
[9] D. H. Gregory, Dalton Perspectives, (1998)
[10] D. H. Gregory, Coordination Chemistry Reviews, ***215***, 301 (2001)
[11] E. Krobe, Angew. Chem.-Int. Edit., ***41***, 77 (2002)
[12] R. Juza, H. Hahn, Z. Anorg. Allg. Chem, ***244***, 125 (1940)
[13] R. Schwarz, A. Jeanmaire, Ber. Deut. Chem. Ges., ***65***, 1443 (1932)
[14] R. Schwarz, A. Jeanmaire, Ber. Deut. Chem. Ges., ***65***, 1662 (1932)
[15] N. Scotti, W. Kockelmann, J. Senker, S. Traßel, H. Jacobs, Z. Anorg. Allg. Chem, ***625***, 1435 (1999)
[16] N. E. Christensen, I. Corczyca, Phys. Rev. B, ***50***, 4397 (1994)
[17] N. Brese, M. O'Keeffe, Structure and Bonding, ***79***, 307 (1992)
[18] F. Lévy, P. Hones, P. E. Schmid, R. Sanjines, M. Diserens, C. Wiemer, Surf. Coat. Technol., ***121***, 284 (1999)
[19] S. Veprek, J. Vac. Sci. Technol. A, ***17***, 2401 (1999)
[20] V. V. Brazhkin, A. G. Lyapin, R. J. Hemley, Phil. Mag. A, ***82***, 231 (2002)
[21] F. A. Ponce, D. P. Bour, Nature, ***386***, 351 (1997)
[22] S. Nakamura, Semiconduct. Semimet., ***48***, 391 (1997)
[23] D. A. Papaconstantopoulos, W. E. Pickett, B. M. Klein, L. L. Boyer, Phys. Rev. B, ***31***, 752 (1985)
[24] *Handbook of Chemistry and Physics*, 71st ed., CRC Press, **1990**.
[25] B. Eck, R. Dronskowski, M. Takahashi, S. Kikkawa, J. Mater. Chem., ***9***, 1527 (1999)
[26] R. Ahuja, O. Eriksson, J. M. Wills, B. Johansson, Phys. Rev. B, ***53***, 3072 (1996)
[27] R. N. Katz, Science, ***208***, 841 (1980)
[28] A. R. West, *Solid State Chemistry and its applications*, Wiley, New York, **1989**.
[29] A. Kelly, N. H. MacMillan, *Strong Solids*, Oxford University Press, New York, **1986**.
[30] S. Wild, P. Grieveson, K. H. Jack, Spec. Ceram., ***5***, 385 (1972)
[31] K. Blegen, Spec. Ceram., ***6***, 223 (1975)
[32] K. Kato, Z. Inoue, K. Kijima, T. Yamane, J. Kawada, J. Am. Ceram. Soc., ***58***, 90 (1975)
[33] K. Kohatsu, J. W. McCauley, Mat. Res. Bull., ***9***, 917 (1974)
[34] S. N. Ruddlesden, P. Popper, Acta Cryst., ***11***, 465 (1958)

[35] R. Marchand, Y. Laurent, J. Lang, M. T. LeBihan, Acta Crystallographica B, ***25***, 2157 (1972)
[36] M. B. Kruger, J. H. Nguyen, Y. M. Li, W. A. Caldwell, M. H. Manghnani, R. Jeanloz, Phys. Rev. B, ***55***, 3456 (1997)
[37] R. Grün, Acta Cryst. B, ***35***, 800 (1979)
[38] P. Goodman, M. O'Keeffe, Acta Cryst. B, ***36***, 2891 (1980)
[39] Y. M. Li, M. B. Kruger, J. H. Nguyen, W. A. Caldwell, R. Jeanloz, Solid State Commun., ***103***, 107 (1997)
[40] S. D. Mo, L. Ouyang, W. Y. Ching, I. Tanaka, Y. Koyama, R. Riedel, Phys. Rev. Lett., ***83***, 5046 (1999)
[41] A. Zerr, G. Miehe, G. Serghiou, M. Schwarz, E. Kroke, R. Riedel, H. Fueß, P. Kroll, R. Boehler, Nature, ***400***, 340 (1999)
[42] T. Sekine, H. He, T. Kobayashi, M. Zhang, F. Xu, Appl. Phys. Lett., ***76***, 3706 (2000)
[43] M. Zhang, H. He, F. F. Xu, T. Sekine, T. Kobayashi, Y. Bando, J. Appl. Phys., ***88***, 3070 (2000)
[44] M. Schwarz, G. Miehe, A. Zerr, E. Kroke, B. T. Poe, H. Fueß, R. Riedel, Advanced Materials, ***12***, 883 (2000)
[45] J. Z. Jiang, K. Ståhl, R. W. Berg, D. J. Frost, T. J. Zhou, P. X. Shi, Europhys. Lett., ***51***, 62 (2000)
[46] E. Soignard, M. Somayazulu, J. Dong, O. F. Sankey, P. F. McMillan, J. Phys.: Condens. Matter, ***13***, 557 (2001)
[47] G. Serghiou, G. Miehe, O. Tschauner, A. Zerr, R. Boehler, J. Chem. Phys., ***111***, 4659 (1999)
[48] M. S. Somayazulu, K. Leinenweber, H. Hubert, P. F. McMillan, G. W. Wolf, In *AIRAPT-17,* ed.: M. H. Manghnani, H. Nellis, M. F. Nicol, University Press, Hyderabad, India, p. 663, (1999).
[49] K. Leinenweber, M. O'Keeffe, M. Somayazulu, H. Hubert, P. F. McMillan, G. W. Wolf, Chem. Eur. J., ***5***, 3076 (1999)
[50] S. K. Deb, J. Dong, H. Hubert, P. F. McMillan, O. F. Sankey, Solid State Commun., ***114***, 137 (2000)
[51] J. Dong, O. F. Sankey, S. K. Deb, P. F. McMillan, Phys. Rev. B, ***61***, 11979 (2000)
[52] J. E. Lowther, Phys. Rev. B, ***62***, 5 (2000)
[53] W. H. Bragg, Phil. Mag., ***30***, 305 (1915)
[54] S. Nishikawa, Proc. Math. Phys. Soc. Tokyo, ***8***, 199 (1915)
[55] K. E. Sickafus, J. M. Wills, N. W. Grimes, J. Am. Ceram. Soc., ***82***, 3279 (1999)
[56] M. Y. Saïdi, R. Koksang, J. Barker, J. Power Sources, ***58***, 145 (1996)
[57] W. P. Kilroy, S. Dallek, J. Zaykoski, J. Power Sources, ***105***, 75 (2002)
[58] G. Steigmann, Acta Cryst., ***23***, 142 (1967)
[59] R. Neigel, H. D. Lutz, Zeitschrift fuer Kristallographie, ***211***, 927 (1996)
[60] A. Payer, A. Kamalowski, R. Schoellhorn, J. Alloys Comp., ***185***, 89 (1992)
[61] Z. Klencsár, E. Kuzmann, Z. Homonnay, A. Vértes, A. Simopoulos, E. Devlin, G. Kallias, J. Phys. Chem. Solids, ***64***, 325 (2003)
[62] A. P. Ramirez, R. J. Cava, J. Krajewski, Nature, ***386***, 156 (1997)
[63] P. Kurske, W. Schafer, H. D. Lutz, Mat. Res. Bull., ***23***, 1805 (1988)
[64] M. Sassmannshausen, I. Solinas, H. D. Lutz, Zeitschrift fuer Kristallographie, ***211***, 819 (1996)
[65] K. J. Range, H. J. Huebner, Zeitschrift fuer Naturforschund, ***38***, 155 (1983)
[66] A. Zerr, M. Kempf, M. Schwarz, E. Krobe, M. Göken, R. Riedel, J. Am. Ceram. Soc., ***85***, 86 (2002)
[67] A. Y. Liu, M. L. Cohen, Phys. Rev. B, ***41***, 10727 (1990)

[68] Z. A. Weinberg, R. A. Pollak, Appl. Phys. Lett., ***27***, 254 (1975)
[69] R. Karcher, L. Ley, R. L. Johnson, Phys. Rev. B, ***30***, 1896 (1984)
[70] R. D. Carson, S. E. Schnatterly, Phys. Rev. B, ***33***, 2432 (1986)
[71] A. Iqbal, W. B. Jackson, C. C. Tsai, J. W. Allen, C. W. Bates, J. Appl. Phys., ***61***, 2947 (1987)
[72] H. He, T. Sekine, T. Kobayashi, K. Kimoto, J. Appl. Phys., ***90***, 4403 (2001)
[73] I. N. Remediakis, E. Kaxiras, Phys. Rev. B, ***59***, 5536 (1999)
[74] W. Y. Ching, S.-D. Mo, I. Tanaka, M. Yoshiya, Phys. Rev. B, ***63***, 064102 (2001)
[75] I. L. Khodakovsky, M. I. Petaev, Geokhimiya, 329 (1981)
[76] J. Nagamatsu, N. Nakagawa, T. Muranaka, Y. Zenitani, J. Akanitsu, Nature, ***410***, 63 (2002)
[77] H. K. Mao, P. M. Bell, J. Appl. Phys., ***49***, 3276 (1978)
[78] G. Brauer, J. Weidlein, J. Strähle, Z. Anorg. Allg. Chem, ***348***, 298 (1966)
[79] J. Strähle, Z. Anorg. Allg. Chem, ***402***, 47 (1973)
[80] N. E. Brese, M. O'Keeffe, P. Rauch, D. F. J, Acta Cryst. C, ***47***, 2291 (1991)
[81] A. L. Bowman, G. P. Arnold, Acta Cryst. B, ***27***, 243 (1971)
[82] M. Lerch, E. Füglein, J. Wrba, Z. Anorg. Allg. Chem, ***622***, 367 (1996)
[83] A. Zerr, G. Miehe, R. Riedel, Nature Materials, ***2***, 185 (2003)
[84] Z. You-Xiang, H. Shou-An, Solid State Commun., ***45***, 281 (1983)
[85] B. T. Matthias, Phys. Rev., ***92***, 874 (1953)
[86] B. T. Matthias, J. K. Hulm, Phys. Rev., ***87***, 799 (1952)
[87] X. Zhao, K.-J. Range, J. Alloys Comp., ***296***, 72 (2000)
[88] A. Bezinge, K. Yvon, J. Muller, Solid State Commun., ***63***, 141 (1987)
[89] J. M. Vandenberg, B. T. Matthias, Mat. Res. Bull., ***9***, 1085 (1974)
[90] G. L. W. Hart, B. M. Klein, Phys. Rev. B, ***61***, 3151 (2000)
[91] R. Marchand, X. Gouin, F. Tessier, Y. Laurent, In *The chemistry of Transition Metal Carbides and Nitrides* (Ed.: S. T. Oyoma), Blackie Academic & Professional, Glasgow, p. 252, (1996).
[92] R. J. Hemley, H. K. Mao, Mineral. Mag., ***66***, 791 (2002)
[93] H. K. Mao, R. J. Hemley, Phil. Trans. R. Soc. Lond. A, ***354***, 1315 (1996)
[94] R. J. Nelmes, M. I. McMahon, J. S. Loveday, S. Rekhi, Phys. Rev. Lett., ***88***, 155503 (2002)
[95] E. Soignard, M. S. Somayazulu, H.-K. Mao, J. Dong, O. F. Sankey, P. F. McMillan, Solid State Commun., ***120***, 237 (2001)
[96] P. F. McMillan, Nature Materials, ***1***, 19 (2002)
[97] P. F. McMillan, In *International School of Physics "Enrico Fermi" Course CXLVII: High Pressure Phenomena,* ed.: R. J. Hemley, G. L. Chiarotti, M. Bernasconi, L. Ulvi, OIS Press, Amsterdam, p. 477, (2001).
[98] H. Wiedemann, *Synchrotron Radiation*, Springer-Verlag, Berlin, **2003**.
[99] R. C. A. Catlow, G. Sankar, In *Microscopic properties and Process in Minerals* (Ed.: K. W. a. R. Catlow), p. 145, (1999).
[100] A. Dadashev, M. P. Pasternak, G. K. Rozenberg, R. D. Taylor, Rev. Sci. Instrum., *77*, 2633 (2001)
[101] A. Jephcoat, S. P. Besedin, Phil. Trans. R. Soc. Lond. A, ***354***, 1333 (1996)
[102] A. P. Hammersley, S. O. Svensson, M. Hanfland, A. N. Fitch, D. Häusermann, High Pressure Res., ***14***, 235 (1996)
[103] G. Landsberg, L. Mandelstam, Naturwissenschaften, ***16***, 557 (1928)
[104] C. V. Raman, K. S. Krishnan, Nature, ***121***, 501 (1928)
[105] C. V. Raman, K. S. Krishnan, Nature, ***121***, 711 (1928)

[106] W. Fateley, G., F. R. Dollish, N. T. McDevitt, F. F. Bentley, *Infrared and Raman Selection Rules for Molecular and Lattice Vibrations*, John Wiley & Sons Inc., New York, **1972**.
[107] P. W. Bridgman, Phys. Rev., ***48***, 825 (1935)
[108] P. W. Bridgman, Proc. Am. Acad. Arts Sci., ***81***, 167 (1952)
[109] R. J. Hemley, H. K. Mao, G. Shen, J. Badro, P. Gillet, M. Hanfland, D. Hausermann, Science, ***276***, 1242 (1997)
[110] R. A. Forman, G. J. Piermarini, J. Dean Barnett, S. Block, Science, ***176***, 284 (1972)
[111] H. K. Mao, P. M. Bell, Science, ***191***, 851 (1976)
[112] H. K. Mao, J. Xu, P. M. Bell, J. Geophys. Res., ***91***, 4673 (1986)
[113] W. A. Bassett, L.-C. Ming, Physics of the Earth and Planets Interiors, ***6***, 154 (1972)
[114] R. Boehler, A. Chopelas, Geophys. Res. Lett., ***18***, 1147 (1991)
[115] R. J. Hemley, H. K. Mao, M. Somayazulu, Y. Ma, P. F. McMillan, G. H. Wolf, In *6rd NIRIM International Symposium on Advanced Materials (ISAM '99)*, National institute for Research in Inorganic Materials, p. 15, (1999).
[116] G. Shen, H. K. Mao, R. J. Hemley, In *3rd NIRIM International Symposium on Advanced Materials (ISAM '96)*, National institute for Research in Inorganic Materials, p. 149, (1996).
[117] A. Zerr, G. Serghiou, R. Boehler, In *5th NIRIM International Symposium on Advanced Materials (ISAM '98)*, National institute for Research in Inorganic Materials, p. 5, (1998).
[118] H. Sumiya, S. Satoh, S. Yusa, Rev. High Pressure Sci. Technol., *7*, 960 (1998)
[119] H. Sumiya, N. Toda, Y. Nishibayashi, S. Satoh, Journal of Crystal Growth, ***178***, 485 (1997)
[120] D. Walker, Am. Min., ***76***, 1092 (1991)
[121] D. Walker, M. A. Carpenter, C. M. Hitch, Am. Min., ***75***, 1020 (1990)
[122] K. Leinenweber, J. Parise, J. Solid State Chem., ***114***, 277 (1995)
[123] C. M. Bertka, Y. Fei, J. Geophys. Res., ***102***, 5251 (1997)
[124] F. D. Murnaghan, Proc. Nat. Acad. Sci. USA, ***30***, 244 (1944)
[125] F. Birch, J. Geophys. Res., ***37***, 227 (1952)
[126] F. Birch, J. Geophys. Res., ***83***, 1257 (1978)
[127] P. Vinet, J. H. Rose, J. Ferrante, J. R. Smith, J. Phys.: Condens. Matter, ***1***, 1941 (1989)
[128] W. Schnick, Angew. Chem. Int Ed., ***38***, 1999 (1999)
[129] A. E. Ringwood, M. Seabrook, Nature, ***193***, 158 (1962)
[130] J. Dong, J. Deslippe, O. F. Sankey, E. Soignard, P. F. McMillan, Phys. Rev. B, ***67***, 094104 (2003)
[131] P. Kroll, in Press, (2003)
[132] G. A. de Wijs, C. M. Fang, G. Kresse, G. de With, Phys. Rev. B, ***65***, art. no. (2002)
[133] H. Cynn, S. K. Sharma, T. F. Cooney, M. Nicol, Phys. Rev. B, ***45***, 500 (1992)
[134] M. Ishii, J. Hiraishi, T. Yamanaka, Phys. Chem. Miner., ***8***, 64 (1982)
[135] M. P. O'Horo, A. L. Frisillo, W. B. White, J. Phys. Chem. Solids, ***34***, 23 (1973)
[136] P. F. McMillan, S. K. Deb, J. Dong, J. Raman Spectrosc., ***34***, 567 (2003)
[137] A. P. Mirgorodsky, M. I. Baraton, P. Quintard, Phys. Rev. B, ***48***, 13326 (1993)
[138] E. G. Ponyatovsky, O. I. Barkalov, Materials Science Reports, ***8***, 147 (1992)
[139] P. F. McMillan, In *International School of Physics "Enrico Fermi" Course CXLVII: High Pressure Phenomena,* ed.: R. J. Hemley, G. L. Chiarotti, OIS Press, p. 511, (2001).
[140] A. Zerr, Phys. Status Solidi B-Basic Res., ***227***, R4 (2001)

[141] P. Kroll, J. von Appen, Phys. Status Solidi B-Basic Res., ***226***, R6 (2001)
[142] W. Lengauer, Journal of Crystal Growth, ***87***, 295 (1988)
[143] F. Cora, P. F. McMillan, in preparation,
[144] D. M. Teter, MRS Bulletin, ***23***, 22 (1998)
[145] K. H. Rieder, W. Drexel, Phys. Rev. Lett., ***34***, 148 (1975)
[146] H. Bilz, W. Kress, *Phonon Dispersion Relations in Insulators, Vol. 10*, Springer, Berlin Heidelberg New York, **1979**.
[147] W. Spengler, R. Kaiser, Solid State Commun., ***18***, 881 (1976)